

Thermo-Hydro-Mechanical-Chemical Modelling for Carbon Capture and Storage: A Mixture Coupling Theory Approach

Sulaiman M. Abdullah

Submitted in accordance with the requirements for the degree of Doctor of Philosophy

University of Leeds
School of Civil Engineering

April 2024

Declaration and publication

The candidate confirms that the work submitted is his own, except where work which has formed part of jointly-authored publications has been included. The contribution of the candidate and the other authors to this work has been explicitly indicated below. The candidate confirms that appropriate credit has been given within the thesis where reference has been made to the work of others.

PUBLICATION LIST:

 The work of chapter 3 has been Published by the journal Transport in Porous Media:

"ABDULLAH, S., MA, Y., CHEN, X. & KHAN, A. 2022. A fully coupled hydro-mechanical-gas model based on mixture-coupling theory. Transport in Porous Media, 143(1), 47-68" (Q1 in Chemical Engineering, IF:2.9)

The contributions of each co-author were as follows:

- Sulaiman Abdullah: Led the writing of the paper, derived the mathematical model, and conducted numerical simulations and validation.
- 2. Yue Ma: Reviewed the mathematical derivation.
- 3. X. Chen: Oversaw the planning and execution of the research activities.
- 4. Amirul Khan: Provided the final work review and checked the writing for clarity.

The work of chapter 4 has been Published by Geomechanics and Geoengineering:
 "ABDULLAH, S., MA, Y., WANG, K., SUBRAMANYAM, S., CHEN, X. & KHAN, A. 2023. Two-phase interaction in isothermal hydro-mechanical-chemical coupling for improved carbon geological sequestration modelling.
 Geomechanics and Geoengineering, 1-19" (Q2 in Geotechnical Engineering and Engineering Geology)

The contributions of each co-author were as follows:

- Sulaiman Abdullah: Led the writing of the paper, derived the mathematical model, conducted numerical simulations, carried out sensitivity analysis, and prepared the draft manuscript.
- 2. Yue MA: Reviewed the mathematical derivation.
- 3. Kai Wang: Reviewed the simulation and results.
- 4. Shashank Subramanyam: Checked the writing and discussion for overall coherence.
- 5. X. Chen: Supervised the overall work and suggested the structure of the paper.
- 6. Amirul Khan: Final review of the overall paper before submitting to the journal.
- The work of chapter 5 has been Published by the journal Transport in Porous Media:
 - "ABDULLAH, S., MA, Y., CHEN, X. & KHAN, A. 2023. Coupled Reactive Two-Phase Model Involving Dissolution and Dynamic Porosity for Deformable

Porous Media Based on Mixture-Coupling Theory. Transport in Porous Media, 151(1), 1-28" (Q1 in Chemical Engineering, IF:2.9)

- Sulaiman Abdullah: Led the writing of the paper, derived the two-phase transport mathematical model, implemented the numerical simulation, and wrote the draft manuscript of the paper.
- 2. Yue MA: Checked the mathematical derivation and provided suggestions.
- 3. X. Chen: Supervised the work and reviewed the abstract, introduction, and results.
- 4. Amirul Khan: Reviewed the final manuscript before submission to the journal.
- The work of chapter 6 has been Published by Geomechanics for Energy and the Environment:
 - "ABDULLAH, S., WANG, K., CHEN, X. & KHAN, A. 2023. The impact of thermal transport on reactive THMC model for carbon capture and storage. Geomechanics for Energy and the Environment, 36, 100511" (Q1 in Geotechnical Engineering, IF:5.1)
 - 1. Sulaiman Abdullah: Led the writing process, derived the mathematical equations, conducted the numerical simulation, and wrote the manuscript.
 - 2. Kai Wang: Reviewed the mathematics and the simulation results.
 - 3. X. Chen: Supervised the work and reviewed the final manuscript.
 - 4. Amirul Khan: Reviewed the final manuscript prior to submitting to the journal.

This copy has been supplied on the understanding that it is copyright material and that no quotation from the thesis may be published without proper acknowledgement.

The right of Sulaiman M. Abdullah to be identified as Author of this work has been asserted by him in accordance with the Copyright, Designs and Patents Act 1988.

Abstract

In pursuit of advancing the field of geoenergy, this thesis presents a Thermo-Hydro-Mechanical-Chemical (THMC) model specifically derived for the simulation of Carbon Capture and Storage (CCS) processes. The introduced model addresses the dynamic interactions of gas migration, water transport, and mechanical deformation in deformable porous media. Building upon mixture-coupling theory and based on non-equilibrium thermodynamics, the model introduces novel perspectives and governing equations that capture the complexities of two-phase fluid dynamics and the details of chemical reactions within a geological context. Moreover, central to this thesis is the characterisation of the coupling effects among fluid phases, solid deformation, and thermal properties, which are crucial in determining the efficiency and sustainability of CCS operations. Through comparison with experimental data from the literature, the developed model showed good agreement with the data. Sensitivity analyses within the studies further shed light on the critical roles of relative permeability and saturation, revealing the subtleties of frictional behaviour and its implications for fluid flow in porous media.

Additionally, the model is further extended by incorporating chemical reaction dynamics, providing insights into the significant influence of calcite dissolution on porosity and permeability alterations. The simulations reveal that chemical reactions are not simply a secondary factor but a driving force in the evolution of geological storage properties. The

research findings also indicate that temperature variations significantly affect dissolution processes, with long-term implications for porosity and permeability.

As the global community confronts the challenges of climate change, the importance of refining CCS strategies cannot be overstated. This thesis extends the existing mixture coupling theory for two-phase transport, accounting for energy losses from two-phase interactions (friction) and solute transport within the mixture. Additionally, it integrates a chemical coupling process into the two-phase model (dissolution process) by utilizing the concepts of affinity and extent of the reaction. Furthermore, thermal coupling is included to develop a novel two-phase THMC coupled model that can be used to simulate CCS process, primarily for academic purposes, with the potential for real-world field applicability through further extensions. Future research directions are proposed to further fine-tune the model, ensuring that it remains responsive to the complex and evolving demands of environmental sustainability and energy management.

List of Abbreviations

CCS Carbon Capture and Storage

EOR Enhanced Oil Recovery

FEM Finite Element Method

GHG Greenhouse Gases

HM Hydro-Mechanical

HMC Hydro-Mechanical-Chemical

HMG Hydro-Mechanical-Gas

THM Thermo-Hydro-Mechanical

THMC Thermo-Hydro-Mechanical-Chemical

Table of Contents

| Abstract | t5 | |
|------------|---|------|
| List of A | Abbreviations7 | |
| List of T | Tables | |
| List of fi | igures | |
| Acknow | ledgment | |
| _ | 1: Introduction | |
| 1.1 | OVERVIEW AND BACKGROUND | . 22 |
| 1.1.1 | l Global Warming | . 22 |
| 1.1.2 | 2 Carbon Capture and Storage | . 27 |
| 1.1.3 | 3 Transport of a Mixture in Porous Media and Coupling Process | . 31 |
| 1.1.4 | 4 Types of Geological Sequestration Based on Targeted Formation | . 33 |
| 1.2 | IMPORTANCE OF MODELLING THE CCS PROCESS | . 34 |
| 1.3 | METHODOLOGY OVERVIEW | . 36 |
| 1.3.1 | l Current Modelling Methodologies | . 37 |
| 1.3.2 | 2 Software | . 38 |
| 1.4 | RESEARCH PROBLEM AND KNOWLEDGE GAP | . 39 |
| 1.4.1 | l Current Challenges in Research | . 39 |
| 1.5 | AIM AND OBJECTIVES OF THE STUDY | . 40 |
| 1.5.1 | l Aims of the Study | . 40 |
| 1.5.2 | 2 Study Objectives | . 41 |
| 1.6 | SIGNIFICANCE OF THE STUDY | . 43 |
| 1.7 | THESIS STRUCTURE | . 44 |
| 1 0 | Cover region | 4 - |

| 2: Literature review | . 46 |
|--|--|
| BACKGROUND | |
| THE IMPORTANCE OF MULTI-PHASE MODELLING IN CCS | |
| ANALYSIS OF PHASE COUPLINGS IN MULTI-PHASE SYSTEMS | |
| Hydro-Mechanical Coupling (HM) (Poroelasticity) | |
| Hydro-Mechanical-Chemical Coupling (HMC) | |
| Thermo-Hydro-Mechanical (THM) Coupling | |
| Thermo-Hydro-Mechanical-Chemical (THMC) Coupling | |
| Software and Simulation Tool | |
| Modelling Carbon Sequestration | |
| THE MODELLING APPROACHES | |
| From Mechanics to Mixtures: A Historical Perspective | |
| Mixture-Coupling Theory: Advancements and CCS Modelling | |
| SURVEYING THE FIELD: RECENT DEVELOPMENTS OF COUPLED MODELLING OF | |
| 72 | |
| Knowledge Gaps | |
| CONCLUSION AND FORWARD TRAJECTORY | |
| • • | |
| Introduction | |
| PHYSICAL MODEL | (|
| Definition of flux, density, volume fraction and saturation | |
| Balance equation | |
| Entropy product and transport law | |
| Hydro-mechanical framework equation | |
| nyaro-mechanicai framework equation | |
| | BACKGROUND THE IMPORTANCE OF MULTI-PHASE MODELLING IN CCS ANALYSIS OF PHASE COUPLINGS IN MULTI-PHASE SYSTEMS. Hydro-Mechanical Coupling (HM) (Poroelasticity) Hydro-Mechanical-Chemical Coupling (HMC) Thermo-Hydro-Mechanical (THM) Coupling Thermo-Hydro-Mechanical-Chemical (THMC) Coupling Software and Simulation Tool MODELLING CARBON SEQUESTRATION. THE MODELLING APPROACHES From Mechanics to Mixtures: A Historical Perspective Mixture-Coupling Theory: Advancements and CCS Modelling SURVEYING THE FIELD: RECENT DEVELOPMENTS OF COUPLED MODELLING OF 72 KNOWLEDGE GAPS CONCLUSION AND FORWARD TRAJECTORY. 3: A Fully Coupled Hydro-Mechanical-Gas Model Based On Mixtupling Theory INTRODUCTION PHYSICAL MODEL Definition of flux, density, volume fraction and saturation Balance equation |

| 3.2. | .5 Coupled hydro-mechanical governing equations | 102 |
|------|---|----------|
| 3.3 | NUMERICAL SOLUTION | 108 |
| 3.4 | Conclusions | 120 |
| - | er 4: Two-Phase Interaction in Isothermal Hydro-Mechanical-Coupling for Improved Carbon Geological Sequestration Modellin | |
| 4.1 | 1. Introduction | 127 |
| 4.2 | PHYSICAL MODEL | 130 |
| 4.2. | .1 Flux equations: | 132 |
| 4.2. | .2 Mass and energy balance equations | 133 |
| 4.3 | DISSIPATION ENTROPY | 134 |
| 4.4 | COUPLED PHASES INTERACTIONS AND PHENOMENOLOGICAL EQUATIONS | 135 |
| 4.5 | CONSTITUTIVE EQUATIONS | 138 |
| 4.5. | .1 Helmholtz free energy density of pore space | 139 |
| 4.5. | .2 Free energy density of solid matrix | 139 |
| 4.5. | .3 Governing field equations | 141 |
| 4.6 | VALIDATION AND NUMERICAL SIMULATION | 146 |
| 4.6. | .1 General model validation | 146 |
| 4.7 | Conclusion | 166 |
| dy | er 5: Coupled reactive two-phases model involving dissoluty ynamic porosity for deformable porous media based on Mixture-theory | Coupling |
| 5.1 | Introduction | 170 |
| 5.2 | MATHEMATICAL MODEL | 175 |
| 5.2. | .1 Flux and diffusion: | 177 |
| 5.2. | .2 Chemical reaction and dissolution | 177 |
| 5.2. | .3 Energy, entropy, and phenomenological equations: | 179 |

| | 5.2.4 | Constitutive relations | 184 |
|-------------------|---|--|--|
| | 5.2.5 | Governing equation for the mechanical behaviour: | 187 |
| | 5.2.6 | Governing equation for the fluid phase transport | 190 |
| | 5.2.7 | Governing equation for the chemical phase transport | 192 |
| 5.3 | | VALIDATION AND COMPARISON WITH OTHER MODELS | 194 |
| 5.4 | | NUMERICAL SIMULATION | 195 |
| | 5.4.1 | Study subject and geometry | 196 |
| | 5.4.2 | Simulation assumptions: | 201 |
| | 5.4.3 | Results and discussion | 201 |
| | | CONCLUSION | 210 |
| 5.5 | | | |
| | | 6: The Impact of Thermal Transport on Reactive THMC Model for rbon Capture and Storage | |
| | Caı | <u>-</u> | |
| Chap | Cai | rbon Capture and Storage | 214 |
| 6.1 6.2 | Cai | rbon Capture and Storage | 214 218 |
| 6.1 6.2 | Cai | The Capture and Storage | 214 218 <i>218</i> |
| 6.1 6.2 | Cai | The Capture and Storage | 214 218 <i>218</i> <i>220</i> |
| 6.1 6.2 | Ca 1 6.2.1 6.2.2 | Thon Capture and Storage | 214 218 218 220 221 |
| 6.1 6.2 | 6.2.1 6.2.2 6.2.3 6.2.4 | Thon Capture and Storage | 214 218 218 220 221 221 |
| 6.1 6.2 6.3 | 6.2.1 6.2.2 6.2.3 6.2.4 | Thon Capture and Storage | 214 218 218 220 221 221 222 |
| 6.1 6.2 6.3 | 6.2.1 6.2.2 6.2.3 6.2.4 | The balance of internal energy. | 214 218 218 220 221 221 222 222 |
| 6.1 6.2 6.3 | 6.2.1 6.2.2 6.2.3 6.2.4 6.3.1 | The balance of internal energy. | 214 218 218 220 221 221 222 222 222 |
| 6.1 6.2 6.3 | 6.2.1 6.2.2 6.2.3 6.2.4 6.3.1 | INTRODUCTION | 214 218 218 220 221 221 222 222 223 223 |

| 6.4.3 | Helmholtz free energy of pore space | 228 |
|----------|---|-----|
| 6.4.4 | Free energy density of the solid matrix and Maxwell relations | 228 |
| 6.5 | THMC governing equations | 231 |
| 6.5.1 | Solid phase behaviour | 231 |
| 6.5.2 | Liquid phase behaviour | 233 |
| 6.5.3 | Supercritical phase behaviour | 235 |
| 6.5.4 | Chemical transport | 235 |
| 6.5.5 | Thermal transport | 236 |
| 6.6 | NUMERICAL SOLUTION: | 237 |
| 6.6.1 | Chemical reaction | 239 |
| 6.6.2 | Properties and constants | 242 |
| 6.7 | RESULTS AND DISCUSSION | 244 |
| 6.8 | CONCLUSION | 257 |
| Chapter | 7: Conclusion and future work recommendations | 260 |
| 7.1 | CONCLUSION | 260 |
| 7.2 | LIMITATION, AND FUTURE WORK RECOMMENDATIONS | 263 |
| Referenc | es | 267 |

List of Tables

carbon

| Table 1.1: Atmospheric Lifetime and Global Warming Potential (GWP) of Various |
|---|
| Greenhouse Gases (Forster et al., 2021) |
| Table 2.1: Minerals that may considered in the coupled chemical process (Zhang et |
| al., 2015) 60 |
| Table 4.1: Parameters used for Liakopoulos drainage test (Liakopoulos, 1965b).149 |
| Table 4.2: Rock sample parameters |
| Table 5.1: Physical parameters used in the conceptional model (Zhou and Burbey, |
| 2014b; Hart and Wang, 1995; Parkhurst and Appelo, 2013) 199 |
| Table 6.1: Properties/ parameters used in the simulation |

List of figures

| Figure 1.1: Global CO ₂ emission by countries (Crippa et al., 2022) |
|--|
| Figure 1.2: CO_2 emission changes in the main sector (1990-2021) (Crippa et al., |
| 2022) |
| Figure 1.3: Global temperature and atmospheric CO ₂ change (Matthews and |
| Wynes, 2022) |
| Figure 2.1: THM triangle coupling relationship (Wang et al., 2014) 59 |
| Figure 2.2: THMC coupled process (Tao et al., 2019) |
| Figure 3.1: Initial and boundary conditions for Liakopoulos (1965a) drainage test.111 |
| Figure 3.2: Simulation results vs Liakopoulos' experiment data (water pressure)114 |
| Figure 3.3: Simulation results vs Schrefler and Scotta's results (water pressure)115 |
| Figure 3.4: Simulation results vs Schrefler and Scotta's results (air pressure) 115 |
| Figure 3.5: Simulation results vs Schrefler and Scotta's results (capillary pressure)116 |
| Figure 3.6: Simulation results vs Schrefler and Scotta's results (water saturation)116 |
| Figure 3.7: Simulation results vs Schrefler and Scotta's results (displacement) 117 |
| Figure 3.8: Simulation results vs Islam et al. results (displacement) |

| Figure 3.9: 2D triangular mesh geometry created and solved using COMSOL |
|--|
| Multiphysics |
| Figure 3.10: Simulation results vs experimental data |
| Figure 4.1: Initial and boundary conditions for Liakopoulos drainage tes (Liakopoulos, 1965b) |
| Figure 4.2: Liakopoulos (1965b) experiment vs simulation results of liquid pressure (p^l) distributed through sand column at different times |
| Figure 4.3: Simulation and Schrefler and Scotta (2001) results for air pressure (p^8) |
| Figure 4.4: Air pressure (p^g) distribution at 0, 10, 30, 60, and 120 min 154 |
| Figure 4.5: Simulation and Schrefler and Scotta (2001) results for liquid saturation S^{T} |
| Figure 4.6: Simulation and Schrefler and Scotta (2001) results for mechanical deformation of porous medium |
| Figure 4.7: Mass fraction change due to diffusion (chemical transport) in sand column |
| Figure 4.8: Chemical concentration (mass fraction of NaCl) distribution at 1, 20 60, and 120 min |
| Figure 4.9: Initial and boundary conditions of rock sample |

| Figure 4.10: Water pressure at coordinate point (0.1,0.25) at different r_1 and r_2 |
|--|
| values |
| Figure 4.11: Supercritical pressure at coordinate point (0.1,0.25) at different r_1 and |
| <i>r</i> ₂ values |
| Figure 4.12: Horizontal deformation at coordinate point (0.1,0.25) at different r_1 |
| and r_2 values |
| Figure 4.13: Supercritical and water saturation at different times (hours), across |
| horizontal cross section of the sample with $r_1 = r_2 = 0$ |
| Figure 4.14: Water pressure across horizontal section of sample at different r_1 and |
| <i>r</i> ₂ values |
| Figure 4.15: Supercritical pressure across horizontal section of sample at different |
| r_1 and r_2 values |
| Figure 4.16: Deformation across horizontal section of sample at different r_1 and r_2 |
| values |
| Figure 5.1: Cross couplings relations of the HMC model: 1. Change due to strain |
| term $\zeta \dot{\varepsilon}_{ii}$, 2. Effect the mechanical properties, 3. Change due to pore |

| pressure term $Q\dot{p}^{p}$, 4. Effect the pore pressure, 5. Change due to |
|---|
| chemical reaction term $D\dot{\xi}$, 6. Change in reactive surface area 194 |
| Figure 5.2: Initial and boundary conditions for two-phase flow into carbonate rock |
| sample |
| Figure 5.3: Liquid pressure across the horizontal distance of the sample rock 202 |
| Figure 5.4: CO_2 pressure across the horizontal distance of the sample rock 203 |
| Figure 5.5: Horizontal displacement across the horizontal distance of the sample |
| rock |
| Figure 5.6: Concentration of Ca ⁺ across the horizontal distance of the sample rock. |
| |
| Figure 5.7: Liquid saturation across the horizontal distance of the sample rock.205 |
| Figure 5.8: ScCO ₂ saturation across the horizontal distance of the sample rock.206 |
| Figure 5.9: Porosity and permeability change at Point1 of 2D sample rock 206 |
| Figure 5.10: Comparison between the porosity change due to strain term and |
| chemical reaction term across the horizontal distance of the sample |
| rock |

| Figure 5.11: Comparison between the porosity change due to pressure term and |
|--|
| chemical reaction term across the horizontal distance of the sample |
| rock |
| Figure 5.12: Effects of liquid pressure, supercritical pressure, and the extent of |
| reaction on the volumetric strain at Point 1 in the 2D rock sample.209 |
| Figure 5.13: Dissolution rate at across the horizontal section of the sample rock.210 |
| Figure 6.1: Representative Elementary Volume (REV) |
| Figure 6.2: 2D model of cylindrical limestone rock sample with injection port in |
| the centre left side |
| Figure 6.3: Temperature change for THMC model in a non-isothermal system.246 |
| Figure 6.4: Dissolution rate <i>r</i> for THMC vs HMC model |
| Figure 6.5: Calcium ions concentration in isothermal (HMC) vs non-isothermal |
| (THMC) condition |
| Figure 6.6: $\zeta \mathcal{E}_{ii}$, Qp^p , $D\xi$, and NT coupling terms of the dynamic porosity for |
| THMC model |
| Figure 6.7: Change in porosity and permeability for HMC vs THMC model in |
| 3000h |
| Figure 6.8: Change in porosity and permeability for HMC vs THMC model in 20 |
| vears 250 |

| Figure 6.9: The porosity returns to its initial value in about 7.5 months 25 | 51 |
|--|----|
| Figure 6.10: Horizontal displacement across the rock sample at different times for | or |
| HMC vs THMC model | 52 |
| Figure 6.11: Horizontal displacement (deformation) and capillary pressure at Point | nt |
| 1 in the sample for HMC vs THMC model | 52 |
| Figure 6.12: Liquid pressure for isothermal and non-isothermal conditions | at |
| various times across the horizontal section of the sample rock for | or |
| HMC vs THMC model | 54 |
| Figure 6.13: ScCO ₂ pressure for isothermal and non-isothermal conditions | at |
| various times across the horizontal section of the sample rock for | or |
| HMC vs THMC model | 54 |
| Figure 6.14: Permeability of the liquid for HMC vs THMC model | 55 |
| Figure 6.15: Permeability of the ScCO ₂ for HMC vs THMC model | 55 |
| Figure 6.16: Liquid saturation for HMC vs THMC model | 56 |
| Figure 6.17: ScCO ₂ saturation for HMC vs THMC model | 56 |

Acknowledgment

I would like to extend my deepest gratitude to my advisor, Dr. Xiaohui Chen, for his invaluable guidance, unwavering support, and insightful feedback throughout my PhD journey. His dedication to excellence and commitment to fostering a nurturing and intellectually stimulating environment have profoundly impacted my personal and professional growth. Dr. Chen's mentorship has been a cornerstone of my academic achievements, and for that, I am eternally grateful.

I also wish to express my sincere appreciation to my second supervisor, Dr. Amirul Khan, for his expert advice, constructive criticisms, and encouraging words. Dr. Khan's vast knowledge and analytical rigor have significantly enriched my research experience, pushing me to explore new frontiers and challenging me to think more deeply and critically.

My heartfelt thanks go to Kuwait Petroleum Company for their generous sponsorship and unwavering faith in my potential.

I am also indebted to my colleagues and friends, who have been a source of inspiration, encouragement, and companionship. Their shared enthusiasm and collective wisdom have greatly enhanced my PhD experience.

Finally, I cannot express enough thanks to my family for their love and support throughout my academic journey. Their endless patience, understanding, and encouragement have been my stronghold. This achievement is not only mine but also theirs.

This journey has been challenging, enlightening, and ultimately rewarding. I am grateful to everyone who played a part in making my PhD experience both memorable and successful.

Chapter 1: Introduction

1.1 Overview and Background

1.1.1 Global Warming

Human activities have become one of the major sources of harmful gases known as greenhouse gases (GHG). GHG include CO_2 , methane, nitrous oxide, ozone, and other gases. They represent one of the most significant problems threatening the environment. GHGs do not trap sunlight directly; instead, they predominantly trap outgoing long-wavelength radiation from the Earth's surface, rather than incoming solar radiation. This process causes heat to be retained in the atmosphere, leading to global warming and climate change. CO_2 naturally exists in the atmosphere and is necessary for life to continue. The plant system on Earth forms the basis of life, and plants rely on CO_2 for photosynthesis. In addition to trees, marine plants and plant-like organisms are the primary sources of oxygen in the atmosphere. Marine plants are responsible for 70% of the atmosphere's oxygen; they absorb a considerable amount of CO_2 and produce oxygen (Kumar et al., 2021).

 CO_2 gas by itself is not the most effective element among the GHG in term of the ability to store and re-emit the thermal energy, some other gases have a higher ability to absorb and trap the thermal energy in the atmosphere. However, there smaller quantity makes them less effective than CO_2 . One way to determine the capability of a gas to trap the heat in the atmosphere is global warming potential (GWP). GWP is an index that

measures the ability of greenhouse gases to absorb the infrared thermal radiation over a specific period, if added to the atmosphere. The GWP represented as a multiple of the radiation absorbed by an equivalent mass of CO_2 , which serves as the reference gas with a GWP value of 1.

However, the atmospheric lifetime of the gas is also considered in the GWP, for example, methane has shorter lifetime than ${\rm CO_2}$ but higher ability to absorb and radiate the thermal infrared energy, because of that, the GWP for methane is higher when consider short time period (ex. 20 years) but has a lower value when consider long period time (ex. 100 years). Table 1.1 shows a table of GHGs GWP at 20, 100, and 500 years period (Forster et al., 2021).

Table 1.1: Atmospheric Lifetime and Global Warming Potential (GWP) of Various Greenhouse Gases (Forster et al., 2021)

| GHG | Lifetime (years) | Radiative Efficiency (Wm ⁻² ppb ⁻¹ , molar basis) | GWP (20 years) | GWP (100 years) | GWP (500 years) |
|----------------------------------|---------------------|---|-------------------|--------------------|-----------------|
| CO_2 | Multiple | 1.37×10^{-5} | 1 | 1 | 1 |
| CH ₄ | 12 | 5.7×10^{-4} | 83 | 30 | 10 |
| CH ₄ | 12 | 5.7×10^{-4} | 81 | 27 | 7.3 |
| N ₂ O | 109 | 3×10^{-3} | 273 | 273 | 130 |
| CCl ₃ F | 52 | 0.29 | 8,321 | 6,226 | 2,093 |
| CCl ₂ F ₂ | 100 | 0.32 | 10,800 | 10,200 | 5,200 |
| CHClF ₂ | 12 | 0.21 | 5,280 | 1,760 | 549 |
| CH ₂ F ₂ | 5 | 0.11 | 2,693 | 771 | 220 |
| CH ₂ FCF ₃ | 14 | 0.17 | 4,144 | 1,526 | 436 |
| CF ₄ | 50,000 | 0.09 | 5,301 | 7,380 | 10,587 |
| C ₂ F ₆ | 10,000 | 0.25 | 8,210 | 11,100 | 18,200 |
| SF ₆ | 3,200 | 0.57 | 17,500 | 23,500 | 32,600 |
| NF ₃ | 500 | 0.2 | 12,800 | 16,100 | 20,700 |

Despite the fact that the CO_2 has relatively lower GWP compared to other greenhouse gases, CO_2 is a significant concern and considered as the main gas that need to be reduced now. This is because of the high quantity human produced annually, its long

atmospheric lifetime, and its dominant role in driving human-caused climate change. CO_2 is emitted in large quantities from activities like burning fossil fuels, deforestation, and industrial processes, making it the most common greenhouse gas in the atmosphere. Its long-lasting existence means that the CO_2 released today will continue to impact the climate for many years. The other GHG either has lower quantity production or it is out of our control to reduce. To show how dramatically the CO_2 is generated annually, Figure 1.1 shows CO_2 emissions in the recent years, the significant quantity of CO_2 produced makes it the most threating GHG that need to be under control. CO_2 emissions have increased even more in recent years, which accelerate the danger of getting to a point where reducing the CO_2 emission alone is not enough anymore

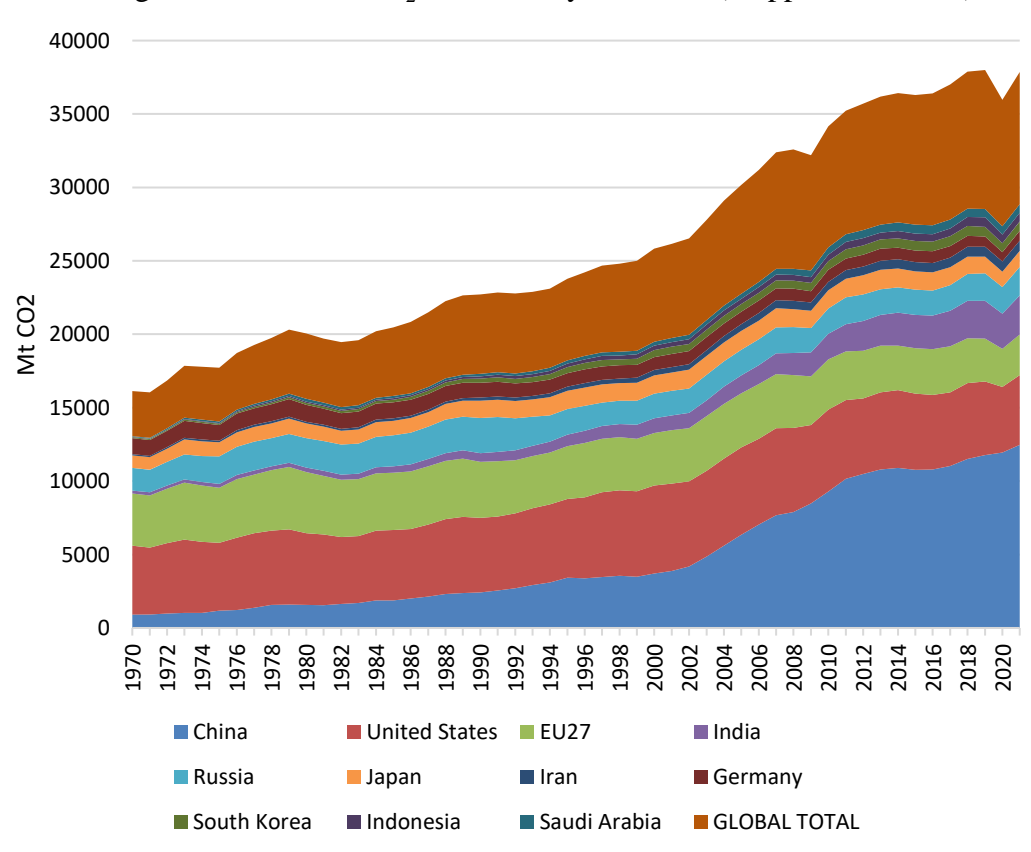
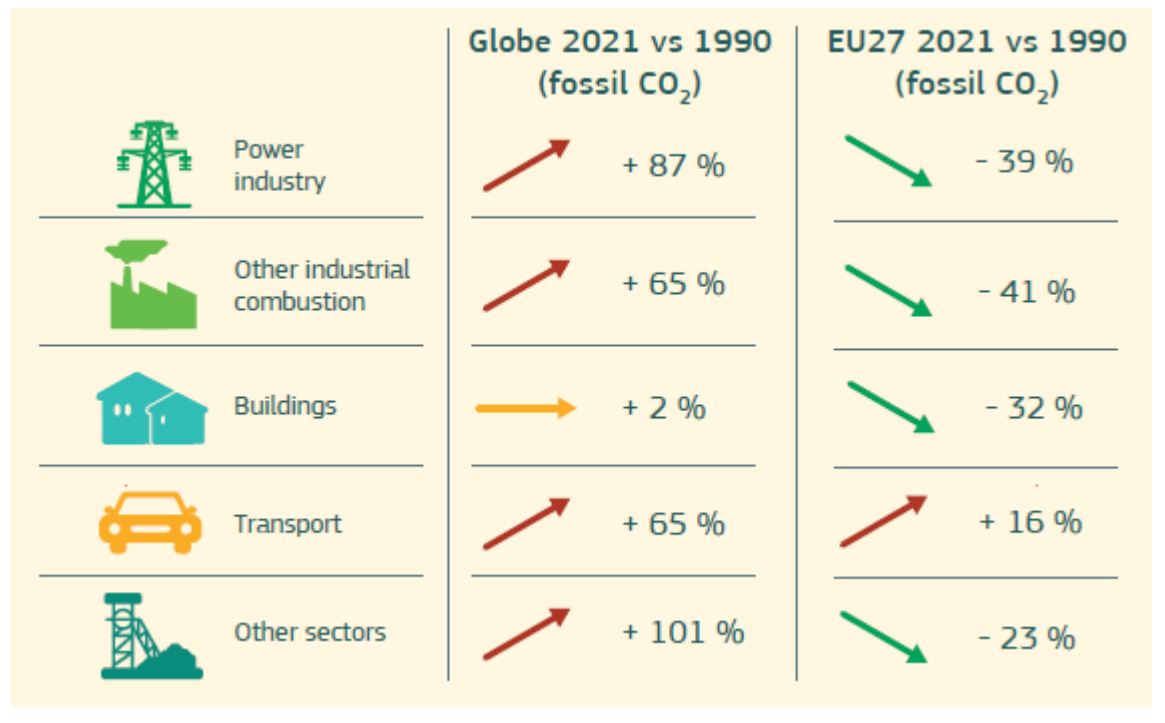


Figure 1.1: Global CO₂ emission by countries (Crippa et al., 2022)

 ${
m CO}_2$ increased since the Industrial Revolution due to the increasing demand for energy and transportation. While natural sources like volcanoes and wildfires contribute to ${
m CO}_2$ levels, human activities, particularly energy production and transportation, are the major contributors to the rise in emissions. Figure 1.2 shows the ${
m CO}_2$ emission changes in the main sector in the recent 30 years. As humans began cutting trees and burning fossil fuels, they started producing an exponentially increasing amount of ${
m CO}_2$, driven by population growth and energy demand. This excess ${
m CO}_2$ raises atmospheric temperatures, leading to polar ice melt, rising sea levels, and the destruction of marine reefs, all of which threaten both wildlife and human habitats.

Figure 1.2: ${\rm CO_2}$ emission changes in the main sector (1990-2021) (Crippa et al., 2022)



The impact of CO_2 emissions on our atmosphere since 1850 resulted in an increase in the average global temperature by approximately 1.2 °C as shown in Figure 1.3. Many

governments and organizations established rules and regulations to deaccelerate GHG emissions such as the agreement known as Paris agreement that aims to reduce the GHG emissions and thus reduce the average global warming by 1.5 °C. However, until now, there was no major change in the emission rate (Matthews and Wynes, 2022). Meanwhile, researchers found ways to use some GHG for human favour, such as CO₂. For example, ${\rm CO}_2$ can be injected into the ground (${\rm CO}_2$ sequestration) to enhance oil and gas recovery (Wei et al., 2020a).

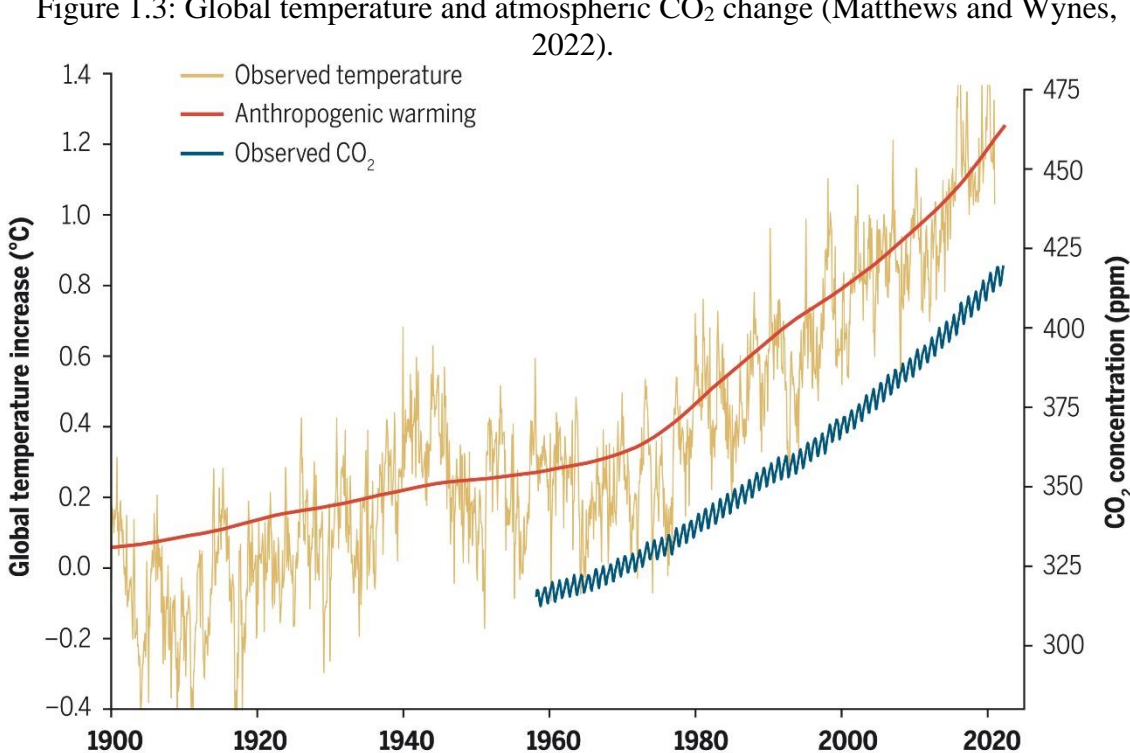


Figure 1.3: Global temperature and atmospheric CO₂ change (Matthews and Wynes,

Moreover, the energy transition presents a significant challenge. Given the current size of the fossil fuel market in the economy, switching to green energy will require major changes in investments and infrastructure, including power plants, automobiles (switching to electric), and more. This transition could take decades to fully implement, and certain parties may resist to protect their profitable investments in fossil fuels. In the meantime, Carbon Capture and Storage (CCS) offers a viable solution during this transition period. Waiting for decades without addressing ${\rm CO_2}$ emissions could result in irreversible environmental damage or significantly delay recovery.

1.1.2 Carbon Capture and Storage

Human activities have led to the massive extraction and burning of fossil fuels, releasing enormous amounts of carbon dioxide into the atmosphere and contributing to climate change, as fossil fuel combustion converts stored carbon into ${\rm CO}_2$. While it might seem that the simple solution is to stop burning fossil fuels, this is far from easy due to the complicated balance required by the energy trilemma. Our global infrastructure relies heavily on fossil fuels to ensure energy security, providing a stable and reliable energy supply. Additionally, energy equity demands that energy remains affordable and accessible, particularly in regions where alternatives like renewables are not yet easy to access. Meanwhile, environmental sustainability calls for urgent reductions in greenhouse gas emissions. Given these complexities, Carbon Capture and Storage (CCS) has emerged as a necessary solution. By capturing and storing ${\rm CO}_2$ emissions from fossil fuel use, CCS allows us to continue meeting energy demands while mitigating environmental impact. Thus, CCS plays a critical role in the transition toward a more sustainable energy future.

Carbon Capture and Storage (CCS) is a crucial technology designed to mitigate the impact of greenhouse gas emissions by capturing ${\rm CO_2}$ produced from industrial and energy-related processes before it reaches the atmosphere. The CCS process involves

three main steps: capture, transport, and storage. ${\rm CO_2}$ is first captured from sources such as power plants and industrial facilities using various methods, including pre-combustion, post-combustion, and oxy-fuel combustion techniques. Once captured, the ${\rm CO_2}$ is then transported, typically via pipelines, to storage sites. Finally, the ${\rm CO_2}$ is injected into deep underground geological formations, such as depleted oil and gas fields or saline aquifers, where it is securely stored for long periods, preventing it from contributing to atmospheric greenhouse gas levels.

Todays, CCS reflects both significant progress and ongoing challenges. The number of CCS projects globally continues to grow; in 2023, the projected CO_2 capture capacity for 2030 increased by 35%, reaching approximately 435 million tonnes (Mt) per year, while storage capacity announcements rose by 70%, bringing it to around 615 Mt per year. Despite this progress, these figures represent only about 40% and 60%, respectively, of the roughly 1 Gt CO_2 per year target set in the Net Zero Emissions by 2050 Scenario (the International Energy Agency (IEA)).

Many countries are starting to implement CCS technologies to achieve their CO_2 emission reduction targets. For instance, Indonesia is aiming to cut carbon emissions by 29% by 2030 and achieve net-zero emissions by 2050. The Indonesian government has initiated 15 CCUS projects scheduled to begin by 2026, which include pilot programs, feasibility studies, and phased implementation utilizing existing oil and gas infrastructure. During the demonstration phase, CO_2 injection will expand to multiple wells at rates of 500–2700 t/d over ten years. The final industrial phase targets large-scale CO_2 capture

of 2700–30,000 t/d, injecting it into various sink locations to significantly reduce emissions (Ramadhan et al., 2024).

Moreover, several large-scale CCS projects such as the Sleipner Project in Norway, the Alberta Carbon Trunk Line in Canada, and the Quest CCS Project, have consistently demonstrated high technical performance, storing significant amounts of CO_2 and providing valuable insights into operational challenges. For instance, the Sleipner Project has stored over 20 million tonnes of CO_2 since 1996, while the Weyburn Project in Canada has safely stored over 35 million tonnes since 2000, showcasing CCS's potential for large-scale deployment (Ma et al., 2022a; Chadwick et al., 2010; Brown et al., 2017). These projects emphasize the importance of reliable infrastructure, public acceptance, and favourable regulatory environments. Key lessons learned include the feasibility of large-scale CCS, effective integration with EOR (Enhanced Oil Recovery), and the need for long-term monitoring. Despite these successes, challenges persist in scaling CCS for lower concentration CO_2 sources and achieving broader commercialization without relying on EOR. The ongoing efforts, such as the BD3 facility in Saskatchewan, highlight progress but also underscore the need for continued innovation to address these challenges (Ma et al., 2022a).

As CCS technology continues to evolve, there is a growing emphasis on increasing efficiency and reducing costs associated with carbon capture, transport, and storage. Recent studies, such as the work by Dods et al. (2021) explore advanced methods like deep CCS, which target capture rates exceeding the conventional 90%. These approaches have the potential to significantly reduce residual emissions from fossil-fuel power plants,

potentially improving the need for extensive Carbon Dioxide Removal (CDR) techniques. Furthermore, emerging policies in regions like the U.S. and Europe are increasingly focused on maximizing the climate impact of CCS, with supportive frameworks being put in place to encourage broader deployment and innovation.

There are three main methods to store CO_2 : terrestrial sequestration, geological sequestration, and ocean sequestration (Punnam et al., 2022). Terrestrial sequestration uses a natural process to absorb the emissions into minerals embedded in the soil, primarily as soil organic matter. Ocean sequestration also occurs naturally through the dissolving process of CO_2 in the ocean. It has been estimated that half of the carbon emissions produced each year are absorbed by these two natural processes, while the rest accumulates in the atmosphere, causing the global warming phenomenon (Kelemen et al., 2019). However, terrestrial sequestration and ocean sequestration can be enhanced artificially using different techniques that allow the soil to absorb more CO_2 or by dissolving more CO_2 into the ocean (Caserini et al., 2022; Kumar and Sangwai, 2023; Wang et al., 2023b).

This research focuses on the third type of CCS, which is geological sequestration methods. In this type of CCS, CO_2 is isolated from a large facility that produces significant emissions, such as a power plant, by capturing the CO_2 before it is released into the atmosphere. The CO_2 is then transported through pipelines, usually in liquid phase at low temperatures near -52°C (Vilarrasa and Rutqvist, 2017), to the injection location. The CO_2 is then heated up and pressurized in deep wells. The injected phase is

usually in supercritical (Sc) or saturated brine ($^{\rm CO}_2$ dissolved in a liquid fluid). The Sc phase is generally preferred since it possesses lower viscosity than the liquid phase and exhibits higher density, enabling it to occupy less volume space in the formation. This characteristic allows for more substantial long-term storage (André et al., 2007b).

Given the vast capacity of geological formations to store CO_2 and the potential for long-term, secure storage, geological sequestration may be considered one of the most promising methods for large-scale CO_2 sequestration. However, it also brings unique challenges, which will be explored in the following chapters. By exploring the viability and efficiency of geological sequestration, this research aims to contribute to a broader understanding of how CCS can be modelled using a coupled constitutive framework and simulated with the finite element method (FEM) for improved planning and a better understanding of transport mechanisms.

1.1.3 Transport of a Mixture in Porous Media and Coupling Process

To better understand the CCS process, the transport of the mixture (CO_2 , water, solutes) needs to be studied. The transport of a mixture in deformable porous media is a complex process that many researchers have attempted to study. This process should consider the transport of multi-phase fluid (liquid, gas, supercritical) and the chemical solutes such as salts and other dissolved minerals in the liquid.

The mixture transport process in CCS is usually accompanied by chemical reactions between the acidic fluid and formation minerals, changes in pressure and temperature, and changes in many other parameters that affect the transport process (Dai et al., 2020).

This complex relationship between parameters is called the coupling relation. The term "coupled processes" is used when a particular process's parameters depend on another process's solution. In the context of Thermo-Hydro-Mechanical-Chemical (THMC) processes, coupling refers to the interdependencies among these four processes: thermal, hydraulic, mechanical, and chemical. For example, if the pressure of the injected fluid rises, the temperature is expected to increase as well, which will increase the velocity of the fluid and accelerate the chemical reactions. This may lead to the dissolution of minerals such as calcite (CaCO₃), thus increasing the porosity (Zhang et al., 2016; Rathnaweera et al., 2017; Sigueira et al., 2017; Akono et al., 2019; Tao et al., 2019; Bager and Chen, 2022). On the other hand, increasing the temperature to a certain level may decrease the solubility of CO₂ in liquid water, thus reducing the acidity of the liquid solution (increasing the pH level) (Abidoye et al., 2015; Peng et al., 2015; Vilarrasa and Rutqvist, 2017; Luo et al., 2022). This will decrease the dissolution rate of the calcite and may lead to precipitation, which could decrease the porosity. This is just one example; however, the pressure, temperature, viscosity, density, state of the fluid, and thermal properties are all incorporated into the coupling process.

Fortunately, the coupling process can be anticipated by deriving a fully coupled framework to simulate the transport process. However, the downside is that such a model can become complicated and solving it requires significant computational power (Vilarrasa et al., 2010; Park et al., 2011; Vilarrasa and Rutqvist, 2017; Buchwald et al., 2021; Ladd and Szymczak, 2021). Furthermore, many models are not fully coupled but are simpler and relatively easier to compute, making them useful tools when high accuracy of the results is not a requirement (Kolditz et al., 2012).

1.1.4 Types of Geological Sequestration Based on Targeted Formation

Many formations can be used to store CO_2 , and their suitability depends on the goal and application. Examples of applications and mechanisms used to store CO_2 through CCS include improving oil and gas recovery (Khurshid and Fujii, 2021; Wei et al., 2020a; Jia et al., 2019; Zhu et al., 2018a; Zhou et al., 2017; Cavanagh and Ringrose, 2014; Adu et al., 2019; Chaturvedi and Sharma, 2023), enhancing methane gas recovery (Mazzotti et al., 2009; Ma et al., 2017; Wang et al., 2017; Fan et al., 2019b), storing by mineralization (Luo et al., 2012; Meng et al., 2021), and storing by dissolving CO_2 in deep saline aquifers (Jayasekara and Ranjith, 2021; Stewart and Riddell, 2022; Wang et al., 2023a; Wang et al., 2022; Riaz and Cinar, 2014).

The state of the fluid (liquid, supercritical, saturated brine), along with the temperature and pressure at which CO_2 is injected, depends on the formation pressure, temperature, and the desired state. Some researchers suggest that injecting CO_2 at a cool temperature may cause a shrinking effect in the formation and thus induce high mechanical stress, potentially leading to fracture instability for the formation and the caprock (Ma et al., 2017; Vilarrasa and Rutqvist, 2017). Furthermore, many researchers have investigated the risk of leakage from the caprock, which prevents CO_2 from escaping to the surface (Ellis et al., 2013; Wertz et al., 2013; Yamamoto et al., 2013; Jayasekara and Ranjith, 2021). The caprock, typically a very low permeability shale layer, might fracture if the pressure of the reservoir exceeds a certain limit (Kaldi et al., 2013; Khazaei and Chalaturnyk, 2017). Such leaks could cause an environmental disaster, affecting nearby

water reservoirs, underground freshwater sources, rivers, or lakes (Petit et al., 2021; Lichtschlag et al., 2021).

As mentioned, injecting CO₂ can be done in a liquid, supercritical, or brine-saturated state. The liquid state is the least common option due to the extremely low temperature requirement (approximately -52°C) to keep the fluid in a liquid state and the potential for creating fractures in the caprock layer (Vilarrasa and Rutqvist, 2017). On the other hand, brine saturation occurs when CO₂ is dissolved in a liquid solution and injected into the well as a liquid. Alternatively, CO₂ can be injected in a supercritical state (ScCO₂), where it is neither a liquid nor a gas. At a pressure of 7.38 MPa and a temperature of 32.8°C (Jayasekara and Ranjith, 2021), the viscosity of CO₂ dramatically decreases compared to its liquid phase, and its density increases compared to the gas phase, resulting in a fluid with relatively low viscosity and high density. This has the advantage of easy injection due to the low viscosity and the reduced volume occupied by the fluid due to its high density (250-700 kg/m³) (Vilarrasa and Rutqvist, 2017).

The advantages and disadvantages of each injection scenario can only be accurately estimated using a robust, fully THMC-coupled mathematical model.

1.2 Importance of Modelling the CCS Process

As mentioned earlier, modelling the transport of mixtures for the CCS process is crucial due to the importance of understanding the benefits and assessing potential risks in the long term. Scientists face many decisions before injecting CO₂ into deep geological formations, such as which rock formation should be chosen and at what pressure,

temperature, and state the CO₂ should be injected. To answer these questions, scientists must create and simulate models with different scenarios and select the optimal options.

Enhancing the modelling techniques for CCS includes improving model accuracy, complexity, and computational efficiency, introducing new modelling approaches to the CCS field, and integrating different modelling approaches. One early mention of the CCS concept, albeit indirectly, can be found in a paper by Nobel laureate in Chemistry Melvin Calvin, published in Science in 1976 (Calvin, 1976). Calvin discussed the importance of carbon management and briefly mentioned the idea of underground storage of CO₂. The concept of CCS, as we understand it today, capturing CO2 from industrial and energyrelated sources, transporting it to a storage location, and isolating it from the atmosphere long-term, began to gain traction in the late 1990s and early 2000s (Stevens et al., 2001; Bachu et al., 1994; Gunter et al., 1993; Bowker and Shuler, 1991). This field has been developed by many scientists and engineers worldwide, drawing upon disciplines such as geology, chemistry, physics, engineering, and environmental science. Researchers continue to improve and enhance the accuracy of these models. Given the complexity of the process and the variety of scenarios in which the CCS process can be implemented, significant research has focused on improving CCS modelling. Enhancing the models typically aims to improve the accuracy of predicted results. However, since CCS is a relatively new application with limited actual case studies, determining accuracy remains challenging. Today, there are some published data about ongoing CCS projects that have been used by researchers to validate their model accuracy (Alcalde et al., 2021; Ahmadi Goltapeh et al., 2022; Rahman et al., 2022; Hill et al., 2020; White et al., 2020; Rangriz Shokri et al., 2021; Matter et al., 2009; Bissell et al., 2011; Li et al., 2016; Khazaei and Chalaturnyk, 2017; Petit et al., 2021).

Improving the modelling framework is crucial to maximizing the benefits of the CCS process. The complex process needs continuous enhancement, especially for the coupling process that includes chemical transport, thermal transport, multi-phase flow, mass transfer, porosity evolution, and changes in permeability. The aim of this research is to advance the modelling process by enhancing the coupling terms between the thermal, hydrological, mechanical, and chemical processes to develop a more accurate reactive model.

1.3 Methodology Overview

Many scientists focus on mathematical approaches, wherein a constitutive framework is created, and the coupling process is embedded within the main governing equation. There are two principal approaches to these mathematical models: mechanical approaches and energy approaches. The energy approaches include mixture theory and mixture-coupling theory. The distinctions between the mechanical and energy approaches, as well as between mixture theory and mixture-coupling theory, will be discussed in the next chapter.

Mathematical models are further classified by their reactivity into reactive and non-reactive models. The process of modelling the transport of a mixture in porous media is complex, involving both physical and chemical interactions. A reactive model accounts for the chemical reactions occurring between the transported fluid and the formation of rocks/minerals. These reactions affect the properties of the host porous media, and

subsequent changes are integrated into the calculations of the transport process. The choice between reactive and non-reactive models depends on the specific characteristics of the storage site and the level of detail required by the study. For sites with negligible reactivity or where the interest's timescale is relatively short, a non-reactive model may serve the purpose. Conversely, for sites with significant reactivity or studies that require long-term analysis, a reactive model is likely to provide a more accurate prediction of CCS performance.

1.3.1 Current Modelling Methodologies

Currently, many researchers utilize the mechanical, mathematical approach to describe the movement of fluid mixtures in deformable porous media (Schrefler and Xiaoyong, 1993; Thomas and Sansom, 1995; Gawin et al., 2003; Seetharam et al., 2007; Graziani and Boldini, 2012; Gawin and Sanavia, 2009). However, this approach has some challenges when it comes to chemical reactions. The challenge lies in accurately modelling the complex interactions and energy exchanges involved in chemical reactions within the porous media. Without a thermodynamic framework, these models might struggle to capture the full extent of these interactions, leading to less precise or incomplete predictions of material behaviour. This is why some researchers (Laloui et al., 2003; Chen et al., 2009b; Siddique et al., 2017; Islam et al., 2020) prefer to use the energy approach (mixture theory) to create a reactive THMC-coupled model. On the other hand, the mixture-coupling theory (Chen and Hicks, 2011; Heidug and Wong, 1996) is relatively new and appears not yet implemented for such multi-phase fully coupled models. The mixture-coupling theory has its own advantages, and this research will focus on utilizing it to model a multi-phase reactive fully coupled THMC model for the CCS

transport process. The thermodynamic approach in constitutive modelling (such as mixture-coupling theory) offers an advantage by ensuring models align with the fundamental laws of thermodynamics, thus avoiding thermodynamically unrealistic results. This method provides a structured framework that facilitates accurate integration of various coupled processes, including mechanical deformation, fluid flow, heat transfer, and chemical reactions. As a result, it yields more reliable and broadly applicable models for predicting the behaviour of subsurface rocks in geo-energy applications (Siddiqui et al., 2024).

The approach proposed by Heidug and Wong (1996) provides a general framework for modelling single-phase mixture transport in porous media. The literature review (Chapter 3) will discuss the advantages of the mixture-coupling theory.

1.3.2 Software

Currently, multiple simulation software tools are available that can model a mixture's transport in porous media. For instance, the TOUGHREACT and TOUGH2 code family, widely used for simulating CCS processes, were originally developed by Lawrence Berkeley National Laboratory and have since been commercialized. Many researchers include TOUGH2 in their CCS studies, attempting to enhance the modelling process by integrating multiple codes (Zhu et al., 2018b; Taron and Elsworth, 2009; Lei et al., 2020) or by investigating the effects of specific parameters such as temperature (Xu and Pruess, 2001), chemical reactions (Xu et al., 2003; Xu et al., 2010; Liu et al., 2011), or porous media methodology such as porosity and permeability (Zhang and Liu, 2016), or analysing the leakage risk from the caprock (Shevalier et al., 2014; Pruess, 2005).

Other software tools include PHREEQC, OpenGeoSys (OGS), PFLOTRAN, MINTEQA2, and SUPCRT92 (Luo et al., 2022). These computer codes rely on various numerical computation algorithms, which are sometimes combined with relatively simple governing equations, to simulate the transport process.

COMSOL Multiphysics® software will be used in this research. It is a general-purpose finite element method (FEM) simulation tool that features built-in basic physics tools such as Darcy's law for fluid dynamics, heat transfer, and transport of solute in diluted media. Although these built-in physics tools are based on basic equations, fortunately, these equations are flexible and can be manually modified to match the final constitutive governing equations that will be derived in this research.

1.4 Research Problem and Knowledge Gap

1.4.1 Current Challenges in Research

Recent research has extensively modelled the transport of mixtures in porous media; however, the coupling of THMC models remains imperfect and is far from being 'fully coupled'. Current models lack the ability to address strong coupling for multi-phase mixture transport, particularly between chemical reactions and other parameters such as temperature, pressure, stress, porosity, and permeability.

Existing approaches that simulate the CCS transport process in deformable porous media have primarily been derived using the mechanical approach. On the other hand, general approaches like the mixture-coupling theory, which are capable of adapting to chemical coupling, could be utilized for the CCS transport process. Including the coupling of thermal effects, pressures, mechanical stress, and chemical reaction influences in all

governing equations is essential. Employing such an approach to model CCS could lead to a more accurate representation of the coupling process between thermal transport, fluid pressures, solid mechanics, and chemical reactions (THMC). More details about the research gap will be discussed in the literature review chapter (Chapter 2) by reviewing research conducted in this field and identifying what is missing.

1.5 Aim and Objectives of the Study

1.5.1 Aims of the Study

The primary objective of this research is to develop an advanced and reliable reactive two-phase THMC coupled model that can simulate the ${\rm CO_2}$ injection process through rock/soil formations. This new model will simulate the coupled chemical and physical reactions between liquid, gas/supercritical phases and the host rock/soil formation. The process is complex, and the mixture-coupling theory approach will provide a solid foundation for such a model. The literature suggests that there is room for such development, which may become a valuable tool for the industry in the future.

This research aims to advance the existing model further and improve the coupling relations of the THMC framework specifically for the CCS injection process. This improvement is achieved through rigorous derivation of coupling terms, grounded in thermodynamic principles. The mixture-coupling theory, a relatively new approach used in various fields such as radioactive waste transport (Chen, 2013), will be adapted to model the transport process of CO₂ after it is injected into deep aquifer formations during the CCS process. The final constitutive framework should be capable of simulating a fully

coupled THMC process with high accuracy and expandable potential for future improvements.

This new model aims to improve our understanding of the coupled THMC processes occurring as the gas/liquid mixture is transported through deformable porous media (earth formations). It should help the industry, particularly during the planning phase, and may be used by oil companies. The injection of ${\rm CO}_2$ will enhance oil production and reduce the greenhouse gas effect on the climate.

1.5.2 Study Objectives

To achieve the research target, the main research is broken down into four key objectives, each including theoretical modelling and numerical simulation. The objectives are summarized as follows:

1. Create a Coupled HMG Model

Develop and validate a comprehensive two-phase Hydro-Mechanical-Gas (HMG) model by extending an existing Hydro-Mechanical (HM) model (Chen and Hicks, 2011) to more effectively reflect the interactions between gas and liquid flows. This model, which integrates the gas phase into the Helmholtz free energy balance using phenomenological equations, is applied in a two-dimensional finite element simulation to accurately describe multi-phase flow in porous media. The model's validation involves comparing simulation results against benchmark experiments from the literature, ensuring its accuracy and applicability for studying complex geoenergy processes.

2. Develop the Model to Capture the Chemical Transport Process (HMGC)

In this step, the model will be developed to capture the coupled chemical transport process (HMGC). The relationship between the solute transport and the driving forces will be established using phenomenological equations, and new parameters are expected to appear in these equations. The effects of these parameters on the transport process will be investigated by conducting a sensitivity analysis. At this stage, the HM-coupled model remains non-reactive since no chemical reactions are considered yet. The model will be validated using literature experiments before the sensitivity analysis. This chapter will provide a better understanding of the coupled relation between the two-phase flow of the mixture in the CCS process.

3. Extend the Model to Include Reactive Processes with Dynamic Porosity/ Permeability

Here, the model will be turned into a reactive model by including the coupled chemical reaction (dissolution). The chemical reaction between the CO_2 in the aquatic phase/solid minerals will be coupled with the physical reactions of the saline water/porous media. The chemical affinity will be used as a driving force for the chemical reactions. This step will be considered a key step in this research. A conceptual experiment will be simulated to investigate the effect of the chemical dissolution of calcite on dynamic porosity and permeability.

4. Adding the Thermal Transport Process (THMGC)

Adding the thermal component will be the final step in this research. The thermal aspect is critical in the carbon sequestration process under non-isothermal conditions. In real-

world scenarios, injecting CO₂ thousands of feet underground requires high pressure, which creates high-temperature gas flow. The formation fluids are transported as a mixture, causing thermal exchange with the rock/soil medium. The chemical reactions between the gas/rock/soil/liquid may be affected by temperature and other physical processes. This coupled effect will be investigated in this chapter of the research.

1.6 Significance of the Study

This research makes important contributions to the development of CCS by improving a fully coupled two-phase Thermo-Hydro-Mechanical-Chemical (THMC) model. The model introduces several key innovations, including the extension of Mixture-Coupling Theory to simulate energy losses, solute transport and chemical reactions, all coupled with heat transfer processes, which have not been extensively studied in previous CCS models. One of the primary advancements lies in improving the accuracy of two-phase fluid dynamics and chemical reaction simulations, leading to better predictive capabilities in CCS models. By incorporating thermal coupling and chemical dissolution processes, the model offers a more realistic representation of CCS operations under varying environmental and geological conditions. Moreover, it addresses phenomena that have been largely unexplored, such as the interaction between two-phase flow and chemical reactions, which gives a better understanding the efficiency of CO₂ sequestration.

In addition, this research is among the first to apply Mixture-Coupling Theory in the context of CCS, providing a novel approach to understanding the interaction between mechanical deformation, chemical reactions, and fluid transport. This new perspective

expands the scope of CCS modelling and lays a foundation for future studies to expand upon these methods.

1.7 Thesis Structure

This thesis primarily consists of a collection of published papers, each forming a main chapter:

Chapter 2: Presents a literature review on CCS research, discussing coupled modelling approaches used in CCS and other transport applications in porous media involving multiphase fluids. It reviews current research and identifies gaps.

Chapter 3: Extends the Hydro-Mechanical (HM) coupled model to a two-phase Hydro-Mechanical-Gas (HMG) model. Three constitutive governing equations are established for the solid, liquid, and gas phases. The model is validated using data from two published experiments.

Chapter 4: Extends the HMG model to include the chemical transport process and the energy loss due to two-phase interaction (friction). Two new coupling terms are added to the governing equations, introducing new parameters. A sensitivity analysis is conducted after the model is validated through Finite Element Method (FEM) simulations, with results compared to published experimental data.

Chapter 5: This chapter makes the model reactive by including chemical affinity and the extent of reaction in the derivation process. The model can now consider the dissolution process of solid minerals. Additionally, porosity changes dynamically, coupled with

strain, pressure, and chemical processes. The relationships between changes in permeability and other parameters are investigated alongside porosity.

Chapter 6: Introduces the thermal coupling process, making the model fully reactive and coupled. The impact of adding thermal transport to the CCS transport process is examined. Two cases are solved numerically and compared to illustrate the significance of thermal transport.

Chapter 7: Discusses the overall conclusion, model limitations, and suggestions for future work to improve the newly developed reactive two-phase fully coupled model.

1.8 Conclusion

This chapter introduced the effects of GHG and CCS process. It discussed the importance of enhancing mathematical models for such complex processes. The aims and objectives of this study were outlined, establishing four main objectives to achieve a fully coupled THMC framework. The mixture-coupling theory approach was selected for modelling due to its advantages over other approaches and its relatively unexplored application in CCS. Numerical solutions will be implemented using COMSOL Multiphysics® software. This research is critical as CCS represents one of the few viable solutions to mitigate the impending global warming crisis. Accurate modelling of this process is crucial for effective simulation and strategic planning.

The next chapter will present a literature review of existing models established to simulate the transport of a mixture in a deformable porous medium. It will highlight their differences and further explore the current knowledge gaps, setting the groundwork for the research that unfolds in the subsequent chapters.

Chapter 2: Literature review

2.1 Background

Carbon Capture and Storage (CCS) is a complicated process, involving various phases that contribute to its complexity. These phases, each with its unique properties and behaviours, play a major role in the effectiveness and efficiency of CCS operations. This section discusses these critical phases, shedding light on their significance in the broader context of CCS.

A typical interaction in CCS processes is between liquid water (or saline water) and CO_2 gas (or supercritical). When CO_2 is introduced into subsurface reservoirs, it often encounters resident brine or liquid water. This interaction can lead to various phenomena, such as the dissolution of CO_2 into the water and creation of carbonic acid H_2CO_3 , which can influence factors like reservoir pressure, buoyancy-driven flow, trigger chemical reactions, and overall storage dynamics (Song et al., 2023).

At certain depths, depending on the pressures and temperatures, CO_2 gas may transform into its supercritical state, showing behaviour of both liquids and gases. Supercritical CO_2 ($ScCO_2$) is denser than its gaseous state, making it a favourable candidate for deep storage in saline aquifers. Its interaction with liquid water is critical, especially given the unique phase behaviour and solubility dynamics at these conditions (Rutqvist and Tsang, 2002; André et al., 2007b).

Another example of a multiphase interaction for CCS, is in case of depleted gas reservoirs, often considered for CO₂ storage, still contain traces of methane gas. When CO₂ is introduced into these reservoirs, it doesn't simply displace the methane; the two gases can mix, creating a composite phase with changed properties. This interaction can influence the storage capacity, pressure dynamics, and may enhance the potential for methane recovery. To address the complexities arising from such multiphase interactions, the development and application of Equations of State (EoS) and constitutive models for gas mixtures have become crucial. These models enable the prediction of phase behaviour, thermodynamic properties, and fluid dynamics of the CO₂/methane mixtures under varying reservoir conditions. By incorporating EoS and constitutive models into reservoir simulations, engineers can more precisely estimate storage capacity, understand pressure dynamics, and optimize strategies for enhanced methane recovery (Ershadnia et al., 2021; Fan et al., 2023).

 CO_2 plays a transformative role in enhanced oil recovery (EOR) processes. When injected into oil reservoirs, CO_2 interacts with the resident liquid oil, potentially swelling it, reducing its viscosity, and enhancing its mobility. This interaction not only optimizes oil extraction but also offers a dual benefit of sequestering CO_2 in the process (Zhu et al., 2018a; Jia et al., 2019; Khurshid and Fujii, 2021).

Over the years, multi-phase modelling techniques and approaches have evolved to address these challenges. From fundamental models in the early days of CCS to modern simulations that leverage advanced computational techniques, the field has come a long way (Veveakis et al., 2017; Nardi et al., 2014; Song et al., 2023). Current state-of-the-art

models consider multiple factors and interactions, offering good accuracy and insight. For example, both the mixture theory approach (Heidug and Wong, 1996; Coussy et al., 1998) and the mechanics approach (Lewis and Schrefler, 1998b; Lewis and Schrefler, 1987) have been developed to handle multi-phase systems. Numerical methods also have evolved to adapt to such simulation challenges (Rutqvist et al., 2002; Pruess et al., 2004; Hu et al., 2022; Rutqvist, 2017; Favier et al., 2024).

Many challenges remain in the current models and require more development. For instance, there is a lack of models that effectively handle the complex chemical coupling processes involving variables like porosity and permeability within a thermo-hydromechanical system, especially when considering both liquid and gas phases. These gaps in knowledge and modelling capabilities will be discussed more thoroughly in a subsequent section.

This literature review focuses on the concepts of multi-phase systems in CCS, examining the complexities of phase interactions and tracking the development of modelling methods over time. It highlights major works while identifying ongoing challenges that shape the current research in CCS modelling.

By presenting a comprehensive overview of existing knowledge and recent advancements, this review sets a good foundation for introducing novel research contributions. It highlights the evolving nature of CCS modelling and shows the critical role of innovative approaches in addressing the challenges posed by multi-phase systems, ultimately contributing to more effective climate change mitigation strategies.

2.2 The Importance of Multi-Phase Modelling in CCS

To develop accurate and reliable models for CCS, a deep understanding of each individual phase is required. In many applications, a simple one phase transport framework can be sufficient for the modelling. The model can still have coupling equations such as a thermo-hydro-mechanic-chemical (THMC) model; however, the interaction in the model is between one flowing fluid and the solid matrix only. In real applications, the single-phase model does not consider the existence of other fluids. Other fluids could be gas, supercritical or liquid. They can either pre-exist in the porous media or be mixed with the primary fluid and injected into the porous media. An example of pre-existing fluid in a solid matrix is underground water, oil, and natural gas. Examples of mixed fluids are a CO_2/N_2 mixture which used sometimes in the injecting process (Wu et al., 2020; Zhou et al., 2015; Pesavento et al., 2017).

However, in case of CCS, modelling the systems as single-phase phenomena can lead to significant inaccuracies. For instance, ignoring the gaseous phase of CO₂ during injection can result in overestimations of sequestration capacity. Moreover, single-phase models might not capture crucial phase transition dynamics, risking safety assessments (Kelemen et al., 2019). Moreover, ignoring the interaction between the supercritical/gas phase and liquid phase (water/solute solution) will result into inaccuracy estimation of the potential chemical reaction that may occurs due to the reaction of carbonic acid and solid menials in the formation. This reaction is crucial of estimation of porosity and permeability change that effect many other parameters such as pressure and mechanical properties of the solid matrix itself (Abidoye et al., 2015).

Geological CCS is challenging because it occurs deeply underground, and the transport of the mixture cannot be directly observed by researchers. However, theoretically, researchers can model the transport of the mixture after understanding what are the materials and minerals that exists in the reservoir, the phase of each element, as well as the condition parameters such as the pressure, temperature, acidity level (pH) of the fluids.

There are many types of geological reservoir that can be used to store CO_2 . Deep saline aquifer is a common choice, where global saline aquifers have the potential to store between 20% and 500% of the total CO_2 emissions projected over the next 50 years (Birkholzer et al., 2009; Shukla Potdar and Vishal, 2016). In this case, the water exists in liquid, and vapour states, while the injected fluid may be in liquid (dissolved CO_2 in brine), gas, or supercritical phase. The injected fluid phase may change depending on reactivity (dissolution/precipitation), miscibility, or changes in pressure and temperature. Predicting these phase interactions is challenging, especially when considering coupling relations.

While modelling the interaction of multi-phase transport is a bit tricky, understanding the fundamental of the transport for each phase is essential. Over the last century, researchers established fundamental laws that are still used today for such modelling process. These laws include Darcy law for fluid transport, Fourier's law for thermal transport, Fick's law for chemical diffusion, and Terzaghi effective stress principle for the mechanical interaction. For example, for liquid phase (l), that has viscosity of v^l , intrinsic

permeability of k^l , relative permeability k^{nl} , and gradient liquid pressure ∇p^l , it will has liquid flux \mathbf{u}^l that can be determine by:

$$\mathbf{u}^{l} = -\mathbf{k}^{l} \frac{k^{n}}{v^{l}} \nabla p^{l} \tag{2.1}$$

The diffusion of the chemical c withing the liquid phase then can be calculated using Fick's law:

$$\mathbf{J}^c = -D\nabla c^c \tag{2.2}$$

where \mathbf{J}^c is the diffusion of the chemical in the liquid phase, D is the chemical diffusion coefficient, and ∇c^c is the gradient of chemical concentration.

For the thermal transport, the heat flux by conduction \mathbf{q}' can be determine by knowing the thermal conductivity λ and the temperature T as:

$$\mathbf{q}' = -\lambda \nabla T \tag{2.3}$$

For deformation calculation of the porous media, the effective stress can be calculated using Terzaghi effective stress principle as:

$$\mathbf{\sigma}' = \mathbf{\sigma} - p^{l} \mathbf{I} \tag{2.4}$$

where σ' is the effective stress tensor, σ is the total stress tensor, and I is the unit tensor.

Accurate multi-phase modelling is important for assessing the feasibility, safety, and financial viability of CCS projects. Proper modelling can lead to better yield, safer storage scenarios, and more efficient operations. By that said, the more accurate the model in capturing the change in the crucial variables of the process the more valuable it become to the industry sectors and engineering applications.

But multi-phase modelling is not without its challenges. Factors like phase transitions, variable properties across phases, and intricate phase interactions add layers of complexity to the modelling process. Moreover, from a computational standpoint, multi-phase models require more intensive resources due to increased degrees of freedom and non-linear interactions (Baqer and Chen, 2022; Buchwald et al., 2021). In fact, this complexity of the multi-phase modelling made some of well-known advanced approaches limited when it comes to multi-phase transport, one example is such the traditional mixture theory approached (Siddiqui et al., 2024; Siddique et al., 2017).

In conclusion, multi-phase modelling is essential in CCS systems. As the analysis continues, the importance of precise, thorough, and detailed multi-phase modelling becomes more apparent for understanding the complexities involved in CCS processes.

2.3 Analysis of Phase Couplings in Multi-Phase Systems

Understanding the state of the art in coupling modelling is important for pushing the boundaries of CCS technology. It not only informs the development of more accurate and reliable models but also guides practical implementation strategies that ensure the effective and safe storage of CO₂.

Multi-phase models can incorporate secondary flow into the equations. This type of model has high complexity, especially if it is a fully coupled model such as a THMC full coupling model. The coupling process of THMC model can be broken down into three main processes as follows (Manninen et al., 1996; Yin et al., 2011; Zhang et al., 2012; Tao et al., 2019):

- Mechanical processes are coupled with the hydraulic and thermal process (poroelasticity process), where the porosity and permeability may also be affected.
- Hydraulic processes are coupled with the thermal process.
- Chemical reaction processes:
 - ➤ Reactive chemical processes are coupled with the hydraulic process.
 - ➤ Reactive chemical processes are coupled with the mechanical process via porosity changes due to dissolution and precipitation.
 - ➤ Reactive chemical processes are coupled with thermal processes via the change in temperature-dependent chemical reaction rates.

In general speaking, the chemical reaction is the most complicated process among the THMC process (Zhang et al., 2015).

2.3.1 Hydro-Mechanical Coupling (HM) (Poroelasticity)

At the intersection between the fluid and solid rock formation is called the hydromechanical (HM) coupling. The injected CO_2 affects the pore pressure within the reservoir, leading to changes in the mechanical behaviour of the rock. From potential deformations in the reservoir to concerns about caprock integrity, understanding this coupling is critical for ensuring the safe and efficient storage of CO_2 (Rahman et al., 2022; Gaus et al., 2005; Kaldi et al., 2013; Khazaei and Chalaturnyk, 2017; Ahmadi Goltapeh et al., 2022). The HM coupling fundamentally connects pore pressure to the effective stress in porous media. Effective stress is the stress carried by the solid matrix,

which is reduced by pore pressure. When pore pressure increases, the effective stress decreases, potentially causing rock deformation or failure, especially in cases involving cracks. As deformation increases, pore spaces expand, reducing pore pressure. This interplay is crucial in CCS, where crack growth can lead to enhanced permeability, impacting storage integrity and fluid migration pathways. The HM coupled model has been extensively studied by numerous researchers such as (Lewis and Schrefler, 1998a; Sanavia et al., 2002; Fall et al., 2014b; Chen and Hicks, 2011; Chen, 2013). Meanwhile, other scholars have employed the HM coupled model specifically to explore carbon storage processes (Figueiredo et al., 2015; Bjørnarå et al., 2014; Unger and Kempka, 2015; Alonso et al., 2012; Bea et al., 2012; Chen et al., 2019; Sampath et al., 2020; Bai and Tahmasebi, 2022).

Poroelasticity theory is a common way to describe the mathematical relation of HM coupling, this relation originally developed by Biot (1955), also called general Biot's consolidation theory. I can be applied for isotropic linear elastic system such as deformable porous media as (Detournay and Cheng, 1993):

$$\sigma_{ij} = \left(K - \frac{2G}{3}\right) \varepsilon_{kk} \,\delta_{ij} + 2G \,\varepsilon_{ij} - \zeta \,p^{\,p} \,\delta_{ij} \tag{2.5}$$

$$\zeta = 1 - \frac{K}{K^s}.\tag{2.6}$$

where G is the rock shear modulus, $p^c = p^{Sc} - p^I$ is the capillary pressure, p^{Sc} is supercritical phase pressure, p^I is the liquid phase pressure, K and K_s are the bulk modulus of solid matrix and the bulk modulus of the solid grain respectively, ζ is Biot's coefficient, σ_{ij} is the stress tensor, and δ_{ij} is the Kronecker delta. This equation

represents the physical behaviour of porous materials that deform under mechanical stress and involve the movement of fluid within the pores. It describes how the solid matrix of a porous material responds to external forces (such as pressure) and how this deformation affects the fluid flow within the material. Biot's consolidation theory is established for fully saturated conditions, which means only the liquid phase exists; however, it can be extended to unsaturated conditions (two-phase), as shown in the work of Lewis and Schrefler (1987).

2.3.2 Hydro-Mechanical-Chemical Coupling (HMC)

Saline aquifers are among the common storage sites for CCS. In these aquifers, water carries a mix of dissolved salts, minerals, and organic compounds. When CO₂ interacts with this brine (a mixture of water and dissolved minerals), it can trigger a chain of chemical reactions. This hydro-chemical coupling, where fluid interactions lead to chemical alterations, will affect CO₂ solubility, the porosity and permeability of the reservoir. Such changes can, over time, either enhance storage capacity (e.g., by increasing porosity through dissolution) or pose challenges, such as when mineral precipitation reduces formation porosity and permeability. Addressing these challenges is essential for ensuring the long-term success of carbon storage (Darmon et al., 2014; Zhou et al., 2016; Wang and Bauer, 2019). An example of hydro-chemical coupling is solid dissolution in carbonic acid; this chemical process leads to shrinkage in solid volume (increase in porosity and permeability), while the result of the dissolution is an increment in fluid mass and volume. The change in porosity/permeability and the increment in the mass/volume will influence the hydraulic pressures of the system.

Beyond fluid dynamics, the chemical reactions initiated by CO₂ injection have mechanical implications too. Minerals dissolve or precipitate due to these reactions, and they can alter the mechanical properties of the reservoir rock. This mechanical-chemical coupling is significant when considering factors like fracture propagation, rock strength, and the long-term stability of the storage site (Fischer et al., 2013; Klein et al., 2013; Carroll et al., 2016; Iyer et al., 2022; Bemer and Lombard, 2010). Moreover, as the surface area of the solid increases due to the chemical dissolution process or mechanical deformation, the chemical reaction such as dissolution also increases (Xu et al., 2017; Rochelle et al., 2004; Gholami et al., 2021).

Mathematically, relating chemical transport to the HM process can be done by utilizing Fick's law. However, Fick's law describes the movement of chemical species driven by a concentration gradient only. Since it is also affected by the movement of the fluid phase (flow), the Advection-Diffusion-Reaction Equation can be used to describe this process (Bird et al., 2006):

$$\frac{\partial c^c}{\partial t} + \mathbf{v}^l \cdot \nabla c^c = D \nabla^2 c + R \tag{2.7}$$

Physical meaning of the equation can be explained as:

 $\frac{\partial c^c}{\partial t}$: Represents the time rate of change of the concentration c^c at a point.

 $\mathbf{v}^l \cdot \nabla c^c$: Represents advection, which is the transport of c^c due to the velocity of the medium \mathbf{v}^l .

 $D\nabla^2 c^c$: Represents diffusion, where the substance spreads out due to concentration gradients, governed by Fick's Law.

R: Represents reaction, which accounts for the generation or depletion of the substance due to chemical reactions.

Moreover, the chemical reactions can also be linked to the chemical potential μ via affinity A (driving force of the reaction). The chemical potential is a fundamental concept in thermodynamics that represents the change in a system's free energy as particles are added, while keeping temperature and volume constant. It is essentially the potential energy associated with the addition of one particle to a system. In this case, the chemical potential can be used to couple the chemical reaction to the thermodynamics of the system.

In non-equilibrium thermodynamics, the Gibbs-Duhem Equation can be written as (Katchalsky and Curran, 1965):

$$\gamma dT - V dp + \sum_{i=1}^{k} n_i d \mu_i = 0$$
 (2.8)

where T is the absolute temperature, γ is the entropy, V is the volume, n_i are the moles of the i-th component, μ_i is the chemical potential, and p is the pressure. This equation connects the chemical potential to the entropy and the other thermodynamic elements, thus linking chemical reactions to the system via affinity.

2.3.3 Thermo-Hydro-Mechanical (THM) Coupling

Introducing CO2 into a reservoir means there is heat energy to consider, too. The temperature changes accompanying CO2 injection can influence both fluid behaviour and rock mechanics, adding more complexity to the process. This thermo-hydromechanical coupling is especially relevant in deep reservoirs where even slight temperature variations can have clear effects on storage dynamics (Yue et al., 2022; Ma et al., 2022b; Wang et al., 2023c). The THM coupled model is an extension of the coupling relationship of the HM model that includes the heat transfer process. In this model, two coupling processes are created. The first one describes the thermal-elasticity process (TM), which represents the thermal stress and expansion of the solid matrix. The second one is the poroelasticity prosses (HM), which represents the deformation of the porous media. The TH relation should also be considered in the fully coupled models since heat affects fluid viscosity, which affects fluid flow and pressure. Figure 1 shows these coupling processes. Many researchers have investigated and tried to conduct a good, fully coupled THM model (Chen et al., 2014; Chen et al., 2009a; Wang et al., 2014; Tong et al., 2010; Thomas et al., 1998). The THM-coupled approach is also used to model the CO₂ injecting process (Vilarrasa et al., 2017; Li and Laloui, 2016a; Li and Laloui, 2017).

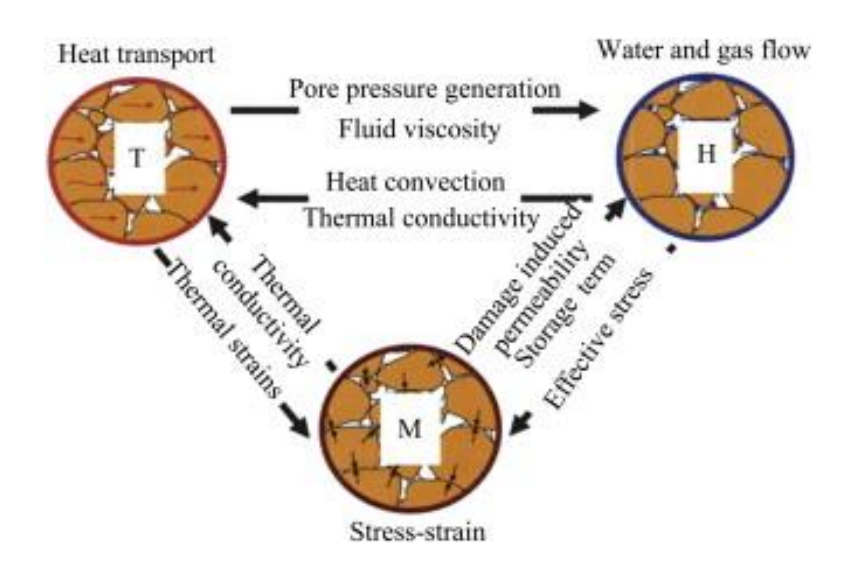


Figure 2.1: THM triangle coupling relationship (Wang et al., 2014)

2.3.4 Thermo-Hydro-Mechanical-Chemical (THMC) Coupling

In complex scenarios, various interactions play a crucial role. Factors such as temperature, fluid dynamics, rock mechanics, and chemistry intersect and influence one another. The THMC coupling embodies this complexity in CCS modelling, necessitating a comprehensive approach to accurately represent the relationship of these factors. The THMC coupled model is particularly challenging because it combines both physical processes and chemical reactions. As fluids navigate through porous media, they initiate chemical reactions. Significantly, these reactions, which involve minerals undergoing dissolution or precipitation, can markedly affect porosity and permeability. This is because the dissolution/precipitation process can either enhance permeability by dissolving minerals that may obstruct flow or reduce it when extra solid particles accumulate. To illustrate this, Figure 2 provides a visual representation of the intricate relationships inherent in THMC coupling, while Table 1 lists specific minerals that play a crucial role in the chemical process of CO₂ sequestration. A focal point will be the shift

in porosity-permeability, which serves as a vital link connecting the chemical reactions to the overarching physical model.

Table 2.1: Minerals that may considered in the coupled chemical process (Zhang et al., 2015).

| Mineral | Chemical compositions |
|-------------------|---|
| Primary mineral | |
| Quartz | SiO ₂ |
| Calcite | CaCO ₃ |
| Oligoclase | $CaNa_4Al_6Si1_4O_{40}$ |
| Smectite-Na | $Na_{0.29}Mg_{0.26}Al_{1.77}Si_{3.97}O_{10}(OH)_{2}$ |
| Chlorite | $Mg_{2.5}Fe_{2.5}Al_2Si_3O_{10}(OH)_8$ |
| Kaolinite | $Al_2Si_2O_5(OH)_4$ |
| K-feldspar | KAlSi ₃ O ₈ |
| Secondary mineral | |
| Magnesite | $MgCO_3$ |
| Low-albite | NaAlSi ₃ O ₈ |
| Siderite | FeCO ₃ |
| Ankerite | $CaMg_{0.3}Fe_{0.7}(CO3)_2$ |
| Dawsonite | $NaAlCO_3(OH)_2$ |
| Smectite-Ca | $Ca_{0.145}Mg_{0.26}Al_{1.77}Si_{3.97}O_{10}(OH)_{2}$ |

The chemical process may include swelling of the solid matrix in shale media, chemical osmosis, hydration, and mineral dissolution/precipitation (Zheng and Samper, 2008). Many attempts have been made to model a fully coupled THMC model that may simulate a more realistic scenario of injecting CO₂ (Zhang et al., 2015; Zhang et al., 2016; Yin et

al., 2011). Some examples of the chemical reactions that may occurs between the injected ${\rm CO_2}$ and formation that involves minerals mentioned in Table 1 are discussed in the next section.

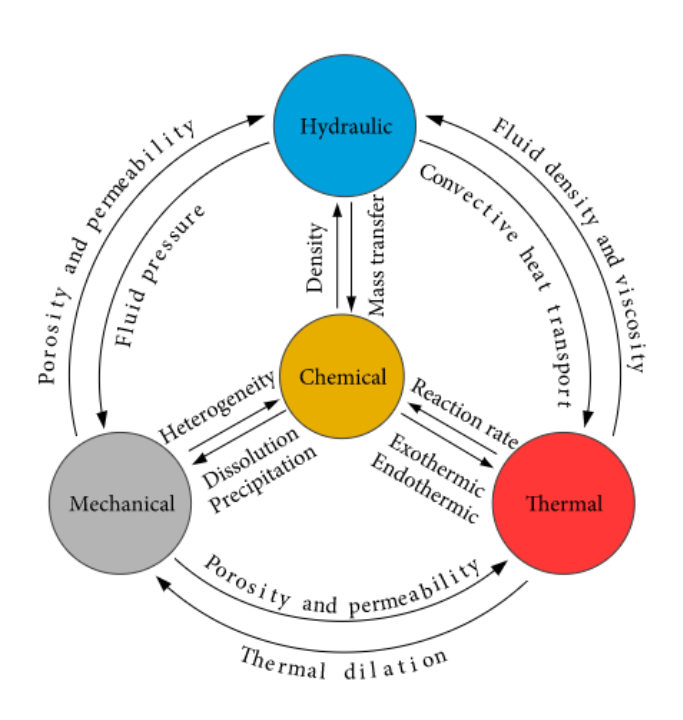


Figure 2.2: THMC coupled process (Tao et al., 2019)

2.3.5 Software and Simulation Tool

When considering the simulation software for this research, several options are available, however, since this research goal is to model and derive a rigorous mathematical model, then even general finite elements solver (FEM) software could be a good option. COMSOL Multiphysics is a finite element coupling capabilities and advanced features, making it a prime candidate While tools like PHREEQC specialize in chemical reactions, they lack the ability to simulate mechanical physics. TOUGHREACT and SCALE2000, as noted by André et al. (2007a). However, these software programs use their own mathematical approach, which is unlike this research, limited to non-deformable porous

media. Since this research focuses on the rigorous derivation of mathematical equations rather than FEM simulations, COMSOL Multiphysics seems to be a good choice. The software is easy to use and can efficiently handle complex coupled physical and basic chemical reactions which is fine for validation purposes. Furthermore, COMSOL was chosen due to its ability to support fully coupled modelling, alongside its Segregated approach for solving complex equations. It is worth mentioning that integrating COMSOL with PHREEQC through ICP could enhance its utility, combining COMSOL's strengths in solute transport simulation with PHREEQC's geochemical analysis capabilities, as supported by researchers like Nardi et al. (2014) and Sainz-Garcia et al. (2017). However, COMSOL on its own is capable of simulating basic chemical reactions, which is sufficient for the objectives of this research. The goal of this research is not to simulate a large number of chemical reactions but to create coupled equations linking hydro-mechanical physics with chemical reactions and thermal physics. In such a case, using a few chemical reactions within COMSOL alone will result in faster and more computationally efficient simulations. While ICP allows for capturing more complex chemical reactions through PHREEQC, it has some drawbacks. Introducing third-party software increases the processing load and slows down the process, posing challenges for simulating complex coupled systems that require rapid, automated iterations.

2.4 Modelling Carbon Sequestration

There are three major types of carbon sequestration: terrestrial carbon sequestration, geological sequestration, and ocean sequestration. This research will focus on modelling geological sequestration, such as CO_2 injection. The model that will be established at the end of this research will simulate the transport process of the gas/liquid mixture through

the injected formation, which could be oil and gas reservoirs, saline aquifers, or coal seams (Ma et al., 2017). The transport of fluid mixture in deformable porous media can be modelled using continuum mechanics and thermodynamic approach. Two main approaches are commonly used to model a coupled mixture transport in a deformable porous media: the mechanics approach and the mixture-coupling theory approach.

The CO₂ injection process will create a chemical disequilibrium and hence initiate a chemical reaction. The reaction can be caused by the formation of water, host aquifer (ex. siliciclastic or carbonate), caprock (the seal), or borehole material. This chemical reaction will affect the porosity and, thus, the permeability of the porous medial (the host formation). The change in permeability will have a direct influence on the CO₂ injection rate, while porosity will affect the storage capacity. CO₂ capturing and storing in geological formations can be done using different methods. These methods include structural/stratigraphic trapping, where CO₂ is physically trapped beneath impermeable rock layers, and diffusion/solubility trapping, which involves the dissolution of CO₂ into formation water. Mineral trapping occurs when CO₂ reacts with reservoir rock and brine to form stable minerals. Residual trapping happens when CO₂ is immobilized in pore spaces of rocks due to capillary forces, preventing further movement. (Zhou et al., 2017; Shukla Potdar and Vishal, 2016).

 CO_2 trapping mechanisms function over different timescales. Structural trapping occurs immediately as CO_2 is contained by the reservoir. Solubility and mineral trapping take years to millennia, as CO_2 dissolves in brine or forms stable compounds. Residual

trapping is relatively quick, with capillary forces holding CO₂ in place. The success of these methods depends on factors like rock porosity, permeability, and caprock quality.

The ideal phase for storing the CO_2 is the supercritical condition (31.04 °C and 7.38 MPa); however, it is not a necessary condition. Supercritical CO_2 reacts differently than CO_2 solution, where CO_2 the solution is more chemically reactive than Supercritical CO_2 . Moreover, the supercritical phase is a high-density phase which allows occupying less volume space. Usually, the CO_2 hydro-mechanical injection process dissolves the CO_2 into the water to create a CO_2 solution to inject or inject CO_2 in the supercritical phase (as in most cases).

A solution containing carbonic acid H_2CO_3 is considered as the injection fluid. For carbonate aquifer, the chemical reaction between CO_2 solution and Water/formation rocks can be written as (André et al., 2007a):

$$CO_2 + H_2O \Leftrightarrow H_2CO_3$$
 (2.9)

$$H_2CO_3 \Leftrightarrow H^+ + HCO_3^-$$
 (2.10)

Calcite +
$$H^+ \Leftrightarrow HCO_3^- + Ca^{2+}$$
 (2.11)

Dolomite
$$+ 2H^+ \Leftrightarrow 2HCO_3^- + Ca^{2+} + Mg^{2+}$$
 (2.12)

Siderite +
$$H^+ \Leftrightarrow HCO_3^- + Fe^{2+}$$
 (2.13)

$$H_2O + CO_2 + CaCo_3 \Leftrightarrow Ca(HCO_3)_2$$
 (2.14)

The precipitation $Ca(HCO_3)_2$ is a primary cause of the reduction in permeability in carbonate media.

For Ca-rich feldspar (Gunter et al., 1997b), trapping could be in a mineral phase (calcite):

$$CaAl_2Si_2O_8$$
 (anorthite) + $CO_{2(aq)}$ + $2H_2O$

$$\Rightarrow CaCO_3 \text{ (calcite)} + Al_2Si_2O_5\text{(OH)}_4\text{(kaolinite)}$$
(2.15)

For K-rich feldspar in saline solutions (Johnson et al., 2001) have postulated the precipitation of a different carbonate mineral:

$$\begin{split} \text{KAlSi}_3\text{O}_8 \text{ (K-feldspar)} + \text{Na}^+ + \text{CO}_{2(\text{aq})} + \text{H}_2\text{O} \implies \text{NaAlCO}_3(\text{OH})_2 \text{ (dawsonite)} \\ + 3\text{SiO}_2 \text{ (quartz/chalcedony/cristobalite)} + \text{K}^+ \end{split}$$

Other silicate mineral reactions might trap CO_2 as a dissolved species such as bicarbonate (Gunter et al., 1997b):

$$7\text{NaAlSi}_3\text{O}_8 \text{ (albite)} + 6\text{CO}_{2(\text{aq})} + 6\text{H}_2\text{O} \Rightarrow \text{Na-smectite}$$

$$+ 6\text{HCO}_3^- + \text{SiO}_2 + 6\text{Na}^+$$
 (2.17)

Two reactions have been suggested that could cause porosity reduction within the base of shales (Johnson et al., 2001; Johnson et al., 2004). The first is dawsonite precipitation, as detailed in equation (2.16), which can increase the solid volume of the reaction by between 17-25.4%. The second, more critical, the reaction is Fe-Mg-carbonate precipitation, as represented by magnesite:

$$KAlSi_{3}O_{8} (K-feldspar) + 2.5Mg_{5}Al_{2}O_{10}(OH)_{8} (Mg-chlorine) + 12.5CO_{2(aq)}$$

$$\Rightarrow KAlSi_{3}O_{10}(OH)_{2} (muscovite) + 1.5Al_{2}Si_{2}O_{5}(OH)_{4} (kaolinite) +$$

$$12.5MgCO_{3} (magnesite) + 4.5SiO_{2} (quartz/chalcedony) + 6H_{2}O$$

The reaction in equation (2.18) can give a solid volume increase to about 18.5% and reduce shale porosity to approximately 50% (Rochelle et al., 2004).

Researchers such as Li et al. (2022) investigated the kinetic equations of mineral trapping reactions for long-term CCS geological storage (10,000 years). They found that different kinetic rate equation approaches greatly affect simulation results. They tested five main approaches (transition state theory rate equation TST, L.A. rate equation, H.T. rate equation, and BSZ rate equation). The study shows that different reaction rate equations influence how quickly minerals trap CO_2 over time. Linear equations are the most responsive, while nonlinear equations reduce the reaction rate by up to 58%. Although the overall trend in mineral evolution remains the same, the rate of sequestration varies significantly. After 10,000 years, mineral trapping can differ by over 50% depending on the equation used, highlighting the importance of selecting the correct reaction model for accurate long-term CO_2 storage.

2.5 The Modelling Approaches

Researchers have been developing the modelling approaches for transport of mixtures in porous media for many years, including its applications in areas such as CCS. To understand current modelling frameworks, it is important to review the development of approaches that have led to the current state. Many approaches have led to general frameworks that can be used for any mixture fluid moving in deformable media such as concrete, living cells/tissues, rocks, soil, and more. However, some of these models can be very useful if adjusted and employed for CCS applications. In the following section, the approaches reviewed are not necessarily developed specifically for CCS but are

general transport models that have been adjusted in many cases to capture the CCS process.

2.5.1 From Mechanics to Mixtures: A Historical Perspective

Two main approaches are used to model a coupled mixture transport in a deformable porous media: the mechanics approach and the energy-based approach (such as mixture theory). Historically, the foundational approach to modelling in CCS revolved around classical mechanics. Using principles of continuum mechanics, early models provided insights into the behaviour of geological transport during fluid injection and storage (Grisak and Pickens, 1980; Biot and Temple, 1972; Meiri, 1981; Lewis and Schrefler, 1987). While effective for understanding basic dynamics, the mechanics-based approach may oversimplify complex interactions, especially when multiple phases are involved.

The mechanic's approach is based on the classical consolidation theory described by Terzaghi (1925) and Biot's theory (Biot, 1941; Biot, 1955; Biot, 1962; Biot and Temple, 1972). The basic model describes a coupled relationship between stress-strain and pore pressure, which is described as an HM-coupled model. The model was extended to include the thermal process (THM).

Many researchers worked on developing a coupled THM model using the mechanics approach (Ma et al., 2017; Fan et al., 2019a; Li and Laloui, 2016a; Lewis and Schrefler, 1998a). However, the injection process usually involves chemical reactions that may have significant effects on the results. Researchers tried to establish chemical formulation coupled with the system; however, the complexity of these chemical reactions makes it tricky to develop it further using the mechanic's approach.

On the other hand, as researchers focus on understanding multi-phase systems, the mixture theory which is based on energy approach became an important development. Grounded in thermodynamic principles, this theory provided a comprehensive framework for modelling the behaviour of multiple coexisting phases (Siddiqui et al., 2024). This approach is often referred to as the 'energy approach' due to its reliance on non-equilibrium thermodynamics. The mixture theory's ability to depict complex interactions marked a significant leap in the understanding of CCS dynamics. Over the years, it underwent refinements, adapting to the ever-evolving challenges posed by real-world CCS scenarios.

This theory was first developed by Truesdell (1957). It is considered as a macroscopic approach that is based on the second law of thermodynamics, where the entropy is incorporates continuum mechanics involved. It also and non-equilibrium thermodynamics (Chen and Hicks, 2010). This makes the mixture theory approaches more flexible in dealing with coupled chemical reactions. By modifying and extending the original theory, it is also used to model the coupled HM, THM, HMC and THMC relations. Where Heidug and Wong (1996) present first coupled model that capture hydration swelling of water-absorbing saturated rocks under isothermal condition. Additionally, Coussy et al. (1998) made significant contributions to expanding the mixture theory, specifically to encapsulate coupling effects.

The advantage of working with mixture coupling theory approaches when creating a chemical coupling framework is the role of entropy, which represents a key factor. The chemical potential can be linked to entropy through the Gibbs-Duhem equation in non-equilibrium thermodynamics shown in equation (2.8), Then, the affinity of a reaction, *A*,

which represents the driving force for any chemical reaction, links the chemical reaction to the change in chemical potential, which is the driving force for the transport of matter (Katchalsky and Curran, 1965):

$$\sum_{i=1}^{n} \mu_i dn_i = -A d \xi \tag{2.19}$$

 ξ is extent of reaction.

This creates a coupling between the entropy change and the chemical reaction, while the energy losses from chemical transport can also be captured by employing the phenomenological relations that will be introduced in the next chapters. This method ensures that the frameworks are rigorously derived and maintain thermodynamic consistency.

Moreover, the mixture coupling theory utilizes the balance equation for Helmholtz free energy in a system composed of solid, water, and gas phases. This equation serves as a fundamental basis for both the mechanical and mixture theory approaches. Assuming a representative microscopic domain large enough to encompass all phases, its boundary *S* is fixed to the surface, allowing only fluids (such as water or gas) to pass through:

$$\frac{D}{Dt} \int_{V} \psi dV = \int_{S} \mathbf{\sigma} \mathbf{n} \cdot \mathbf{v}^{s} dS - \int_{S} \mu^{l} \mathbf{I}^{l} \cdot \mathbf{n} dS - \int_{S} \mu^{g} \mathbf{I}^{g} \cdot \mathbf{n} dS - T \int_{V} \gamma dV$$
 (2.20)

where: ψ is Helmholtz free energy density, σ is the Cauchy stress tensor, μ^l is the chemical potential of liquid, μ^s is the chemical potential of gas, T is temperature, γ is the entropy production per unit volume. To further develop the framework, the balance equations for solid mass, liquid, and other phases are written separately for each phase.

By using entropy production and transport laws along with Darcy's law, the basic equation for deformation can be established. The coupling in mixture coupling theory is derived from a coupling matrix based on Maxwell's relations. Additionally, Onsager's reciprocal relations are applied, which state that the matrix of phenomenological coefficients is symmetric. This process will be further clarified in the next chapter, where each step of the derivation will be discussed.

Using the mixture coupling theory approach to derive constitutive models has the advantage of automatically satisfying the laws of thermodynamics, giving them broad applicability across various systems while ensuring accurate and physically consistent results. The two main equations in this approach are the free energy and dissipation functions. The remaining components of the model, such as chemical swelling stress, stress-strain relationships, pore pressure effects, flow laws, and other key components, can then be determined. It can be said that the main advantage of developing constitutive models using a thermodynamics-based framework is that they ensure physically consistent results in accordance with thermodynamic laws. This builds confidence in the analysis by preventing unrealistic or inaccurate outcomes (Siddiqui et al., 2024).

On the other hand, many researchers such as Pesavento et al. (2012), have used the classical mechanical approach to include some chemical coupling in their frameworks. However, when modelling complex chemical reactions that need to be fully coupled with other physics in the frameworks, it is easier to use the thermodynamic approach (e.g., mixture coupling theory), where deriving and relating the chemical reaction and energy dissipation to entropy takes care of the coupling process (as done in Chapter 5).

2.5.2 Mixture-Coupling Theory: Advancements and CCS Modelling

While various energy approaches based on mixture theory have emerged under different names, they all align with modified mixture theories. However, there are differences in derivation details. For example, Heidug and Wong (1996), used entropy in their method, differing from Coussy et al. (1998). The main difference lies in the fact that Heidug did not use the Balance of linear momentum equation in his derivation process but relied on entropy. Chen and Hicks (2011) used this approach to improve Heidug and Wong (1996) framework by considering unsaturated condition. Chen et al. (2016) later introduced the term "mixture-coupling theory," refining the approach. This theory, leveraging Maxwell's based relations and phenomenological equations, provides a strong framework for multiphase CCS modelling and has evolved to handle unsaturated and non-isothermal conditions (Chen et al., 2016; Chen et al., 2018a; Chen et al., 2018b; Ma et al., 2022b; Yue et al., 2022; Ge et al., 2023; Ma et al., 2023; Wang et al., 2023c).

The mixture-coupling theory relies on Maxwell's relation to establish coupling matrix, and the phenomenological equations to establish well-constructed coupling in the final framework. This approach combines the best aspects of earlier models, blending the thorough analysis provided by mixture theory with the flexibility found in its later versions. The mixture-coupling theory characterises the ongoing drive for improvement in the field, representing a suitable way of multi-phase modelling for carbon capture and storage.

Researchers developed the coupling relations within the mixture theory throughout the years and extended it to include unsaturated rocks and non-isothermal conditions (Chen and Hicks, 2010; Chen, 2013). Many research papers aim to conduct a full THMC model;

however, only very few fully coupled models have been created, especially for a large-scale problem such as the wellbore scale (Cailly et al., 2005; Gaus et al., 2008a; Yin et al., 2011). Such fully coupled model simulation could analyse stress, pressure, heat transfer and reactive chemical transport changes while injecting the carbon and predict any flow leakage chance from the wellbore. This will prevent potential pollution and protect underground water from such contamination.

Incorporating gas migration in a multi-phase fully coupled model is an advanced step forward. However, this step is an essential step to model the CO₂ injection process. Many researchers, such as Schrefler and Xiaoyong (1993), developed an HMG model based on the mechanic approach. In the next chapter (Ch.3), the HMG fully coupled model will be established based on the mixture-coupling theory approach. Although the final governing equations are close to the mechanic approach done by Schrefler and Xiaoyong (1993), the final governing equation of the solid matrix (mechanical part) is modified to capture more details. In addition, it is important to develop a fully coupled HMG model based on the mixture-coupling theory approach to add a coupled chemical reaction to the model. The mixture-coupling theory approach is more adaptable for capturing the coupled chemical reaction processes. Considering all the above, developing an HMG-coupled model based on the mixture-coupling theory is the first step in modelling a reliable, fully coupled THMGC model that can simulate the CO₂ injection process efficiently.

2.6 Surveying the Field: Recent Developments of Coupled Modelling of CCS

To accurately model and predict the behaviours and interactions inherent in CCS processes, an approach of "coupled modelling" has become essential. Over the past

decades, numerous researchers have attempted to contribute to this field, each adding a unique twist or innovation to the understanding of coupled phenomena in CCS.

The field of THMC modelling is quite large, and there are many studies in this area. In this review, the research includes coupled and non-coupled models, general transport models used for other applications (not directly related to CCS), and simulation studies that do not reveal the mathematical derivation process. These studies have been excluded from the review due to their indirect relevance or lack of benefit to this research, which focuses on deriving a fully coupled THMC framework for CCS. After filtering these studies, only a few stood out. These are the studies with clear mathematical derivations, fully or partially coupled models, and are either directly related to CCS or can be compared to the THMC model developed in the following chapters.

While general transport models for mixtures in porous media, including THMC-coupled models, existed long before CCS technology was recognized, applying them to the CCS process required adjustments to better capture the process with greater accuracy. CCS modelling can be traced back to the early 1990s. One of the early studies, conducted by Van der Meer (1992), was associated with the Sleipner Project in the North Sea, which began in 1996 as the first large-scale CO₂ storage project. The study investigated the feasibility of CCS, focusing on the technical feasibility, geological constraints, and implications of storing CO₂ in aquifers. His modelling primarily addressed hydraulic aspects, such as pressure changes, CO₂ plume migration, and the physical processes involved in CO₂ injection and storage. However, the modelling and numerical simulations were relatively simple compared to more advanced models developed later,

which include the coupled processes (thermal, mechanical, and chemical) found in modern THMC models. Van der Meer analysed two hypotheticals CO_2 storage reservoirs to assess their potential for long-term carbon storage, providing insights into CO_2 behaviour in underground reservoirs, including pressure effects, phase behaviour, and caprock integrity. The study estimated the Sleipner project's capacity at 1.2 Gt. Since then, more researchers have developed frameworks aimed at capturing the carbon sequestration process more comprehensively.

Šimůnek and Suarez (1993) conducted a study on the development of a model called SOILCO2, which simulates CO₂ transport and production in soil. The model did not use a mechanical approach or mixture theory as a fully coupled THMC model would. Instead, it primarily focused on the thermal and hydraulic aspects of CO₂ transport in soil, without considering the mechanical component. The model relies on process-oriented modelling, primarily using Richards' equation for water flow and convection-diffusion equations for gas transport, combined with empirical relationships for CO₂ production and temperature effects.

In the following years, more researchers began publishing computer simulation results for CCS in different scenarios. For example, the Alberta Research Council has many publications (Gunter et al., 1993; Hitchon, 1996; Gunter et al., 1997a) that used two main computer codes, STARS and PATHARC.94, to study CCS. STARS is a multi-phase model capable of simulating hydrogeological processes. The studies predicted that up to 25% of CO₂ would dissolve into formation water, with the remainder as a supercritical phase, migrating less than 5 km from the injection point. On the other hand,

PATHARC.94 is used for reactive transport modelling, such as fluid-rock interactions and reaction kinetics, and is based on a partially coupled (THC) framework. In the simulations, the fluid phase was assumed to be saturated with CO₂, and realistic mineral dissolution rates were applied. The results predicted that significant CO₂-trapping reactions would have occurred in experiments at 105°C and 90 bar over a timescale of 6-40 years. It was found that dissolution mechanisms were dominant in the early stages of the simulations and were expected to occur closer to the injection well. Neither STARS nor PATHARC.94 uses a fully coupled THMC framework, as they both lack the ability to model mechanical deformation.

In the early 2000s, CCS models and simulations began to accelerate in the academic field. Rutqvist and Tsang (2002) made a notable step in coupled modelling with their integration of TOUGH2 and FLAC3D computer codes. Their work offered a good platform for thermal–hydrologic–mechanical (THM) analysis in both fractured and porous rock formations. The integration allows the model to adapt and reflect real-time changes, that demonstrated the strength of this coupled approach in understanding CCS dynamics. The published research introduces a basic mathematical model that primarily uses a mechanics-based approach. They employed empirical hydromechanical coupling relationships while the continuum equations were discretized in space using the integral finite-difference method. Additionally, the sequential explicit solution applied in their study could be insufficient for problems that exhibit rapid hydro-mechanical changes.

In 2004, TOUGHREACT, which can be considered an upgrade of TOUGH2, was introduced. It is a numerical simulation program for reactive chemical transport, developed by integrating geochemical processes into the existing framework of the non-

isothermal, multi-component fluid, and heat flow simulator TOUGH2 (Pruess et al., 2004; Xu et al., 2004a; Xu et al., 2004b; Pruess, 2005; Xu et al., 2005). The development of TOUGHREACT enabled the modelling of reactive chemical transport processes in addition to thermal and hydrological aspects. The key advantage of TOUGHREACT over TOUGH2 is its ability to model reactive chemical transport, in addition to the fluid and heat flow capabilities that TOUGH2 already offers. TOUGHREACT integrates geochemical processes such as mineral dissolution/precipitation, ion exchange, and aqueous speciation, which are not included in TOUGH2. This allows for simulating interactions between fluids and rocks during processes like carbon sequestration, contaminant transport, and geothermal energy extraction (Xu et al., 2006). TOUGHREACT is based on a mechanical approach, utilizing classical principles of fluid mechanics, heat transfer, and geochemistry, rather than the mixture theory approach used in some fully coupled THMC models. TOUGHREACT is not a fully coupled Thermo-Hydro-Mechanical-Chemical (THMC) framework, though it does couple several key processes. It does not simulate the mechanical responses of the porous media and cannot consider the deformation of the porous media.

Since then, more researchers have focused on developing mathematical derivations of transport models for the CCS process. For example, Bea et al. (2012) presents a process-based reactive transport model to investigate CO₂ sequestration in ultramafic mine tailings, focusing on natural CO₂ mineralization through the weathering of serpentine and brucite minerals. The introduced model relies on Darcy's Law for fluid flow and Fick's Law for vapor diffusion, combined with kinetic and equilibrium reactions for geochemical processes. These are classic continuum-based reactive transport models, not

a mechanical or mixture theory-based approach. However, the model is coupled in the sense that it integrates thermal, hydrological, and chemical processes, making it a THC model. The model includes unsaturated flow, vapor diffusion, and energy balance, fully coupled with solute transport, gas diffusion, and geochemical reactions. Simulations predict that CO_2 sequestration rates range between 0.6 and 1 kg/m²/year, mainly driven by the dissolution of serpentine and subsequent precipitation of hydromagnesite. Limitations include the lack of mechanical coupling, the omission of barometric pressure effects, and simplifications in CO_2 transport processes, leading to potential underprediction of sequestration rates.

Kolditz et al. (2012) addressed deformable porous media in CCS modelling by presenting a numerical framework for simulating two-phase flow in deformable porous media, focusing on CO_2 sequestration in deep geological formations. The objective was to model the interactions between fluid flow (CO_2 and brine), mechanical deformation, and thermal effects during CO_2 injection into saline aquifers. The model accounts for fluid motion via extended Darcy's law, the effective stress principle for solid matrix deformation, and constitutive models for porosity and permeability as functions of fluid saturation. The model uses a mechanical approach based on Biot's consolidation theory, which describes the interaction between fluid flow and the deformation of the solid matrix. This approach treats the solid and fluid phases separately, with the effective stress principle applied to the solid matrix to account for mechanical deformation due to fluid pressure changes. Three simulations were conducted, and the findings show that solid deformation significantly influences CO_2 migration and stress distribution near the

injection well, highlighting the importance of considering mechanical coupling in CO_2 storage simulations. The limitations include potential challenges with phase changes in CO_2 under different conditions, as well as the need for further validation with field data and more realistic heterogeneous subsurface conditions.

Nasvi et al. (2014) also used a mechanical approach, specifically poroelasticity, to describe the interaction between fluid flow (CO₂) and solid deformation (geopolymer). The THM coupled model is used to address only one phase (CO₂), using COMSOL Multiphysics, with results validated against experimental data. The goal is to predict how permeability and flow characteristics change under different conditions to ensure wellbore integrity. Key findings indicate that permeability decreases with increasing pressure due to pore volume shrinkage, and advection is the primary transport mechanism during injection, with diffusion playing a minimal role. Darcy's velocity, CO₂ pressure, and concentration decrease with increasing confinement but rise with higher injection pressure. This demonstrates geopolymer's superiority in CO₂-rich environments compared to conventional cement. The model excludes chemical reaction coupling and sorption effects, which may affect real-world applicability.

Bea et al. (2016) presents a thermo-hydro-mechanical-chemical (THMC) coupled model for analyzing fluid flow, heat transport, and geochemical reactions in deep sedimentary basins influenced by glaciation cycles. The chemical reactions are integrated through reactive transport, modeling mineral dissolution, precipitation, and ion exchange processes in brine-dominated environments. This study introduces enhancements over the previous one (Bea et al., 2012), where the new study incorporating mechanical

deformation of the rock due to ice-sheet loading by solving stress-strain relationships for the porous medium, adding terms for vertical strain and pore pressure evolution due to mechanical loading through $\frac{\partial P}{\partial t} + \zeta \frac{\partial \sigma_{zz}}{\partial t} = \nabla . (k \nabla P)$, where ζ is the loading efficiency coefficient, σ_{zz} is the vertical stress, and P is the fluid pressure. Additionally, the study models thermal transport and its coupling with fluid flow and chemical reactions, accounting for heat transfer in the system. This introduces an energy balance equation $\frac{\partial T}{\partial t} + \upsilon \cdot \nabla T = \nabla \cdot (\lambda \nabla T), \text{ where } T \text{ is temperature and } \lambda \text{ is the thermal conductivity. The model is simulated using the MIN3P-THCm reactive transport code, designed to simulate these processes over long timescales.}$

Islam et al. (2020) used a mechanics-based approach to construct constitutive relations to model leakage through compromised wells. The framework couple's two-phase fluid flow (liquid and gas) with solid-phase deformation. However, it does not incorporate thermal or chemical processes, limiting the coupling scope to hydro-mechanical (HM) coupling. The authors explore two computational schemes: one using capillary pressure and gas pressure as primary variables (PP scheme) and the other using liquid pressure and gas saturation (PS scheme). Innovations in this paper include the use of mass lumping and upwinding techniques to improve numerical stability in heterogeneous media, particularly in the context of fluid infiltration through compromised wells. These techniques are validated against benchmark problems such as Terzaghi's consolidation and the Kueper and Frind tests. The study emphasizes the importance of selecting appropriate primary variables and computational schemes for accurate modelling in leakage scenarios, which is critical for assessing the risk of well integrity failures.

Lu and Zhang (2020) improved the model further by using the Peng–Robinson equation of state in a coupled THM model to simulate CO₂ sequestration in saline aquifers, focusing on the interactions between CO2 injection, temperature, pressure, and mechanical deformation of geological formations. This enhancement incorporates continuous physical property parameters (e.g., CO₂ density and viscosity) using the Peng-Robinson equation of state, allowing for more accurate predictions of CO2 behaviour during phase transitions. They used the Peng-Robinson pressure equation: $P = \frac{RT}{V_m - b} - \frac{a(T)}{V_m (V_m + b) + b (V_m - b)}, \text{ where } P \text{ is the pressure of the gas, } T \text{ is the}$ temperature of the gas, R is the universal gas constant, V_m is molar volume of the gas (volume per mole) and a(T) is attraction parameter, which is temperature-dependent, and b is the repulsion parameter, representing the volume excluded by a mole of gas molecules. Their framework provides detailed insights into spatial CO₂ distribution and injection pressure, making it particularly valuable for preventing issues like caprock fracture. It provides a more comprehensive treatment of phase changes and uses COMSOL Multiphysics for efficient simulation.

Besides the above attempts to improve the model by incorporating continuous physical property parameters, another study published by Carrillo and Bourg (2021) introduced a new computational framework, the Darcy-Brinkman-Biot (DBB) model, for simulating multiphase flow within and around deformable porous media. It combines the Darcy-Brinkman formulation (for fluid flow) with Biot's theory (for mechanics) to represent deformation in porous media. The DBB framework captures the interaction between fluid flow, material deformation, and fracturing. Although it did not consider chemical or

thermal coupling, the DBB model offers stronger two-way coupling between fluid and solid phases, accounting for complex feedback mechanisms like flow-induced deformation and fracturing. This is particularly advantageous in cases involving material failure, which is more difficult to capture with earlier models.

In summary, the journey of coupled modelling in CCS has been one of innovation, refinement, and continuous learning. Each study discussed above has contributed a unique perspective, enriching the collective understanding of the field. As CCS endeavours continue to grow in importance and scale, the insights and advancements in coupled modelling will, without a doubt, play a crucial role in guiding future successes.

2.7 Knowledge Gaps

Although a significant development has been achieved in fluid transport in deformable porous media and carbon sequestration throughout the years, all research done on this subject is fairly new. Most of the studies were done either after the oil and gas industry became a major source of the modern economy, where underground fluids transport studies funded by oil companies, or after nuclear energy was discovered and radioactive waste became an environmental issue. Moreover, carbon sequestration has started recently, and therefore, long-term results are not available yet. Transport of multi-phase fluid in deformable porous media is a complex process, and most models made too many assumptions in an attempt to simplify the model. These assumptions reduce the results' accuracy. The mixture-coupling theory approach has been widely used in Geoenvironmental Engineering to model the transport of fluids in a deformable porous media; however, little research has been done on gas coupling.

Moreover, there is no complete model that captures the full chemical coupling process that can be used to simulate CO_2 injection. Especially the one that focuses on the effect of the coupling relation between dissolution /precipitation and the variable value of porosity/permeability.

Furthermore, some published research such as André et al. (2007a) has chemical coupling but deals with one phase only. There is no good model, yet that can deal with complicated chemical coupling progress that includes porosity and permeability variables with the thermo-hydro-mechanical coupled system, especially when liquid and gas phases are both considered. Moreover, much work remains to be done to understand the complex inter-relationship between the different chemical reactions, especially for the caprock and borehole wall (Rochelle et al., 2004). Although two decades have passed since this paper, Khan et al. (2024) also noted that this knowledge gap still needs to be addressed.. They concluded that CO₂-brine-rock interactions involve complex chemical reactions, and our understanding at the pore and grain scale is still limited. This gap raises concerns about unexpected changes during CO₂ injection in geological carbon storage. Four key reactions impact these systems: (1) CO₂ dissolving in brine, (2) secondary minerals forming from CO₂-enriched brine reactions, (3) interactions between water, rock, and CO_2 , and (4) near-wellbore reactions influenced by factors like temperature, pressure, and rock type. These processes can create nanoparticles, affecting pore structure and potentially changing the wettability of the reservoir rock. Additionally, Lu et al. (2024) highlighted the knowledge gap regarding the kinetics of such chemical reactions. According to the U.S. Department of State's long-term strategy report (2021), technologies such as "enhanced mineralization" are still in the early stages of research and development. As a result, the potential for emissions reduction and the timeframes in which these methods might be effective are uncertain. This is especially relevant in addressing existing knowledge gaps in geochemical kinetics, highlighting the need to overcome these scientific challenges to meet the urgent demands of climate mitigation efforts. The paper also highlights another knowledge gap regarding the interactions between primary and secondary minerals and emphasizes the need to understand how these minerals are coupled and how their interactions influence one another. Hurter et al. (2007) presented simulation results for a CO₂ injection project. The author suggested that even though many simulators and codes are available today, they all have limitations. The author stated that all simulators and codes have a shortcoming in common: the impact of precipitation on the injecting process cannot be predicted accurately. This is because of the lack of accurate generic relationships and correlations between pore space changes, which results in permeability modifications. The author added that the existing research is still fundamental in assessing the impact of precipitation. Audigane et al. (2007) presented a two-dimensional reactive transport model of long-term storage of CO₂. The effect of mineral dissolution and precipitation on porosity is considered. TOUGHREACT software is used to simulate the model. The author considers that coupled modelling of geochemical reactions with multi-phase flow and transport remains a challenging task. He advises improving the model by adding thermal coupling solid solution kinetics and redox phenomena.

Gaus et al. (2008a) highlight the repeated emphasis on the importance of exploring the connections between fluid flow, geochemistry, and geomechanics. They stress the need

for further research to better understand how dissolution and precipitation processes influence the relationship between porosity and permeability. This area of study is critical to improving predictive models for subsurface behaviours, especially in the context of carbon capture and storage (CCS) and other geotechnical applications.

The mixture-coupling theory approach will be used in this research because it can cover the knowledge gap between the geochemistry and geomechanics fields. While geochemistry science focuses on molecular reactions smaller than 1 nanometre in size, geomechanics researchers have their approaches that deal with particles larger than 100 nanometres. The knowledge gap is between 1-100 nanometres, which has an excellent coupling potential between the chemical and physical states. This gap can be covered by developing a fully coupled thermo-hydro-mechanical-chemical-gas (THMCG) model that is based on the mixture-coupling theory. Many researchers developed (THMC) model; however, their models do not deal with coupled variable porosity/permeability nor gas/liquid coupled phases.

Finally, most of the fully coupled codes are limited to single-phase liquid flow. In this research, A fully coupled thermo-hydro-mechanic-chemical-gas model (THMCG) will be developed. In addition to the contribution that will be made in the coupling process between the chemical and THM process, the model will be modified to consider both gas flow phase and liquid flow phase simultaneously.

The next chapter will develop a two-phase coupled transport model using mixturecoupling theory. This model will then be validated against experimental data and findings from other researchers. This two-phase model will serve as the foundation for subsequent thesis chapters, where it will be incrementally expanded to address additional complexities.

2.8 Conclusion and Forward Trajectory

The development of a fully coupled THMC two-phase model for CCS applications represents a key advancement in the field. Moving from a simpler two-phase HM model to a complete THMC framework shows the importance of addressing all aspects of CCS systems. This comprehensive approach is essential for effectively tackling the complex interactions within CCS, ensuring a more accurate and reliable prediction of the system's behaviour.

Moreover, the adoption of mixture-coupling theory within this research paves the way for a more nuanced understanding of the interactions between various phases and components within CCS systems. By meticulously incorporating coupling terms, this model seeks to offer a more accurate representation of real-world phenomena, thereby enhancing the predictability and reliability of CCS technologies.

As this research progresses, it will investigate the complexities of thermal, hydraulic, mechanical, and chemical interactions within CCS systems, offering insights into their synergistic effects. This comprehensive approach will not only address existing gaps in the literature but also contribute to the development of more efficient, safe, and economically viable CCS solutions.

Future chapters will meticulously detail the methodologies employed in the development of the THMC model, along with a rigorous analysis of its performance under various conditions. In Chapter 3, a two-phase fully coupled model will be established using the

mixture-coupling theory, serving as the base model for the CCS THMC model. By systematically enhancing the model with additional coupling terms in subsequent chapters, a fully coupled two-phase THMC model will be developed by the end of this research. This research will demonstrate the model's adaptability and potential to accurately simulate complex CCS operations.

The culmination of this research is expected to offer a significant contribution to the field of CCS, providing a robust tool for researchers, policymakers, and industry practitioners. Offering a more detailed and integrated model aims to facilitate better decision-making processes, optimise CCS operations, and ultimately contribute to the global effort to mitigate climate change through effective carbon management strategies.

Chapter 3: A Fully Coupled Hydro-Mechanical-Gas Model Based On Mixture-Coupling Theory

Abstract

The interactions of gas migration, water transport and mechanical deformation of rocks are significant for geoenergy industry (e.g., Carbon Capture and Storage, radioactive waste disposal), however, the hydro-mechanical-gas coupled model remains a challenge due to the gap between multiple disciplines (e.g. Geomechanics and Geoenergy). This work presents a novel hydro-mechanical framework model of fully coupled two-phase fluid transport in a deformable porous media through extending mixture-coupling theory which is based on non-equilibrium thermodynamics. The main difference between the mixture-coupling theory approach and other approaches (ex., mechanic's approach) is that the mixture-coupling theory uses energy and entropy analysis by utilizing the unbalanced thermodynamics, while the mechanic's approach analyses the stress-strain tensors. The gas free energy has been included in the Helmholtz free energy balance equation. Three main governing equations have been obtained for solid, liquid and gas phases. Benchmark experiments and modelling based on classical continuum mechanics approaches are used to validate the model by comparing the measured data to the simulation results. The results have a good agreement with experimental data, demonstrating that gas migration has a great influence on water transport and deformation of the solids. The novelty of this study is that it is providing a new approach to study the multiphase flow coupling in porous media rather than the classic mechanic's approach.

List of notations

| d d | Displacement tensor | m |
|---------------------------|----------------------------------|---------------|
| C_s | Specific moisture capacity | m^{3}/m^{3} |
| E | Green strain | Dimensionless |
| $E_{\it ij}$ | Green Strain tensor | Dimensionless |
| F | Deformation gradient | Dimensionless |
| G | The rock's shear modulus | Pa |
| I | Unit tensor | Dimensionless |
| J | Jacobian | Dimensionless |
| k | Bulk modulus | Pa |
| k_{abs} | Medium Intrinsic permeability | m² |
| K_{s} | Bulk modulus of the solid matrix | Pa |
| K_{w} | Bulk modulus of water | Pa |
| K_{g} | Bulk modulus of gas. | Pa |
| k_w | Water intrinsic permeability | m² |
| \mathbf{k}_{g} | Gas intrinsic permeability | m² |
| k_{rw} | Water relative permeability | Dimensionless |
| k_{rg} | Gas relative permeability | Dimensionless |
| p^{w} | Pore water pressure | Pa |
| p^{g} | Pore gas pressure | Pa |
| \overline{p} | Average pressure in pore space | Pa |

| S | Boundary attached on the surface | m² |
|---|--|---------------|
| S^w | Saturation of water | Dimensionless |
| S^{g} | Saturation of gas | Dimensionless |
| T | Temperature | K |
| T_{ij} | Piola-Kirchhoff stress | Pa |
| t | Time | s |
| \mathbf{u}^{w} | Darcy velocity of pore water | m/s |
| \mathbf{u}^g | Darcy velocity of pore gas | m/s |
| V | Arbitrary microscopic domain | m^3 |
| \mathbf{V}^{w} | Water velocity | m/s |
| \mathbf{v}^g | Gas velocity | m/s |
| \mathbf{v}^s | Solid velocity | m/s |
| $ u^w$ | Water viscosity | Pa·s |
| $ u^g$ | Gas viscosity | Pa·s |
| $ ho^{\scriptscriptstyle w}$ | Water density relative to the unit volume of the | kg/m^3 |
| | fluid-solid mixture | |
| $ ho^{s}$ | Gas density relative to the unit volume of the | kg/m³ |
| | fluid-solid mixture | |
| $ ho^s$ | Solid density relative to the unit volume of the | kg/m³ |
| | fluid-solid mixture | |
| $ ho_t^{\scriptscriptstyle W}$ | Water true mass density | kg/m³ |
| $ ho_{\scriptscriptstyle t}^{\scriptscriptstyle g}$ | Gas true mass density | kg/m³ |

| $\phi^{\scriptscriptstyle W}$ | Water volume fraction | Dimensionless |
|----------------------------------|--|-------------------|
| ϕ^g | Gas volume fraction | Dimensionless |
| ϕ | Porosity | Dimensionless |
| Ψ | Helmholtz free energy density | J/m^3 |
| 1// | Helmholtz free energy density of the pore | J/m^3 |
| $\Psi_{\it pore}$ | Constituent | |
| Ψ | Free energy in the reference configuration | J |
| σ | Cauchy stress tensor | Pa |
| $\mu^{\!\scriptscriptstyle w}$ | Chemical potential of water | J/mol |
| μ^g | Chemical potential of gas | J/mol |
| ${\cal E}_{ij}$ | Strain tensor | Dimensionless |
| $\sigma_{\scriptscriptstyle ij}$ | Cauchy stress | Pa |
| γ | Entropy production per unit volume | $J/K\!\cdot\!m^3$ |
| $oldsymbol{arrho}^w$ | Volume fraction of pore water in the reference | Dimensionless |
| υ | configuration | |
| v^{g} | Volume fraction of pore gas in the reference | Dimensionless |
| U | configuration | |
| 5 | Biot's coefficient | Dimensionless |
| θ | Poisson's ratio | Dimensionless |
| ∇ | Gradient | m^{-1} |
| ð | Partial Differential | - |

3.1 Introduction

Over the past years, fluid transport in porous media has become an area of great interest for researchers. It is now considered an essential part of studies in the oil industries and environmental institutes. However, modelling the transport of fluids in porous media is complicated due to the coupled nature of the phenomena and the corresponding governing equations with large number of variables. Many approaches have been developed to capture the transportation process. Moreover, coupling between solid and fluid phases can be modelled using two main approaches: the mechanics approach and the mixture-coupling theory approach based on the mixture theory. The mechanics approach is based on a classical consolidation theory described by (Biot, 1941; Biot, 1955; Biot, 1962; Biot and Temple, 1972) and extended from the derivation of stress-strain balance equations. Biot created a coupled relation between fluid flow and linear elasticity for solid deformation (poroelasticity), which was used to calculate the deformation in the porous media.

On the other hand, the mixture theory approach, developed by Truesdell (1957), Truesdell and Toupin (1960), is based on the derivation of the energy balance equation of non-equilibrium thermodynamics using continuum mechanics. Bowen (1980); Bowen (1982) used the mixture theory to model incompressible fluids in porous media. The approach maintains the individuality of the solid and fluid phases and takes into account the phase interaction effects. Heidug and Wong (1996) present the first coupled model based on the mixture theory that capture hydration swelling of water-absorbing saturated rocks under isothermal condition

Chen and Hicks (2011) used the mixture-coupling theory to model the hydro-mechanical effect in unsaturated rock. Their model is a result of combining the non-equilibrium thermodynamics and Biot's poroelasticity. They built their model by deriving Darcy's law for unsaturated flow from the dissipation process and establishing a relationship between stress and pore pressure changes using Helmholtz free energy. Chen and Hicks proposed that their model is capable of capturing both small and large deformation of rocks.

Nowadays, the mixture theory approach is widely used in various fields, including the biomechanics field, where it is used to model the biological interstitial tissue growth, solid tumours and blood flow (Please et al., 1998; Klika, 2014; Cardoso et al., 2013). The mixture theory is also used in the oil field and earth sciences to model carbon capture and storage, reservoir modelling and enhancing oil recovery. Furthermore, the mixture theory method is used in the environmental field to study nuclear waste disposal and groundwater contamination, and in construction studies, to analyse asphalt concrete (Siddique et al., 2017; Krishnan and Rao, 2000).

The mixture-coupling theory can deal with molecular scale effects, and this gives it a great potential to couple chemical reactions process with the hydro-mechanical calculations. As a result, mixture-coupling theory can bridge the gap between the geomechanics and geochemistry field.

The mixture-coupling theory may be used to couple multi-equations together, such as the poroelasticity process (HM), the thermo-poroelasticity process (THM), the poroelasticity-chemical reactions process (HMC) or all together as (THMC).

In soil mechanics, gas migration in the unsaturated formation, such as soil and rocks, is crucial. The big difference in viscosity, density and compressibility between the gas phase and liquid phase cause a significant coupled impact on the hydro-mechanical part. Additionally, gases such as CO₂ or other organic gases may have a considerable chemical impact. In real applications, such as enhancing hydrocarbon production or carbon injection and storage, gas migration needs to be considered. Therefore, including gas migration in the mathematical model is a vital step. The existing mechanics approach can handle coupled hydro-mechanics-chemical- thermal interaction. However, the chemical coupling can be complicated and has many limitations when the mechanics approach is used. Schrefler and Scotta (2001) used the mechanics approach to establish three coupled equations that describe the mechanical behaviour, hydraulic behaviour of the water and the hydraulic behaviour of the air. The equations were then solved numerically using the finite element method. The model was validated by simulating an experiment of semisaturated soil behaviour, triaxial load experiment with clay specimen, and other two examples. However, solving such a problem using the mixture-coupling theory is a step forward.

In this work, anew model is presented based on the mixture-coupling theory approach. the model will be used to capture and evaluate the hydro-mechanical effect of gas and water flow in porous media.

3.2 Physical Model

An arbitrary microscopic domain V, which is large enough to include all types of phases, is selected. S is the surface boundary enclosing the domain V. Only fluids (e.g. water or gas) are allowed to pass through the boundary.

3.2.1 Definition of flux, density, volume fraction and saturation

The mass flux of water and gas is defined as

$$\mathbf{I}^{w} = \rho^{w} \left(\mathbf{v}^{w} - \mathbf{v}^{s} \right), \ \mathbf{I}^{g} = \rho^{g} \left(\mathbf{v}^{g} - \mathbf{v}^{s} \right)$$
(3.1)

where the superscripts w, g and s denote water, gas and solid, respectively. ρ^w , ρ^g are The mixture densities of water and gas are related to the volume of the mixture system. \mathbf{v}^w , \mathbf{v}^g and \mathbf{v}^s are the velocities of each phase.

 ρ^w , ρ^g are related to the true mass density (associated with the volume of phases) of water ρ^w_t and gas ρ^g_t through:

$$\rho^{w} = \phi^{w} \rho_{t}^{w}, \rho^{g} = \phi^{g} \rho_{t}^{g} \tag{3.2}$$

where ϕ^w and ϕ^g are the volume fractions of water and gas.

$$\phi = \phi^w + \phi^g \tag{3.3}$$

 ϕ is the porosity.

The saturation of water and gas are:

$$S^{w} = \frac{\phi^{w}}{\phi}, S^{g} = \frac{\phi^{g}}{\phi}$$
 (3.4)

Clearly, there is a relationship:

$$S^g = 1 - S^w \tag{3.5}$$

3.2.2 Balance equation

The balance equation for Helmholtz free energy in a mixture system including solid, water and gas is:

$$\frac{D}{Dt} \int_{V} \psi dV = \int_{S} \mathbf{\sigma} \mathbf{n} \cdot \mathbf{v}^{s} dS - \int_{S} \mu^{w} \mathbf{I}^{w} \cdot \mathbf{n} dS - \int_{S} \mu^{g} \mathbf{I}^{g} \cdot \mathbf{n} dS - T \int_{V} \gamma dV$$
(3.6)

where: ψ is Helmholtz free energy density, σ is the Cauchy stress tensor, μ^w is the chemical potential of water, μ^g is the chemical potential of gas, T is temperature, γ is the entropy production per unit volume. Equation (3.6) is an extension of the Helmholtz free energy balance equation under constant temperature presented by Heidug and Wong (1996), by adding the gas flux to represent the free energy change due to gas flowing into/out the selected domain. It is worth noting that this equation originates from a mechanistic approach modelling background. While there are many common equations between the mechanics approach and the mixture coupling theory approach, the key difference lies in the use of the entropy production balance equation and thermodynamic relations.

The material time derivative is

$$\frac{D}{Dt} = \partial_t + \mathbf{v}^s \cdot \nabla \tag{3.7}$$

in which ∂_t is the time derivative and ∇ the spatial gradient.

The differential form of the balance equation (3.6) for the free energy is expressed as

$$\dot{\psi} + \psi \nabla \cdot \mathbf{v}^s - \nabla \cdot (\sigma \mathbf{v}^s) + \nabla \cdot (\mu^w \mathbf{I}^w) + \nabla \cdot (\mu^g \mathbf{I}^g) = -T \gamma \le 0$$
(3.8)

Balance equation for water mass is

$$\frac{D}{Dt} \left(\int_{V} \rho^{w} dV \right) = -\int_{S} \mathbf{I}^{w} \cdot \mathbf{n} dS \tag{3.9}$$

The differential form is

$$\dot{\rho}^{w} + \rho^{w} \nabla \cdot \mathbf{v}^{s} + \nabla \cdot \mathbf{I}^{w} = 0 \tag{3.10}$$

Balance equation for gas mass is

$$\frac{D}{Dt} \left(\int_{V} \rho^{g} dV \right) = -\int_{S} \mathbf{I}^{g} \cdot \mathbf{n} dS \tag{3.11}$$

The differential form is

$$\dot{\rho}^g + \rho^g \nabla \cdot \mathbf{v}^s + \nabla \cdot \mathbf{I}^g = 0 \tag{3.12}$$

3.2.3 Entropy product and transport law

The entropy product arises from the dissipative processes, namely, the friction generated at the solid/fluid phase boundary when the fluid moves through a solid matrix. The entropy product can be divided into two parts: entropy induced by water fraction and gas

fraction. By using non-equilibrium thermodynamics, the entropy production is described by Katachalsky and Curran (1965) as:

$$-\mathbf{I}^{w} \cdot \nabla \mu^{w} - \mathbf{I}^{g} \cdot \nabla \mu^{g} = T \gamma \ge 0 \tag{3.13}$$

The Darcy velocity of pore water \mathbf{u}^w and gas \mathbf{u}^g are:

$$\mathbf{u}^{w} = S^{w} \phi \left(\mathbf{v}^{w} - \mathbf{v}^{s} \right) \tag{3.14}$$

$$\mathbf{u}^{g} = S^{g} \phi \left(\mathbf{v}^{g} - \mathbf{v}^{s} \right) \tag{3.15}$$

Then, based on the entropy product $T \gamma^w = -\mathbf{I}^w \cdot \nabla \mu^w$ and $T \gamma^g = -\mathbf{I}^g \cdot \nabla \mu^g$, the Darcy's Law for water and gas transport can be obtained through using Phenomenological Equations (Chen and Hicks, 2011):

$$\mathbf{u}_{w} = -\mathbf{k}_{w} \frac{k_{w}}{v^{w}} \nabla p^{w} \tag{3.16}$$

$$\mathbf{u}_{g} = -\mathbf{k}_{g} \frac{k_{rg}}{v^{g}} \nabla p^{g} \tag{3.17}$$

where k_w , k_g are the intrinsic permeability for water and gas, k_{nw} and k_{rg} are the relative permeability, v^w and v^g are the viscosity, p^w and p^g are the pore water pressure and pore gas pressure. Darcy's Law can be derived using these phenomenological equations that take entropy production into account, although this is not the most common method. Usually, Darcy's Law is derived in a simpler, empirical way. To determine the Darcy coefficient, experimental data is needed, or it can be compared with other methods to get accurate results.

3.2.4 Hydro-mechanical framework equation

3.2.4.1 Basic equation for deformation

The soil/rock is assumed to be in mechanical equilibrium, so that $\nabla \cdot \mathbf{\sigma} = \mathbf{0}$. With the entropy production (3.13) and balance equation (3.8), the equation for ψ can be written as:

$$\dot{\psi} + \psi \nabla \cdot \mathbf{v}^s - (\boldsymbol{\sigma} : \nabla \mathbf{v}^s) + \mu^w \nabla \cdot \mathbf{I}^w + \mu^g \nabla \cdot \mathbf{I}^g = 0$$
(3.18)

The classic continuum mechanics is used here to measure the rock's deformation state. Some basic relationships are needed: for an arbitrary reference configuration \mathbf{X} , with time denoted by t and position by \mathbf{x} , the expression of Green strain \mathbf{E} , and deformation gradient \mathbf{F} are expressed as:

$$\mathbf{F} = \frac{\partial \mathbf{x}}{\partial \mathbf{X}} (\mathbf{X}, t) , \mathbf{E} = \frac{1}{2} (\mathbf{F}^{\mathrm{T}} \mathbf{F} - \mathbf{I})$$
 (3.19)

where **I** is a unit tensor.

The second Piola-Kirchhoff stress T is introduced to measure the stress in the reference configuration, and it is related to the Cauchy stress σ by:

$$\mathbf{T} = \mathbf{J}\mathbf{F}^{-1}\mathbf{\sigma}\mathbf{F}^{-T} \tag{3.20}$$

where J is the Jacobian of \mathbf{F} :

$$J = \frac{dV}{dV_0}, \dot{J} = J\nabla \mathbf{v}^s \tag{3.21}$$

dV is the volume in the current configuration and dV_0 is the volume in the reference configuration.

From the equation (3.10), (3.12) ,and (3.18), with equations (3.19) ,(3.20), and (3.21) it leads to:

$$\dot{\Psi} = tr(\mathbf{T}\dot{\mathbf{E}}) + \mu^{w} \dot{m}^{w} + \mu^{g} \dot{m}^{g} \tag{3.22}$$

in which: $\Psi = J\psi$ is the free energy in the reference configuration, $m^{\beta} = J \rho^{\beta} = JS^{\beta}\phi\rho_t^{\beta}$ is the mass density of the pore water ($\beta = w$)/gas($\beta = g$) in the reference configuration

3.2.4.2 Helmholtz free energy density of pore water/gas

The Helmholtz free energy density of the pore constituent, including water and gas, is denoted as ψ_{pore} . Then, based on classical thermodynamics, the free energy density of pore space can be written as:

$$\psi_{pore} = -\bar{p} + S^{w} \rho_{t}^{w} \mu^{w} + S^{g} \rho_{t}^{g} \mu^{g}$$
(3.23)

where \bar{p} is the average pressure in pore space and is described as:

$$\overline{p} = p^w S^w + p^g S^g \tag{3.24}$$

By substituting equation (3.24) into equation (3.23), \bar{p} can be eliminated as:

$$\dot{\psi}_{pore} = -\left(p^{w}S^{w}\right) - \left(p^{g}S^{g}\right) + \dot{\mu}^{w}\left(S^{w}\rho_{t}^{w}\right) + \mu^{w}\left(S^{w}\rho_{t}^{w}\right) + \dot{\mu}^{g}\left(S^{g}\rho_{t}^{g}\right) + \mu^{g}\left(S^{g}\rho_{t}^{g}\right)$$

(3.25)Applying Gibbs-Duhem equation in a constant temperature to pore water and gas separately, it leads to:

$$S^{w} \dot{p}^{w} = \dot{\mu}^{w} S^{w} \rho_{t}^{w}$$

$$S^{g} \dot{p}^{g} = \dot{\mu}^{g} S^{g} \rho_{t}^{g}$$
(3.26)

and then, with equation (3.25) and (3.26), it leads to

$$\dot{\psi}_{pore} = -p^{w} \dot{S}^{w} - p^{g} \dot{S}^{g} + \mu^{w} \left(S^{w} \rho_{t}^{w} \right) + \mu^{g} \left(S^{g} \rho_{t}^{g} \right)$$
(3.27)

3.2.4.3 Free energy density of the wetted mineral matrix

The free energy density of the wetted matrix can be obtained by subtracting the free energy of pore water/gas from the total free energy of the combined rock/water/gas system.

From equation (3.22) and (3.27), the free energy of the wetted mineral matrix is obtained as:

$$(\Psi - J\phi \psi_{pore}) = tr(\mathbf{T}\dot{\mathbf{E}}) + \bar{p}\dot{\upsilon}$$
(3.28)

Where $v = J\phi$ is the volume fraction of the pores in the reference configuration.

The dual potential can be expressed as

$$W = (\Psi - J\phi\psi_{pore}) - \bar{p}\upsilon \tag{3.29}$$

By substituting equation (3.28) into the time derivation of the equation (3.29), it leads to:

$$\dot{W} = tr(\mathbf{T}\dot{\mathbf{E}}) - \dot{\bar{p}}\upsilon \tag{3.30}$$

where W is a function of \mathbf{E} , and \bar{p} , so the expression of \mathbf{T} , and v can be given. Equation (3.30) implies the time derivative of $W(\mathbf{E}, \bar{p})$ satisfies the relation:

$$\vec{W}(\mathbf{E}, \vec{p}) = tr(\mathbf{T}\dot{\mathbf{E}}) - \dot{\vec{p}}\upsilon$$
 (3.31)

and then

$$T_{ij} = \left(\frac{\partial W}{\partial E_{ij}}\right)_{\bar{p}}, \upsilon = -\left(\frac{\partial W}{\partial \bar{p}}\right)_{E_{ij}}$$
 (3.32)

and

$$\vec{W} (\mathbf{E}, \bar{p}) = \left(\frac{\partial W}{\partial E_{ij}}\right)_{\bar{p}} \dot{E} + \left(\frac{\partial W}{\partial p}\right)_{E_{ij}} \dot{\bar{p}}$$

$$(3.33)$$

$$\vec{T}_{ij} = L_{ijkl} \dot{E}_{kl} - M_{ij} \dot{\bar{p}} \tag{3.34}$$

(3.35)

where the parameters L_{ijkl} , M_{ij} , Q are as following group equations

 $\dot{\upsilon} = M_{ii} \dot{E}_{ii} + Q \dot{\bar{p}}$

$$L_{ijkl} = \left(\frac{\partial T_{ij}}{\partial E_{kl}}\right)_{\bar{p}} = \left(\frac{\partial T_{kl}}{\partial E_{ij}}\right)_{\bar{p}}$$

$$M_{ij} = -\left(\frac{\partial T_{ij}}{\partial \bar{p}}\right)_{E_{ij}} = \left(\frac{\partial \upsilon}{\partial E_{ij}}\right)_{E_{ij}}$$
(3.36)

$$Q = \left(\frac{\partial \upsilon}{\partial \overline{p}}\right)_{E_{ii}}$$

3.2.5 Coupled hydro-mechanical governing equations

3.2.5.1 Mechanical behaviour

Equations (3.34), (3.35) provided the general coupled equation for the mechanical behaviour, water pressure, gas pressure, large deformation, and anisotropic condition. This article focuses on the coupling of mechanical-water-and gas, so some assumptions are made to simplify the discussion:

i. The mechanical behaviour is regarded to be a small strain condition, so the Green Strain tensor E_{ij} and Piola-Kirchhoff stress T_{ij} can be replaced by strain tensor ε_{ij} and Cauchy stress σ_{ij} .

$$E_{ii} \approx \varepsilon_{ii} , T_{ii} \approx \sigma_{ii}$$
 (3.37)

ii. The parameters L_{ijkl} , M_{ij} , Q are material-dependent constants, and the material is isotropic. Therefore, the tensor M_{ij} is diagonal and can be written in the forms of scalars ζ as

$$M_{ij} = \zeta \delta_{ij} \tag{3.38}$$

iii. To avoid mathematical complexity, in this model, The porous media is assumed to has a completely isotropic behaviour (isotropic material).

Based on the assumption (ii), the elastic stiffness L_{ijkl} can be a fourth-order isotropic tensor as

$$L_{ijkl} = G\left(\delta_{ik}\,\delta_{jl} + \delta_{il}\,\delta_{jk}\right) + (K - \frac{2G}{3})\delta_{ij}\,\delta_{kl} \tag{3.39}$$

Here G denotes the rock's shear modulus and K denotes the bulk modulus.

The assumption of small strain mechanics was applied at this point to simplify the discussion. While this assumption is valid for most CCS modelling applications, in future work, the model could be extended to account for scenarios where large deformations are significant, such as in high-stress environments. This is why I maintained these assumptions until the end of the derivation process.

With equations (3.38), (3.39) and (3.37), the governing stress equation (3.34) can be simplified to

$$\dot{\sigma}_{ij} = \left(K - \frac{2G}{3}\right) \dot{\varepsilon}_{kk} \,\delta_{ij} + 2G \,\dot{\varepsilon}_{ij} - \dot{\bar{p}} \,\delta_{ij} \tag{3.40}$$

the incremental relationship between stress and pore fluid pressure is:

$$\dot{\sigma}_{ij} = -\dot{\bar{p}}\,\delta_{ij} \tag{3.41}$$

where \bar{p} is the average pressure in the pore space, and

$$\overline{p} = p^{w} S^{w} + p^{g} S^{g} = p^{w} S^{w} + p^{g} - S^{w} p^{g}$$
(3.42)

strain rate is related to the average pore pressure by

$$\dot{\varepsilon}_{ij} = -\frac{\dot{\bar{p}}}{3K_s} \delta_{ij} \tag{3.43}$$

where K_s is the bulk modulus of the solid matrix.

and volume change is related to pore fluid pressure by:

$$\dot{\upsilon} = -\phi \frac{\dot{\bar{p}}}{K_s} \tag{3.44}$$

Substituting equation (3.41) and (3.43) into equation (3.40):

$$-\dot{\bar{p}}\delta_{ij} = \left(K - \frac{2G}{3}\right)\left(-\frac{\dot{\bar{p}}}{K_s}\delta_{ij}\right) + 2G\left(-\frac{\dot{\bar{p}}}{3K_s}\delta_{ij}\right) - \zeta\dot{\bar{p}}\delta_{ij}$$
(3.45)

From equation (3.45), it leads to:

$$\zeta = \left(1 - \frac{K}{K_s}\right) \tag{3.46}$$

The quantity ζ is defined as the Biot's coefficient and is related to the bulk modulus K and K_s as described in equation (3.46).

From equation (3.42), the average pressure can be rewritten as:

$$\dot{\bar{p}} = (S^w + C_s p^c) \dot{p}^w + (S^g - C_s p^c) \dot{p}^g$$
 (3.47)

where $C_s = \frac{\partial S^w}{\partial p^c}$ is the specific moisture capacity, and can be determined from the soil water characteristic curve (SWCC) or by experiments (Van Genuchten, 1980b; Milly, 1982; Maina and Ackerer, 2017). $p^c = (p^g - p^w)$ is the capillary pressure.

Then, equation (3.40) can be written as:

$$\dot{\sigma}_{ij} = \left(K - \frac{2G}{3}\right) \dot{\varepsilon}_{kk} \, \delta_{ij} + 2G \, \dot{\varepsilon}_{ij} - \zeta \left(S^w + C_s p^c\right) \dot{p}^w \, \delta_{ij} - \zeta \left(S^g - C_s p^c\right) \dot{p}^g \, \delta_{ij}$$

$$(3.48)$$

By assuming mechanical equilibrium condition $\partial \sigma_{ij}/\partial x_j=0$, and using displacement variables d_i (i=1,2,3) through $\varepsilon_{ij}=\frac{1}{2}(d_{i,j}+d_{j,i})$, it leads to

$$G\nabla^{2}\dot{\mathbf{d}} + \left(\frac{G}{1-2\theta}\right)\nabla(\nabla\cdot\dot{\mathbf{d}}) - \zeta\nabla\left[\left(S^{w} + C_{s}p^{c}\right)\dot{p}^{w}\right] - \zeta\nabla\left[\left(S^{g} - C_{s}p^{c}\right)\dot{p}^{g}\right] = 0$$
(3.49)

In which θ is Poisson's ratio

3.2.5.2 Fluid-phase

By substituting water density equation (3.2), and saturation equation (3.4) in to water partial mass equation (3.10):

$$\left(\rho_{t}^{w}\phi S^{w}\right)\cdot+\rho_{t}^{w}\phi S^{w}\nabla\cdot\mathbf{v}^{s}+\nabla\cdot\left(\rho_{t}^{w}\phi S^{w}\left(\mathbf{v}^{w}-\mathbf{v}^{s}\right)\right)=0$$
(3.50)

By using Darcy velocity equation (3.14):

$$\left(\rho_t^w \phi S^w\right) + \rho_t^w \phi S^w \nabla \cdot \mathbf{v}^s + \nabla \cdot \left(\rho_t^w \mathbf{u}^w\right) = 0 \tag{3.51}$$

By multiplying both side by the Jacobian J and using Euler identity as $\dot{J} = J\nabla v_s$ and $v = J\phi$, the conservation equation of water can be written as:

$$(S^{w} \upsilon \rho_{t}^{w}) + \nabla \cdot (\rho_{t}^{w} \mathbf{u}^{w}) = 0$$

$$(3.52)$$

By expanding the derivation terms:

$$S^{w} \dot{\upsilon} \rho_{t}^{w} + \dot{S}^{w} \upsilon \rho_{t}^{w} + S^{w} \upsilon \dot{\rho}_{t}^{w} + \nabla \cdot (\rho_{t}^{w} \mathbf{u}^{w}) = 0$$
(3.53)

By using assumption (i), and equation (3.38), equation (3.35) can be written as:

$$\dot{\upsilon} = \zeta \delta_{ij} \dot{\varepsilon}_{ij} + Q \dot{\overline{p}} \tag{3.54}$$

The parameter Q can be obtained by eliminating \dot{v} , and $\dot{\varepsilon}_{ij}$ by using equations (3.43), and (3.44) into equation (3.54):

$$-\phi \frac{\dot{\bar{p}}}{K_s} = \zeta \delta_{ij} \left(-\frac{\dot{\bar{p}}}{K_s} \right) + Q\dot{\bar{p}}$$
 (3.55)

$$Q = \frac{\zeta - \phi}{K_s} \tag{3.56}$$

Substituting equations (3.54), and Darcy's law for water (3.16) in to equation (3.53):

$$S^{w}\left(\zeta\delta_{ij}\dot{\varepsilon}_{ij} + Q\dot{\bar{p}}\right)\rho_{t}^{w} + \dot{S}^{w}\upsilon\rho_{t}^{w} + S^{w}\upsilon\dot{\rho}_{t}^{w} + \nabla\cdot\rho_{t}^{w}\left(-\mathbf{k}_{w}\frac{k_{nw}}{v^{w}}\nabla p^{w}\right) = 0 \quad (3.57)$$

By using displacement variables d_i (i = 1, 2, 3) through $\varepsilon_{ij} = \frac{1}{2}(d_{i,j} + d_{j,i})$, equation (3.47) to eliminate the average pore pressure rate, and Q value from equation (3.56) into equation (3.57):

$$\zeta S^{w} \rho_{t}^{w} \nabla \cdot \dot{\mathbf{d}} + \frac{\zeta - \phi}{K_{s}} S^{w} \rho_{t}^{w} \left(S^{w} + C_{s} p^{c} \right) \dot{p}^{w} + \frac{\zeta - \phi}{K_{s}} S^{w} \rho_{t}^{w} \left(S^{g} - C_{s} p^{c} \right) \dot{p}^{g} + \dot{S}^{w} \upsilon \rho_{t}^{w} + S^{w} \upsilon \dot{\rho}_{t}^{w} + \rho_{t}^{w} \left(-\mathbf{k}_{w} \frac{k_{w}}{v^{w}} \nabla^{2} p^{w} \right) = 0$$

$$(3.58)$$

The water density change equation:

$$\dot{\rho}_{t}^{w} = \rho_{t}^{w} \left(\frac{1}{\rho_{t}^{w}} \frac{\partial \rho_{t}^{w}}{\partial p^{w}} \right) \frac{\partial p^{w}}{\partial t} = \rho_{t}^{w} \frac{1}{K_{w}} \dot{p}^{w}$$
(3.59)

where K_w is the bulk modulus of water

By combining (3.59) with (3.58) leads to:

$$\zeta S^{w} \rho_{t}^{w} \nabla \cdot \dot{\mathbf{d}} + \left(\frac{\zeta - \phi}{K_{s}} S^{w} \rho_{t}^{w} \left(S^{w} + C_{s} p^{c} \right) + \frac{S^{w} \phi \rho_{t}^{w}}{K_{w}} \right) \dot{p}^{w} +$$

$$\frac{\zeta - \phi}{K_{s}} S^{w} \rho_{t}^{w} \left(S^{g} - C_{s} p^{c} \right) \dot{p}^{g} + \dot{S}^{w} \phi \rho_{t}^{w} + \rho_{t}^{w} \left(-k_{w} \frac{k_{rw}}{v^{w}} \nabla^{2} p^{w} \right) = 0$$
(3.60)

Separate the C_s terms from the brackets and recall the definition of C_s , then equation (3.60) becomes:

$$\zeta S^{w} \nabla \cdot \dot{\mathbf{d}} + \left(\frac{\zeta - \phi}{K_{s}} S^{w} S^{w} + \frac{S^{w} \phi}{K_{w}}\right) \dot{p}^{w} + \frac{\zeta - \phi}{K_{s}} S^{w} S^{g} \dot{p}^{g}
+ \left(-\frac{\zeta - \phi}{K_{s}} S^{w} p^{c} + \phi\right) \dot{S}^{w} + \left(-k_{w} \frac{k_{nw}}{v^{w}} \nabla^{2} p^{w}\right) = 0$$
(3.61)

3.2.5.3 Gas phase

With a similar derivation process to section 2.4.2, the final gas governing equation can be obtained:

$$\zeta S^{g} \nabla \cdot \dot{\mathbf{d}} + \left(\frac{\zeta - \phi}{K_{s}} S^{g} S^{g} + \frac{S^{g} \phi}{K_{g}} \right) \dot{p}^{g} + \frac{\zeta - \phi}{K_{s}} S^{g} S^{w} \dot{p}^{w}
+ \left(\frac{\zeta - \phi}{K_{s}} S^{g} p^{c} + \phi \right) \dot{S}^{g} + \left(-k_{g} \frac{k_{rg}}{v^{g}} \nabla^{2} p^{g} \right) = 0$$
(3.62)

where K_g is the bulk modulus of gas.

3.3 Numerical solution

Many researchers (Schrefler and Scotta, 2001; Laloui et al., 2003; Hu et al., 2011; Kim and Kim, 2013; Islam et al., 2020; Wei et al., 2020b) have used the drainage test performed by Liakopoulos (1965a) as a benchmark test to validate numerical models for unsaturated porous media. In this work, COMSOL Multiphysics software is used to simulate the drainage test to validate the proposed model. Three physical domains: solid mechanics, Darcy's law for water, and Darcy's law for gas were incorporated into the model builder environment. The parameters for each physics domain were adjusted to align with the governing equations previously outlined. The simulation results were then compared with experimental data to evaluate the model's accuracy. However, since Liakopoulos (1965a) only measured the water pore pressure and the water outflow rate of the system, the rest of the results, such as air pressure, displacement, capillary pressure and water saturation, are compared to Schrefler and Scotta (2001).

The objective of the Liakopoulos (1965a) experiment is to study the fully saturation condition in a gradual desaturation state development. In the proposed experiment, 1.0 m length and 10 cm diameter Perspex column was filled with Del Monte sand with top and bottom exposed to the atmospheric pressure. The walls of the tube walls are assumed to

be rigid and impermeable for both water and air (no lateral displacement at the sides boundary and no flow). Tensiometers were used to measure the change of pore pressure along with column height. Only gravitational force is considered in the process. The column of sand is then constantly fed with water from the top until a constant flow rate is established through the column, and the drainage flow from the bottom through a filter becomes steady (inflow=outflow). After achieving the uniform flow condition, the water flow supply from the top is terminated (considered as time t=0). The water then starts to drain due to gravity.

In this numerical simulation, the capillary pressure calculation is valid for saturation $S^w > 0.91$. The relative permeability is calculated using Brooks and Corey (1966) model as following:

$$S^{w} = 1 - 0.10152 \left(\frac{p^{c}}{\rho_{w} g}\right)^{2.4279}, \quad k_{rw} = 1 - 2.207 (1 - S^{w})^{1.0121}$$
 (3.63)

Table 3.1 shows the experiment's parameter; however, some of these properties were not provided by Liakopoulos himself, such as Young's modulus and Poisson's ratio. However, they were estimated by other researchers such as Lewis and Schrefler (1998b).

Table 3.1: Material parameters

| Physical meaning | Values and units |
|----------------------|-----------------------------------|
| Young's modulus | E = 1.3 MPa |
| Water density | $\rho^{w} = 1000 \mathrm{kg/m^3}$ |
| Gas density (air) | $\rho^g = 1.2 \mathrm{kg/m^3}$ |
| Solid density (sand) | $\rho^s = 2000 \mathrm{kg/m^3}$ |
| Poisson's ratio | $\theta = 0.2$ |
| Biot's coefficient | $\zeta = 1$ |
| Porosity | $\phi = 0.2975$ |

Intrinsic permeability of the solid (sand) $k_{abs} = 4.5 \times 10^{-13} \text{ m}^2$ Dynamic viscosity of water $v^w = 1 \times 10^{-3} \text{ Pa s}$ Dynamic viscosity of gas (air) $v^g = 1.8 \times 10^{-5} \text{ Pa s}$ Bulk modulus of water $K_w = 2.0 \times 10^3 \text{ MPa}$ Bulk modulus of solid (sand) $K_g = 0.1 \text{ MPa}$

For the numerical solution, assumptions have been made to conform with the laboratory conditions; first, the drainage process occurs due to gravity force only along the vertical direction. Second, at t = 0, the porous media is fully saturated with water $(S^w = 1)$. Moreover, for the sake of simplicity, the porosity change is neglected in this simulation.

For the relations above, the capillary pressure should be constrained by $P^c > 0$. Moreover, to have a stable numerical solution through the transition phase from fully saturated to partially saturated state, a lower bound of 1×10^{-4} air relative permeability k_{rg} is applied. This lower bound will simulate the micro-bubbles of the air while the system was approximating to the fully saturated state (Schrefler and Xiaoyong, 1993; Hu et al., 2011). For numerical convergence testing, several tests were performed, including mesh refinement and timestep sensitivity analyses, under different boundary conditions and saturation transitions to verify convergence behavior. The results were consistent, showing minimal variation.

Boundary and initial conditions:

Liakopoulos (1965a) assumed that the lateral boundary of the tube is impermeable for both water and gas. However, some researchers, such as Hu et al. (2011) suggested that the interface between the sand column and the cylinder in Liakopoulos (1965a) drainage

test might provide a fair passage for the air, and the experiment was not guaranteed to be a gas-tight on the lateral boundaries. Hu et al. (2011) discussed this issue and compared the two assumptions, and concluded that having a gas permeable lateral boundary in the simulation gives a much better match to the experiment (outflow measurements). In this paper, the boundary condition for the air pressure at the lateral walls, the top and the bottom end of the sand column will be set as $p^g = p_{atm}$. For the initial conditions, Narasimhan (1979) mentioned that at t = 0, $S^w = 1$ and the pressure head was zero everywhere in the column as measured in several tensiometers distributed through the column. Because of that, the initial gas and water pressure will be set as zero ($p^w = 0$, $p^g = 0$). Figure 3.1 shows the initial and boundary conditions for the experiment simulation.

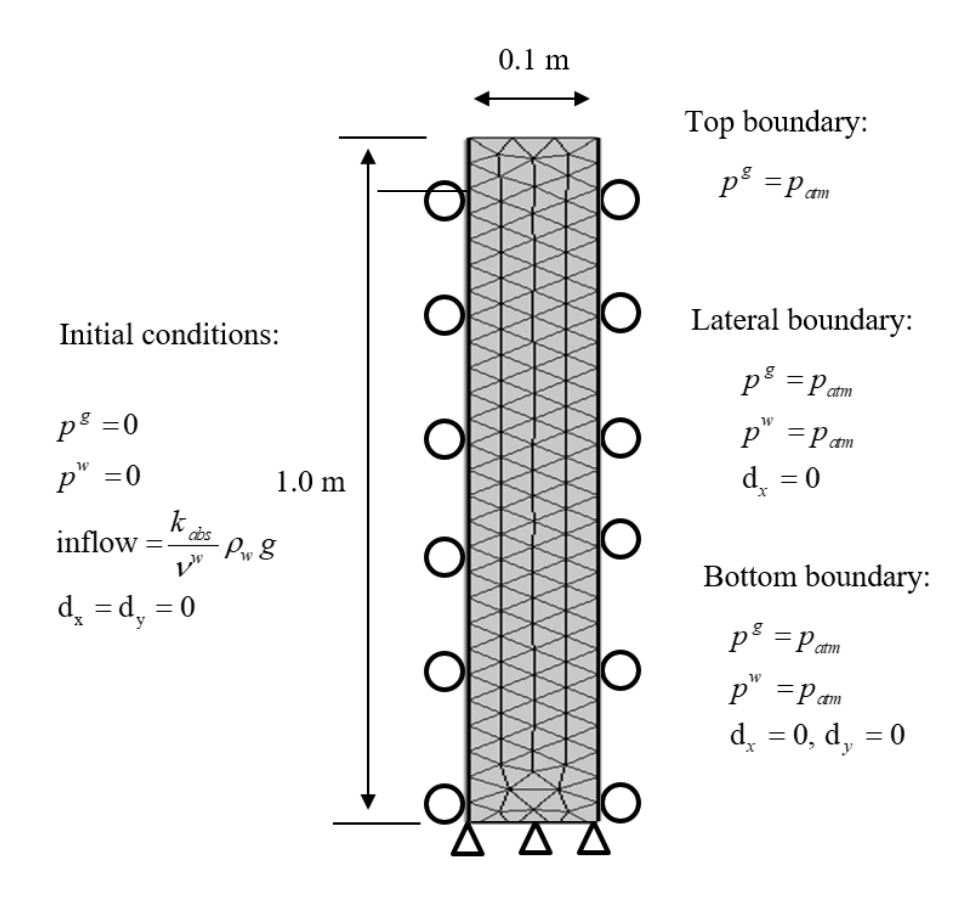


Figure 3.1: Initial and boundary conditions for Liakopoulos (1965a) drainage test.

Figure 3.2 compares the simulation results with Liakopoulos (1965a) experimental results. The figure shows the water pressure change through the vertical distance of the sand column at different time intervals (5, 10, 20, 30, 60 and 120 minutes). The numerical and the experimental results have a good agreement after 20 minutes, however, prior to this, the measured water pressure seems to decrease more slowly than the numerical solution, which dropped more rapidly. Schrefler and Scotta (2001) and many other researchers observed a similar phenomenon (Islam et al., 2020; Wei et al., 2020b; Kim and Kim, 2013; Gawin et al., 1997; Bandara et al., 2016) and justify it to the simplified model used for the simulation. In general, the differences between the simulation results and experimental data could be attributed to the chosen solution strategies and the specific framework used, as different approaches yield slightly different outcomes. This is because each method relies on its own set of assumptions to simplify the derivation process. For example, the assumptions listed in the "Mechanical Behaviour" section of this chapter (Section 3.2.5.1) influence the results. Additionally, the simulation assumes that the drainage process occurs solely due to gravity in the vertical direction, and changes in porosity are neglected. Furthermore, some key material properties, such as Young's modulus and Poisson's ratio, were not provided by Liakopoulos himself and were reverse calculated.

Figure 3.3 through Figure 3.7 compares the numerical solution with Schrefler and Scotta (2001) simulation's results. There is a clear difference in the gas (air) pressure results, as shown in Figure 3.4, where the pressure peaks in Schrefler and Scotta's simulation shifted down through the column more aggressively. These differences are due to some differences in the governing equations and the numerical solution logarithm. However,

Kim and Kim (2013) conducted an experiment and compared the result with Schrefler and Scotta (2001) air pressure results and found that the air pressure peaks do not move down in such a violent wayt is worth noting that Schrefler and Scotta's (2001) research provides a solid foundation for comparison and has been widely cited by others, including Kim and Kim (2013) and Islam et al. (2020). While Kim and Kim focused on pressure simulations and comparing various solution strategies, this study primarily explored other aspects, such as displacement and water saturation. Therefore, benchmarking against their work was not considered necessary, as it would not have provided additional insights beyond the differences in air pressure results. The capillary pressure in Figure 3.5 is expected to be slightly different from Schrefler and Scotta's since it is directly related to the air pressure values ($p^c = p^g - p^w$). Figure 3.6 shows the water saturation results. The results seem close to Schrefler and Scotta's data; nonetheless, differences are justified because the water saturation calculation estimated based on Brooks and Corey (1966) model is a function of capillary pressure, as shown in equation (3.63). Finally, Schrefler and Scotta's displacement results show almost the same trend but with 36% less deformation than the mixture-coupling theory model, as shown in Figure 3.7. Though, when the displacement is compared to other researchers such as Islam et al. (2020), the results are almost identical.

Overall, the simulation results of the proposed model have a good agreement with Liakopoulos (1965a) experiment's results. The comparison between the proposed model solution and Schrefler and Scotta (2001) shows close findings with some differences that can be justified by the differences in the governing equations and the numerical approach. However, these differences are still consistent with other researchers results, as discussed

earlier. As there are no reliable benchmark experimental data that shows the exact air pressure and solid-phase displacement, it is difficult to determine which model is more accurate.

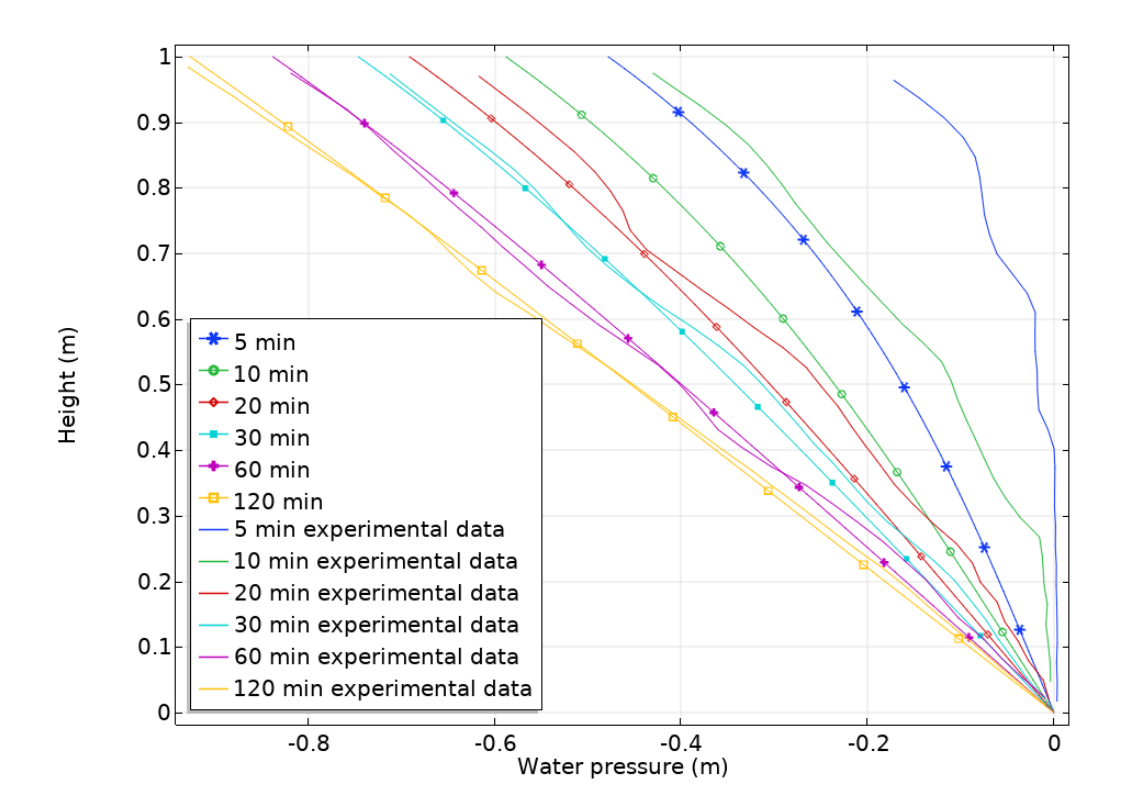


Figure 3.2: Simulation results vs Liakopoulos' experiment data (water pressure)

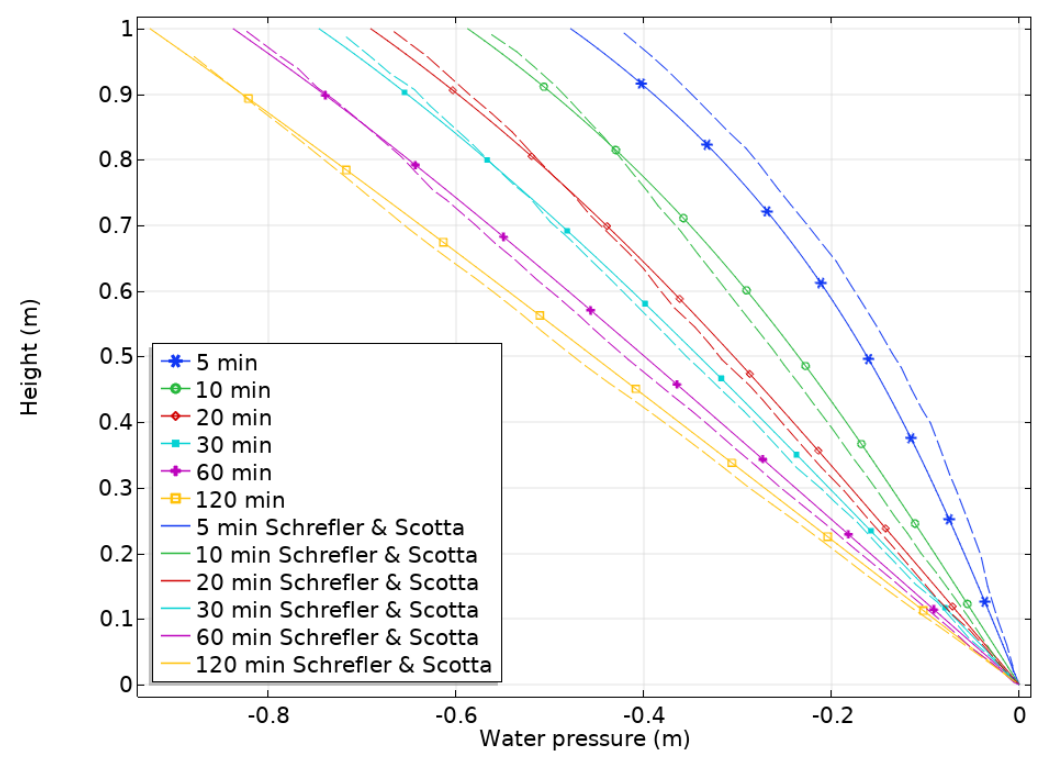


Figure 3.3: Simulation results vs Schrefler and Scotta's results (water pressure)

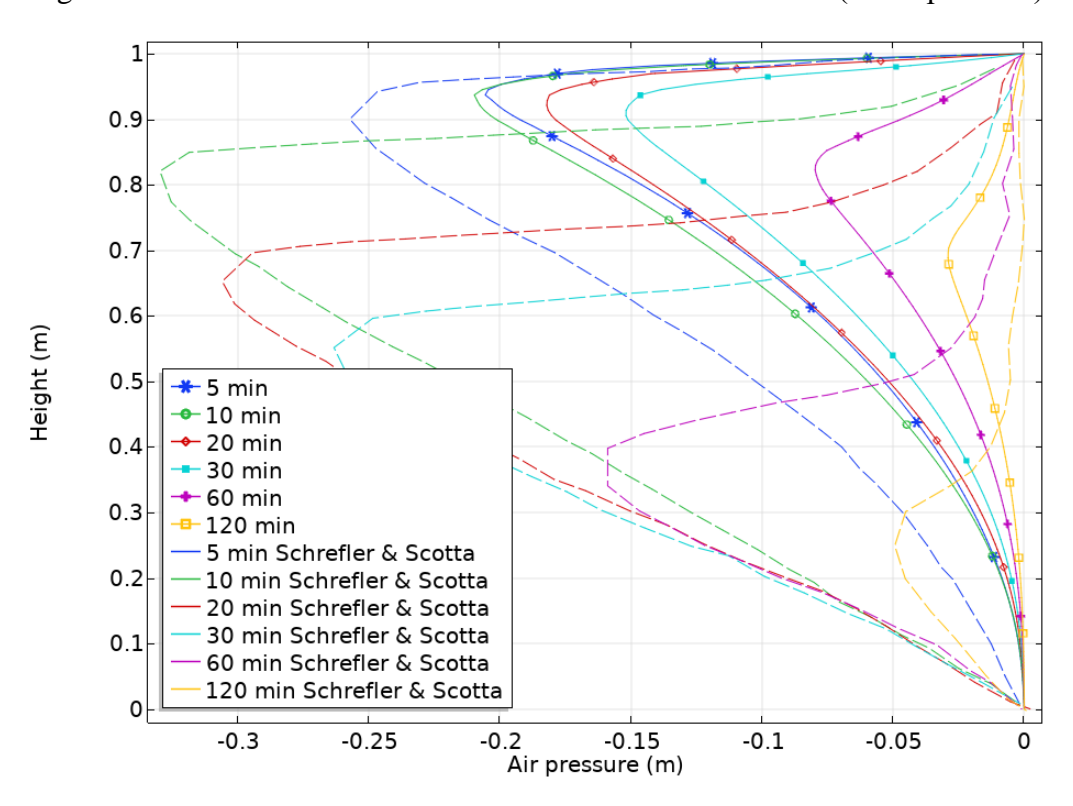


Figure 3.4: Simulation results vs Schrefler and Scotta's results (air pressure)

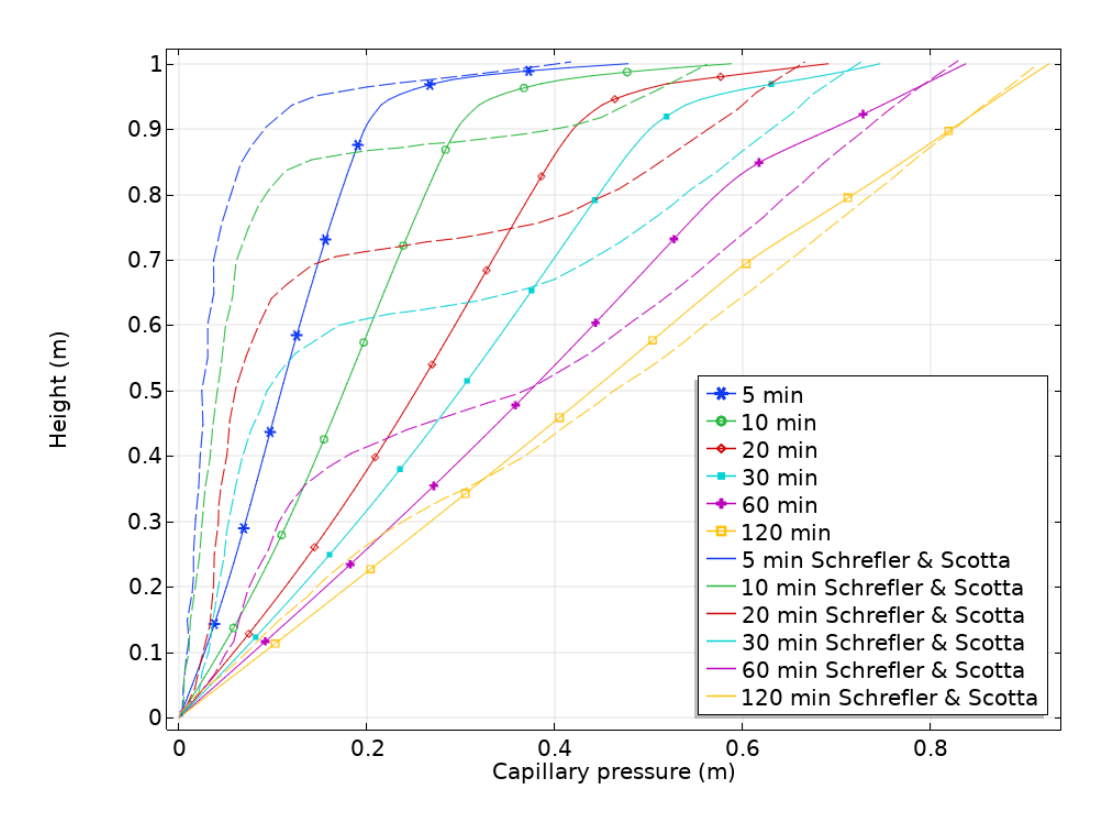


Figure 3.5: Simulation results vs Schrefler and Scotta's results (capillary pressure)

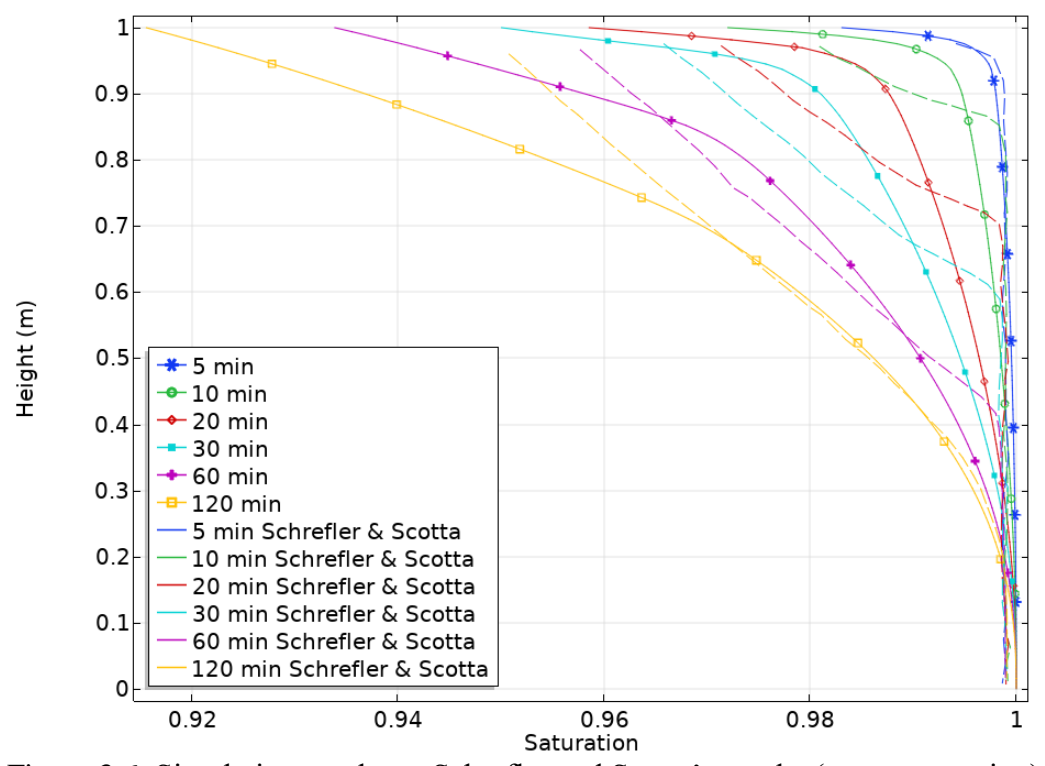


Figure 3.6: Simulation results vs Schrefler and Scotta's results (water saturation)

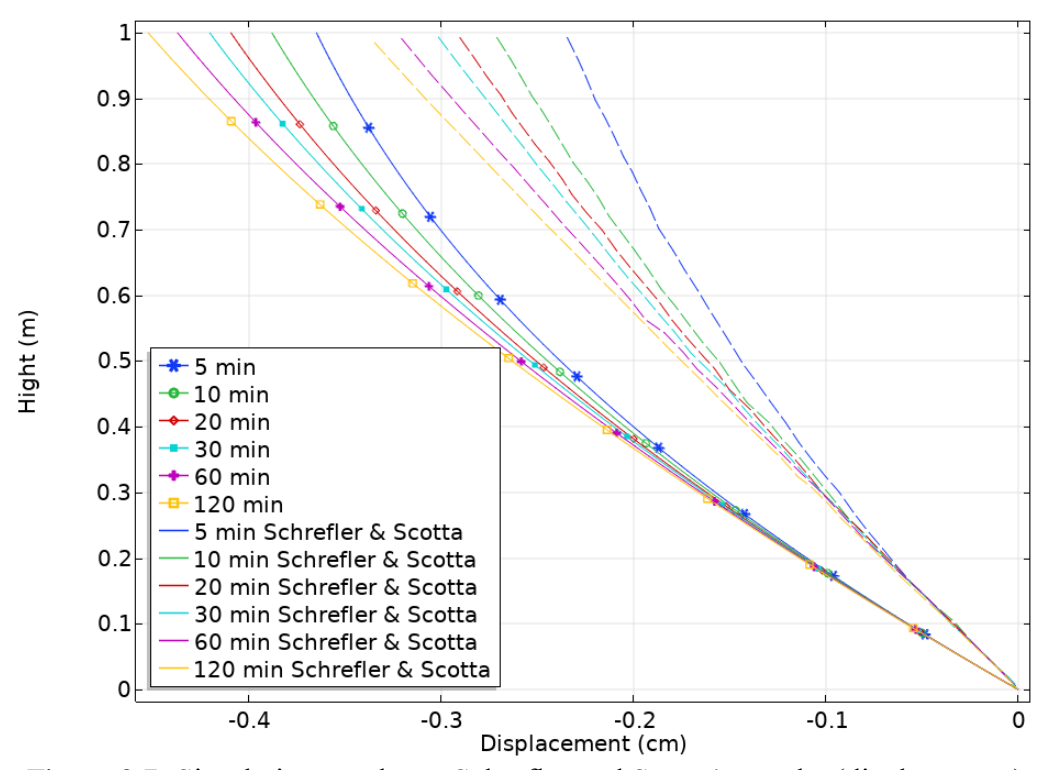


Figure 3.7: Simulation results vs Schrefler and Scotta's results (displacement)

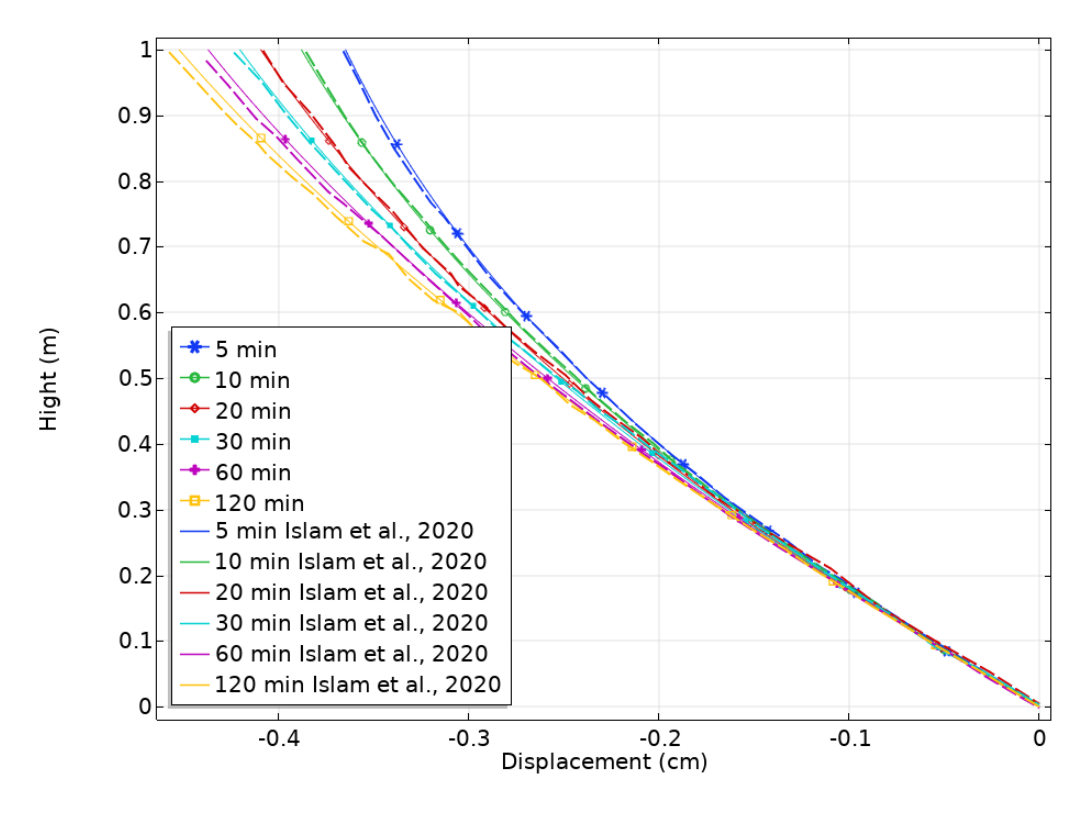


Figure 3.8: Simulation results vs Islam et al. results (displacement)

Triaxial pressure device experiment:

Liakopoulos (1965a) did not measure the gas pressure or flowrate in the conducted experiment; thus, another experiment is required to validate gas pressure/flowrate results. Popp et al. (2008) conducted a laboratory experiment using a triaxial pressure device with ultrasonic sensors to measure gas flow speed. Researchers such as Fall et al. (2014a) used this experiment to validate their HM model. The model proposed in this research will be used to simulate the experiment and compared with the experiment results (Popp et al., 2008).

Laboratory experiments were performed on the Opalinus Clay specimen (contains 6% water). The specimen was sampled from Mont Terri (Switzerland). Triaxial loading, strength, and gas injection tests were applied to the clay samples. The specimen was 150.45mm in length with 73.59 mm in diameter. The acoustic velocities and gas permeability were measured parallel to the sample axis during the experiment. The top and the bottom of the specimen were drilled, and nitrogen gas was injected at control pressure in the central borehole from the bottom side of the sample. The gas flow rate at the upper outflow borehole was then measured using ultrasonic sensors. A hydrostatic loading with a constant confinement pressure was applied, and the gas (nitrogen) presser increased as a step function. A detailed description of the experiment and characteristics of the clay is given by Popp and Salzer (2007) and Popp et al. (2008)

A 2D model geometry is created in COMSOL Multiphysics with extra-fine triangular mesh (as shown in Figure 3.9) to simulate and validate the proposed HMG model using the experiment. The figure shows the boundary condition as described in the original paper (Popp et al., 2008).

Figure 3.10 compares the gas flowrate experiment data and the simulation result of the proposed HMG model. During the experiment, the specimen started to crack (fails), which induced a noticeable increment in the permeability at 13,150 sec.

The simulation result agrees with the experimental data in the elastic phase; however, since the proposed model is an elastic-model and deals only with constant permeability, the plastic deformation (crack) cannot be captured using such a model.

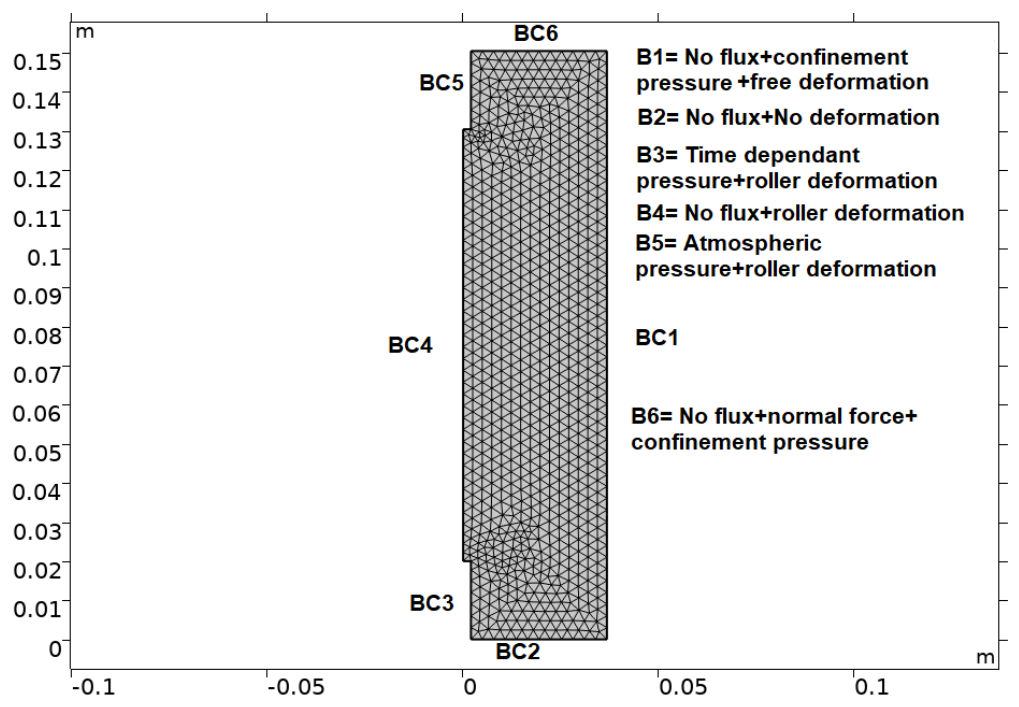


Figure 3.9: 2D triangular mesh geometry created and solved using COMSOL Multiphysics

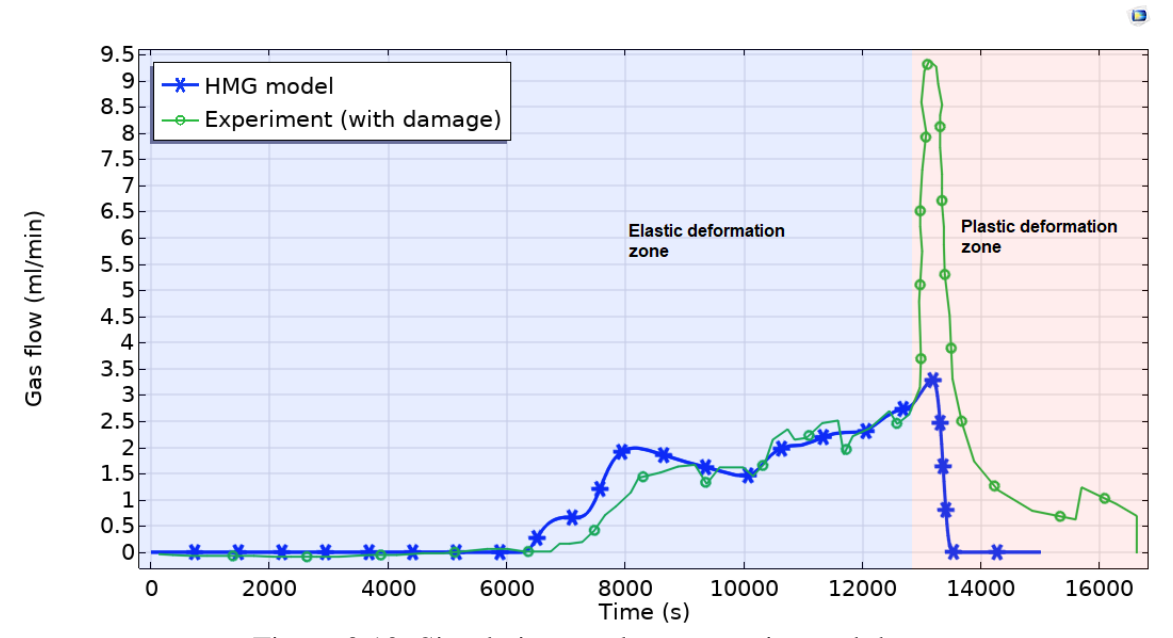


Figure 3.10: Simulation results vs experimental data

3.4 Conclusions

A Fully coupled hydro-mechanical-gas (HMG) model based on the mixture-coupling theory approach for water and gas flow was developed in this research. The coupled model is based on Helmholtz free energy equations and Biot's model. The model takes into consideration the coupled relation of solid deformation with the change in pressure. The change in water saturation and relative permeability is also considered since gas flow is included. The model was validated using Liakopoulos (1965) and Popp et al. (2008) experiment's data. The simulation results also compared to Schrefler and Scotta (2001) solution. The model was solved numerically using COMSOL software (Finite element method software). The required parameters, Initial and boundary conditions were chosen from the available literature. The model showed good agreement with Liakopoulos' experimental data. The air pressure results showed slight differences from Schrefler and Scotta's results, which could be justified by some differences in the governing equations

and the choice of solution algorithm. Since Liakopoulos (1965a) did not measure the air pressure, Popp et al. (2008) triaxial experiment's data has been used to validate the gas behaviour part. The gas flowrate from the simulation showed a good agreement with the experimental data in the elastic phase. The model can be beneficial to many fields, particularly oil field studies as a CO_2 injection simulation. This study offers opportunities for further future research. For example, this study could be extended by including a variable boundary condition to simulate a real case scenario, where the pressure and the porous media are not controlled at boundaries. Furthermore, more experiments on the flow of two-phase fluid in deformable porous media are required to measure and validate the air gas pressure and solid phase deformation behaviour.

In the next chapter, the two-phase model will be further developed to include the transport of chemical solutes. However, it will initially not account for chemical mass transport; only the energy impacts of solute transport will be considered. The incorporation of mass transport will be addressed in later chapters (Chapter 5 and 6). Additionally, the model will also account for energy losses resulting from interactions between the two phases.

Chapter 4: Two-Phase Interaction in Isothermal Hydro-Mechanical-Chemical Coupling for Improved Carbon Geological Sequestration Modelling

Abstract

Geological sequestration is an established method to store carbon deep underground. Many studies have proposed coupled constitutive models that can simulate such a complicated process; however, the coupling effect of multi-phase fluid flow and transport of chemical solutes in the liquid phase remains to be investigated. This study presents a multi-phase non-reactive hydro-mechanical-chemical constitutive framework under mixture-coupling isothermal conditions based on theory. Non-equilibrium thermodynamics is used to generate an entropy production equation, and phenomenological equations use this to derive the chemical transport and interaction between two-phase fluid flows. This study proposes novel terms in the final governing equations. The model results are in good agreement with the results of a benchmark experiment and those found in the literature; the model has been used to compare the behaviour of carbon dioxide in the gas and supercritical phases. Sensitivity analysis was conducted to determine the effect of the parameters in the new terms. Sensitivity analysis revealed the significant impact of relative permeability and saturation values on the new terms, emphasizing the importance of understanding frictional behaviour in porous media for accurate fluid flow modelling and prediction. This study urges further experimentation and model refinement to improve carbon sequestration modelling in larger formations.

List of notations

| d | Displacement tensor |
|----------------------|--------------------------------------|
| c ^s | Specific moisture capacity |
| c^w | Chemical concentration of water |
| c^{c} | Chemical concentration of the solute |
| E | Green strain |
| E | Young modulus |
| F | Deformation gradient |
| G | The rock's shear modulus |
| I | Unit tensor |
| \mathbf{I}^{β} | Mass flux of the phase/species |
| J | Jacobian |
| \mathbf{J}^{β} | Diffusion flux |
| K | Rock's Bulk modulus |
| k_{abs} | Intrinsic permeability |

| K^{s} | Bulk modulus of the solid matrix |
|--------------|--|
| K^{eta} | Bulk modulus of the phase/species |
| $k_{r\beta}$ | Phase/species relative permeability |
| m^{eta} | mass density of the phase flows in the reference configuration |
| M^{c} | Molar mass of the chemical solute |
| n | The outward unit normal vector |
| R | universal gas constant |
| S | Boundary attached on the surface |
| p^{c} | Capillary pressure |
| p^{eta} | Phase/species pressure |
| p^{p} | Average pore pressure |
| S^{β} | Saturation of the phase/species |
| T | Constant temperature |
| T | Second Piola-Kirchhoff stress tensor |
| t | Time |

| \mathbf{u}^{β} | Darcy velocity of the phase/species |
|-----------------------|---|
| V | Arbitrary microscopic domain |
| $V^{ eta }$ | Volume occupied by phase/species |
| $V^{\ pore}$ | Volume of the pore space |
| W | Dual potential |
| \mathbf{v}^{β} | Phase/species velocity |
| β | Phase or species (s, w, l, Sc, c) |
| v^{β} | Phase/species viscosity |
| $ ho_eta^eta$ | Phase density |
| $ ho^{eta}$ | Mixture density |
| $oldsymbol{\phi}^eta$ | Phase volume fraction (phase porosity) |
| φ | Porosity |
| Ψ | Helmholtz free energy density |
| $\psi^{^{pore}}$ | Helmholtz free energy density of the pore Constituent |
| Ψ | Free energy in the reference configuration |

Cauchy stress tensor σ μ^{β} Chemical potential of the phase $\boldsymbol{\mathcal{E}}_{ij}$ Strain tensor Entropy production per unit volume γ Porosity in the reference configuration υ ζ Biot's coefficient θ Poisson's ratio ∇ Gradient

4.1 1. Introduction

Recent research has included novel studies on a fully coupled multi-phase hydromechanical-supercritical-chemical phase transport model for carbon sequestration applications (André et al., 2007b; Sasaki et al., 2008; Alonso et al., 2012; Nasvi et al., 2013; Yamamoto et al., 2013; Li and Laloui, 2016a; Zhang et al., 2016; Islam et al., 2020; Lu and Zhang, 2020; Bao et al., 2014). These efforts aim to advance our understanding and application of carbon storage techniques, contributing significantly to efforts to mitigate our carbon footprint. Additionally, certain researchers are exploring how to leverage the carbon sequestration process not just for environmental remediation, but also as a means to enhance hydrocarbon production such as methane (Fan et al., 2019b; Fan et al., 2023). Within the broader context of subsurface processes, recent studies have also shed light on coal-water interactions and their influence on gas extraction from coal, as well as on the multi-physics coupling involved in coal and gas outbursts (Liu et al., 2021a; Liu et al., 2021b). The carbon sequestration process usually requires multi-phase flow modelling because the storing process is often conducted in aquifers or formations that contain other fluids, such as oil and natural gas. Early research, such as Meiri (1981) and Schrefler and Xiaoyong (1993), attempted to develop a general two-phase hydromechanical (HM) model to describe the transport of fluids (such as water) and air in deformable porous media. Whereas Meiri (1981) used a basic model to simulate a 1D air storage case, the Schrefler and Xiaoyong (1993) model was more advanced and had better validation against known cases, such as Liakopoulos (1965b). However, the mechanical governing equations were relatively simple, and the model lacked the ability to simulate the effect of chemical solute transport and two-phase interaction energy dissipation on

the total energy of the system. Later, Li and Laloui (2016b) proposed a coupled multiphase modelling framework for the carbon sequestration process in the supercritical phase. The presented thermo-hydro-mechanical model (THM) simulated the supercritical CO₂ (ScCO₂) injection process. The main innovation of the model was thermal coupling, in which the Joule-Thomson effect was incorporated into the THM model. Although the presented model appeared to have a good thermal coupling capability, it is a more simplified version with just mechanical coupling, and the transport of chemical solutes being ignored. Moreover, the dissipation energy due to the two-phase interaction fluids remained uninvestigated. Due to the complexity of chemical coupling transport in the multi-phase, many researchers prefer to use simulators such as TOUGHREACT or AD-GPRS/GFLASH to simulate the ScCO₂ sequestration process when chemical transport and reactions are considered (Zhang et al., 2015; Wolf et al., 2016; Xu et al., 2003; André et al., 2007b; Taron and Elsworth, 2009; Xiao et al., 2009; Xu et al., 2010; Liu et al., 2011; Zhang et al., 2012; Zhang et al., 2016; Siqueira et al., 2017; Voskov et al., 2017). The simulators have acceptable results; however, the scope of this research is to focus on the mathematical derivation and governing equations rather than simulations. Islam et al. (2020) presented a two-phase coupled model for a ${\rm CO_2}$ sequestration project to investigate the possibility of fluid leakage. The authors derived a general form of the coupled equations and obtained two schemes: the capillary and gas pressure scheme and the liquid pressure and gas saturation scheme. This method attempted to simplify the solution of the numerical simulation while retaining the coupled HM interaction. The model was then compared to others in the literature, such as those developed in Refs. (Richards, 1931; Liakopoulos, 1965b; Kueper and Frind, 1991; Schrefler and Xiaoyong, 1993); however, the model neglected the chemical solute transport and friction results from the interaction between solid/gas-Sc, solid/liquid, and liquid/gas-Sc flows.

The effects of transported solutes and the friction dissipation energy on some parameters such as pressure, deformation, saturation and other properties due to the multi-flow of ScCO₂ and formation liquid have yet to be fully explored. This study investigates the effect of solute transport within a liquid on fluid energy and the effect of friction between each phase. A mathematical model is developed using the mixture-coupling theory approach. Mixture-coupling theory is an energy approach which was developed by Heidug and Wong (1996). Since then, the model has been known by modified mixture theory or mixture-coupling theory (Chen, 2010; Chen and Hicks, 2011; Chen et al., 2016; Ma et al., 2020b; Abdullah et al., 2022). The mixture-coupling theory is modification of the mixture theory by viewing a fluid-infiltrated rock/soil as a single continuum instead of explicitly discriminating between the solid and fluid phase (Heidug and Wong, 1996). Moreover, it overcomes the challenges in mixture theory and shows advantages over the classic mechanics approach (Coussy et al., 1998). Additionally, Unlike the classical mechanics approach, which uses the stress-strain tensor and balance of linear momentum, mixture-coupling theory is based on non-equilibrium thermodynamics and uses energy and entropy analysis. The difference between the two methods is discussed with more detail in Refs. (Chen and Hicks, 2011; Abdullah et al., 2022). The mixture-coupling theory, in contrast to some other energy approaches that also utilize non-equilibrium thermodynamics, omits the momentum conservation balance equation. The objective of this research is not to explore the differences between the mixture-coupling theory and other methods. For that, readers are directed to Siddiqui et al. (2023), who discuss the THCM continuum modelling, emphasizing thermodynamics-based constitutive models in depth.

The remainder of this paper is organised as follows. Section 4.2 introduces a model of the transport of two-phase fluids in a deformable porous medium, before Sec. 4.3 models the dissipation entropy of the system. Section 4.4 describes the coupling of the models in Secs. 4.2 and 4.3 and develops the phenomenological equations of the system. Section 4.5 determines the constitutive equations, and Sec. 4.6 validates the model against numerical simulations. The study and its contributions are listed in Sec. 4.7.

4.2 Physical model

This model considers the transport of two-phase fluids, ScCO₂ and saline water flows, in a deformable porous medium under isothermal conditions. The couplings between the fluids and deformation are considered. Because saline water consists of water and a chemical (NaCl), the chemical transport modulus is also studied. To simplify the discussion, the following are assumed: (I) chemical reactions, either between/within the fluids or between fluid-solid, are not considered; (II) the chemical solute/minerals only exist in the liquid phase (saline water); (III) carbon dioxide in the supercritical phase is chemically non-reactive; (IV) the system is immiscible, in which the mass does not exchange between the liquid and supercritical phases through dissolution; (V) the process is under isothermal conditions; and (VI) the porous media has a completely isotropic behaviour (isotropic material). These assumptions simplify the complex process of the two-phase fluid transport model, but this simplification may affect what really happens in real-world scenarios. Ignoring chemical reactions, assuming chemicals only exist in

the liquid phase, and treating supercritical CO₂ as non-reactive simplify real-world behaviours where chemical interactions often occur. The immiscibility assumption overlooks mass exchange between phases, which is common in practical CCS scenarios. Assuming isothermal conditions and isotropic porous media simplifies the model but doesn't reflect the variability of temperature and material properties in real settings. The assumption of linearity can make the model easier to solve but is typically unrealistic due to the non-linear nature of fluid flow and deformation in porous media.

Although the assumptions above may seem to limit the scope suggested by the chapter title, which focuses on improving CCS modelling, the novelty of this chapter lies in both the extension of the model from the previous chapter and its application to CO₂ storage. This chapter specifically incorporates dissipation energy from chemical solute transport and phase interactions within a non-reactive model. These two innovations can have a noticeable impact on CCS simulations under certain conditions.

To develop the constitutive model, an arbitrary microscopic domain which is large enough to include all phases, with surface boundary S enclosing the domain V, is selected. Only fluids are allowed to pass through the boundary.

Let the superscript Sc represent $ScCO_2$ and l represent saline water; the volume of the two flows are V^{Sc} and V^{l} , respectively. If the volume of the pore space is V^{pore} , the following relationship can be obtained:

$$V^{pore} = V^{Sc} + V^{l}, \ \phi = \phi^{Sc} + \phi^{l}, \ S^{Sc} + S^{l} = 1,$$
 (4.1)

where $\phi = V^{pore}/V$, $\phi^{Sc} = V^{Sc}/V$, and $\phi^l = V^l/V$ are the volume fractions (porosity) of the pore space, $ScCO_2$, and saline water, respectively; $S^{Sc} = V^{Sc}/V^{pore}$ is the saturation of the $ScCO_2$; and $S^l = V^l/V^{pore}$ is the saturation of the saline water.

The mixture density (mass divided by total mixture volume) can be linked to the phase density (mass divided by phase volume) using

$$\rho^{l} = \phi^{l} \rho_{l}^{l}, \ \rho^{Sc} = \phi^{Sc} \rho_{Sc}^{Sc}, \tag{4.2}$$

where ρ^l and ρ^{sc} are the mixture densities and ρ^l_l and ρ^{sc}_{sc} are the phase densities.

Any constituent in one phase follows a similar density relationship. For example, for the chemical c and water w in the saline water, the following holds:

$$\rho^{w} = \phi^{l} \rho_{l}^{w}, \ \rho_{l}^{c}, \text{ and } \rho^{l} = \rho^{w} + \rho^{c},$$
 (4.3)

where ρ_l^w is the mass of the water divided by the total liquid (phase) volume and ρ_l^c is the mass of the chemical divided by the total liquid (phase) volume, ρ^c is chemical mixture density.

4.2.1 Flux equations:

Let β represent either the saline water flow l or supercritical $ScCO_2$ flow Sc, as well as the sub-constituents in saline water, such as water and chemical; the mass flux of β is defined as

$$\mathbf{I}^{\beta} = \rho^{\beta} \left(\mathbf{v}^{\beta} - \mathbf{v}^{s} \right), \tag{4.4}$$

where ρ^{β} is the mixture density of β , \mathbf{v}^{β} is the velocity of β , and \mathbf{v}^{s} is the velocity of the solid.

The diffusion flux \mathbf{J}^{β} of $\boldsymbol{\beta}$, relative to the barycentric velocity can be expressed as:

$$\mathbf{J}^{\beta} = \rho^{\beta} \left(\mathbf{v}^{\beta} - \mathbf{v}^{l} \right), \ \beta \in l \ , \tag{4.5}$$

$$\mathbf{J}^{\beta} = \rho^{\beta} \left(\mathbf{v}^{\beta} - \mathbf{v}^{Sc} \right), \ \beta \in Sc \ , \tag{4.6}$$

where $\mathbf{v}^l = \frac{\rho^w}{\rho^l} \mathbf{v}^w + \frac{\rho^c}{\rho^l} \mathbf{v}^c$ is the barycentric velocity of saline water.

In Eq. (4.6), because we regarded the $ScCO_2$ flow to be composed of a single constituent, $\mathbf{v}^\beta = \mathbf{v}^{sc}$, which means the diffusion flux of the $ScCO_2$ flow is zero. However, in Eq. (4.5), saline water flow contains water and a chemical; therefore, $\mathbf{v}^w \neq \mathbf{v}^t$ and $\mathbf{v}^c \neq \mathbf{v}^t$.

Considering the flux equation (4.4), the diffusion flux (4.5) can be written as

$$\mathbf{J}^{\beta} = \mathbf{I}^{\beta} - \rho^{\beta} \left(\mathbf{v}^{l} - \mathbf{v}^{s} \right). \tag{4.7}$$

4.2.2 Mass and energy balance equations

4.2.2.1 Helmholtz free energy

The Helmholtz free energy balance equation for the considered mixture system can be written as (Heidug and Wong, 1996):

$$\frac{D}{Dt} \left(\int_{V} \psi dV \right) = \int_{S} \mathbf{\sigma} \mathbf{v}^{s} \cdot \mathbf{n} d\Gamma - \left(\int_{S} \mu^{w} \mathbf{I}^{w} + \int_{S} \mu^{sc} \mathbf{I}^{sc} + \int_{S} \mu^{c} \mathbf{I}^{c} \right) \cdot \mathbf{n} dS - T \int_{V} \gamma dV ,$$

$$(4.8)$$

where ψ is the Helmholtz free energy density; σ is the Cauchy stress tensor; \mathbf{n} is the outward unit normal vector; μ^w , μ^{Sc} , and μ^c are chemical potentials of the water, ScCO₂

, and chemical (NaCl), respectively; T . is the constant temperature; and γ is the entropy production per unit volume.

The material time derivative following motion of the solid is $\frac{d(\cdot)}{dt} = \frac{\partial(\cdot)}{\partial t} + \mathbf{v}^s \cdot \nabla(\cdot)$; then, the differential form of the balance equation of the free energy density can be written as:

$$\dot{\psi} + \psi \nabla \cdot \mathbf{v}^{s} - \nabla \cdot (\sigma \mathbf{v}^{s}) + \nabla \cdot (\mu^{w} \mathbf{I}^{w} + \mu^{Sc} \mathbf{I}^{Sc} + \mu^{c} \mathbf{I}^{c}) = -T \gamma \leqslant 0.$$
 (4.9)

4.2.2.2 Fluid balance equation:

Because no reactions are considered, the change of mass is only through the flux; therefore, the balance equation for the fluid can be expressed as (Chen, 2013; Chen et al., 2018a):

$$\frac{D}{Dt} \left(\int_{V} \rho^{\beta} dV \right) = -\int_{S} \mathbf{I}^{\beta} \cdot \mathbf{n} dS , \qquad (4.10)$$

and the local form is:

$$\dot{\rho}^{\beta} + \rho^{\beta} \nabla \cdot \mathbf{v}^{s} + \nabla \cdot \mathbf{I}^{\beta} = 0. \tag{4.11}$$

4.3 Dissipation entropy

The entropy product results from dissipative processes, such as the friction generated at the solid/fluid phase boundary when fluid moves through a solid matrix. Moreover, the transport of the solute (chemical transport) has a dissipation effect. The entropy product can be divided into three parts: entropy induced by the saline water fraction, entropy induced by the supercritical fraction, and entropy by chemical transport. By using non-equilibrium thermodynamics, entropy production is described by Katachalsky and Curran (1965) as:

$$0 \le T \gamma = -\mathbf{I}^{w} \cdot \nabla \mu^{w} - \mathbf{I}^{Sc} \cdot \nabla \mu^{Sc} - \mathbf{I}^{c} \cdot \nabla \mu^{c} . \tag{4.12}$$

The Darcy velocity l applies to both the liquid (including the chemicals/solute) and supercritical, and can be written as

$$\mathbf{u}^{l} = S^{l} \phi \left(\mathbf{v}^{l} - \mathbf{v}^{s} \right), \ \mathbf{u}^{Sc} = S^{Sc} \phi \left(\mathbf{v}^{Sc} - \mathbf{v}^{s} \right). \tag{4.13}$$

Using the relationship in Eqs. (4.7) and (4.13), as well as substituting the density relationship (4.2) into Eq. (4.12), the following is obtained.

$$0 \le T \gamma = -\mathbf{u}^l \cdot \nabla p^l - \mathbf{J}^c \cdot \nabla (\mu^c - \mu^w) - \mathbf{u}^{Sc} \cdot \nabla p^{Sc}, \qquad (4.14)$$

in which $-\mathbf{u}^l \cdot \nabla p^l$ represents the liquid Darcy velocity driven by liquid pressure p^l , $\mathbf{J}^c \cdot \nabla \left(\mu^c - \mu^w \right)$ represents the chemical diffusion in the liquid water driven by chemical potentials, and $-\mathbf{u}^{Sc} \cdot \nabla p^{Sc}$ represents the supercritical Darcy velocity driven by supercritical pressure.

Equation (4.14) describes the entropy production with the driving forces of each flow. To describe the interaction between flows and driving forces as a linear relationship, the concept of the phenomenological equation may be used (Chen et al., 2018a).

4.4 Coupled phases interactions and phenomenological equations

As each flux may influence another flux (coupled), the interaction between flows and driving forces can be expressed as the linear dependence of the three flows on their corresponding force equations (phenomenological equations). The three flows $\rho_t^l \mathbf{u}^l$, $\rho_t^{Sc} \mathbf{u}^{Sc}$, and \mathbf{J}^c , and the three major driving forces ∇p^l , ∇p^{Sc} , and $\nabla (\mu^c - \mu^w)$ can be calculated using mass transport in isotropic media (Chen et al., 2018a; Karrech, 2013):

$$\rho_l^l \mathbf{u}^l = -\frac{L_{11}}{\rho_l^l} \nabla p^l - \frac{L_{12}}{\rho_{Sc}^{Sc}} \nabla p^{Sc} - L_{13} \nabla \left(\mu^c - \mu^w\right), \tag{4.15}$$

$$\rho_{t}^{Sc}\mathbf{u}^{Sc} = -\frac{L_{21}}{\rho_{t}^{l}}\nabla p^{l} - \frac{L_{22}}{\rho_{Sc}^{Sc}}\nabla p^{Sc} - L_{23}\nabla (\mu^{c} - \mu^{w}), \qquad (4.16)$$

$$\mathbf{J}^{c} = -\frac{L_{31}}{\rho_{l}^{l}} \nabla p^{l} - \frac{L_{32}}{\rho_{Sc}^{Sc}} \nabla p^{Sc} - L_{33} \nabla \left(\mu^{c} - \mu^{w}\right), \tag{4.17}$$

where L_{ij} are phenomenological coefficients.

Equations (4.15)-(4.17) describe the coupled fluid flows (liquid water/ $ScCO_2$) and diffusion flux in the liquid phase (NaCl/liquid water) with the coupled influence of liquid and supercritical pressures and chemical potential difference.

Since using chemical potentials is uncommon in geomechanics, it is replaced with chemical concentration c^{α} . Using non-equilibrium thermodynamics, the difference in chemical potential can be written as (Chen et al., 2018a):

$$\mathbf{u}^{l} = -k_{abs} \frac{k_{rl}}{v^{w}} \left(\nabla p^{l} - r_{1} \frac{\rho_{l}^{l}}{\rho_{Sc}^{Sc}} \nabla p^{Sc} - r_{2} \rho_{l}^{l} \left(\frac{1}{c^{w}} \frac{\partial \mu^{c}}{\partial c^{c}} \nabla c^{c} \right) \right), \tag{4.18}$$

$$\mathbf{u}^{Sc} = -k_{abs} \frac{k_{rSc}}{v^{Sc}} \left(-r_3 \frac{\rho_{Sc}^{Sc}}{\rho_l^l} \nabla p^l + \nabla p^{Sc} - \rho_{Sc}^{Sc} r_4 \left(\frac{1}{c^w} \frac{\partial \mu^c}{\partial c^c} \nabla c^c \right) \right), \quad (4.19)$$

$$\mathbf{J}^{c} = -\left(\frac{L^{l} \rho_{l}^{l}}{p^{l}}\right) \nabla p^{l} - \left(\frac{L^{Sc} \rho_{Sc}^{Sc}}{p^{Sc}}\right) \nabla p^{Sc} - D \rho^{l} \nabla c^{c}, \qquad (4.20)$$

coefficients can be defined as:

$$k_{abs} \frac{k_n}{v^w} = \frac{L_{11}}{\left(\rho_l^l\right)^2}, r_1 = -\frac{L_{12}}{L_{11}}, r_2 = -\frac{L_{13}}{L_{11}}, r_3 = -\frac{L_{21}}{L_{22}},$$

$$r_4 = -\frac{L_{23}}{L_{22}}, L^l = -\frac{L_{31}p^l}{\left(\rho_l^l\right)^2}, L^{Sc} = -\frac{L_{32}p^{Sc}}{\left(\rho_{Sc}^{Sc}\right)^2}, D = \frac{L_{33}}{c^w \rho_l^l} \frac{\partial \mu^c}{\partial c^c}$$

where k_{abs} is the absolute (intrinsic) permeabilities, k_{n} and k_{rSc} are the relative permeabilities, v^w and v^{Sc} are the viscosities, and p^l and p^{Sc} are the pore pressures, each for saline water and . ., respectively. c^w and c^c are the mass fraction of water and chemical solute (NaCl), respectively. Parameters r_1 and r_3 relate to the two-phase friction/dissipation and r_2 and r_4 relate to the chemical transport energy dissipation.

Equation (4.18) contains the three coupling terms that effect the Darcy velocity of the liquid phase (saline water): ∇p^l represents the main driving force, which is the pressure gradient of the liquid; $r_1 \frac{\rho_l^l}{\rho_{Sc}^{Sc}} \nabla p^{Sc}$ represents the effect of the supercritical-phase friction/dissipation on the Darcy velocity of the liquid; and $\rho_{Sc}^{Sc} r_4 \left(\frac{1}{c^w} \frac{\partial \mu^c}{\partial c^c} \nabla c^c \right)$

represents the coupling effect between the supercritical-phase and solute. The same terms apply to Eq. (4.19) for the second phase flow (supercritical).

The terms mentioned above represent the key findings of this study. The effects of these coupling terms will be discussed in the subsequent section, where they are incorporated

into the governing equations. Utilizing these phenomenological relations enables this approach to capture the impact of each flow on the others, specifically in terms of friction.

4.5 Constitutive equations

The solid/rock is assumed to be in mechanical equilibrium (e.g. $\nabla \cdot \mathbf{\sigma} = 0$). Using the entropy product in Eq. (4.12) and the free energy equation (4.9), the equation for Helmholtz free energy density ψ can be written as

$$\dot{\psi} + \psi \nabla \cdot \mathbf{v}^{s} - (\mathbf{\sigma} : \nabla \mathbf{v}^{s}) + \mu^{w} \nabla \cdot \mathbf{I}^{w} + \mu^{Sc} \nabla \cdot \mathbf{I}^{Sc} + \mu^{c} \nabla \cdot \mathbf{I}^{c} = 0.$$
 (4.21)

To use classic continuum mechanics to determine the rock deformation, several basic relationships are required. For an arbitrary reference configuration \mathbf{X} at time t and position \mathbf{x} , the deformation gradient \mathbf{F} and Green strain \mathbf{E} can be expressed as (Wriggers, 2008):

$$\mathbf{F} = \frac{\partial \mathbf{x}}{\partial \mathbf{X}} (\mathbf{X}, t), \mathbf{E} = \frac{1}{2} (\mathbf{F}^{\mathsf{T}} \mathbf{F} - \mathbf{I}), \tag{4.22}$$

where I is a unit tensor. The second Piola-Kirchhoff stress tensor T is introduced to measure stress in the reference configuration; the relationship between T and σ is:

$$\mathbf{T} = \mathbf{J}\mathbf{F}^{-1}\mathbf{\sigma}\mathbf{F}^{-T} , \qquad (4.23)$$

where J is the Jacobian of \mathbf{F} , expressed as:

$$J = \frac{dV}{dV_0}, \dot{J} = J\nabla \mathbf{v}^s, \tag{4.24}$$

where dV and dV_0 are the volumes of the current and reference configurations, respectively.

The following hold at the reference configuration:

$$\Psi = J\psi, m^{\beta} = J\rho^{\beta} = JS^{\beta}\phi\rho_{\beta}^{\beta}, \qquad (4.25)$$

where Ψ is the free energy in the reference configuration and m^{β} is the mass density of the three flows in the reference configuration. Then, using Eqs. (4.11) and (4.21) with Eqs. (4.22)-(4.25), the differential form of the free energy in the reference configuration can be written as:

$$\dot{\Psi} = tr\left(\mathbf{T}\dot{\mathbf{E}}\right) + \mu^{w}\dot{m}^{w} + \mu^{Sc}\dot{m}^{Sc} + \mu^{c}\dot{m}^{c}. \tag{4.26}$$

4.5.1 Helmholtz free energy density of pore space

The Helmholtz free energy density of the pore, which contains saline water and ${\rm CO_2}$ in the supercritical phase, is denoted as $\psi^{\it pore}$. From classical thermodynamics,

$$\psi^{pore} = -p^{p} + S^{l} \left(\mu^{w} \rho_{l}^{w} + \mu^{c} \rho_{l}^{c} \right) + S^{Sc} \mu^{Sc} \rho_{Sc}^{Sc}, \tag{4.27}$$

where p^p is the average pressure in the pore space.

The derivative form can be written as:

$$\dot{\psi}^{\text{pore}} = \mu^{w} \left(S^{l} \rho_{l}^{w} \right) + \mu^{c} \left(S^{l} \rho_{l}^{c} \right) + \mu^{Sc} \left(S^{Sc} \rho_{Sc}^{Sc} \right) . \tag{4.28}$$

4.5.2 Free energy density of solid matrix

The free energy density stored in the solid matrix can be calculated by subtracting the free energy of the pore liquid/supercritical $J\phi\psi^{pore}$ from the total free energy of the combined rock/liquid/supercritical system Ψ (e.g. $\Psi-J\phi\psi^{pore}$). $\upsilon=J\phi$ is the pore

volume fraction in the reference configuration. Using Eqs (4.26) and (4.28), the free energy of the wetted mineral matrix is obtained as:

$$\left(\Psi - J\phi\psi^{pore}\right) = tr\left(\mathbf{T}\dot{\mathbf{E}}\right) + p^{p}\dot{\upsilon}. \tag{4.29}$$

The dual potential can be expressed as

$$W = (\Psi - J\phi^{w}\psi_{\text{pore}}) - p^{p}\upsilon. \tag{4.30}$$

Substituting Eq. (4.29) into the time derivative of Eq. (4.30) yields

$$\dot{W}\left(\mathbf{E}, p^{p}\right) = tr\left(\mathbf{T}\dot{\mathbf{E}}\right) - \dot{p}^{p}\upsilon, \tag{4.31}$$

where W is a function of **E** and p^p ; therefore, it can be written as

$$\vec{W}\left(\mathbf{E}, p^{p}\right) = \left(\frac{\partial W}{\partial E_{ij}}\right)_{p^{p}} \dot{E}_{ij} + \left(\frac{\partial W}{\partial p^{p}}\right)_{E_{ij}} \dot{p}^{p} \tag{4.32}$$

and

$$T_{ij} = \left(\frac{\partial W}{\partial E_{ij}}\right)_{p^p}, \upsilon = -\left(\frac{\partial W}{\partial p^p}\right)_{E_{ij}}, \tag{4.33}$$

$$\dot{T}_{ii} = L_{iikl} \dot{E}_{kl} - M_{ii} \dot{p}^{p} , \qquad (4.34)$$

$$\dot{\upsilon} = M_{ii} \dot{E}_{ii} + Q \dot{p}^{p}, \qquad (4.35)$$

where the parameters L_{ijkl} , M_{ij} , and Q can be described as

$$L_{ijkl} = \left(\frac{\partial T_{ij}}{\partial E_{kl}}\right)_{p^p} = \left(\frac{\partial T_{kl}}{\partial E_{ij}}\right)_{p^p}$$

$$M_{ij} = -\left(\frac{\partial T_{ij}}{\partial p^{p}}\right)_{E_{ij}} = \left(\frac{\partial \upsilon}{\partial E_{ij}}\right)_{p^{p}}.$$
 (4.36)

$$Q = \left(\frac{\partial v}{\partial p^{p}}\right)_{E_{ij},\mu^{b}}$$

by using the porosity definition in Eq. (4.11):

$$\frac{\partial \left(\phi^{\beta} \rho_{\beta}^{\beta}\right)}{\partial t} + \left(\phi^{\beta} \rho_{\beta}^{\beta}\right) \nabla \cdot \mathbf{v}^{\beta} + \nabla \cdot \mathbf{I}^{\beta} = 0. \tag{4.37}$$

by using mixture density equation (4.2) and (4.37), then substituting into equation (4.7), it leads to:

$$S^{l} \upsilon \rho_{l}^{l} \frac{\partial c^{\beta}}{\partial t} + \rho_{l}^{l} \mathbf{u}^{l} \cdot \nabla c^{\beta} + \nabla \cdot \mathbf{J}^{\beta} = 0.$$
 (4.38)

4.5.3 Governing field equations

4.5.3.1 Mechanical behaviour

To simplify discussion of the mechanical phase, three assumptions are made:

iv. The mechanical behaviour is regarded as a small strain condition; therefore, the Green strain tensor E_{ij} and Piola-Kirchhoff stress T_{ij} can be replaced by strain tensor ε_{ij} and Cauchy stress σ_{ij} , respectively.

$$E_{ii} \approx \varepsilon_{ii} , T_{ii} \approx \sigma_{ii}$$
 (4.39)

v. For mechanical equilibrium, it can be assumed that $\frac{\partial \sigma_{ij}}{\partial x_j} = 0$. Additionally, L_{ijkl} , M_{ij} , and Q are assumed to be material dependent constants. Moreover, the material is assumed to be fully isotropic, in which M_{ij} is diagonal and can be expressed as:

$$M_{ii} = \zeta \delta_{ii} \,, \tag{4.40}$$

where ζ is Biot's coefficient.

vi. The porous medium is assumed to exhibit completely isotropic behaviour; it is an isotropic material.

The elastic stiffness L_{ijkl} can be written as a fourth-order isotropic tensor:

$$L_{ijkl} = G\left(\delta_{ik}\delta_{jl} + \delta_{il}\delta_{jk}\right) + \left(K - \frac{2G}{3}\right)\delta_{ij}\delta_{kl}, \qquad (4.41)$$

where G and K are the rock shear and bulk moduli, respectively.

The governing stress equation (4.34) can be written as

$$\dot{\sigma}_{ij} = \left(K - \frac{2G}{3}\right) \dot{\varepsilon}_{kk} \,\delta_{ij} + 2G \,\dot{\varepsilon}_{ij} - \zeta \,\dot{p}^{\,p} \,\delta_{ij} \,. \tag{4.42}$$

The porosity change is related to the strain and pore fluid pressure by

$$\dot{\upsilon} = \zeta \dot{\varepsilon}_{ii} + Q \dot{p}^{p} . \tag{4.43}$$

From Heidug and Wong (1996), Q and ζ can be expressed as:

$$Q = \frac{\zeta - \phi}{K^s},\tag{4.44}$$

$$\zeta = 1 - \frac{K}{K^s} \,. \tag{4.45}$$

The mechanical governing equation can be expressed as:

$$G\nabla^{2}\dot{\mathbf{d}} + \left(\frac{G}{1 - 2\theta}\right)\nabla(\nabla \cdot \dot{\mathbf{d}}) - \zeta\nabla\dot{p}^{p} = 0.$$
(4.46)

where **d** is displacement and θ is Poisson's ratio. The average pore pressure in the pore space can be expressed as (Lewis and Schrefler, 1987)

$$p^{p} = p^{l} S^{l} + p^{Sc} S^{Sc} = p^{l} S^{l} + p^{Sc} - S^{l} p^{Sc}.$$
 (4.47)

Then, by using Eq. (4.47), Eq. (4.46) can be expanded to the final governing equation for the mechanic behaviour:

$$G\nabla^{2}\dot{\mathbf{d}} + \left(\frac{G}{1-2\theta}\right)\nabla\left(\nabla\cdot\dot{\mathbf{d}}\right) - \zeta\nabla\left[\left(S^{l} + c^{s}p^{c}\right)\dot{p}^{l}\right] - \zeta\nabla\left[\left(S^{Sc} - c^{s}p^{c}\right)\dot{p}^{Sc}\right] = 0,$$

$$(4.48)$$

where $c^s = \frac{\partial S^l}{\partial p^c}$ is the specific moisture capacity and $p^c = p^{Sc} - p^l$ is the capillary pressure.

4.5.3.2 Fluid phase

Using Eq. (4.37), the balance equation for fluid component can be described as:

$$\frac{\partial \phi^l \rho_l^l}{\partial t} + \phi^l \rho_l^l \nabla \cdot \mathbf{v}^s + \nabla \cdot \mathbf{I}^l = 0.$$
 (4.49)

Then, by using Eqs. (4.4), (4.43), (4.44), (4.47), and the relationship between the chemical potential, temperature, molar mass, and universal gas constant (Katchalsky and Curran, 1965; Chen et al., 2018a) the final governing equation for the liquid phase is as follows:

$$\zeta S^{l} \nabla \cdot \dot{\mathbf{d}} + \left(\frac{\zeta - \phi}{K^{s}} S^{l} S^{l} + S^{l} \frac{\phi}{K^{w}} \right) \dot{p}^{l} + \frac{\zeta - \phi}{K^{s}} S^{l} S^{sc} \dot{p}^{Sc} + \left(-\frac{\zeta - \phi}{K^{s}} S^{l} p^{c} + \phi \right) \dot{S}^{l} + \left[-\nabla \cdot k_{abs} \frac{k_{rl}}{v^{l}} \left(\nabla p^{l} - r_{1} \frac{\rho_{l}^{l}}{\rho_{Sc}^{Sc}} \nabla p^{Sc} - r_{2} \rho_{l}^{l} \frac{1}{c^{w} c^{c}} \frac{RT}{M^{c}} \nabla c^{c} \right) \right] = 0$$

$$(4.50)$$

where M^c is the molar mass, R is the universal gas constant, and K^w and K^s are the bulk modulus of water and the solid, respectively.

Similarly, the governing equation for the supercritical phase can be written as

$$\zeta S^{Sc} \nabla \cdot \dot{\mathbf{d}} + \left(\frac{\zeta - \phi}{K^{s}} S^{Sc} S^{Sc} + S^{g} \frac{\phi}{K^{Sc}} \right) \dot{p}^{Sc} + \frac{\zeta - \phi}{K^{s}} S^{Sc} S^{l} \dot{p}^{l} + \left(\frac{\zeta - \phi}{K^{s}} S^{Sc} p^{c} + \phi \right) \dot{S}^{Sc} + \left[-\nabla \cdot k_{abs} \frac{k_{rSc}}{v^{Sc}} \left(\nabla p^{Sc} - r_{3} \frac{\rho_{Sc}^{Sc}}{\rho_{l}^{l}} \nabla p^{l} - r_{4} \rho_{Sc}^{Sc} \frac{1}{c^{w} c^{c}} \frac{RT}{M^{c}} \nabla c^{c} \right) \right] = 0$$

$$(4.51)$$

where K^{Sc} is the bulk modulus of ScCO₂.

4.5.3.3 Chemical phase

The governing equation for the chemical transport (dissolved salt) can be derived using Eq. (4.11):

$$\dot{\rho}^c + \rho^c \nabla \cdot \mathbf{v}^c + \nabla \cdot \mathbf{I}^c = 0. \tag{4.52}$$

By using Eqs. (4.2), (4.7), (4.13), and (4.24) and assuming a small deformation (J = 1), the final governing equation for the chemical transport (salt) can be written as:

$$\left(\phi S^{l} \rho_{l}^{l}\right) \dot{c}^{c} + \rho_{l}^{l} \mathbf{u}^{l} \cdot \nabla c^{c} + \nabla \cdot \mathbf{J}^{c} = 0.$$

$$(4.53)$$

4.5.3.4 Extra terms and novelty

The final derived governing equations for the liquid and supercritical phases are relatively similar to the classic transport equations for two-phase transport introduced by other researchers (Schrefler and Xiaoyong, 1993; Abdullah et al., 2022; Islam et al., 2020). Nevertheless, there are new coupling terms introduced in Eqs (4.50) and (4.51) that did not exist in previous research. For example, in the literature, the Darcy flow term only contains the pressure of the liquid (e.g. $\nabla \cdot k_{abs} \frac{k_{rl}}{v^{l}} (\nabla p^{l})$), but in Eq. (4.50), new terms are added. The first is the coupling term $-r_3 \frac{\rho_{Sc}^{Sc}}{\rho_l^l} \nabla p^l$, that determines the dissipation energy from the liquid flow due to the supercritical/liquid interaction (friction). The second term $-r_4 \rho_{Sc}^{Sc} \frac{1}{c^w c^c} \frac{RT}{M^c} \nabla c^c$ represents the coupling relation between the solute in the liquid, supercritical fluid density, and liquid (saline water) flow. This term was used in some papers to determine the osmosis effect on the transport in very low permeability conditions (Chen et al., 2018a). Therefore, it is anticipated that the effect of this parameter on pressure, temperature, and mechanical deformation would be relatively lesser than the impact of the friction parameter.

The following section details the sensitivity effect of these terms on the main dependent variables, such as pressure and displacement of solid porous media, and the estimates of r_1 and r_3 . Parameters r_2 and r_4 are expected to have a negligible effect due to the low energy dissipated during chemical transport. Moreover, the terms of the chemical dissipation energy could be useful when caprock leakage is investigated (low permeability) or when osmosis is present.

Finally, in the proposed model, the coupling term between the transport equations of twophase is derived using the thermodynamics framework. This approach ensures that the equations are more rigorous and systematic, as the entire constitutive model can be obtained using a single driving force 'entropy production'. In contrast, other research in the field, such as the work by Qiao et al. (2018), has used additional coefficients to represent the mechanical influence between phases in their equations.

4.6 Validation and numerical simulation

This part of the article is divided into two sections: (6.1) validation of the general equations, and (6.2) sensitivity analysis for the new friction term parameters r_1 and r_3 .

4.6.1 General model validation

The model is validated against results from experimental works reported in literature, and the effect and importance of the new extra terms discussed in the sensitivity analysis section. First, the constitutive equations are solved numerically using the finite element method. Unfortunately, limited documented experiments have been conducted for a two-phase flow in a deforming porous medium. Since there is no analytical solution for such a complicated system, some researchers have attempted to validate their mathematical models by comparing them to results of known cases (Meiri, 1981; Schrefler and Xiaoyong, 1993; Gawin and Sanavia, 2009).

Liakopoulos (1965b) conducted an experiment consisting of a column filled with a porous material to investigate water transport under unsaturated conditions. This experiment became a benchmark, with many researchers, such as (Narasimhan and Witherspoon,

1978; Gawin et al., 1997; Schrefler and Scotta, 2001; Laloui et al., 2003; Hu et al., 2011; Kim and Kim, 2013; Islam et al., 2020; Wei et al., 2020b; Abdullah et al., 2022), using the drainage experiment to validate their mathematical models.

In this research, the drainage experiment (Liakopoulos, 1965b) is used to test the general governing equations of the fully coupled framework model and confirm that the new terms do not cause numerical issues. The model is solved numerically using COMSOL Multiphysics® (COMSOL, Inc.) software, and the results are compared to experimental data. COMSOL Multiphysics is a numerical software that is widely used in both the academic and industrial filed to solve relatively complex models using the finite element method. COMSOL Multiphysics was chosen due to its flexibility in customizing equations, its inherent Multiphysics capabilities, and the trustworthiness it demonstrated in previous benchmark studies. This adaptability was essential given the uniqueness of the research parameters and the need for specific modifications. In this model, both the Darcy law physics, and solid mechanics physics were adjusted, and equations were solved using an extra-fine triangle mesh setting. Liakopoulos only measured the liquid phase pressure (water) and did not include data for the gas phase (air pressure), the Schrefler and Scotta (2001) numerical results are used. Moreover, no chemical was included in this experiment. Nevertheless, because this simulation aims to test the effect of the new governing equations terms, the simulation results can be compared to the experiment and other results.

Drainage test experiment:

The Liakopoulos experiment consisted of a sand column (Perspex and Del Monte sand).

The tube column was 1.0 m long and 10 cm in diameter. The bottom of the column was

exposed to atmospheric pressure, and the tube wall was assumed to be rigid and impermeable.

Tensiometers were used to measure the pore pressure change with column height. The column was fed with water from the top to ensure a constant flow rate throughout the column. When the drainage water at the bottom became equal to the filling rate, the water flow supply from the top was stopped and the experiment started (considered as t=0). The water continued draining from the tube due to gravity.

Water pressure measurements were taken at various times (*t*=5, 10, 20, 30, 60, and 120 min). The water saturation and relative permeability were calculated based on capillarity pressure according to the Brooks and Corey (1966) model as follows:

$$S^{w} = 1 - 0.10152 \left(\frac{p^{c}}{\rho_{t}^{w} g}\right)^{2.4279}, \quad k_{rw} = 1 - 2.207 (1 - S^{w})^{1.0121}. \tag{4.54}$$

The above equations are valid in a porous medium with water saturation $S^w > 0.91$ and capillary pressure $p^c > 0$. Moreover, for the numerical simulation, some assumptions were set to ensure a stable numerical solution:

- i. The drainage flow occurs due to gravity and is in the vertical direction only.
- ii. When the experiment starts (t=0), the sand column is fully saturated ($S^w = 1$).
- iii. The porosity value does not change during the experiment.

Table 4.1 summarises the material data used for the numerical simulation. For parameters not provided by Liakopoulos, such as Young's modulus and Poisson's ratio, values estimated by other researchers were used (Schrefler and Xiaoyong, 1993; Schrefler and

Scotta, 2001). Figure 4.1 shows the initial and boundary conditions used in the numerical simulation.

Table 4.1: Parameters used for Liakopoulos drainage test (Liakopoulos, 1965b).

| Table 4.1: Parameters used for Liakopoulos drainage test (Liakopoulos, 1965b). | | | | |
|--|-------------------------------|---|--|--|
| Physical meaning | Reference | Values and units | | |
| Young's modulus | Schrefler and Scotta,) (2001 | E =1.3 MPa | | |
| Water density | Schrefler and Scotta,) (2001 | $\rho_w^w = 1000 \text{ kg/m}^3$ | | |
| Gas density (air) | Schrefler and Scotta,) (2001 | $\rho_g^g = 1.2 \text{ kg/m}^3$ | | |
| Solid density (sand) | Schrefler and Scotta,) (2001 | $\rho^s = 2000 \text{ kg/m}^3$ | | |
| Poisson's ratio | Schrefler and Scotta,) (2001 | $\theta = 0.4$ | | |
| Biot's coefficient | Schrefler and Scotta,) (2001 | $\zeta = 1$ | | |
| Porosity | Schrefler and Scotta,) (2001 | $\phi = 0.2975$ | | |
| Intrinsic permeability of the solid (sand) | Schrefler and Scotta,) (2001 | $k_{abs} = 4.5 \times 10^{-13} \text{ m}^2$ | | |
| Dynamic viscosity of water | Schrefler and Scotta,) (2001 | $v^{w} = 1 \times 10^{-3} \text{ Pa.s}$ | | |
| Dynamic viscosity of gas (air) | Schrefler and Scotta,) (2001 | $v^g = 1.8 \times 10^{-5} \text{ Pa.s}$ | | |
| Bulk modulus of water | Schrefler and Scotta,) (2001 | $K_{w} = 2.0 \times 10^{3} \mathrm{MPa}$ | | |
| Bulk modulus of gas (air) | Schrefler and Scotta,) (2001 | $K_g = 0.1 \text{ MPa}$ | | |

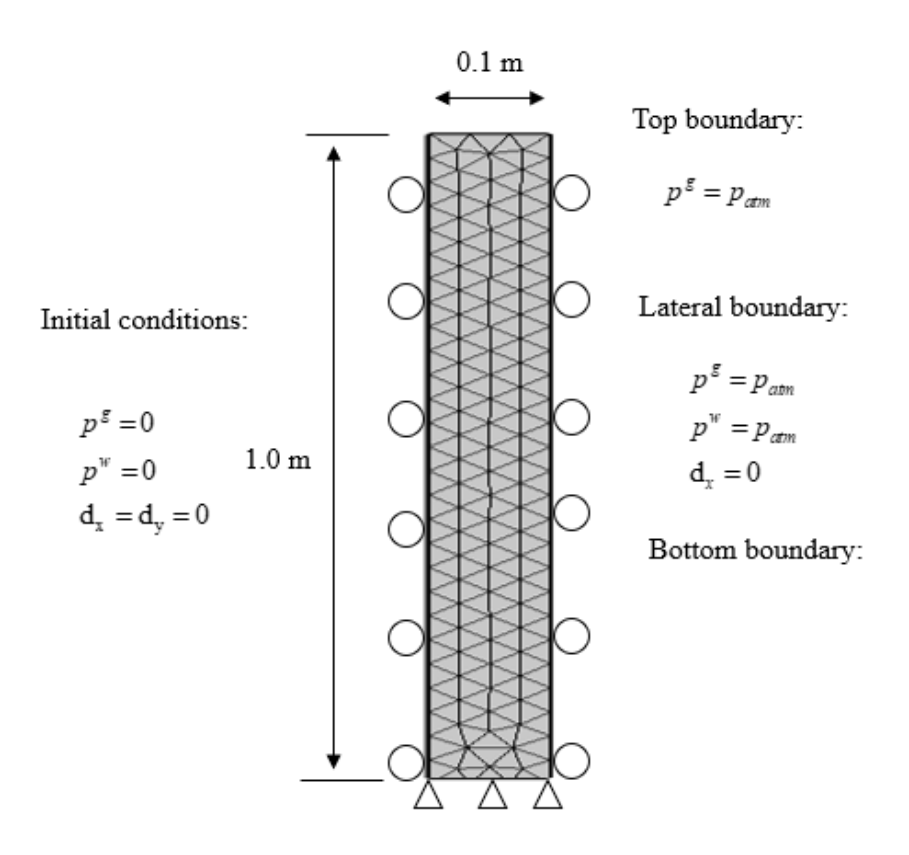


Figure 4.1: Initial and boundary conditions for Liakopoulos drainage test (Liakopoulos, 1965b).

Equations (4.50) and (4.51) contain the four parameters r_1 , r_2 , r_3 , and r_4 . These parameters must be obtained through laboratory testing. Typically, determining each coefficient requires multiple experimental setups, with specific laboratory measurements. As referenced by Katchalsky and Curran (1965), extensive research has been conducted on determining the phenomenological coefficients. Detailed experimental approaches for obtaining these coefficients can be found in various studies (Rastogi et al., 1969; Kedem and Katchalsky, 1961; Panelli and Ambrozio Filho, 2001; Quibén and Thome, 2007; Nath, 2024). These studies outline experimental protocols, such as measuring transport processes, fluxes, and forces, which are used to compute the relevant coefficients.

For now, the values will be estimated by trial and error. Parameters r_1 and r_3 relate to the first new term, that represents the effect of the entropy generated by the two-phase interaction, whereas r_2 and r_4 are linked to the loss caused by chemical transport in the system. It has been observed, as discussed in the following section, that parameters r_1 and r_3 have a more significant impact on pressure behaviour than r_2 and r_4 . This is because the entropy generated due to the transport of such a small amount of chemical (NaCl has a mass fraction of 0.1) is almost negligible; however, the friction induced by the interaction between the multi-phase flow is much higher. Parameters r_1 and r_3 need to be estimated based on the fluids, porous medium, and experimental setup. For now there are assumed to be 0.1, while r_2 and r_4 are assumed to be 1. Figure 4.2 shows the numerical results of the water pressure of the proposed coupled model compared to the experimental results. The simulation was in good agreement with the experimental measurements. However, at the start of the experiment (t=5 and 10 min), there was a shift in the water pressure, which other researchers experienced when comparing their models to the experiment (Schrefler and Xiaoyong, 1993; Schrefler and Scotta, 2001; Islam et al., 2020).

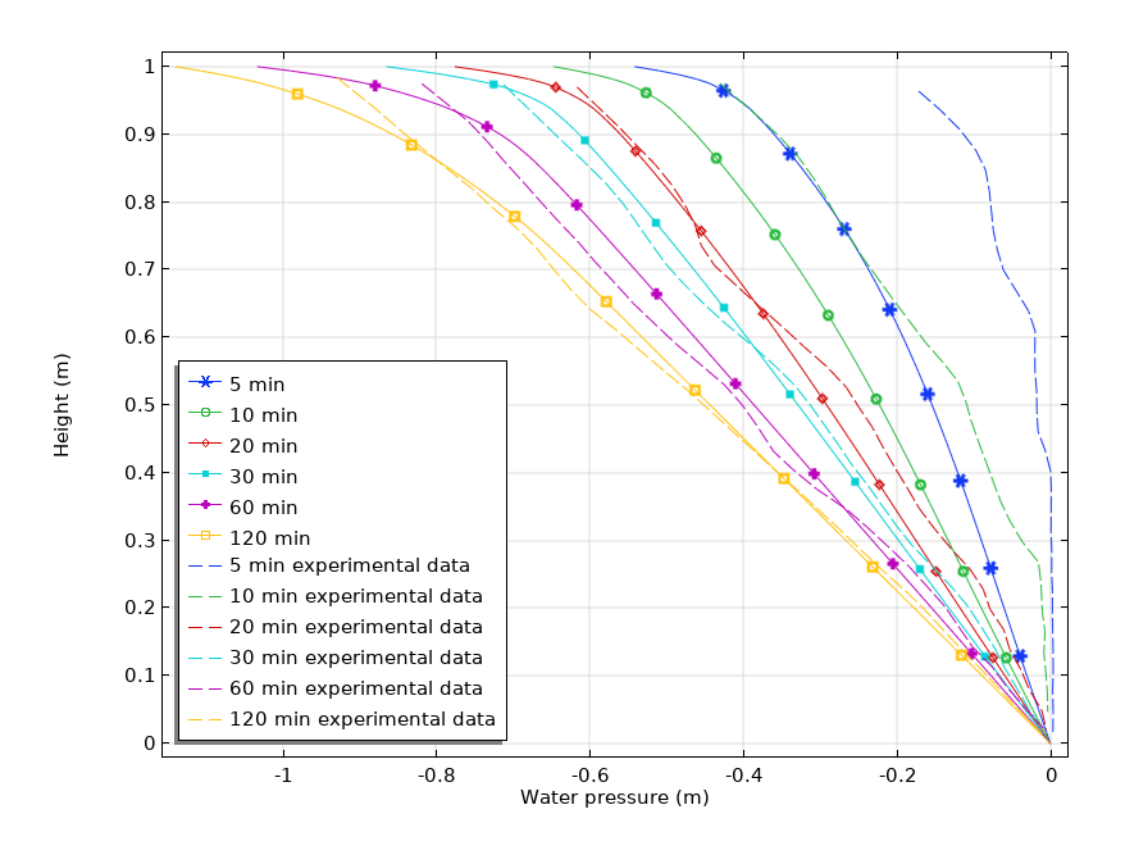


Figure 4.2: Liakopoulos (1965b) experiment vs simulation results of liquid pressure (p^{l}) distributed through sand column at different times.

Figure 4.3, Figure 4.5, and Figure 4.6 show the numerical results of the proposed model compared with the Schrefler and Scotta (2001) model. Figure 4.4 shows a 2D plot of the air pressure moving through the column at various times. In Figure 4.3, the peak pressure moves more aggressively across the sand column, with higher pressure values. This behaviour was observed and discussed by Schrefler and Scotta (2001), who compared it with other researchers. Hu et al. (2011) obtained results that are more similar to the simulation results in this work, which is due to the assumptions made regarding boundary conditions. In this simulation, the space between the sand and the tube walls was assumed to be gas permeable, while in the original experiment, the boundaries condition was based on the gas-tight assumption. However, researchers such as Hu et al. (2011) obtained a better match with the experiment when the gas was assumed to have fair passage between

the sand and inner wall of the tube. This could be an experimental error in which the space between the inner wall and filling sand was not 100% insulated. Figure 4.4 shows a 2D graph of the air leaking from the sides into the porous medium.

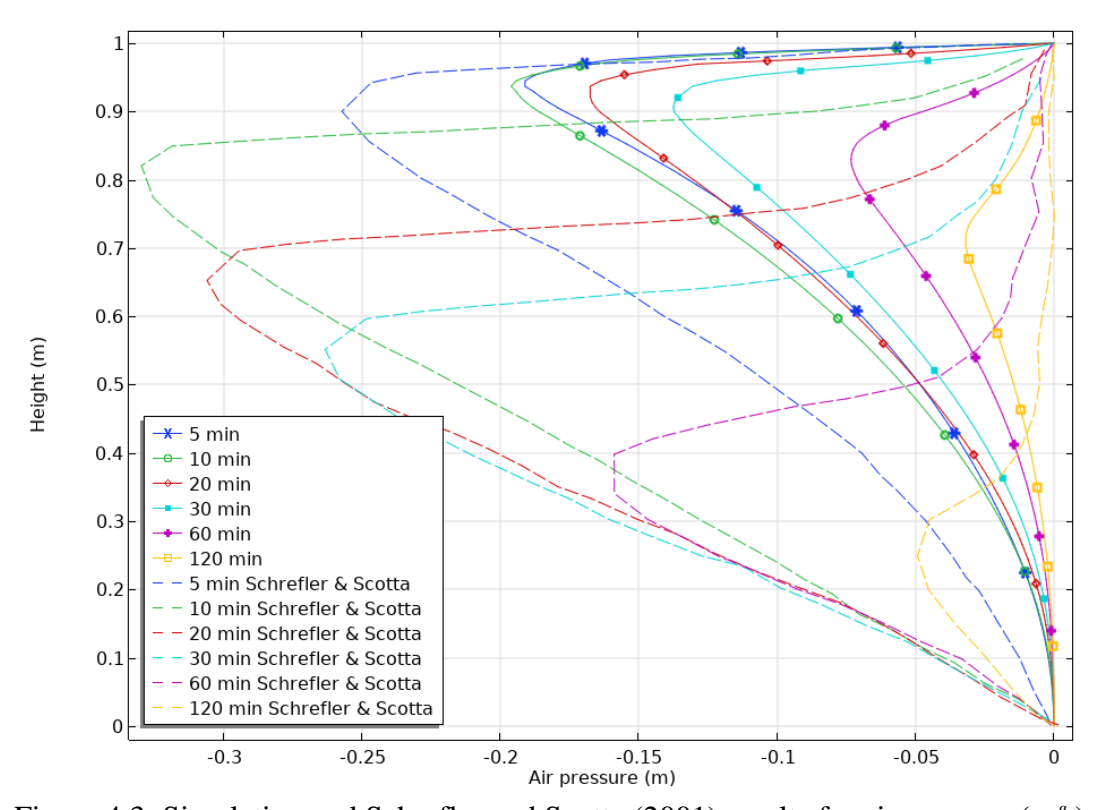


Figure 4.3: Simulation and Schrefler and Scotta (2001) results for air pressure (p^{g}).

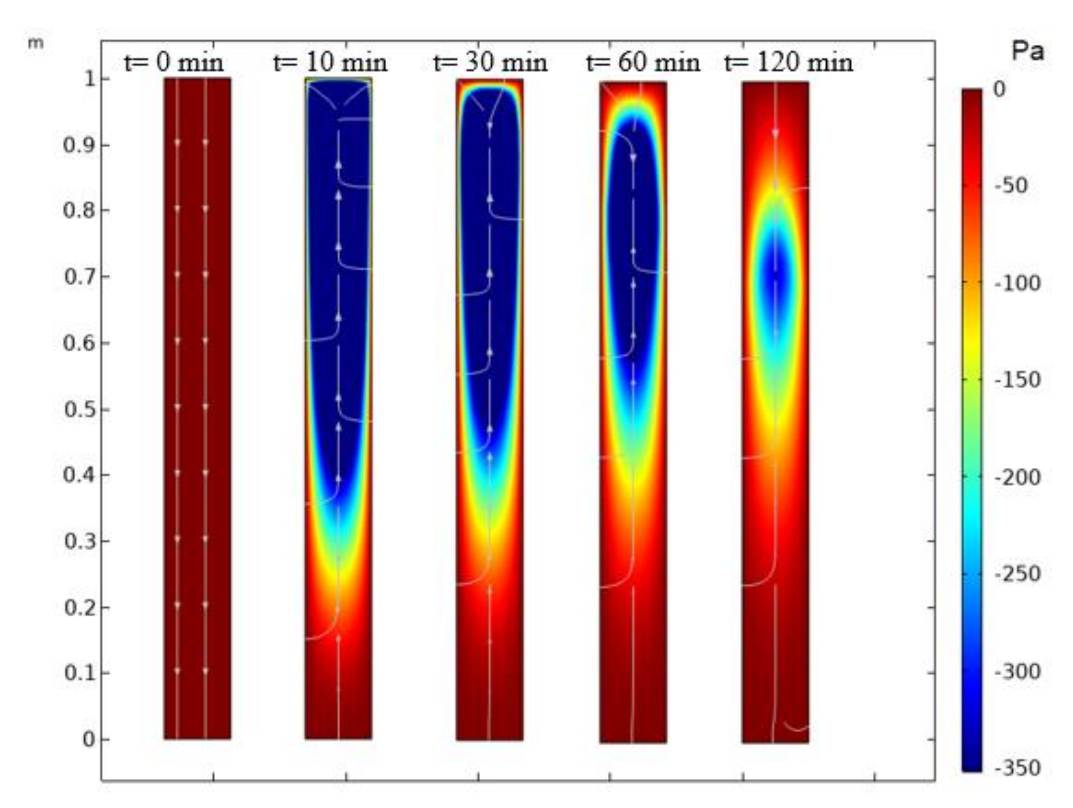


Figure 4.4: Air pressure (p^{g}) distribution at 0, 10, 30, 60, and 120 min.

Figure 4.5 shows the water saturation of the sand column. Unfortunately, Liakopoulos (1965a) did not measure the saturation in his experiment, and thus it not possible to compare the values to the experiment's results. The difference between the simulation results and Schrefler and Scotta (2001) is partially due to the difference in the gas pressure values. That is because the water saturation is a function of the capillary pressure that is the difference between the gas pressure and the water pressure.

Figure 4.6 displays the mechanical deformation of the sand. The simulation results exhibit qualitative similarity to (Schrefler and Scotta, 2001), although the magnitude is shifted by approximately 0.1mm (36% less). This difference may be attributed to the variation in the boundary condition, which affected the gas pressure and hence the mechanical deformation. It is worth noting that other researchers (Islam et al., 2020) have reported results closer to our simulation.

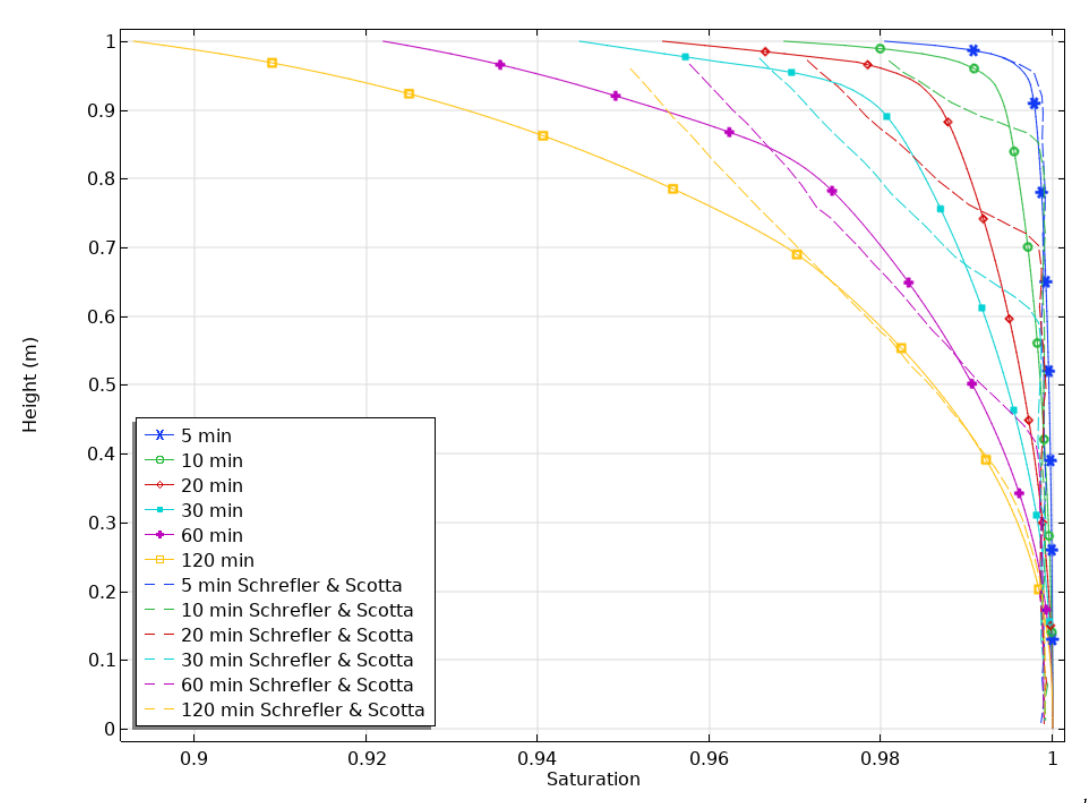


Figure 4.5: Simulation and Schrefler and Scotta (2001) results for liquid saturation $S^{\, l}$.

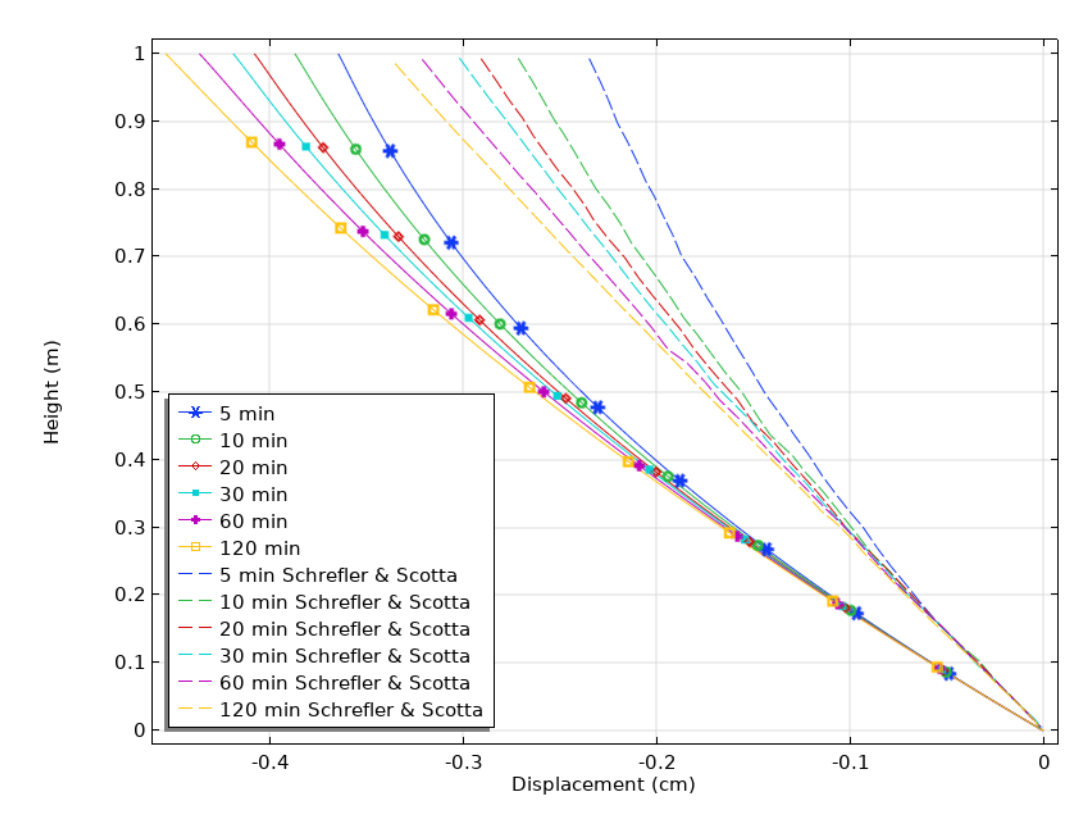


Figure 4.6: Simulation and Schrefler and Scotta (2001) results for mechanical deformation of porous medium.

Figure 4.7 and Figure 4.8 show the chemical transport (NaCl) in the system at different times. As expected, the mass fraction of the sodium chloride was transported from the top to the bottom of the column. The effect of transporting such a low concentration of chemical in a low water flow (only gravity was considered) is minor. However, for the case of CO₂ injection under high pressure and a higher chemical concentration (salts and minerals), the coupling effect of the chemical transport is expected to be higher. It is important to note that the solute transport behaviour in this model is based on theoretical assumptions and was not part of the actual experiment, as solute transport was not included in the experimental setup. For better validation, a dedicated laboratory experiment may be conducted to further validate the model, which could be outlined as future work.

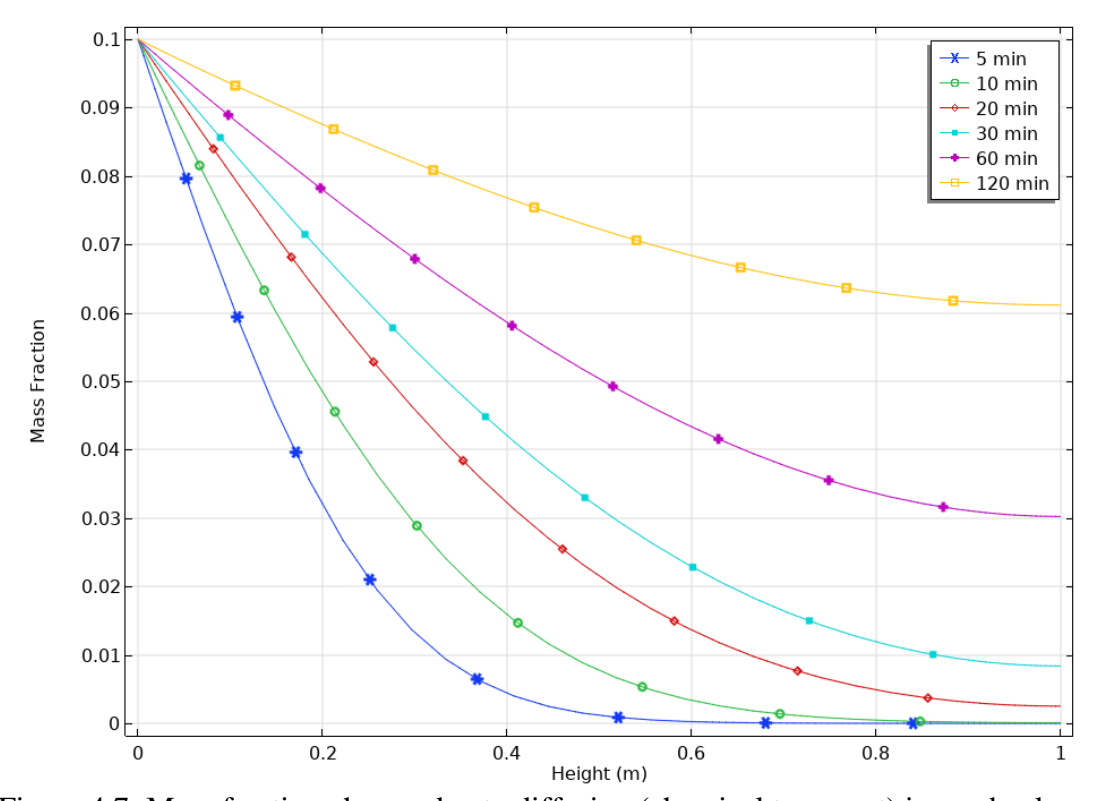


Figure 4.7: Mass fraction change due to diffusion (chemical transport) in sand column.

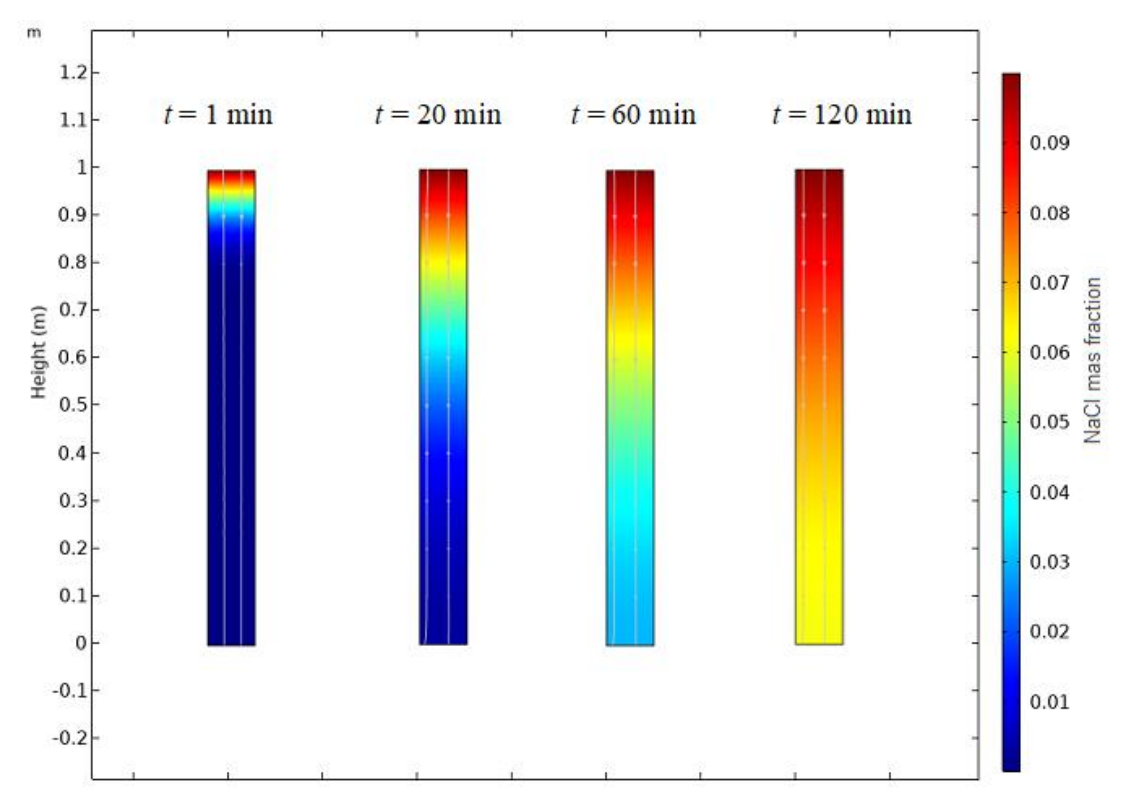


Figure 4.8: Chemical concentration (mass fraction of NaCl) distribution at 1, 20, 60, and 120 min.

Upon comparing the results from the column experiment simulations in Chapter 3 and Chapter 4, it is clear that there are no noticeable differences between Figure 4.2 and Figure 3.2. The differences observed are negligible, which can be explained by the slow flow, mainly driven by gravity. The changes in the parameters r_2 and r_4 did not have a significant impact on the simulation outcomes. The purpose of the initial set of simulations (Figures 4.1–4.8) was to check the solute transport equation and ensure the model was working as expected. This was to confirm the correct setup of the model, including the chemical transport equation, which had not been tested in the earlier chapter.

Another simulation was carried out to investigate the influence of the r-terms as part of the sensitivity analysis. It was found that under conditions controlled only by gravity, the

extra terms added to the model did not greatly affect the results. Therefore, direct comparisons with the previous chapter were not considered necessary.

To better show the impact of the added terms, a sensitivity model with higher pressure will be introduced. This model is designed to see how the new terms affect the system under stronger conditions, such as faster flow rates. The main goal of these simulations was to confirm that the extra terms and chemical transport equations worked as expected and to study their effects under different conditions, providing a better understanding of the model's behaviour.

Sensitivity analysis

In this section, a sensitivity analysis for the new parameters r_1 and r_3 is conducted to assess their impact on the transport process. To simplify the discussion, a conceptional 2D model is considered. The model is 50 cm \times 20 cm of porous media (limestone rock sample). The right-side boundary of the system is assumed to be impermeable, preventing any fluid from passing through. The initial and boundary conditions are shown in Figure 4.9. For water saturation calculations, Van Genuchten relationship is used as:

$$k_{rw} = (S^{w})^{0.5} \times \left[1 - \left(1 - \left((S^{w})^{\frac{1}{m}}\right)\right)^{m}\right]^{2}$$
(4.55)

where the water saturation can be calculated by:

$$S^{w} = \left[\left(-\frac{p^{c}}{M} \right)^{\frac{1}{1-m}} + 1 \right]^{-m}$$
 (4.56)

M and m are Van Genuchten parameter. The parameters of the model were obtained from the literature and are listed in

Table 4.2. Under these conditions, the initial saturation S^w is found to be 96.42%. To simplify the discussion, the densities of CO_2 and water are assumed to remain constant.

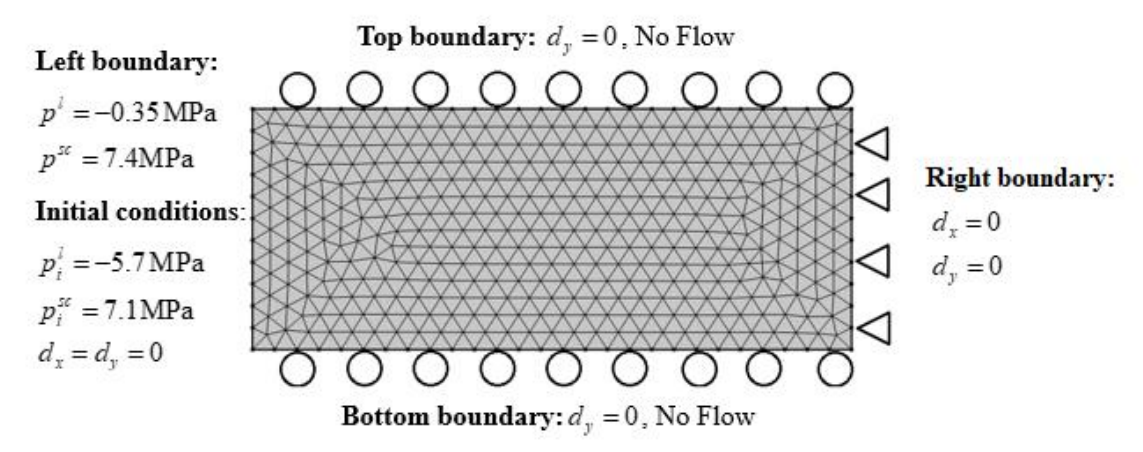


Figure 4.9: Initial and boundary conditions of rock sample

Table 4.2: Rock sample parameters.

| Physical meaning | Reference | Values and units |
|---------------------------|------------------------------|--|
| Young's modulus | Zhou and Burbey,) (2014a | E = 33 GPa |
| Water density | Zhou and Burbey,) (2014a | $\rho_w^w = 1000 \mathrm{kg/m^3}$ |
| ScCO ₂ density | Zhou and Burbey,) (2014a | $\rho_{Sc}^{Sc} = 660 \mathrm{kg/m^3}$ |
| Solid density | Zhou and Burbey,) (2014a | $\rho^s = 2600 \mathrm{kg/m^3}$ |
| Poisson's ratio | Zhou and Burbey,) (2014a | θ = 0.26 |
| Biot's coefficient | (Chen et al., 2016) | $\zeta = 1$ |
| Porosity | Zhou and Burbey,) (2014a | $\phi = 0.123$ |

| Intrinsic permeability of the solid | (Assumed) | $k_{abs} = 1.4 \times 10^{-20} \text{ m}^2$ |
|--|---------------------------|---|
| Dynamic viscosity of water | Zhou and Burbey,) (2014a | $v^{w} = 1 \times 10^{-3} \mathrm{Pa}\mathrm{s}$ |
| Dynamic viscosity of ScCO ₂ | Zhou and Burbey,) (2014a | $v^{Sc} = 6 \times 10^{-5} \mathrm{Pa}\mathrm{s}$ |
| Bulk modulus of water | Zhou and Burbey,) (2014a | $K_{w} = 2.2 \times 10^{3} \mathrm{MPa}$ |
| Bulk modulus of $ScCO_2$ | Zhou and Burbey,) (2014a | $K_{Sc} = 58 \mathrm{MPa}$ |
| Bulk modulus of solid | Zhou and Burbey,) (2014a | $K_s = 74 \mathrm{GPa}$ |
| Van Genuchten parameter | (Chen et al., 2016) | m = 0.43 |
| Van Genuchten parameter | (Chen et al., 2016) | M = 51MPa |

In this analysis, parameters r_1 and r_3 were simulated at different values to discern their impact on the results. When a value was given to one parameter, the other was assumed to be zero. The selection of these values was primarily driven by a trial-and-error process. By exploring a range of values, the maximum and minimum thresholds at which the model converged were identified. This approach was taken due to the absence of available experimental data for these phenomenological coefficients, and hence, trial-and-error provided a means to approximate these limits which found to be $r_1, r_3 = 0.01 \sim 0.1$.

Considering the compact size of the rock sample and the heightened pressure of the fluid, permeability was assumed to be minimal. Such an assumption guarantees the fluid flows at a satisfactory rate, preventing it from rapidly reaching equilibrium. Figure 4.10-12 show the liquid pressure, supercritical pressure, and solid deformation for r_1 and r_3 values

of 0.01 and 0.1 respectively. The data displayed corresponds to the coordinate point (0.1, 0.25), centrally located within the conceptual 2D model. Parameter r_1 in the governing equation for the liquid relates directly to the supercritical flow's impact on the liquid flow. Notably, the figures reveal that the influence of r_1 is greater than r_3 . This prominence arises from the elevated water saturation value, resulting in a reduced saturation level for the supercritical phase ($S^T + S^{Sc} = 1$). Since the saturation value aligns with the capillary pressure (as detailed in the Van Genuchten relations), it is contingent on both initial and boundary conditions.

In Figure 4.13, which shows water saturation exceeding 96%, the implications of this saturation are examined further: the energy losses stemming from the interaction between the two-phase flow correlate directly with the fluid volume present within the pore (saturation). The role of r_1 lead to increment in liquid and supercritical pressure. Upon closer inspection, an elevation in r_1 values lead to an increase in both the liquid and supercritical pressures, suggesting diminished energy losses from fluid interactions.

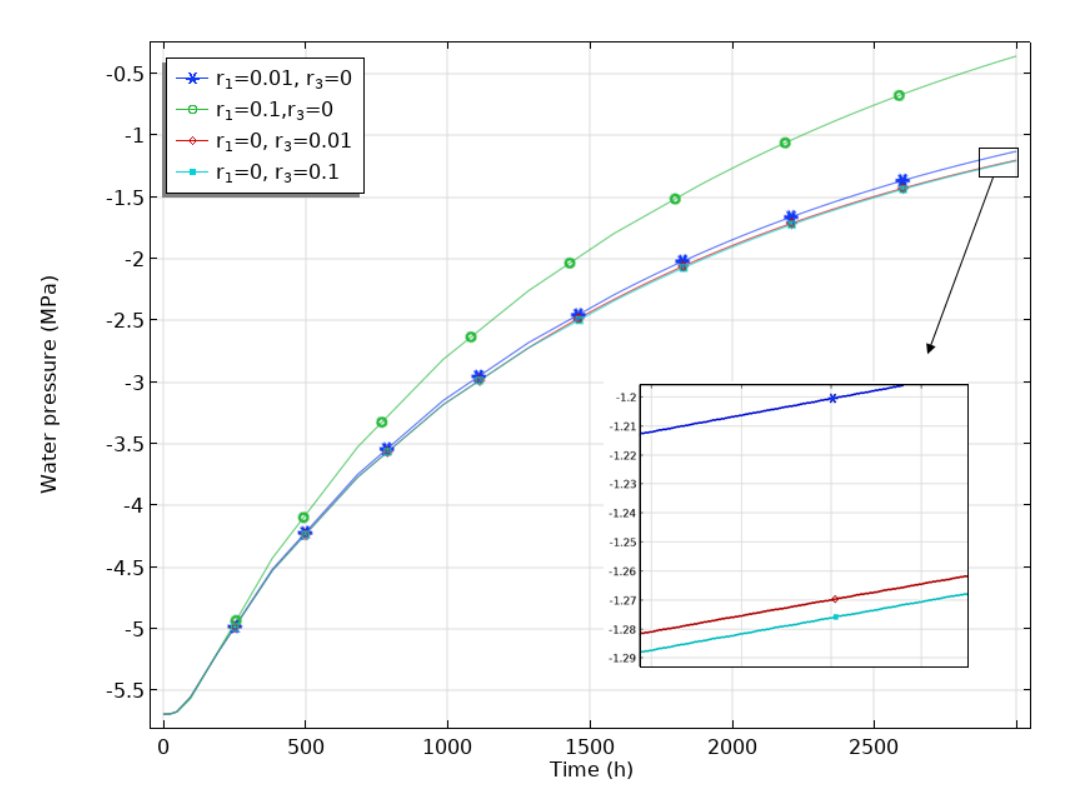


Figure 4.10: Water pressure at coordinate point (0.1,0.25) at different r_1 and r_2 values.

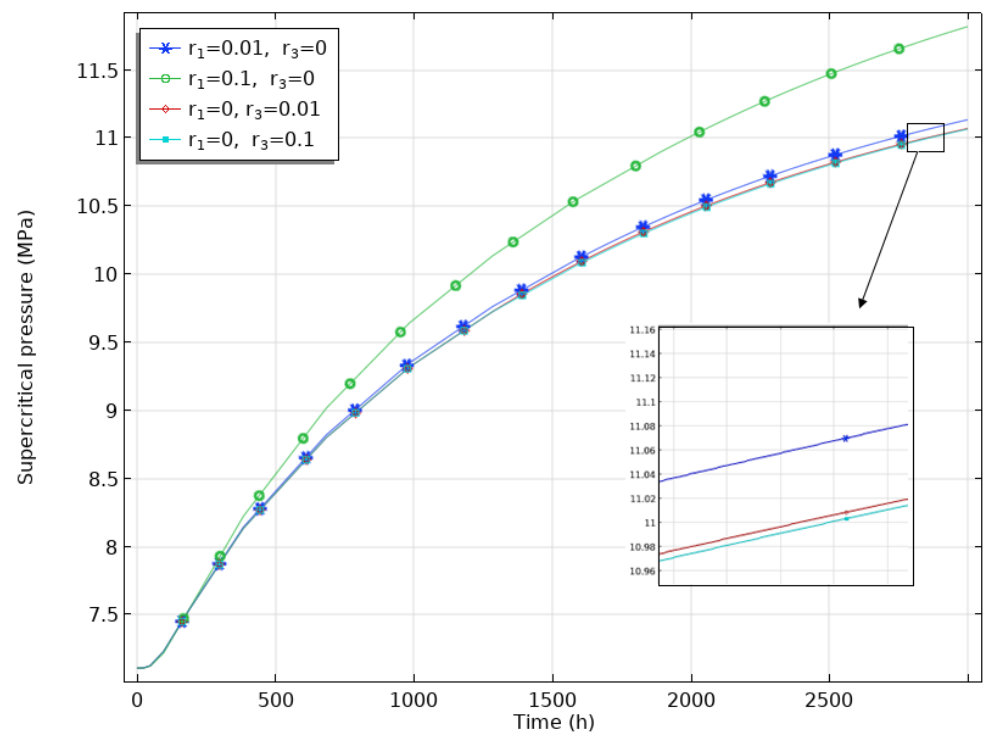


Figure 4.11: Supercritical pressure at coordinate point (0.1,0.25) at different r_1 and r_2 values.

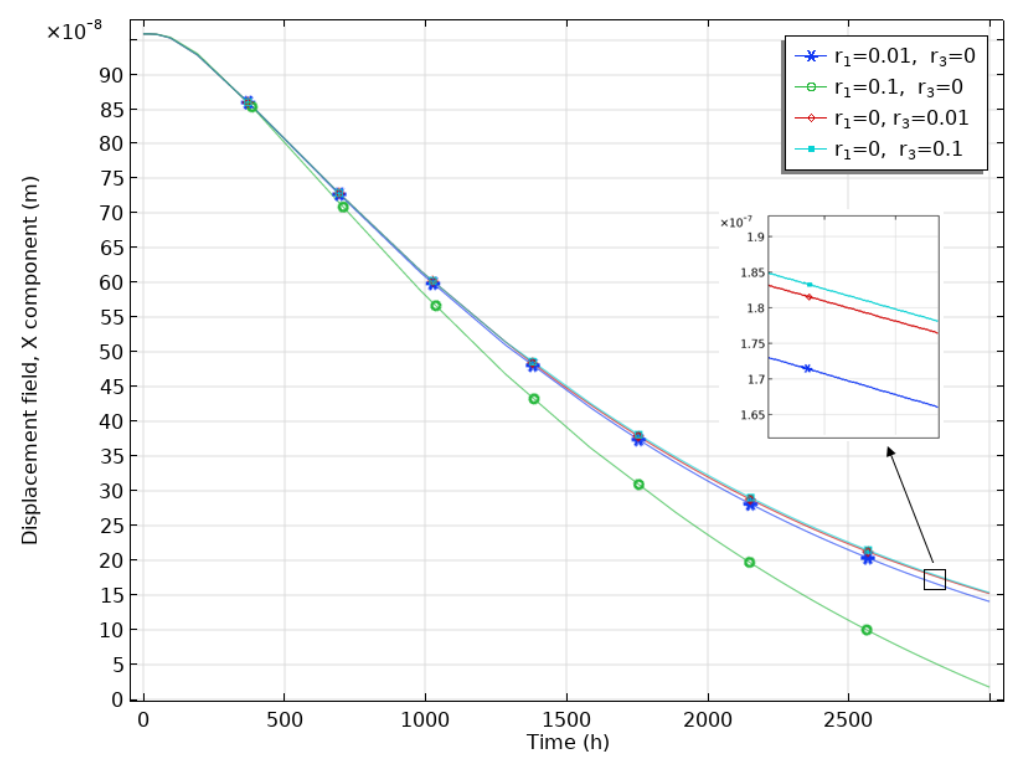


Figure 4.12: Horizontal deformation at coordinate point (0.1,0.25) at different r_1 and r_2

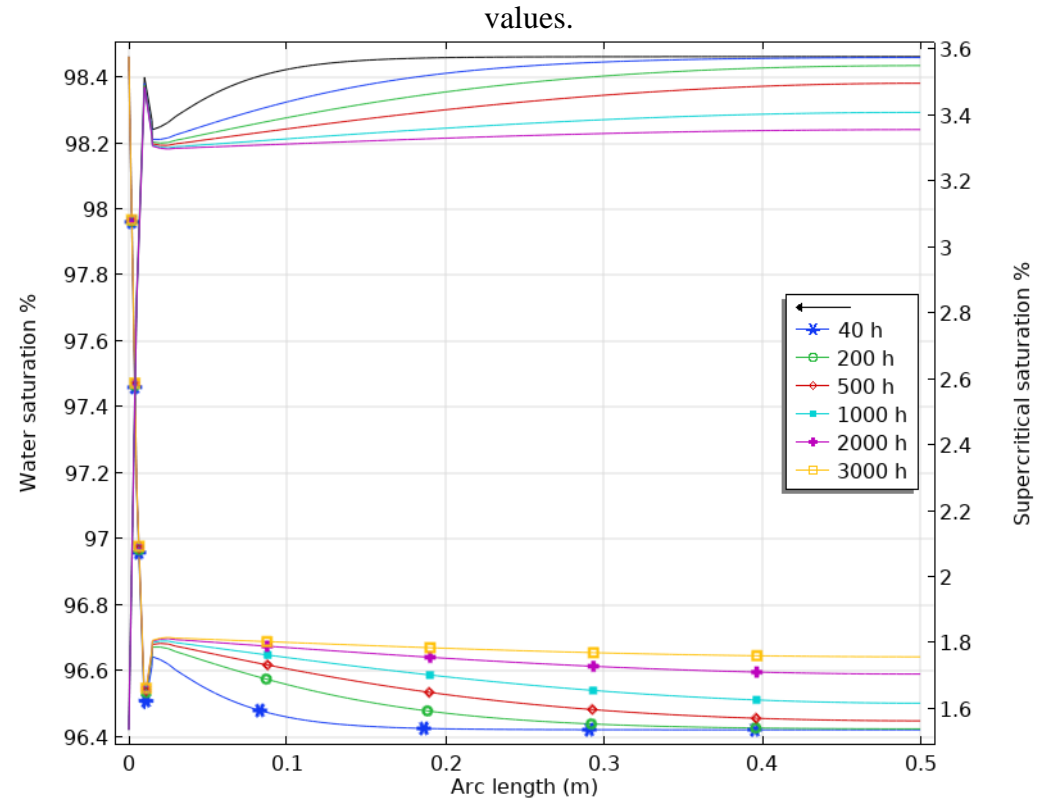


Figure 4.13: Supercritical and water saturation at different times (hours), across horizontal cross section of the sample with $r_1 = r_2 = 0$.

Figure 4.14-16 probe deeper into the sensitivities of parameters r_1 and r_3 across a horizontal cross-section of the sample at the 2000-hour mark. From a detailed examination, one discernible pattern is the apex of these parameters' influence post-entry into the formation, a crucial juncture where the two flows converge and begin mixing. This observation implies a localized, maximum interaction effect right after entry, which then diminishes as the fluids travel deeper, hinting at lessening interactions or stabilization of the two fluids over distance. The supercritical pressure in the plot seems to increase sharply near the injection point. This is likely due to the complex interactions between water pressure and the pressurized CO_2 flow. The pressure increase could also be a result of the sudden applied pressure above the initial baseline, which may have caused this phenomenon.

The modulation of these parameters indeed has pronounced effects on the outcomes. However, these impacts are intrinsically tied to the saturation value. For instance, r_3 's sway is more pronounced when water saturation nears the supercritical saturation, a fact buttressed by equations (4.50), and (4.51). Here, the relative permeabilities for water and the supercritical phase get multiplied by r_1 , and r_3 respectively. On the other hand, parameter r_3 , present in the supercritical phase's governing equation and associated with the liquid's effect on the supercritical phase, registers negligible influence on the results.

Lastly, moving into the second term of the governing equation, the small effect of chemical entropy is highlighted. It gains relevance predominantly in scenarios marked by low permeability or evident osmosis. Yet, this term stands as a potential indicator for tracking CO₂ leakage via low permeability caprock resulting from osmosis.

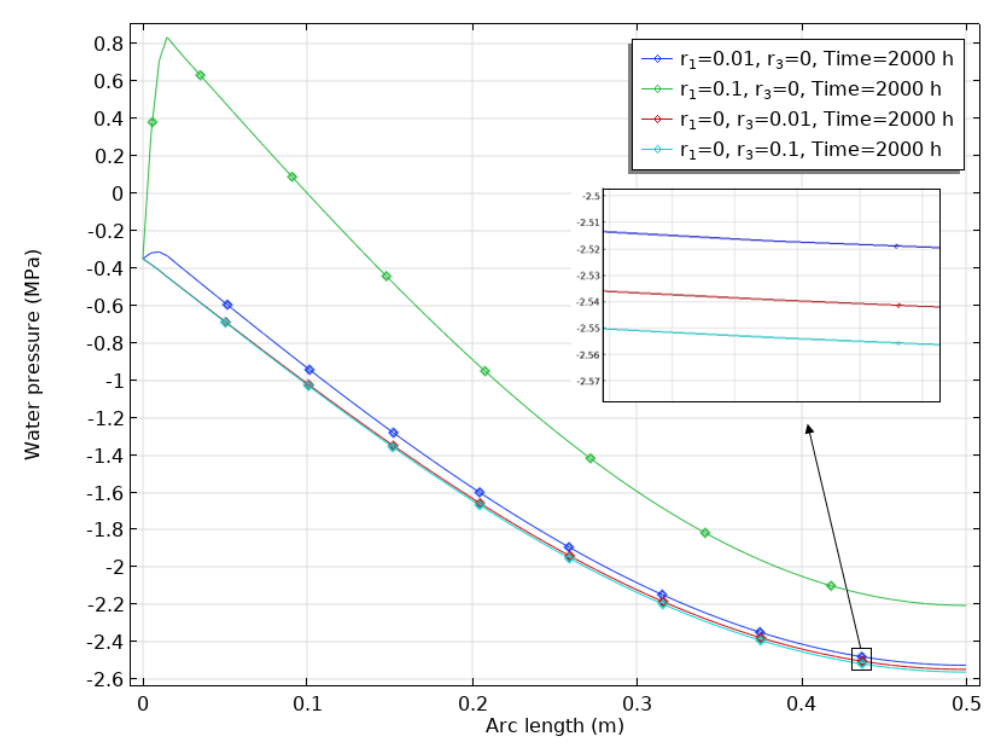


Figure 4.14: Water pressure across horizontal section of sample at different r_1 and r_2

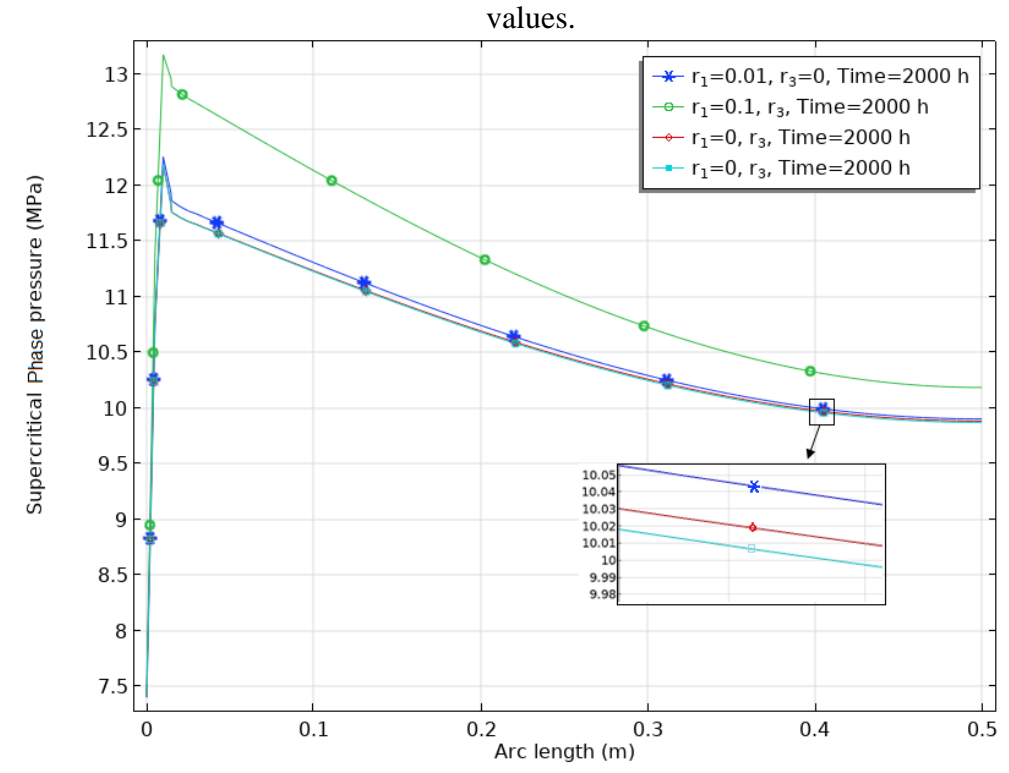


Figure 4.15: Supercritical pressure across horizontal section of sample at different r_1 and r_2 values.

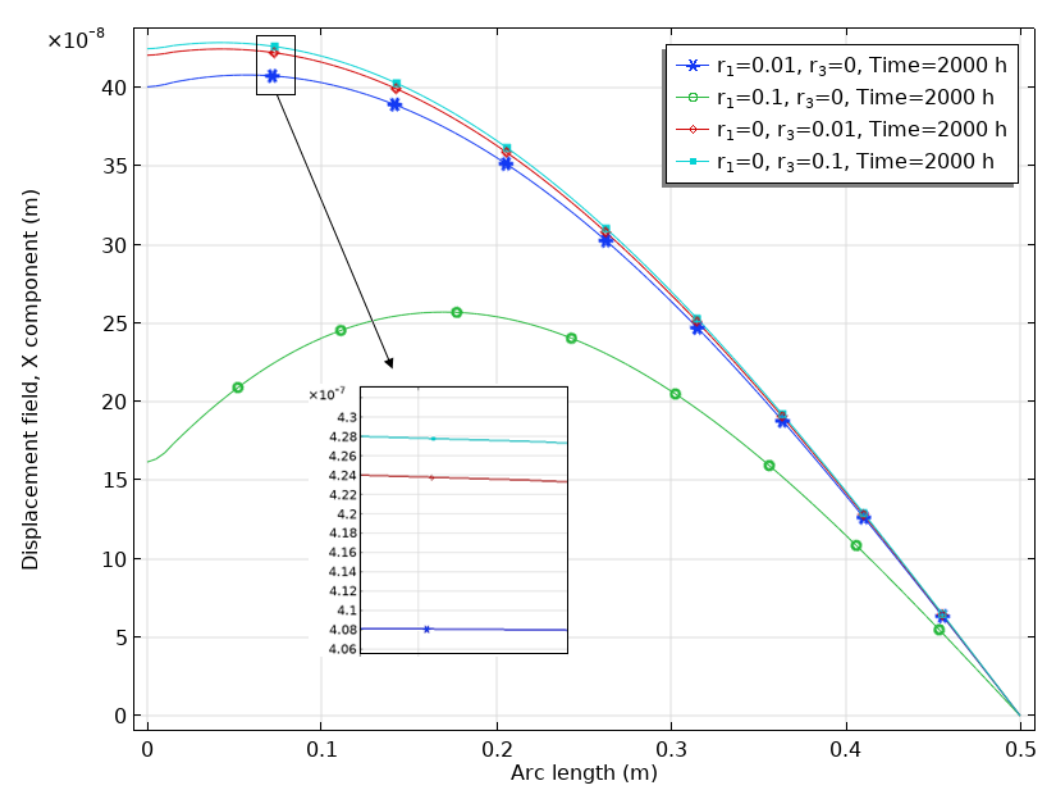


Figure 4.16: Deformation across horizontal section of sample at different r_1 and r_2 values.

4.7 Conclusion

A fully coupled multi-phase HM-supercritical-chemical constitutive framework under isothermal conditions was developed based on the mixture-coupling theory. The phenomenological equations were used to establish two new terms describing the coupled interaction between supercritical and liquid phases and chemical solute transport. The model also considered coupling between the deformation of a solid and the change in pressure. The coupled model was based on Helmholtz's free energy equations and Biot's poroelasticity model. Experimental data were used to validate the model. COMSOL Multiphysics® software was used to numerically solve the model through the finite element method. The numerical simulation results were in good agreement with the experimental results. The sensitivity analysis shows that the effect of the new terms is

highly dependent on the relative permeability which can be directly related to saturation value. A sensitivity analysis also shows that the value of the new terms parameters r_1 and r_3 has a significant impact on the pressures and deformation if the saturation of the phase is high. The solute transport parameters r_2 and r_4 seems to have less influence. However, these terms are useful when investigating the osmosis effect or when CO_2 leakage through low permeability caprock is considered. In this model, only one solute was simulated; however, for a larger field, such as carbon sequestration in a large formation, with more solutes present, a more significant impact is predicted. In summary, the good agreement between the simulation and experimental results confirms the test's fundamental validity. However, the newly introduced terms had minimal influence on the simulation outcomes against the experimental results, leading to the inclusion of a sensitivity analysis. This analysis assessed the potential impact of these terms under extreme conditions, such as high pressures. The results suggest that dissipation due to solute transport and two-phase friction has a minimal effect in slow-moving mixtures with low solute concentrations.

The significance of this paper is its inclusion of energy dissipation due to both friction and solute transport in two-phase interactions, influencing pressure, flow rate, and fluid distribution. More experiments are needed to refine 'r' parameters at diverse injection rates. The results are markedly influenced by dynamic viscosity, a vital element in the abnormal behaviour of supercritical carbon dioxide.

In this chapter, the model has been adjusted to include only the energy losses from twophase interactions and chemical solute transport. In the next chapter, it will be further refined to account for chemical mass transfer resulting from chemical dissolution reactions. Additionally, changes in porosity due to the dissolution process will also be incorporated. Subsequently, a finite element simulation will be conducted to analyse the effects of these enhancements in the reactive model.

Chapter 5: Coupled reactive two-phases model involving dissolution and dynamic porosity for deformable porous media based on Mixture-Coupling Theory

Abstract

Carbon capture and storage (CCS) has attracted significant attention owing to its impact on mitigating climate change. Many countries with large oil reserves are adopting CCS technologies to reduce the impact of fossil fuels on the environment. However, because of the complex interactions between multi-phase fluids, planning for CCS is challenging. One of the challenges is the integration of chemical reactions with multi-phase hydromechanical relationships in deformable porous media. In this study, a multi-phase hydromechanical reactive model for deformable porous media is established by using mixturecoupling theory approach. The non-equilibrium thermodynamic approach is extended to establish the basic framework and Maxwell's relations to build multiscale coupling. Chemical reaction coupling is achieved through the extent of the reaction and chemical affinity. The developed model can simulate CCS by considering the effect of calcite dissolution on porosity and permeability. It has been found from the simulation that the chemical reaction has a major influence on porosity and permeability change comparing to both pressure and mechanical strain effect. Also, as the dissolution reaction takes place, the stress/strain decrease on the solid matrix. The results of this study successfully bridge the knowledge gap between chemical reactions and mechanical deformation. Furthermore, insights from this model hold substantial implications for refining CCS processes. By providing a more accurate prediction of pressure changes and porosity/permeability evolution over time, this research paves the way for improved CCS operation planning, potentially fostering safer, more efficient, and economically feasible climate change mitigation strategies.

5.1 Introduction

Carbon sequestration, particularly geological sequestration, plays a pivotal role in addressing global carbon emissions and is a vital tool in the battle against climate change. As carbon dioxide (CO₂) levels in the atmosphere continue to rise, finding reliable and effective methods to store it becomes necessary. One such method is by injecting CO₂ deep into geological formations. In geological sequestration, CO₂ is injected in deep formations either as a brine–gas-saturated mixture or supercritical phase (ScCO₂). It can be sequestered in various types of formations, such as sandstone, saline aquifers, dolomite, coal, and basalt formation. Chemical reactions are typically induced, and the type and intensity of the reaction depend on the formation type and CO₂ phase (brine/CO₂ mixture or ScCO₂). Mineral carbonation can occur, resulting in the formation of new minerals, such as iron, magnesium, and calcium ions, affecting the porosity and permeability of the rock. This process is known as mineral trapping.

Each formation reservoir undergoes chemical reactions based on the primary minerals present. Chemical reaction coupling is complex. It includes dissolution and precipitation, which affect energy, fluid flow, porosity, and solid deformation. When dissolution occurs, the resulting ions may react with other minerals and acidic solutions to produce carbonate species (precipitation). The temperature and CO₂ solubility in the fluid directly

affect the precipitation/dissolution process because they are related to the pH level of the fluid (Luo et al., 2012; Rathnaweera et al., 2017). Chemical reactions can change the physical properties, such as porosity and permeability, of the solid matrix and affect fluid transport, in which mass flow is added to the liquid. The stress/strain ratio is also affected by this process.

The effect of the chemical reactions between injected CO_2 and surrounding rocks on formation porosity has been investigated in previous studies; however, most reactive models consider only the effect of changing porosity on permeability (Xu et al., 2005; Fischer et al., 2013; Klein et al., 2013; Ilgen and Cygan, 2016; Wolf et al., 2016; Zhou et al., 2016; Dai et al., 2020).

Although several hydro-mechanic-chemical reactive models have been introduced in recent years, a knowledge gap in mechanical-chemical coupling relations, specifically the effect of the dissolution/precipitation process on the applied stress/strain on the solid matrix, still exists. Some researchers such as Olivella et al. (1994) tried to develop a comprehensive thermo-hydro-mechanical (THM) framework for the multi-phase flow of brine and gas through saline media, which incorporated salt species dissolution, precipitation, and deformation via a pressure solution. However, the framework lacked coupling between strain–stress and chemical reactions. Guimarães et al. (2007) attempted to create a fully coupled model by combining the model introduced by Olivella et al. (1994) and the approach of Gens et al. (2002) with reactive transport equations. However, this model only accounted for the change in porosity (dynamic porosity) and thus permeability due to chemical reactions, neglecting the effect of chemical dissolution on the governing equations for deformation and stress. Yin et al. (2011) used a mathematical

model derived by Lewis and Schrefler (1998b) to describe the two-phase transport of fluids. Subsequently, the general transport of the solute equation was incorporated into the model. However, the hydromechanical-chemical coupling was limited to the changes in porosity and permeability without the governing equations for solid, liquid, and gas being modified.

Some researchers attempted to create a coupling between chemical reaction and stiffness of the material and the induced stresses, such as Mehrabi and Atefi-Monfared (2022). The author introduced a model that predicts the spatial distribution of bio-cementation and the resulting enhanced characteristics of microbially induced carbonate precipitation (MICP) treated soils. However, the presented model can handle one phase flow only and more advanced model is required for applications such as Carbon Capture and Storage.

In addition to the work of Mehrabi and Atefi-Monfared (2022), other researchers, including Gawin et al. (2003), Kuhl et al. (2004), Gawin et al. (2008), Haxaire and Djeran-Maigre (2009), Karrech (2013), Zhang and Zhong (2018) have explored the coupling of chemical reactions with solid/stress equations. Recently, Yue et al. (2022) proposed a single-phase transport model that includes dissolution and chemically reactive processes (i.e., changes in porosity due to dissolution). They introduced the concept of 'solid affinity' to couple the dissolution reactions with the hydro-mechanical framework. Although this model addresses the gap in the studies on mechanical-chemical coupling, it only considers one-phase transport, limiting its usefulness for multi-phase flow applications such as carbon sequestration. Moreover, the numerical simulation in that study was simplistic and did not show the effect of the added term on the strain.

One approach that promises to address the shortcomings of traditional models is rooted in a method known as the mixture-coupling theory (Chen et al., 2018a). This method, which was first presented by Heidug and Wong (1996), provides a unique interpretation of fluid-filled rocks or soils. Rather than treating them as separate entities, it views them as a unified whole. This shift in perspective addresses some challenges seen in standard mechanics methodologies and presents clear advantages. While classical mechanics typically hinges on the principles of stress-strain tensor and the balance of linear momentum, the mixture-coupling theory turns to the realms of non-equilibrium thermodynamics, focusing on an energy and entropy-centric approach. This method has been distinguished and differentiated from others in several scholarly contributions, with some pointing out its strategic omission of the momentum conservation balance equation.

With such advancements in modelling frameworks, two key questions remain:

- How can chemical reactions be effectively integrated into a multi-phase hydromechanical-chemical system for CO₂ sequestration?
- How can the influence of these reactions on the hydromechanical framework be accurately captured?

To address this research gap, this study presents a novel approach for modelling a reactive multi-phase hydro-mechanical-chemical system for CO_2 sequestration using coupling mixture theory. The proposed model is simulated under isothermal conditions, and a theoretical CO_2 injection test into limestone sample rock is performed, considering only the chemical reactions that lead to mineral dissolution. The extent of the reaction and

solid affinity is applied to the model to capture the coupled effects of chemical reactions on the hydromechanical framework. Objectives of this study can be set clear as:

- To present a novel approach for modelling a reactive multi-phase hydromechanical-chemical system for CO₂ sequestration using coupling mixture theory by applying the extent of reaction and solid affinity to the model, ensuring the coupled effects of chemical reactions on the hydromechanical framework are effectively captured.
- To simulate the proposed model under isothermal conditions by performing a theoretical CO₂ injection test into limestone sample rock, focusing on chemical reactions that lead to mineral dissolution.

It is important to note that the dissolution process in this study focuses on the dissolution of minerals, such as calcium carbonate (CaCO₃), rather than mass exchange between the two phases, as the system is assumed to be immiscible (i.e., no mass exchange between fluid phases). A miscible system was avoided for now to simplify what is already a complex framework. The approach in this thesis is to introduce new processes incrementally, and for this chapter, incorporating minerals dissolution is the primary innovation. Therefore, mass exchange between the two phases has been left for future research.

5.2 Mathematical model

When CO_2 is injected into a rock formation containing saline water, a considerable amount of the CO_2 fluid dissolves in the water to create carbonic acid. In the proposed model, a two-phase system consisting of a supercritical (Sc) fluid and liquid saline/carbonic water is considered. An immiscible system where the change in mass due to CO_2 solubility in saline water is not considered is assumed (CO_2 is assumed to be already dissolved in saline water). Additionally, the system is assumed to be isotropic under isothermal conditions.

In this paper, the model is defined by selecting an arbitrary microscopic domain of arbitrary size that encompasses all phases, along with a surrounding surface boundary that contains the domain. Fluids are the only substances allowed to pass through this boundary. The subscripts "Sc", "l", "w", and "c" refer to supercritical fluid, saline water, water, and chemical solute (salt), respectively.

The volumes of saline water and supercritical fluid flows are identified as V^{l} and V^{Sc} , respectively. The relationship between the pore space volume, V^{pore} , and these volumes can be expressed as follows (Bear, 2013; Lewis and Schrefler, 1987; Biot, 1955):

$$V^{pore} = V^{Sc} + V^{l},$$

$$\phi = \phi^{Sc} + \phi^{l},$$

$$S^{Sc} + S^{l} = 1.$$
(5.1)

where $\phi = V^{pore}/V$ is the volume fraction (porosity); $\phi^{Sc} = V^{Sc}/V$ is the volume fraction of the $ScCO_2$; $\phi^l = V^l/V$ is the volume fraction of saline water; the saturation of the $ScCO_2$ is denoted by $S^{Sc} = V^{Sc}/V^{pore}$; while the saturation of saline water is represented by $S^l = V^l/V^{pore}$.

The relationship between the mixture density (mass over the volume of mixture) and the phase density (mass over the volume of the phase) can be written as (Chen, 2013)

$$\rho^{l} = \phi^{l} \rho_{l}^{l},$$

$$\rho^{Sc} = \phi^{Sc} \rho_{Sc}^{Sc}.$$
(5.2)

where the symbols ρ^l , ρ^{sc} denote the mixture density, and ρ^l_l , ρ^{sc}_{sc} denote the phase density.

Based on the above relation, the water, chemical solute, and liquid mixture density can be expressed as:

$$\rho^{w} = \phi^{l} \rho_{l}^{w},$$

$$\rho^{c} = \phi^{l} \rho_{l}^{c},$$

$$\rho^{l} = \rho^{w} + \rho^{c}.$$
(5.3)

the variables ρ_l^w and ρ_l^c denote the mass ratios of water and chemical, respectively, to the total volume of the liquid phase.

5.2.1 Flux and diffusion:

The mass flux of β , where β represents either the saline water flow 'l', or the supercritical flow 'Sc', or any of the sub-constituents in saline water (i.e., water 'w' and chemical 'c'), is defined as (Chen, 2013)

$$\mathbf{I}^{\beta} = \rho^{\beta} \left(\mathbf{v}^{\beta} - \mathbf{v}^{s} \right), \tag{5.4}$$

 \mathbf{I}^{β} represents the fluid mass flux, ρ^{β} denotes the mixture density of β , and \mathbf{v}^{β} and \mathbf{v}^{s} refer to the velocities of β and the solid, respectively. To express the diffusion flux \mathbf{J}^{β} in terms of the barycentric velocity, the following equations can be used (Ma et al., 2021):

$$\mathbf{J}^{\beta} = \rho^{\beta} \left(\mathbf{v}^{\beta} - \mathbf{v}^{l} \right), \beta \in l,$$

$$\mathbf{J}^{\beta} = \rho^{\beta} \left(\mathbf{v}^{\beta} - \mathbf{v}^{Sc} \right), \beta \in Sc$$
(5.5)

the barycentric velocity of saline water is denoted by $\mathbf{v}^l = \frac{\rho^w}{\rho^l} \mathbf{v}^w + \frac{\rho^c}{\rho^l} \mathbf{v}^c$. the supercritical flow, since it is considered to be composed of a single constituent, then the diffusion flux of the supercritical flow is 0.

Nether less, saline water flow contains water and chemical, $\mathbf{v}^w \neq \mathbf{v}^l$ and $\mathbf{v}^c \neq \mathbf{v}^l$, therefore, by using equation (4.4) and (4.5) the diffusion flux can be written as

$$\mathbf{J}^{\beta} = \mathbf{I}^{\beta} - \rho^{\beta} \left(\mathbf{v}^{l} - \mathbf{v}^{s} \right). \tag{5.6}$$

5.2.2 Chemical reaction and dissolution

In this study, the dissolution rate is incorporated in the model through chemical affinity, which is directly related to the extent of the reaction. Solute c is only transported in the

liquid and does not react chemically. The reaction occurs only between the rock minerals and carbonic acid.

The dissolution reaction can be expressed as (Katchalsky and Curran, 1965)

$$v_x X_{(s)} + v_y Y_{(aq)} \rightarrow v_z Z_{(aq)},$$
 (5.7)

where X, Y are the reactants and Z is the product, v_x , v_y , and v_z are the stoichiometric coefficient for X, Y, and Z.

There is a direct relation between the extent of reaction and the moles changes $\frac{dn_i}{V} = \chi v_i d\xi,$

where ξ is extent of reaction, dn_i is the change in number of moles, V pore volume. χ equals to 1 for products Z and -1 for reactants X, Y and 0 for anything that does not join the reaction. Furthermore, the driving force reaction (affinity) can be written as (Kondepudi and Prigogine, 2014; Yue et al., 2022)

$$A = -\sum_{i} \chi v_{i} M^{i} \mu^{i} = v_{x} M^{x} \mu^{x} + v_{y} M^{y} \mu^{y} - v_{z} M^{z} \mu^{z}, \qquad (5.8)$$

where A is the affinity, M is the molar mass, and μ is the chemical potential.

5.2.3 Energy, entropy, and phenomenological equations:

5.2.3.1 Helmholtz free energy balance equation

The Helmholtz free energy balance equation in a mixture system comprising saline water, ScCO₂, and chemical solutes can be expressed as (Katchalsky and Curran, 1965; Heidug and Wong, 1996)

$$\frac{D}{Dt} \left(\int_{V} \psi dV \right) = \int_{S} \mathbf{\sigma} \mathbf{v}^{s} \cdot \mathbf{n} dS - \left(\int_{S} \mu^{w} \mathbf{I}^{w} + \int_{S} \mu^{Sc} \mathbf{I}^{Sc} + \int_{S} \mu^{c} \mathbf{I}^{c} \right) \cdot \mathbf{n} dS - T \int_{V} \gamma dV ,$$
(5.9)

In the above equation, the Helmholtz free energy density ψ is analysed in the context of the Cauchy stress tensor σ , the outwards unit normal vector (n), and the chemical potentials for water μ^w , supercritical fluid μ^{Sc} , and chemical solute μ^c , at a fixed temperature T, while considering the entropy production per unit volume γ .

The balance equation of the free energy density can be presented in differential form as follows (Chen et al., 2018a):

$$\dot{\psi} + \psi \nabla \cdot \mathbf{v}^{s} - \nabla \cdot (\sigma \mathbf{v}^{s}) + \nabla \cdot (\mu^{w} \mathbf{I}^{w} + \mu^{Sc} \mathbf{I}^{Sc} + \mu^{c} \mathbf{I}^{c}) = -T \gamma \leqslant 0.$$
 (5.10)

It should be mentioned that the term $\mu^c \mathbf{I}^c$ here represent the energy change caused by the chemical mass exchanging with the surroundings.

5.2.3.2 Fluid mass balance equation:

The balance equation for the fluid component can be expressed as (Katchalsky and Curran, 1965)

$$\frac{D}{Dt} \left(\int_{V} \rho^{\beta} dV \right) = -\int_{S} \mathbf{I}^{\beta} \cdot \mathbf{n} dS + \int_{V} \chi v^{\beta} M^{\beta} \dot{\xi} dV , \qquad (5.11)$$

where the last term in the above equation, i.e., $\int_V \chi v^\beta M^{-\beta} \dot{\xi} dV$, represents the change of fluid components due to the chemical reaction.

The balance equation for the fluid component in the local form is (Chen et al., 2018a):

$$\dot{\rho}^{\beta} + \rho^{\beta} \nabla \cdot \mathbf{v}^{s} + \nabla \cdot \mathbf{I}^{\beta} - \chi v^{\beta} M^{\beta} \dot{\xi} = 0. \tag{5.12}$$

5.2.3.3 Entropy production equation

The dissipation in the mixture including solid/fluid friction can be expressed as (Katchalsky and Curran, 1965; Ma et al., 2022b)

$$0 \le T \ \gamma = -\mathbf{I}^{w} \cdot \nabla \mu^{w} - \mathbf{I}^{Sc} \cdot \nabla \mu^{Sc} - \mathbf{I}^{c} \cdot \nabla \mu^{c} + A \dot{\mathcal{E}}, \tag{5.13}$$

where $\mathbf{I}^w \cdot \nabla \mu^w$, $\mathbf{I}^{Sc} \cdot \nabla \mu^{Sc}$, and $\mathbf{I}^c \cdot \nabla \mu^c$ are the entropy productions caused by the mass flow of the liquid (water), supercritical fluid, and transport of the diluted chemical, respectively. A denotes affinity, and $A\dot{\xi}$ represents the entropy generated by the chemical reaction.

The Darcy velocity, **u**, is for both liquids (including the chemicals), and supercritical phase can be expressed as (Whitaker, 1986; Lewis and Schrefler, 1987)

$$\mathbf{u}^{l} = S^{l} \phi \left(\mathbf{v}^{l} - \mathbf{v}^{s} \right),$$

$$\mathbf{u}^{Sc} = S^{Sc} \phi \left(\mathbf{v}^{Sc} - \mathbf{v}^{s} \right).$$
(5.14)

The Gibbs–Duhem equation for the liquid and supercritical phases can be used to express the pore liquid pressure and supercritical phase pressure as (Chen et al., 2016)

$$\nabla p^{l} = \rho_{l}^{w} \nabla \mu^{w} + \rho_{l}^{c} \nabla \mu^{c},$$

$$\nabla p^{Sc} = \rho_{Sc}^{Sc} \nabla \mu^{Sc}.$$
(5.15)

The relationships in equations (5.3), (5.6), (4.13), and (5.15) can be applied to describe the diffusion of chemical c as $\mathbf{J}^c = -\mathbf{J}^w$, and equation (4.12) can be revised as

$$0 \le T \gamma = -\mathbf{u}^{l} \cdot \nabla p^{l} - \mathbf{J}^{c} \cdot \nabla \left(\mu^{c} - \mu^{w}\right) - \mathbf{u}^{Sc} \cdot \nabla p^{Sc} + A \dot{\xi}, \tag{5.16}$$

where $-\mathbf{u}^l \cdot \nabla p^l$ represents the liquid flow driven by the internal liquid potential difference, $\mathbf{J}^c \cdot \nabla \left(\mu^c - \mu^w \right)$ represents the chemical diffusion in the liquid saline water driven by chemical potential gradient, $-\mathbf{u}^{sc} \cdot \nabla p^{sc}$ represents the supercritical flow driven by the supercritical flow pressure difference, and $A \dot{\xi}$ represent the chemical reaction that causes the dissolution of solid minerals.

Equation (4.14) describes the entropy production through thermodynamics fluxes and their corresponding driving forces. The phenomenological equation concept can be used to describe the interaction between flows and driving forces by assuming a linear relationship between each flow and its driving forces (Chen et al., 2018a).

Several assumptions have been proposed in this model: (I) the chemical solute is present only in the liquid phase (saline water) and does not chemically react; (II) the CO_2 in the supercritical phase is considered chemically non-reactive; (III) the system is immiscible, i.e., no exchange of mass between the liquid and supercritical phases via dissolution occurs; (IV) some of the CO_2 s are already dissolved in the saline water to form carbonate acid and can react with solid minerals (dissolution of solid minerals); (V) the process is

under isothermal conditions; (VI) the porous media exhibits completely isotropic behaviour (isotropic material).

5.2.3.4 Phenomenological equations

Due to the interdependence of fluxes in a coupled system, the relationship between flow and driving forces can be expressed through linear dependence equations, also known as phenomenological equations. In the context of mass transport in an isotropic medium, the calculation of the three major flows $(\rho_l^l \mathbf{u}^l, \rho_{sc}^{sc} \mathbf{u}^{sc}, \text{and } \mathbf{J}^c)$ is dependent on their corresponding driving forces $(\nabla p^l, \nabla p^{sc}, \text{and } \nabla (\mu^c - \mu^w))$ as (Heidug and Wong, 1996; Chen et al., 2018a):

$$\rho_l^l \mathbf{u}^l = -\frac{L_{11}}{\rho_l^l} \nabla p^l - \frac{L_{12}}{\rho_{Sc}^{Sc}} \nabla p^{Sc} - L_{13} \nabla (\mu^c - \mu^w), \tag{5.17}$$

$$\rho_{Sc}^{Sc} \mathbf{u}^{Sc} = -\frac{L_{21}}{\rho_l^l} \nabla p^l - \frac{L_{22}}{\rho_{Sc}^{Sc}} \nabla p^{Sc} - L_{23} \nabla (\mu^c - \mu^w), \qquad (5.18)$$

$$\mathbf{J}^{c} = -\frac{L_{31}}{\rho_{l}^{l}} \nabla p^{l} - \frac{L_{32}}{\rho_{sc}^{Sc}} \nabla p^{Sc} - L_{33} \nabla \left(\mu^{c} - \mu^{w}\right), \tag{5.19}$$

where L_{ij} are phenomenological coefficients, and ρ_l^l is the liquid phase density.

The equations presented above assume that the affinity is a scalar quantity and that the system is isotropic. As a result, there is no coupling between the scalar term and the other vectorial quantities, in accordance with the Curie-Prigogione principle. While this allows the scalar term to be ignored, it also means that the coupling between diffusion and chemical reactions cannot be accounted for in the phenomenological equations for an isotropic system, as noted by Katchalsky and Curran (1965).

Equations (4.15)–(4.17) describe the coupled diffusion flux and liquid water/flow, along with the liquid/supercritical fluid pressures and chemical potential differences. Because chemical potential is not common in the geomechanics field, it would be preferred to replace it with chemical concentration c^{α} . The relation between the chemical potential and the solute mass fraction can be described as (Chen et al., 2018a):

$$\frac{\partial \mu^c}{\partial c^c} = \frac{RT}{M^c c^c}.$$
 (5.20)

The following coefficients are defined.

$$k_{abs} \frac{k_{rl}}{v^{l}} = \frac{L_{11}}{\left(\rho_{l}^{l}\right)^{2}}, r_{1} = -\frac{L_{12}}{L_{11}}, r_{2} = -\frac{L_{13}}{L_{11}}, r_{3} = -\frac{L_{21}}{L_{22}},$$

$$r_4 = -\frac{L_{23}}{L_{22}}, L^l = -\frac{L_{31}p^l}{\left(\rho_l^l\right)^2}, L^g = -\frac{L_{32}p^{Sc}}{\left(\rho_{Sc}^{Sc}\right)^2}, D = \frac{L_{33}}{c^w \rho_l^l} \frac{\partial \mu^c}{\partial c^c}$$

$$\mathbf{u}^{l} = -k_{abs} \frac{k_{rl}}{v^{l}} \left(\nabla p^{l} - r_{1} \frac{\rho_{l}^{l}}{\rho_{Sc}^{Sc}} \nabla p^{Sc} - r_{2} \rho_{l}^{l} \left(\frac{1}{c^{w}} \frac{\partial \mu^{c}}{\partial c^{c}} \nabla c^{c} \right) \right), \tag{5.21}$$

$$\mathbf{u}^{Sc} = -k_{abs} \frac{k_{rSc}}{v^{Sc}} \left(-r_3 \frac{\rho_{Sc}^{Sc}}{\rho_l^l} \nabla p^l + \nabla p^{Sc} - \rho_{Sc}^{Sc} r_4 \left(\frac{1}{c^w} \frac{\partial \mu^c}{\partial c^c} \nabla c^c \right) \right), \quad (5.22)$$

$$\mathbf{J}^{c} = -\left(\frac{L^{l} \rho_{l}^{l}}{p^{l}}\right) \nabla p^{l} - \left(\frac{L^{Sc} \rho_{Sc}^{Sc}}{p^{Sc}}\right) \nabla p^{Sc} - D \rho^{l} \nabla c^{c}, \qquad (5.23)$$

where v^{t} is the viscosity of the liquid saline water and v^{sc} is the viscosity of the supercritical flow, k_{abs} is the absolute permeability of the porous media.

5.2.4 Constitutive relations

Assuming mechanical equilibrium in the solid/rock, in whitch, $\nabla \cdot \mathbf{\sigma} = 0$, Helmholtz free energy density equation can be derived by utilizing equation (4.12) and equation (4.9) as:

$$\dot{\psi} + \psi \nabla \cdot \mathbf{v}^s - (\mathbf{\sigma} : \nabla \mathbf{v}^s) + \mu^w \nabla \cdot \mathbf{I}^w + \mu^{Sc} \nabla \cdot \mathbf{I}^{Sc} + \mu^c \nabla \cdot \mathbf{I}^c + A \dot{\xi} = 0.$$
 (5.24)

Equation (4.21) outlines the free energy density in the current configuration. By applying Fundamental principles of continuum mechanics (Wriggers, 2008) along with equation (4.11), the equation can be transformed to its reference configuration as (Chen and Hicks, 2011; Heidug and Wong, 1996):

$$\dot{\Psi} = tr\left(\mathbf{T}\dot{\mathbf{E}}\right) + \mu^{w}\dot{m}^{w} + \mu^{Sc}\dot{m}^{Sc} + \mu^{c}\dot{m}^{c} - A_{s}\dot{\varsigma}.$$
 (5.25)

where $\Psi = J\psi$, $m^{\beta} = J\rho^{\beta} = JS^{\beta}\phi\rho_{\beta}^{\beta}$, $\zeta = J\xi$. Ψ is the free energy in the reference configuration, while m^{β} represents the mass density of liquid, supercritical and chemical flow in the reference configuration, and ζ is the extent of the reaction in the reference configuration. Furthermore, \mathbf{T} is the second Piola-Kirchhoff stress tensor, \mathbf{E} is the Green strain, A_s is the solid affinity and be expressed as $A_s = v_x M^x \mu^x$. J is the Jacobian and can be expressed as $J = \frac{dV}{dV_0}$, $J = J\nabla \cdot \mathbf{v}^s$, where dV is the volume in the current configuration, and dV_0 is the volume in the reference configuration.

5.2.4.1 Helmholtz free energy density of pore space

The Helmholtz free energy density denoted as ψ^{pore} pertains to a pore containing supercritical CO_2 and saline water. In compliance with classic thermodynamics:

$$\psi^{pore} = -p^{p} + S^{l} \sum_{k} \rho_{l}^{k} \mu^{k} + S^{Sc} \rho_{Sc}^{Sc} \mu^{Sc}, \qquad (5.26)$$

 p^p is the average pressure in the pore space, and k is the chemical species (e.g., w, c). If p^p can be expressed as (Lewis and Schrefler, 1987)

$$p^{p} = p^{l}S^{l} + p^{Sc}S^{Sc} = p^{l}S^{l} + p^{Sc} - S^{l}p^{Sc},$$
 (5.27)

then equation (5.26) can be revised as

$$\psi^{\text{pore}} = -p^{l} S^{l} - p^{Sc} S^{Sc} + S^{l} \left(\mu_{l}^{w} \rho_{l}^{w} + \mu_{l}^{c} \rho_{l}^{c} \right) + S^{Sc} \mu_{Sc}^{Sc} \rho^{Sc}.$$
 (5.28)

5.2.4.2 Free energy density of the solid matrix

To calculate the free energy density stored in a solid matrix the free energy of the pore liquid/supercritical $J\phi\psi^{pore}$ is subtracted from the total free energy of the combined rock/liquid/supercritical system, Ψ (e.g., $\Psi - J\phi\psi^{pore}$). If the pore volume fraction of the reference configuration is represented as $\upsilon = J\phi$, the differential term can be expressed as follows:

$$(\Psi - J\phi\psi^{pore}) = \dot{\Psi} - (J\phi\psi^{pore}) = \dot{\Psi} - (J\phi)\psi^{pore} - J\phi\psi^{pore}.$$
 (5.29)

Equations (4.26) and (5.28) can be used to convert equation (5.29) to

$$\left(\Psi - J\phi\psi^{pore}\right) = tr\left(\mathbf{T}\dot{\mathbf{E}}\right) + p^{p}\dot{\upsilon} - A_{s}\dot{\varsigma}.$$
 (5.30)

The dual potential can be expressed as

$$W = (\Psi - J\phi^{w}\psi_{\text{pore}}) - p^{p}\upsilon. \tag{5.31}$$

By substituting equation (5.30) into the time derivative of equation (4.30), then

$$\dot{W}\left(\mathbf{E}, p^{p}, \varsigma\right) = tr\left(\mathbf{T}\dot{\mathbf{E}}\right) - \dot{p}^{p}\upsilon - A_{s}\dot{\varsigma}, \tag{5.32}$$

the total deformation energy including reaction-induced energy can be written as:

$$\dot{W}\left(\mathbf{E}, p^{p}, \varsigma\right) = \left(\frac{\partial W}{\partial E_{ij}}\right)_{p^{p}, \varsigma} \dot{E}_{ij} + \left(\frac{\partial W}{\partial p^{p}}\right)_{E_{ij}, \varsigma} \dot{p}^{p} + \left(\frac{\partial W}{\partial A_{s}}\right)_{E_{ij}, p^{p}} \dot{\varsigma}, \qquad (5.33)$$

where

$$T_{ij} = \left(\frac{\partial W}{\partial E_{ij}}\right)_{p^p,\varsigma}, \upsilon = -\left(\frac{\partial W}{\partial p^p}\right)_{E_{ij},\varsigma}, A_s = -\left(\frac{\partial W}{\partial \varsigma}\right)_{E_{ij},p^p}.$$
 (5.34)

The above equations can be considered as an extension of Maxwell's relations, where Maxwell's relations are a set of equations that relate the partial derivatives of thermodynamic state functions with respect to their conjugate variables.

The equation frameworks for the stress, pore volume fraction, and chemical potential can be written as

$$\dot{T}_{ii} = L_{iikl} \dot{E}_{kl} - M_{ii} \dot{p}^{p} - H_{ii} \dot{\zeta}, \tag{5.35}$$

$$\dot{\upsilon} = M_{ij} \dot{E}_{ij} + Q \dot{p}^p + D \dot{\varsigma},$$
 (5.36)

$$\dot{A}_{s} = H_{ij}\dot{E}_{ij} + D\dot{p}^{p} + Y\dot{\varsigma}, \tag{5.37}$$

where parameters L_{ijkl} , M_{ij} , H_{ij} , Y, D, and Q are coefficients and can be expressed as

$$L_{ijkl} = \left(\frac{\partial T_{ij}}{\partial E_{kl}}\right)_{p^p,\varsigma} = \left(\frac{\partial T_{kl}}{\partial E_{ij}}\right)_{p^p,\varsigma},$$

$$M_{ij} = -\left(\frac{\partial T_{ij}}{\partial p^{p}}\right)_{E_{ij},\varsigma} = \left(\frac{\partial \upsilon}{\partial E_{ij}}\right)_{p^{p},\varsigma},$$

$$Q = \left(\frac{\partial v}{\partial p^p}\right),$$

$$\boldsymbol{H}_{ij} = -\left(\frac{\partial T_{ij}}{\partial \varsigma}\right)_{E_{ij},p^{p}} = \left(\frac{\partial A}{\partial E_{ij}}\right)_{p^{p},\varsigma},$$

$$D = \left(\frac{\partial \upsilon}{\partial \varsigma}\right)_{E_{ij},p^{p}} = \left(\frac{\partial A}{\partial p^{p}}\right)_{E_{ij},p^{p}},$$

$$Y = \left(\frac{\partial A}{\partial \varsigma}\right)_{E_{ij},p^{p}}.$$
(5.38)

5.2.5 Governing equation for the mechanical behaviour:

Assuming small strain condition yields

expressed as

$$E_{ii} \approx \varepsilon_{ii}, T_{ii} \approx \sigma_{ii}. \tag{5.39}$$

Assuming mechanical equilibrium, it can be inferred that $\frac{\partial \sigma_{ij}}{\partial x_j} = 0$. Moreover, L_{ijkl} , M_{ij} , and Q are assumed to be material-dependent constants. Moreover, Additionally, it is assumed that the material is fully isotropic, and therefore M_{ij} is diagonal and can be

$$M_{ij} = \zeta \delta_{ij}, H_{ij} = \omega_R \delta_{ij}, \qquad (5.40)$$

where ζ is Biot's coefficient. $Q \& \zeta$ can be expressed as (Heidug and Wong, 1996):

$$Q = \frac{\zeta - \phi}{K^s}, \quad \zeta = 1 - \frac{K}{K^s}. \tag{5.41}$$

where K and K_s are the bulk modulus and the bulk modulus of the solid matrix respectively. ζ can be assumed to be 1.

 L_{ijkl} is the elastic stiffness, and it can be described as a fourth-order isotropic tensor as:

$$L_{ijkl} = G\left(\delta_{ik}\,\delta_{jl} + \delta_{il}\,\delta_{jk}\right) + \left(K - \frac{2G}{3}\right)\delta_{ij}\,\delta_{kl},\tag{5.42}$$

where G is the rock shear modulus. From the assumptions and equations (5.40) and (5.42),

$$\dot{\sigma}_{ij} = \left(K - \frac{2G}{3}\right) \dot{\varepsilon}_{kk} \,\delta_{ij} + 2G \,\dot{\varepsilon}_{ij} - \zeta \,\dot{p}^{\,p} \,\delta_{ij} - \omega_R \,\dot{\xi} \delta_{kl} \,, \tag{5.43}$$

where ω_R can be expressed in terms of the bulk modulus, K, as $\omega_R = \omega_r K$, where the dissolution-induced stress can be expressed as

$$\dot{\sigma}_r = \omega_r K \, \dot{\xi}. \tag{5.44}$$

Then,

$$\dot{\sigma}_{ij} = \left(K - \frac{2G}{3}\right) \dot{\varepsilon}_{kk} \,\delta_{ij} + 2G \,\dot{\varepsilon}_{ij} - \zeta \,\dot{p}^{\,p} \,\delta_{ij} - \omega_r K \,\dot{\xi} \delta_{kl}. \tag{5.45}$$

The volumetric strain due to dissolution can be expressed as (Tao et al., 2019)

$$\omega_r = \frac{V^s}{V_o^s} - 1 = \frac{M^x}{\rho_x^s (1 - \phi)},$$
 (5.46)

where V^s is the current solid volume (i.e., the remaining solid matrix), V_0^s is the initial solid volume (before dissolution), M^x is the molar mass of the solid mineral, and ρ_x^s is the phase density of the solid mineral.

Then, the governing equation for the solid phase can be described as:

$$G\nabla^{2}\dot{\mathbf{d}} + \left(\frac{G}{1 - 2\theta}\right)\nabla(\nabla\cdot\dot{\mathbf{d}}) - \zeta\nabla\dot{p}^{p} - \omega_{r}\nabla\dot{\xi} = 0, \tag{5.47}$$

 $c^s = \frac{\partial S^l}{\partial p^c}$ is the specific moisture capacity and $p^c = p^{Sc} - p^l$ is the capillary pressure.

The final equation is:

$$G\nabla^{2}\dot{\mathbf{d}} + \left(\frac{G}{1-2\theta}\right)\nabla\left(\nabla\cdot\dot{\mathbf{d}}\right) - \zeta\nabla\left[\left(S^{t} + c^{s}p^{c}\right)\dot{p}^{t}\right] - \zeta\nabla\left[\left(S^{sc} - c^{s}p^{c}\right)\dot{p}^{sc}\right] - \frac{M^{x}}{\rho_{x}^{x}\left(1-\phi\right)}\nabla\dot{\xi} = 0.$$
(5.48)

It is important to note that if the mineralogy changes due to chemical reactions, the overall stiffness of the rock may change including its shear modulus. However, in this research, it is assumed that the shear modulus G is a constant value and does not change during the chemical dissolution.

Note that the volumetric strain is negative because the solid volume decreases (dissolution). A change in the solid matrix can result in a change in porosity. This relation can be expressed as

$$\dot{\upsilon} = \zeta \dot{\varepsilon}_{ii} + Q \dot{p}^{p} + D \dot{\xi}. \tag{5.49}$$

where D can be expressed as

$$D = \frac{M^x}{\rho_x^x}. (5.50)$$

A change in porosity can be expressed as

$$\dot{\upsilon} = \zeta \dot{\varepsilon}_{ii} + \frac{\zeta - \phi}{K^s} \left[\left(S^l + c^s p^c \right) \dot{p}^l + \left(S^{sc} - c^s p^c \right) \dot{p}^{sc} \right] + \frac{M^x}{\rho_x^s} \dot{\xi}. \tag{5.51}$$

5.2.6 Governing equation for the fluid phase transport

Equation (4.11) can be used to describe the balance equation for the liquid fluid itself as

$$\left(\phi S^{l} \rho_{l}^{l}\right) + \phi S^{l} \rho_{l}^{l} \nabla \cdot \mathbf{v}^{s} + \nabla \cdot \mathbf{I}^{l} - \sum_{\beta \in l} \chi v^{\beta} M^{\beta} \dot{\xi} = 0.$$
 (5.52)

Equation (5.52) represent the change in density for the liquid phase, the summation part at the end of the equation take in account the change in density due to chemical reaction (aqueous reactants and products) where β accounts for liquid reactant/product only.

Equations (4.4) and (4.13) can be applied to express the Jacobian and Euler identities as $\dot{J} = J\nabla \cdot \mathbf{v}^s$, $\upsilon = J\phi$. Moreover, equation (4.18) can be used to obtain the following equation:

$$\dot{S}^{l}\upsilon\rho_{l}^{l}+S^{l}\left(\zeta\dot{\varepsilon}_{ii}+Q\dot{p}^{p}+D\dot{\xi}\right)\rho_{l}^{l}+S^{l}\upsilon\dot{\rho}_{l}^{l}$$

$$+\nabla \cdot \rho_{l}^{l} \left[-k_{abs} \frac{k_{d}}{v^{l}} \left(\nabla p^{l} - r_{1} \frac{\rho_{l}^{l}}{\rho_{Sc}^{Sc}} \nabla p^{Sc} - r_{2} \rho_{l}^{l} \left(\frac{1}{c^{w}} \frac{\partial \mu^{c}}{\partial c^{c}} \nabla c^{c} \right) \right) \right] - \left(v_{y} M^{Y} \mu^{Y} - v_{z} M^{Z} \mu^{Z} \right) = 0.$$

$$(5.53)$$

The displacement variables, d_i (i = 1, 2, 3), through $\varepsilon_{ij} = \frac{1}{2} (d_{i,j} + d_{j,i})$ can be revised as

$$\delta_{ij}\dot{\varepsilon}_{ii} = \nabla \cdot \dot{\mathbf{d}}. \tag{5.54}$$

Using equations (5.27), (5.49), and (5.54) yields

$$\zeta S^{l} \rho_{l}^{l} \nabla \dot{\mathbf{d}} + \frac{\zeta - \phi}{K^{s}} S^{l} \rho_{l}^{l} (S^{l} + c^{s} p^{c}) \dot{p}^{l} + \frac{\zeta - \phi}{K^{s}} S^{l} \rho_{l}^{l} (S^{sc} - c^{s} p^{c}) \dot{p}^{sc}$$

$$+ S^{l} \rho_{l}^{l} D \dot{\xi} + \dot{S}^{l} \upsilon \rho_{l}^{l} + S^{l} \upsilon \rho_{l}^{l} + S^{l} \upsilon \rho_{l}^{l} \frac{1}{K^{w}} \dot{p}^{l} + \nabla \cdot \rho_{l}^{l} \left[-k_{abs} \frac{k_{rl}}{v^{l}} \left(\nabla p^{l} - r_{l} \frac{\rho_{l}^{l}}{\rho_{Sc}^{sc}} \nabla p^{sc} - r_{2} \rho_{l}^{l} \left(\frac{1}{c^{w}} \frac{\partial \mu^{c}}{\partial c^{c}} \nabla c^{c} \right) \right) \right]$$

$$- J \left(v_{y} M^{y} \mu^{y} - v_{z} M^{z} \mu^{z} \right) = 0. \tag{5.55}$$

Finally, if J = 1 (small deformation), the final liquid governing equation for the liquid is given as

$$\zeta S^{l} \nabla \cdot \dot{\mathbf{d}} + \left(\frac{\zeta - \phi}{K^{s}} S^{l} S^{l} + S^{l} \frac{\phi}{K^{w}} \right) \dot{p}^{l} + \frac{\zeta - \phi}{K^{s}} S^{l} S^{sc} \dot{p}^{sc} + \left(-\frac{\zeta - \phi}{K^{s}} S^{l} p^{c} + \phi \right) \dot{S}^{l} + \frac{M^{x}}{\rho_{x}^{x}} S^{l} \dot{\xi} \\
+ \left[-k_{abs} \frac{k_{rl}}{v^{l}} \left(\nabla^{2} p^{l} - r_{1} \frac{\rho_{l}^{l}}{\rho_{sc}^{sc}} \nabla^{2} p^{sc} - r_{2} \rho_{l}^{l} \frac{1}{c^{w} c^{c}} \frac{RT}{M^{c}} \nabla^{2} c^{c} \right) \right] - \frac{\left(v_{y} M^{y} \mu^{y} - v_{z} M^{z} \mu^{z} \right)}{\rho_{l}^{l}} = 0. \\
(5.56)$$

Similarly, for the supercritical phase,

$$\zeta S^{Sc} \nabla \cdot \dot{\mathbf{d}} + \left(\frac{\zeta - \phi}{K^{S}} S^{Sc} S^{Sc} + S^{Sc} \frac{\phi}{K^{Sc}} \right) \dot{p}^{Sc} + \frac{\zeta - \phi}{K^{S}} S^{Sc} S^{I} \dot{p}^{I} + \left(\frac{\zeta - \phi}{K^{S}} S^{Sc} p^{c} + \phi \right) \dot{S}^{Sc} + \frac{M^{x}}{\rho_{x}^{x}} S^{I} \dot{\xi}$$

$$+ \left[-k_{abs} \frac{k_{rSc}}{v^{Sc}} \left(\nabla^{2} p^{Sc} - r_{3} \frac{\rho_{Sc}^{Sc}}{\rho_{I}^{I}} \nabla^{2} p^{I} - r_{4} \rho_{Sc}^{Sc} \frac{1}{c^{w} c^{c}} \frac{RT}{M^{c}} \nabla^{2} c^{c} \right) \right] = 0.$$
(5.57)

Equation (5.57) disregards the chemical reaction between CO_2 and solid phases because previous studies have shown that such reactions are slow and limited in the presence of gaseous or supercritical CO_2 (Lackner et al., 1995; André et al., 2007a; Han et al., 2015).

Instead, this study focuses solely on the chemical reaction between the fluid phase and solid phase, assuming that the reaction occurs only between the aqueous and solid phases when CO_2 dissolves in water to form carbonic acid. As a result, the direct chemical reaction between CO_2 in its supercritical phase and solid minerals can be neglected. Nevertheless, while the chemical reaction does not change the gaseous mass or density, it changes the porosity and hence affect the gas transport.

5.2.7 Governing equation for the chemical phase transport

Using equation (4.11), then

$$\left(\phi^{k} \rho_{l}^{k}\right) + \phi^{k} \rho_{l}^{k} \nabla \cdot \mathbf{v}^{s} + \nabla \cdot \mathbf{I}^{k} - \chi v^{k} M^{k} \dot{\xi} = 0, \tag{5.58}$$

for small deformation (J = 1), with equation (5.6),

$$\left(\phi S^{l} \rho_{l}^{k}\right) + \nabla \cdot \mathbf{J}^{k} + \nabla \cdot \left(\rho_{l}^{k} \mathbf{u}^{l}\right) - \chi v^{k} M^{k} \dot{\xi} = 0, \tag{5.59}$$

The liquid phase is assumed to be incompressible, , if the mass fraction is defined as $c^k = \frac{\rho_l^k}{\rho_l^l}$, then the chemical transport governing equation for the solute can be expressed

as

$$\phi S^{l} \rho_{l}^{l} \dot{c}^{k} + \nabla \cdot \mathbf{J}^{k} + \rho_{l}^{l} \mathbf{u}^{l} \cdot \nabla c^{k} - \chi v^{k} M^{k} \dot{\xi} + c^{k} \sum_{k} \chi v^{k} M^{k} \dot{\xi} = 0.$$

$$(5.60)$$

where the superscript is the different chemical solutes in general form.

The key novelty of this study lies in the incorporation of additional terms into the mechanical, liquid, and gas/supercritical phases. To the best of our knowledge, these

terms have never been used in two-phase flow governing equations to couple chemical reactions to a hydromechanical model for carbon capture and storage applications.

For the mechanical equation (5.48), the term $\frac{M^x}{\rho_x^x(1-\phi)}\nabla\dot{\xi}$ represents the effect of chemical reactions on the strain, providing relief for the strain in dissolution cases. In the liquid and gas/supercritical phases, $\frac{M^x}{\rho_x^x}S^t\dot{\xi}$ is derived from $D\dot{\xi}$, which is the coupling effect of chemical reactions on porosity. This term reflects the impact of chemical reactions on liquid and gas/supercritical flows through changes in porosity. Equation (5.51) shows that porosity is also affected by changes in pressure and strain. For the liquid phase, $(v_y M^y \mu^y - v_z M^z \mu^z)$ represents the chemicals added to the aquatic phase resulting from solid dissolution in liquid flow. Figure 5.1 demonstrates some of the cross-coupling relations of the HMC coupled model.

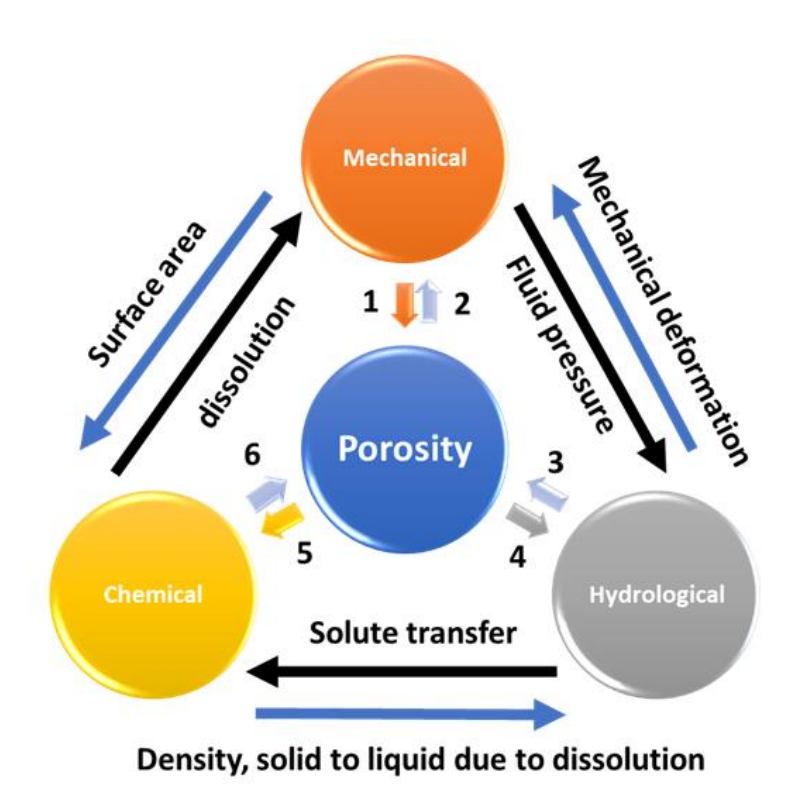


Figure 5.1: Cross couplings relations of the HMC model: 1. Change due to strain term $\zeta \dot{\varepsilon}_{ii}$, 2. Effect the mechanical properties, 3. Change due to pore pressure term $Q\dot{p}^p$, 4. Effect the pore pressure, 5. Change due to chemical reaction term $D\dot{\xi}$, 6. Change in reactive surface area

5.3 Validation and comparison with other models

The final governing equation (5.48) for the solid, equation (5.56) for the liquid, and equation (5.57) for the supercritical phases present more comprehensive framework based on a rigorous mathematical derivation. This is in contrast to the equations presented by Abdullah et al. (2022), which serve as a special case of the present study, excluding considerations of dissolution and dynamic porosity. When compared with the renowned two-phase transport model by Schrefler and Scotta (2001), the fluid equations exhibit similarities. However, their model omits the effects of chemical reactions (dissolution), solute transport, and energy losses due to friction between the two-phase flow; barring these elements, the equations appear congruent Notably, the chemical dissolution term in

the equations parallels that in the governing equation of (Yue et al., 2022), where onephase transport dissolution effects are captured. This is also in line with the governing
equation modelled by (Karrech, 2013). Fall et al. (2014a) did account for a two-phase
flow but regrettably overlooked the chemical reaction aspect. Their governing equation
resonates with the one proposed in this study, but it lacks the chemical reactive term.

Conversely, their model can manage the effects of plasticity, which is not considered in
the present model. In summary, the governing equation introduced in this study
incorporates basic two-phase flow coupling terms, as validated in previous research by
Lewis and Schrefler (1987), Schrefler and Scotta (2001), and Abdullah et al. (2022).

Additionally, this equation integrates chemical dissolution effects, which have been
partially addressed in single-phase flow studies such as those by Karrech (2013) and (Ma
et al., 2022b). For further refinement, it would be beneficial to test these equations against
empirical data in future studies, enhancing our understanding of the coefficients'
empirical values.

The following simulation investigates the fully coupled effect, focusing on the coupling effect of pressure, strain, and chemical dissolution on porosity change.

5.4 Numerical simulation

Numerical simulations will be used for the demonstration purpose of the novel coupled equations derived in this paper. In the numerical section the focus will be on how the chemical reaction will affect the two-phase pressure, saturation, strain and porosity. To simplify the discussion, only one chemical reaction leading to dissolution is considered. Additionally, as the objective of the simulation is to emphasize the novel aspects of the equations, and since the presence of salt in saline water does not significantly affect the

chemical reaction, the simulation will employ pure water instead of saline water to exclude any potential confounding effects of salt. The primary chemical reaction has been described in (Zerai et al., 2006) as follows:

$$CaCO_3 + H_2O + CO_2 \Rightarrow Ca^{2+} + 2HCO_3^{-}. \tag{5.61}$$

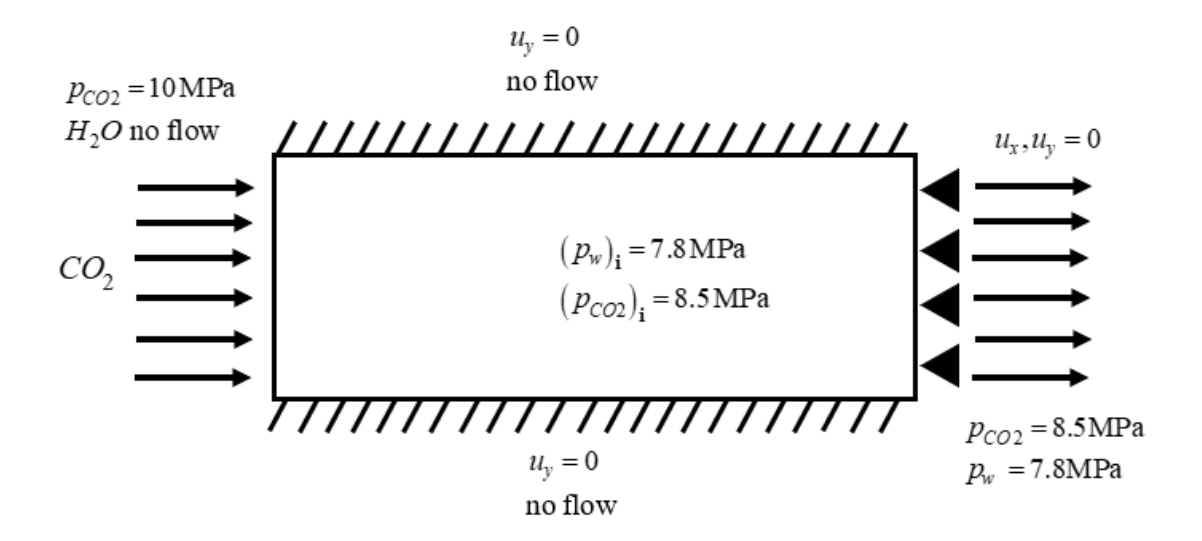
In the numerical model, the dissolution of CO₂ is not simulated, as it is assumed that a large amount of CO₂ is already dissolved in the saline water before the simulation begins (i.e., at t=0This means that the liquid phase is mainly a carbonic acid solution. This assumption, explained in Section IV, simplifies the handling of CO₂ in the system. In the COMSOL setup, the "Transport of Diluted Species" interface is used to model the movement and distribution of solutes, representing the dissolved species without the need to simulate the dissolution process. This method keeps the simulation efficient while still capturing the key behaviour of solute transport in the system.

Moreover, In addition to the term $\frac{M^x}{\rho_x^x(1-\phi)}\nabla\dot{\xi}$ in the general governing equation for the solid phase, three primary coupling terms have a direct implication on two-phase flow through porosity change, as described in equation (5.51). These terms are mechanical strain, pore pressure, and chemical reaction.

5.4.1 Study subject and geometry

To investigate the effects of these terms, a conceptual model, consisting of a block of carbonate rock that contained calcite, with dimensions of 50 cm in length and 20 cm in height, has been created. CO_2 under supercritical conditions is injected through the semi-

saturated sample rock that has an initial water saturation of $\left(S^{w}\right)_{i}$ =61.9% for a time t. The system is assumed to be under isothermal condition with a temperature of $T=350~\mathrm{K}$. Figure 5.2 shows the initial and boundary conditions of the system and the mesh geometry/horizontal cross section line along with cut point 1.



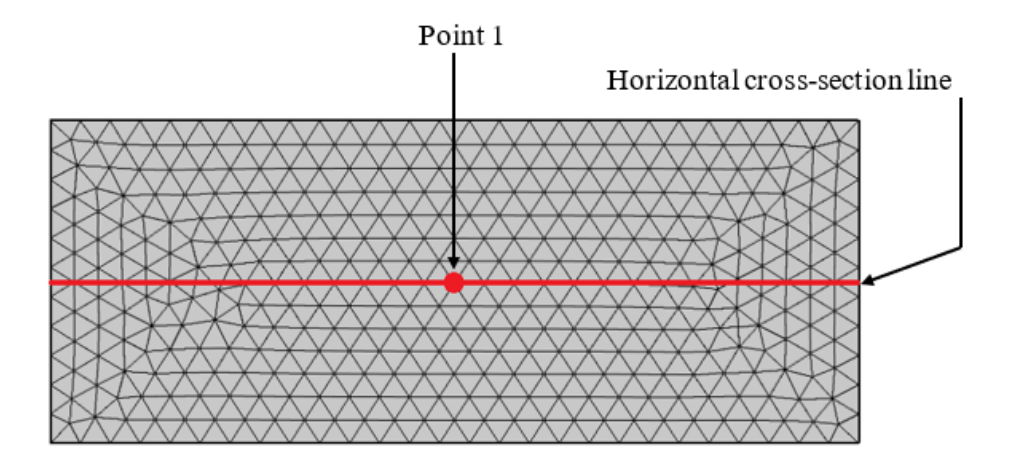


Figure 5.2: Initial and boundary conditions for two-phase flow into carbonate rock sample.

The dissolution of calcite by CO₂ has been extensively investigated (Plummer and Wigley, 1976; Gaus et al., 2005; Kaufmann and Dreybrodt, 2007; Izgec et al., 2008;

Matter et al., 2009; Xu et al., 2010; Van Pham et al., 2012; Peng et al., 2015; Gray et al., 2016; Siqueira et al., 2017). Calcite usually exists widely in limestone formation but not in other formations with less quantity, such as in shale formations (Gaus et al., 2005), carbonate deep saline aquifers (Izgec et al., 2008), and basaltic rocks (Van Pham et al., 2012). This model is assumed to be a calcite-rich rock. The parameters used in the model are listed in Table 1. A finite element general solver (COMSOL Multi-Physics®) is used to solve the system. The reaction rate (dissolution rate) is highly dependent on the temperature and pH level in the fluid (Matter et al., 2009). The kinetics of the reaction rate is expressed as (Steefel and Lasaga, 1994)

$$r = k_{rate} A rea \left(1 - \left(\frac{Q}{K_{eq}} \right)^{\theta} \right)^{n}, \qquad (5.62)$$

The variable r in the equation above represents the rate of dissolution in moles per unit volume of porous media, Area is the reaction surface area, Q is the C_a^+ ions activity product, K_{eq} is the equilibrium constant, θ and n are constants, which are set as 1, and k_{me} is the dissolution rate constant defined as (Steefel and Lasaga, 1994)

$$k_{rate} = k_{r25} \exp \left[-\frac{E_a}{R} \left(\frac{1}{T} - \frac{1}{298.15} \right) \right],$$
 (5.63)

where k_{r25} is the rate constant at 25° C, E_a is the activation energy, R is the gas constant, and T is the temperature (T=350K). The following correlation can be used to calculate the equilibrium constant for calcite minerals at given temperature (Plummer and Busenberg, 1982):

$$\log\left(K_{eq}\right) = -1228.732 - 0.299444\left(T\right) + \frac{35512.75}{T} + 485.818 \times \log(T). \quad (5.64)$$

According to (Gaus et al., 2005; Lee and Morse, 1999), the reactive surface area for calcite in limestone Area is approximately $6.71\times10^{-2}~m^2/g$. The molar volume of calcite is $36.93\times10^{-6}~m^3/mol$. E_a and k_{r25} have been extracted from literature as $k_{r25}=1.6\times10^{-9}~mol~m^2s^1$ and $E_a=41.87~kJ/mol$ (Xu et al., 2003).

Table 5.1: Physical parameters used in the conceptional model (Zhou and Burbey, 2014b; Hart and Wang, 1995; Parkhurst and Appelo, 2013).

| Physical meaning | Values and units |
|--|--|
| Young's modulus (Limestone) | $E = 33 \times 10^3 \text{MPa}$ |
| Toung's modulus (Ennestone) | |
| Liquid density | $\rho_l^l = 1000 \mathrm{kg/m}^3$ |
| CO_2 density (Sc) | $\rho_{Sc}^{Sc} = 660 \mathrm{kg/m^3}$ |
| Solid density | $\rho^s = 2600 \mathrm{kg/m^3}$ |
| Poisson's ratio | θ = 0.26 |
| Biot's coefficient | $\zeta = 1$ |
| Porosity | $\phi = 0.123$ |
| Dynamic viscosity of liquid | $v^l = 1 \times 10^{-3} \mathrm{Pa}\mathrm{s}$ |
| Dynamic viscosity of CO_2 (Sc) | $v^{Sc} = 6 \times 10^{-5} \mathrm{Pa}\mathrm{s}$ |
| Bulk modulus of liquid | $K_{t} = 2.2 \times 10^{3} \text{ MPa}$ |
| Bulk modulus of CO_2 (Sc) | $K_{Sc} = 58 \text{MPa}$ |
| Bulk modulus of solid | $K_s = 74 \mathrm{GPa}$ |
| CaCO ₃ chemical rate constant | $k_{rate} = 1.6 \times 10^{-9} \text{ mol/m}^2/\text{s}$ |
| Specific surface area | $A = 6.71 \times 10^{-2} \mathrm{m}^2/\mathrm{g}$ |

For liquid saturation calculations, the Van Genuchten relationship is used. This relationship is a widely used model in soil science and hydrology that describes the relationship between the volumetric water content of soil and soil water potential. It can be used to predict water movement in soils and rocks, estimate soil hydraulic properties, and simulate soil—water—plant interactions, as in the following (Ma et al., 2020a):

$$k_{rl} = (S^{l})^{0.5} \times \left[1 - \left(1 - \left(S^{l}\right)^{\frac{1}{m}}\right)^{m}\right]^{2},$$
 (5.65)

$$k_{rSc} = (1 - S^{T})^{0.5} \times \left[1 - \left(1 - \left(1 - S^{T} \right)^{\frac{1}{m}} \right)^{m} \right]^{2},$$
 (5.66)

$$S^{l} = \left[\left(\frac{\left| p^{c} \right|}{M} \right)^{\frac{1}{1-m}} + 1 \right]^{-m}, \tag{5.67}$$

where M and m are Van Genuchten parameters related to pore size and shape. For this simulation, the values have been estimated as $M = 500 \,\mathrm{kPa}$ and m = 0.43 (Rutqvist et al., 2002; Van Genuchten, 1980a).

Finally, the change in permeability can be obtained using Kozeny-Carman relation (Bitzer, 1996; Xu et al., 2003):

$$k_{abs} = \left(k_{abs}\right)_i \times \left(\frac{\phi}{\phi_i}\right)^3 \left(\frac{1-\phi_i}{1-\phi}\right)^2$$
 (5.68)

where $(k_{abs})_i$ and ϕ_i are the initial instinct permeability and initial porosity respectively.

5.4.2 Simulation assumptions:

For the simulation, assumptions are made to ensure stability and simplify some computational issues: (I) the rock is assumed to have a high percentage of calcite, which maintains the dissolution reaction for the entire simulation time; (II) the energy dissipation due to solute transport and the friction between the two-phase flow are zeros $(r_1, r_2, r_3, \text{ and } r_4 \text{ in equations } (5.56) \text{ and } (5.57) \text{ are zeros})$; (III) because the sample is small in size and reaches the equilibrium phase rapidly, the initial intrinsic permeability is assumed to be extremely small $(k_{abs} = 1.4 \times 10^{-17} \text{ m}^2)$ in order to hold back the pressure for a longer time; (IV) although the liquid in the formation is assumed to contain dissolved CO_2 (carbonic acid), the properties of the liquid have been approximated as those of liquid water.

5.4.3 Results and discussion

This study simulates the two-flow injection for 2000 h. Figure 5.3, Figure 5.4, and Figure 5.5 show the liquid pressure, supercritical pressure, and solid deformation, respectively, across the sample distance. Because the sample size is relatively small, the simulation time is approximately 2000 h or 83.3 d. The liquid and supercritical pressures show the increase in the pressure across the sample rocks before it stabilises. Because of the assumed chemical reaction in equation (5.61), part of the solid matrix is dissolved, suggesting that the porosity will continue to increase until the solubility equilibrium is reached. Figure 5.5 presents the horizontal displacement within the cross-section line

(shown in Figure 5.2) of the sample rock. The displacement starts at a higher value and decreases with time, this is because the differential pressure is high at the beginning especially at the left boundary, then, the pressure starts to equalize through the pores of the specimen and therefore the displacement decrease. Furthermore, the deformation is relatively small because the Young's modulus is high (33 GPa).

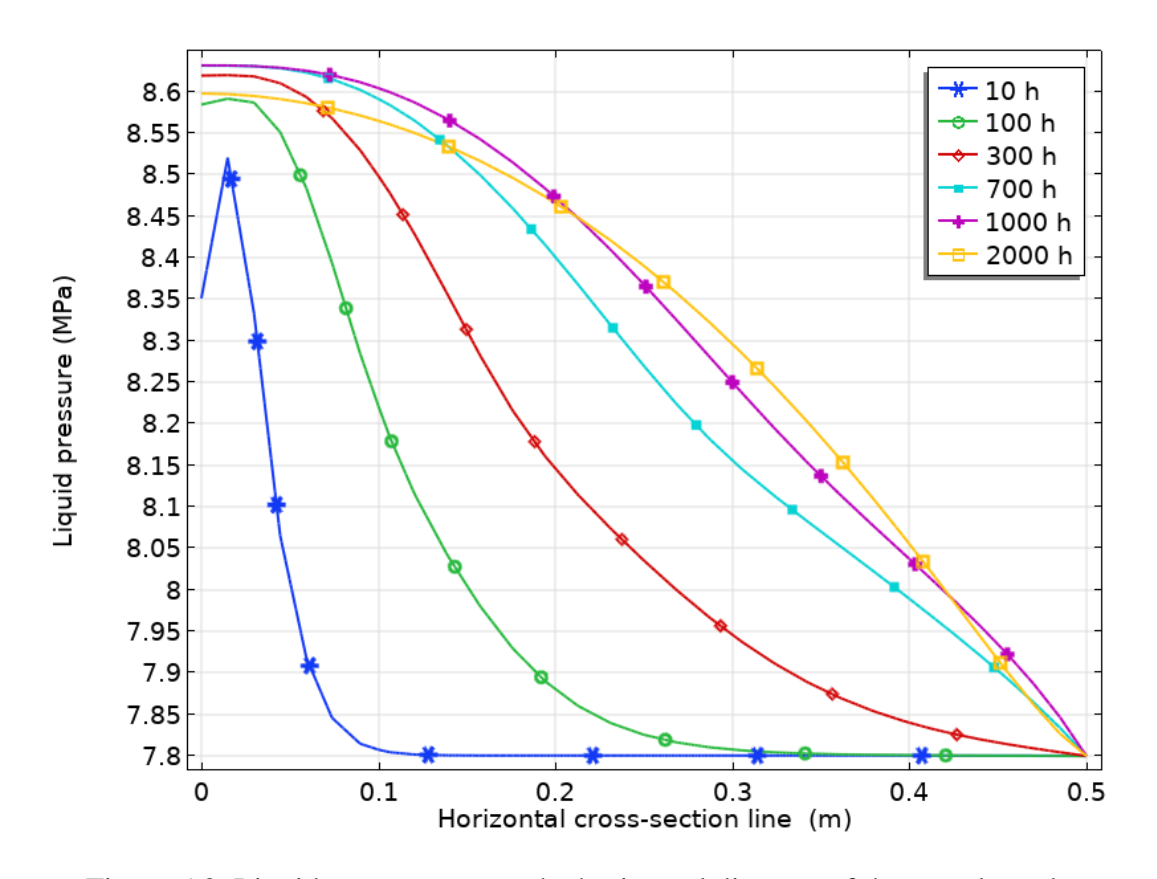


Figure 5.3: Liquid pressure across the horizontal distance of the sample rock.

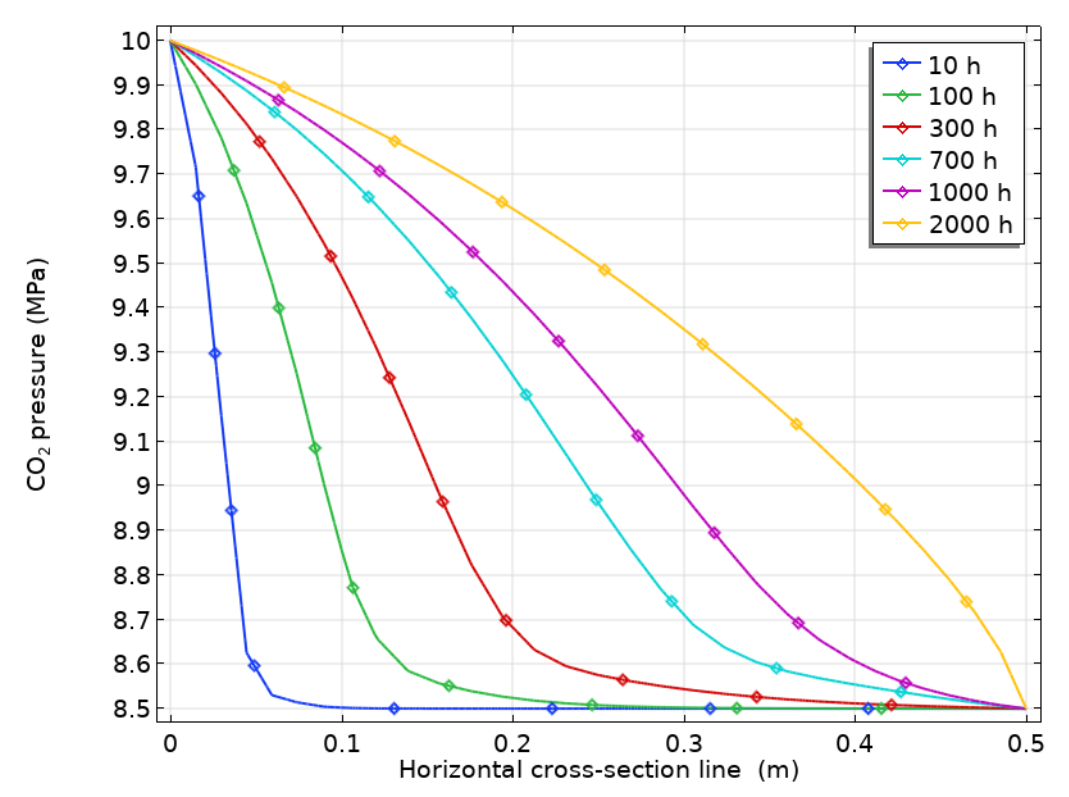


Figure 5.4: CO₂ pressure across the horizontal distance of the sample rock.

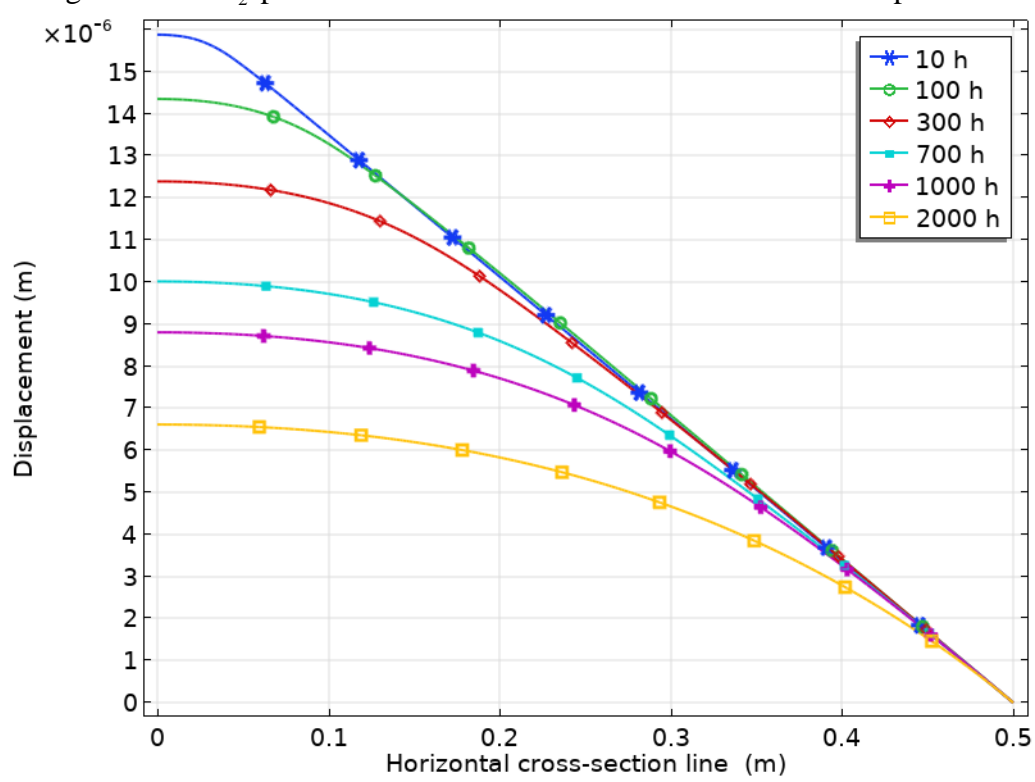


Figure 5.5: Horizontal displacement across the horizontal distance of the sample rock.

Figure 5.6 displays the concentration of calcium ions that dissolve in the sample rock at different time spans. The initial value of the concentration on the left boundary was assumed to be zero. Thus, the concentration started at zero and increased while moving to the right side of the sample. As expected, the concentration increased with time during the chemical reaction and calcium ions increased. It is important to note that, in this case, even though CO₂ dissolution was not considered, factors other than saturation influenced the uneven distribution of calcium ions. Specifically, the coupling between porosity and permeability plays a role. As dissolution increases, porosity and permeability also increase, which enhances flow (related to Darcy's law and liquid flux) and, in turn, affects the calcium ion concentration.

Figure 5.7-8 depicts the liquid and supercritical CO_2 saturation distribution across the sample rock cross-section at different times. At the start of the simulation, the water/liquid saturation starts at 61.9% and then the CO_2 starts to flow from the left side to the right, and the liquid saturation starts to decrease. The liquid saturation in this study is completely dependent on the capillarity pressure, p^c , as per Van Genuchten (1980a) relations shown in equations (5.65)–(5.67). Figure 5.9 shows the change in porosity and permeability over time at Point 1, which is located in the middle of the sample. The results show that the permeability at this point will almost double within 2000 hours.

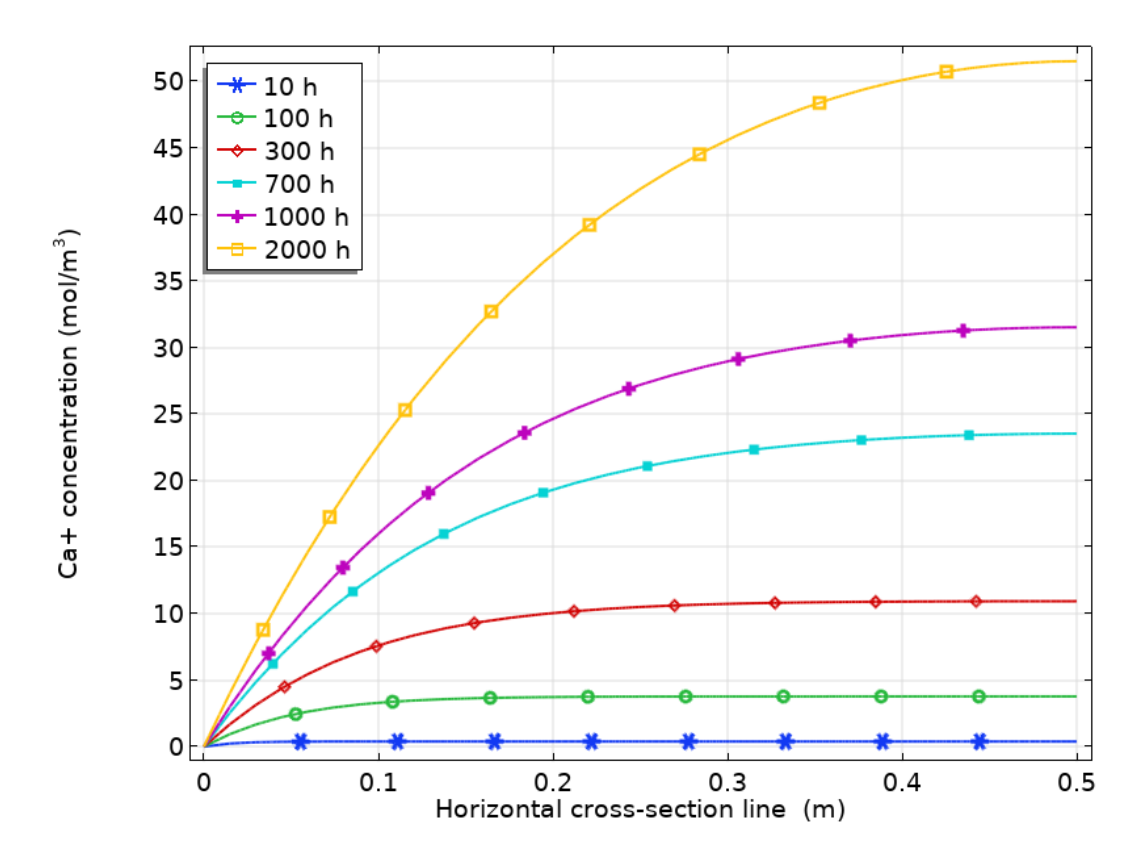


Figure 5.6: Concentration of Ca⁺ across the horizontal distance of the sample rock.

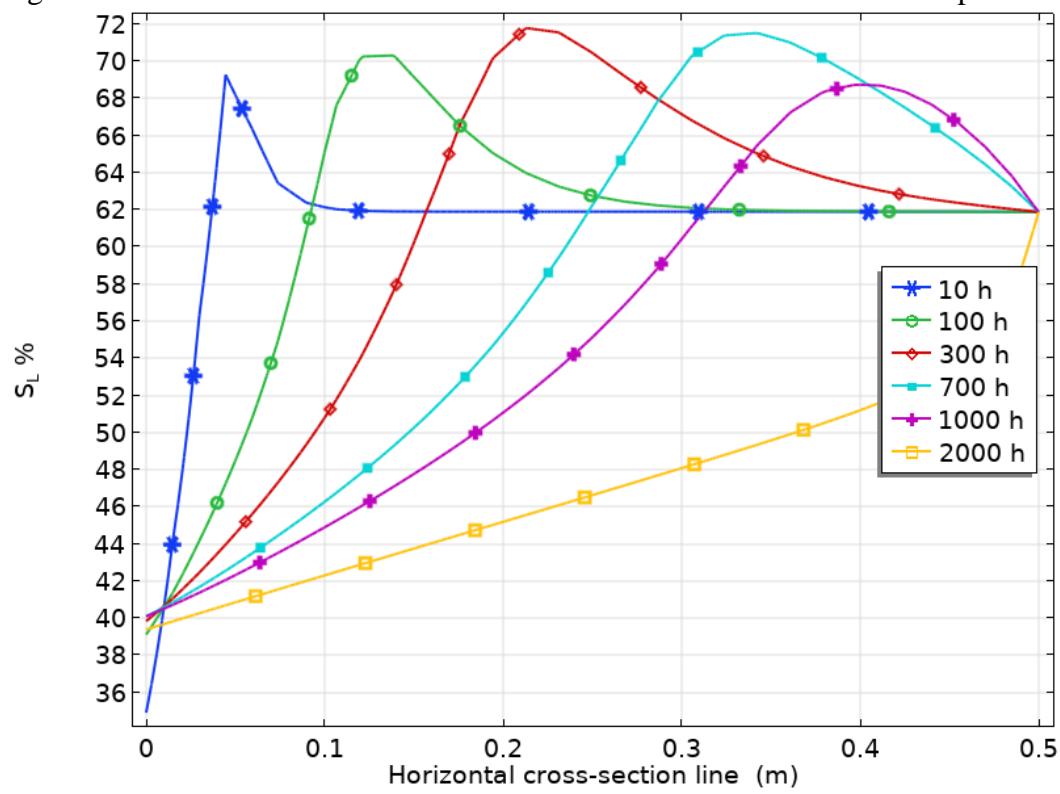


Figure 5.7: Liquid saturation across the horizontal distance of the sample rock.

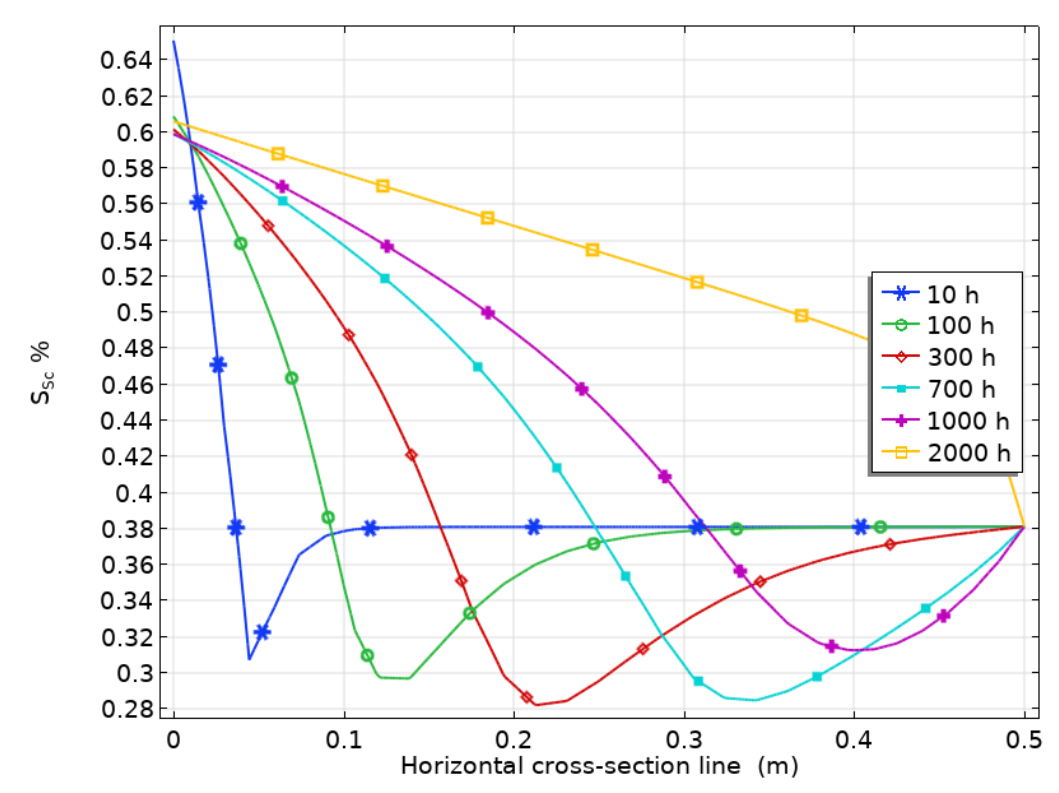


Figure 5.8: ScCO₂ saturation across the horizontal distance of the sample rock.

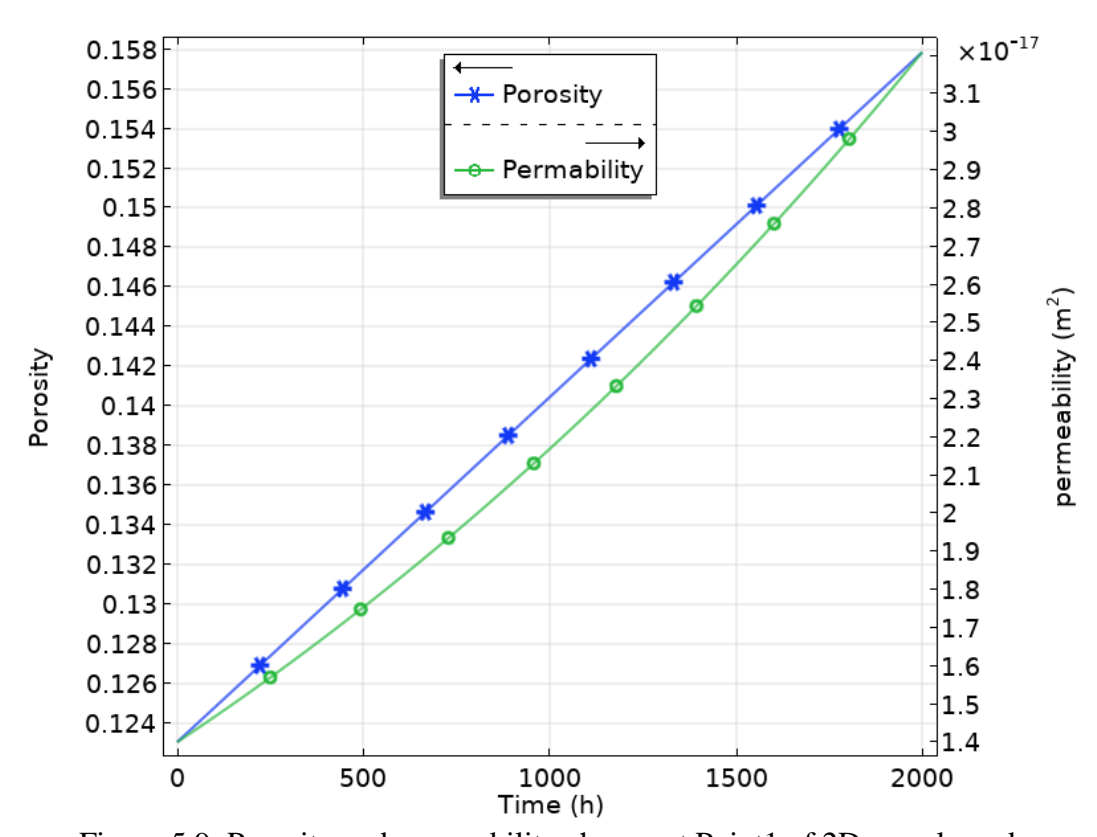


Figure 5.9: Porosity and permeability change at Point1 of 2D sample rock.

Figure 5.10 and Figure 5.11 show the three primary factors influencing porosity change according to equation (50). Compared with pressure and mechanical strain, the chemical reaction has the greatest impact on porosity. Figure 5.10 presents a comparison between the chemical coupling term and the strain term, $\zeta \dot{\varepsilon}_{ii}$, indicating that the chemical reaction has a more significant impact on porosity change than mechanical strain. Similarly, Figure 5.11 presents a comparison between the chemical term and the pressure term, $Q\dot{p}^p$ showing that the chemical reaction has a greater effect on porosity than pressure. The effects of the pressure and strain terms are relatively similar, compares the effects of liquid pressure, supercritical pressure, and the extent of reaction on the volumetric strain at Point 1 in the 2D rock sample. As the strain increases, the extent of reaction undergoes exponential changes, emphasizing the importance of considering the coupling between chemical reactions and mechanical behavior. In Figure 5.13 it can be seen that the dissolution rate at across the horizontal section of the sample decreases as it approaches kinetic equilibrium. Whilst the simulation results from this model are insightful, assumptions underpinning the model introduce certain limitations. Key among these is the presumption that the chemical solute exists solely in the liquid phase (saline water) and remains chemically inert, with the supercritical phase of CO₂ also being treated as non-reactive. This implies that any interactions between the supercritical and solid phases are not captured by the model. Further, the system is considered immiscible, meaning that there's no mass exchange between the liquid and supercritical phases via dissolution. This phenomenon, which is anticipated to be prevalent in actual carbon sequestration processes, is interlinked with temperature changes and variations in the pH levels of the liquid phase, both of which influence the rate of chemical reactions. An additional limitation arises from the model's assumption of isothermal conditions and treating the porous medium as an isotropic material, potentially deviating from real-world scenarios. Moreover, in reality, after injecting CO_2 for a long period of time, the amount of calcite in the formation will start to decrease, which would slow down the chemical reaction. However, to keep things simple, it has been assumed that the calcite remains stable, so this deceleration in the increase of porosity is not shown in the plot. Such a process usually takes much longer in large reservoirs (possibly thousands of years) and would not be noticeable in this 2,000-hour simulation test.

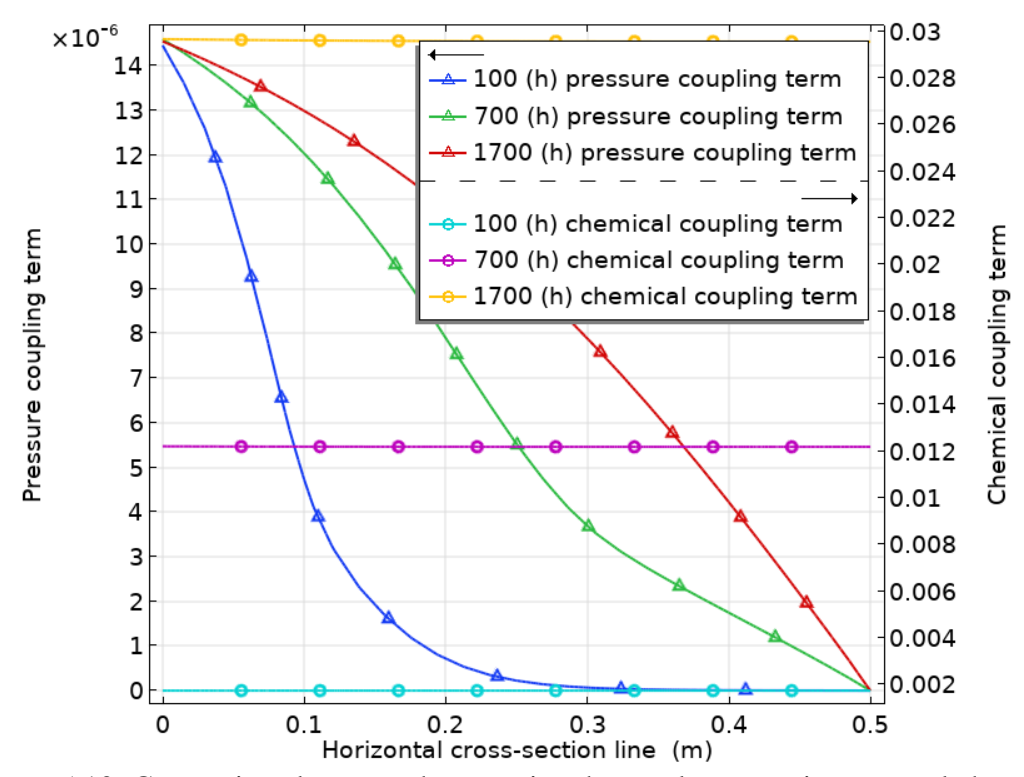


Figure 5.10: Comparison between the porosity change due to strain term and chemical reaction term across the horizontal distance of the sample rock.

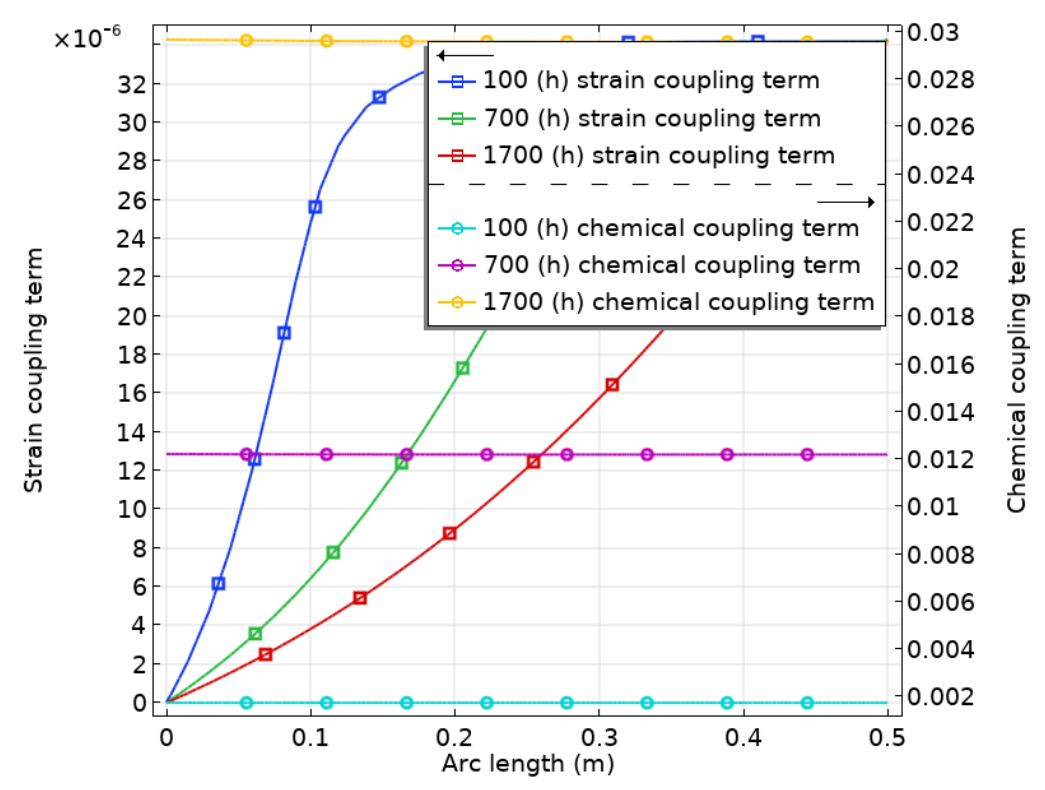


Figure 5.11: Comparison between the porosity change due to pressure term and chemical reaction term across the horizontal distance of the sample rock.

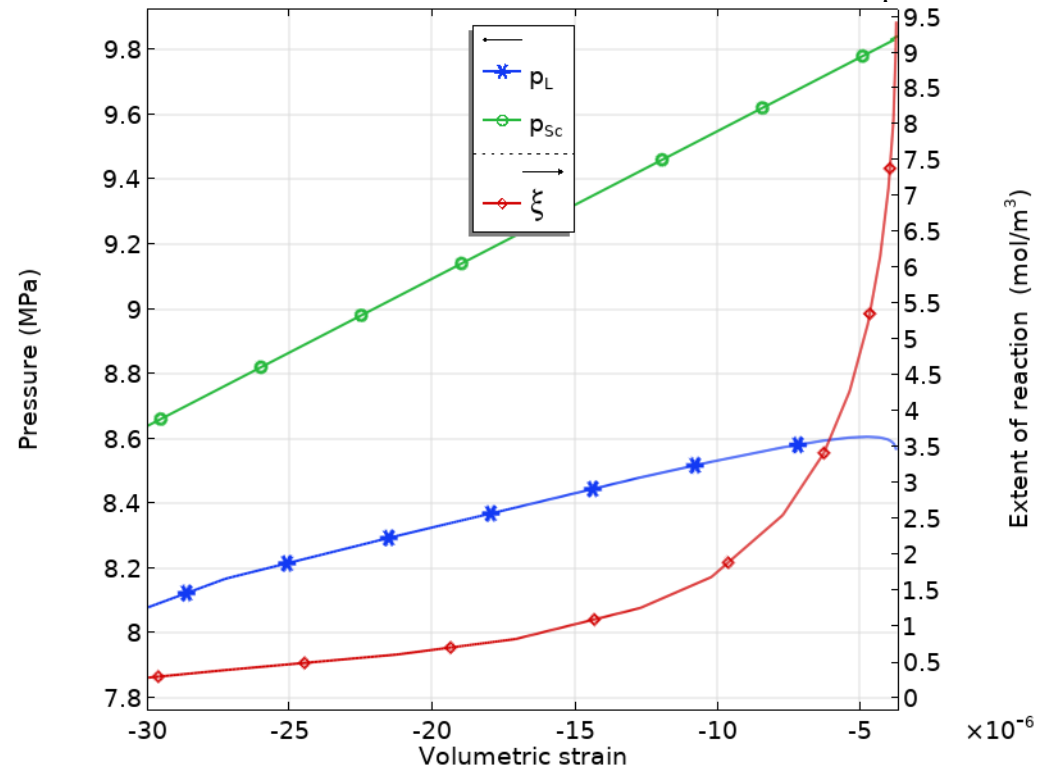


Figure 5.12: Effects of liquid pressure, supercritical pressure, and the extent of reaction on the volumetric strain at Point 1 in the 2D rock sample.

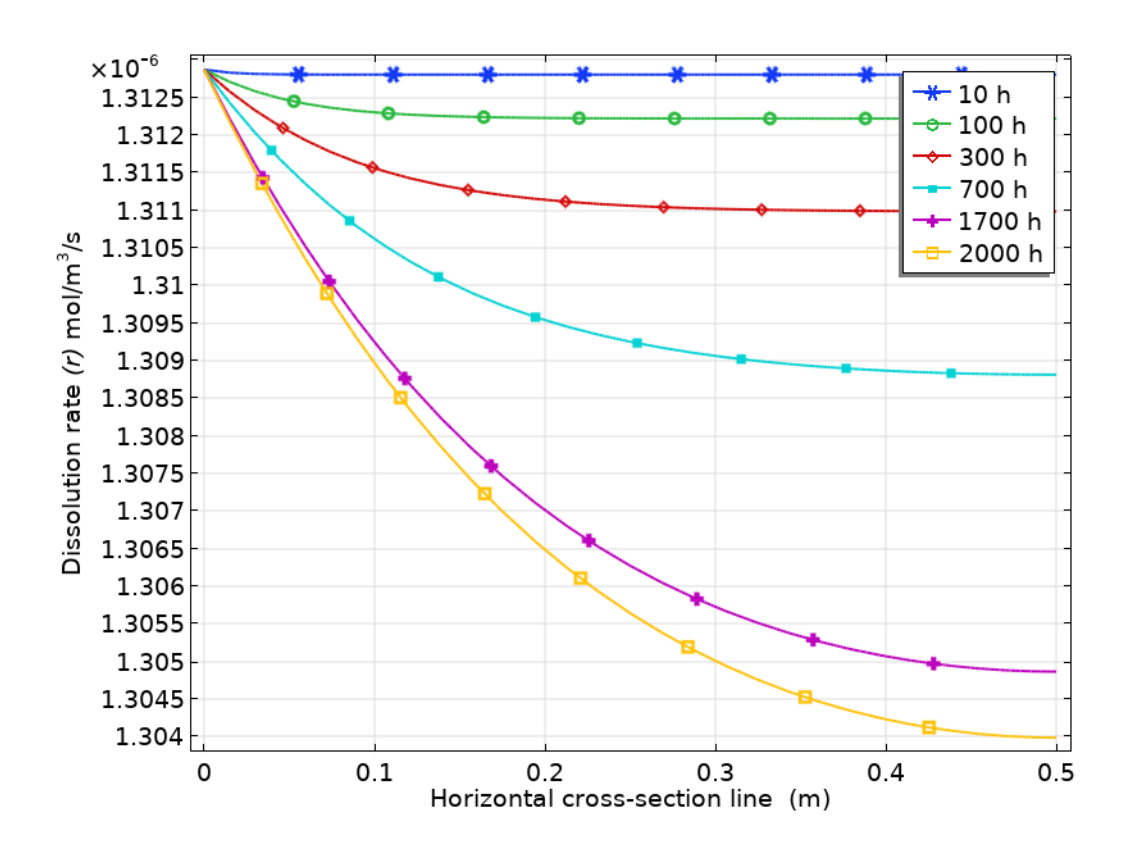


Figure 5.13: Dissolution rate at across the horizontal section of the sample rock.

5.5 Conclusion

In this study, a novel approach for modelling a reactive multi-phase hydro-mechanical chemical system for CO₂ sequestration using coupling mixture theory was presented. Addressing the gap in the coupled relationship between chemical and mechanical properties, it has been linked to stress/strain. The extent of the reaction and solid affinity were employed in the model, spotlighting the interplay of chemical reactions within the hydromechanical framework.

Simulations under isothermal conditions on limestone rock samples highlighted the significant role of chemical reactions in dictating changes in porosity and mechanical strain within geological formations. Observable changes in liquid pressure, supercritical pressure, solid deformation, and porosity over time emphasized the primary influence of

chemical reactions. This research serves as a foundational benchmark for the carbon sequestration domain. Offering a holistic lens, it enables professionals and researchers to better understand chemical reactions' influence on the hydromechanical attributes of geological formations, paving the way for more strategic carbon sequestration decisions. Although only one chemical reaction is included in this formulation, additional reactions can be incorporated using the same approach by following the outlined steps.

While promising, the proposed model operates under certain constraints, notably assumptions of zero energy dissipation due to solute transport, friction between the two-phase flow, and the approximation of liquid properties to water. Future research should investigate the integrating of thermal coupling, precipitation processes, and accounting for mass transfer between gas and the liquid phase to further refine the model's precision and applicability.

While the hydro-mechanical (HM) coupling was validated in previous chapters, the chemical reactive coupling in this chapter has not yet been validated against experimental data. The validation of the chemical coupling in this chapter relies primarily on the rigorous derivation process. The conceptual model simulation presented here serves as a verification tool to ensure that the chemical coupling effects behave logically. For instance, over time, increased dissolution leads to an increase in porosity, which in turn raises permeability, and the ion distribution follows expected patterns. Other aspects of the model, such as the evolution of concentration gradients (e.g., Ca²⁺ ion distribution), also align with theoretical predictions.

Currently, the coupled model is capable of capturing multi-phase transport, energy dissipation from two-phase interactions, energy loss from solute transport, chemical

reactions (specifically dissolution), and changes in porosity and permeability. However, the model operates under isothermal conditions, which may not accurately reflect the real-world scenario of CCS, where the deep formation aquifer has a different temperature than the injected fluid. To address this limitation, the next chapter will introduce heat transfer coupling to the model to account for non-isothermal conditions. Furthermore, the impact of this thermal coupling will be thoroughly investigated to assess its influence on the overall process of mixture transfer.

Chapter 6: The Impact of Thermal Transport on Reactive THMC Model for Carbon Capture and Storage

Abstract

Addressing current limitations in Thermo-Hydro-Mechanical-Chemical (THMC) models is crucial for accurately simulating complex physical and chemical interactions in carbon capture and storage (CCS) processes. This paper presents a new fully coupled THMC model, specifically focusing on investigating thermo-chemo coupling (dissolution) effects for CCS applications. The model is a further extension of the mixture-coupling theory, which incorporates entropy and mass balance equations, phenomenological equations, and Maxwell's relations to describe the intricate coupling between mechanical, hydraulic, chemical, and thermal properties. The model considers a two-phase flow, liquid and supercritical. By deriving new coupling terms from the phenomenological equations, the model provides capacity to account for energy losses due to friction between the two phases, along with energy losses arising from the transport of the solute and the evolution of porosity/permeability. Furthermore, the model incorporates an additional coupling term in the mechanical equation to represent the chemical dissolution effect on volumetric strain relief. Two terms added in the liquid equation account for the friction of newly dissolved minerals particles on liquid transport and the effects of porosity changes on liquid flow through dissolution. Finally, Thermal transport coupling is integrated into the model, as it is a crucial part of CCS applications. Numerical results demonstrate that increasing temperature significantly decreases porosity due to thermal

expansion, but thermal energy triggers chemical dissolution which in the long run increases both porosity and permeability. Chemical dissolution has the most significant incremental effect on porosity over time, while thermal expansion has the greatest impact until thermal equilibrium is reached, with the direct impacts of pressure and strain on porosity falling in between. This research presents a comprehensive coupling framework that accounts for two-phase friction, the dissolution process, and changing permeability, which gives it potential utility in the planning process for CCS applications.

6.1 Introduction

The threat of climate change grows each day, heralding disastrous effects on our planet's natural life and prompting an urgent need for effective ways to mitigate global warming (Masson-Delmotte et al., 2022; Pörtner et al., 2022; Vicente-Serrano et al., 2020). Carbon capture and storage (CCS) technologies may form part of the solution to such problems (Bui et al., 2018; House et al., 2011). Many countries have already adopted such projects. For example, according to Xu et al. (2021) China has built and started constructing more than 25 facilities related to CCS with an annual injection capacity of over 12 megatons. Similarly, Norway, the USA, Australia, Canada, France, Germany, the United Kingdom, and India already have built and are currently constructing CCS facilities with a capacity of about 37 annual megatons. However, for the CCS process to be successful, it requires optimization and a comprehensive understanding of the underlying mechanisms.

To address this need, researchers have turned their attention to Thermo-Hydro-Mechanical-Chemical (THMC) coupled models in recent years. These models are crucial for unravelling the complex interactions between thermal, hydraulic, mechanical, and chemical processes during and after the injection process in CCS. While numerous studies

have explored different aspects of CCS, particularly process development and optimization (Rutqvist et al., 2002; Ennis-King and Paterson, 2005; André et al., 2007b; Taron et al., 2009; Liu et al., 2011; Rutqvist et al., 2011; Zhang et al., 2012; Karrech, 2013; Gan et al., 2021; Lei et al., 2020; Buchwald et al., 2021), existing multi-phase THMC models have limitations in addressing thermal-chemo coupling and its effect on porosity evolution due to the complexity of this process. For instance, Vilarrasa and **Rutqvist** (2017)pointed the impact of geochemical out that (dissolution/precipitation) on the geomechanical properties of different rock types has not been explored in detail. They argued that interdisciplinary collaboration between geochemists and geomechanics experts is needed to clarify this coupled effect. Furthermore, they noted that despite their importance, the coupled Thermo-Hydro-Mechanical-Chemical processes have not been adequately investigated due to the high computational cost involved, suggesting the need for more efficient numerical simulators.

The need to investigate the thermo-chemo effect of CO_2 dissolution on the CCS process was raised up by other researcher such as Gaus et al. (2008b). The author highlighted the necessity of creating an appropriate thermo-chemical coupling, taking in the account high pressure, and investigate its effect on the porosity/permeability changes. These changes, influenced by the precipitation and dissolution of minerals such as calcite, are particularly significant near the CO_2 injection well.

While some researchers have considered the thermo-chemical effects for one-phase flow, extending such fully coupled models to multi-phase flow presents another challenge due to the complex interaction between the fluids. For example, Yin et al. (2011) presented coupled THMC model to study transient stress, pressure, temperature, and solute

concentration near the CCS injection point. The paper investigates the effects of injecting CO₂ saturated water into a carbonate aquifer composed of pure calcite (CaCO₃). The changes in permeability due to dissolution were investigated. The model demonstrated the significant impact of temperature and chemical reactions on the stress and pressure around the injection area. However, the model was developed for one-phase flow only, a limitation justified by the authors due to the problem's complexity. Moreover, the model did not investigate the effect of the chemical dissolution on the solid rock mechanical properties which should affect the stress and strain evolution.

A more refined single-phase model that focused on addressing the chemical dissolution effect on the mechanical stress/strain issue is presented by Yue et al. (2022). The authors introduced a general THMC reactive model based on mixture-coupling theory, taking into account the dissolution process by utilizing chemical affinity. Within this model, a new term was added to the mechanical governing equation to address the effect of chemical dissolution on mechanical characteristics, among other terms. A numerical simulation was applied to a quartz dissolution case. However, the model only considered one-phase flow, and the coupling effects on pressure, temperature, and permeability change were not tested.

To date, the effects of thermo-chemical coupling and the improved chemical-mechanical coupling on the THMC system for CCS remain under-investigated. However, these effects are anticipated to significantly influence the process. Addressing this issue, this research presents a novel fully coupled multi-phase THMC model for CCS process. This model investigates the impact of both thermal-chemo coupling and chemical-mechanical effects on a two-phase transport process involving supercritical carbon dioxide (ScCO₂)

and saline water in deep aquifer. To achieve this aim, the mixture-coupling theory approach (Chen and Hicks, 2011; Wang et al., 2023c; Siddiqui et al., 2023; Abdullah et al., 2022) is employed, utilising the principles of non-equilibrium thermodynamics and continuum mechanics.

Mixture-coupling theory was first proposed by Heidug and Wong (1996) and is grounded in mixture theory (Terzaghi, 1925; Coussy et al., 1998). The methodology employs entropy production equations, mass balance equations, and the Helmholtz free energy equation. Maxwell's relations are used to create coupling relations between stress, pressure, temperature, porosity evolution, and chemical affinity, while phenomenological relations are employed to discern the coupling between each flow and its driving force. The mixture-coupling theory approach presents a significant advantage over the conventional mechanics approach for the thermo-chemical and chemical-mechanical coupling, as it effectively bridges the scale discrepancy between geomechanics and geochemistry (Ge et al., 2023).

This research introduces an advanced Thermo-Hydro-Mechanical-Chemical (THMC) model, offering significant potential for more intricate and precise coupling within carbon capture and storage (CCS) processes. It not only contemplates the impact of chemical dissolution on mechanical stress/strain but also the interplay between chemical reactions, temperature, and phase pressures. It considers two-phase friction, dissolution, and permeability changes. Furthermore, the model integrates thermal transport, highlighting the role of temperature in altering porosity and permeability due to thermal expansion and chemical dissolution. Applicable for investigating CCS in reactive formations, this comprehensive model provides crucial insights for the optimization and effective

implementation of CCS technologies by yielding a deeper understanding of these interacting processes.

6.2 Balance equations

The current model is underpinned by several assumptions. First, it is posited that the system being considered encompasses a two-phase flow, specifically the liquid and supercritical phases. Within this, it is assumed that only a dissolution chemical reaction takes place. This reaction only transpires between CO_2 in the aqueous phase (dissolved in water) and solids (through a minerals dissolution reaction). Secondly, the system is presumed to be immiscible. In this context, the water and supercritical phases are separate and invariant, with no mass interchange occurring between the phases. Lastly, it is projected that the salts present in the saline water will not partake in the chemical reaction. This underlying assumption is integral to the structure of the current model and the interpretations drawn from it.

6.2.1 Density, flux, and diffusion definition

In this study, the 'mixture' is defined as the amalgamation of all fluid phases. The Representative Elementary Volume (REV), assumed to consist of deformable porous media, is characterized by volume V and a boundary surface S, permitting only fluid flow across the boundary S (see Figure 6.1). Owing to the temperature gradient within the REV, thermal energy can be transferred, affecting both fluid and solid components. The pore spaces are occupied by two fluid phases: saline water and supercritical carbon dioxide (ScCO₂). The term 'porosity' (ϕ) is defined as the ratio of the solid matrix

volume (V^s) to the total REV volume (V), whereas the 'phase porosity' (ϕ^β) equates to the ratio of the phase volume (V^β) to the REV volume (V^β).

$$\phi^{\beta} = \frac{V^{\beta}}{V}, \qquad \phi = \sum \phi^{\beta} \tag{6.1}$$

In this context, 'mass density' can be defined in two ways: 'mixture density' (ρ^{β}), based on the total volume of the mixture's pore space, or 'phase density' (ρ^{β}_{β}), which is determined by the volume of the pore space specific to a phase β . The relationship between these two densities is linked to the 'phase porosity' (ϕ^{β}) as

$$\rho^{\beta} = \phi^{\beta} \rho_{\beta}^{\beta} \tag{6.2}$$

Here, β represents sub-constituents' species in saline water (such as water, salt, etc.) or phase β (liquid, supercritical). This paper will consider two fluid phases, the 'liquid' phase 'l', and the 'supercritical' phase 'Sc'. Furthermore, the liquid species include water 'w' and chemicals 'c', whereas the supercritical phase contains only one species, carbon dioxide (CO_2). The densities can be defined based on equation (6.2) as:

$$\rho^{l} = \phi^{l} \rho_{l}^{l} = \rho^{w} + \rho^{c}, \ \rho^{Sc} = \phi^{Sc} \rho_{Sc}^{Sc}, \ \rho^{w} = \phi^{l} \rho_{l}^{w}, \ \rho^{c} = \phi^{l} \rho_{l}^{c}$$
 (6.3)

The mass flux I of saline water, the supercritical flow, or any sub-components present in saline water, such as water and chemicals, are defined as follows:

$$\mathbf{I}^{\beta} = \rho^{\beta} \left(\mathbf{v}^{\beta} - \mathbf{v}^{s} \right) \tag{6.4}$$

 \mathbf{v}^{β} and \mathbf{v}^{s} represent the interstitial velocities of the fluid and solid, respectively. The diffusion in the liquid phase, \mathbf{J} , can be depicted as follows:

$$\mathbf{J}^{\beta} = \rho^{\beta} \left(\mathbf{v}^{\beta} - \mathbf{v}^{l} \right), \qquad \beta \in l$$
 (6.5)

for the liquid phase, the diffusion of chemicals can also be represented as a function of flux, as follows:

$$\mathbf{J}^{\beta} = \mathbf{I}^{\beta} - \rho^{\beta} \left(\mathbf{v}^{l} - \mathbf{v}^{s} \right), \qquad \beta \in l$$
 (6.6)

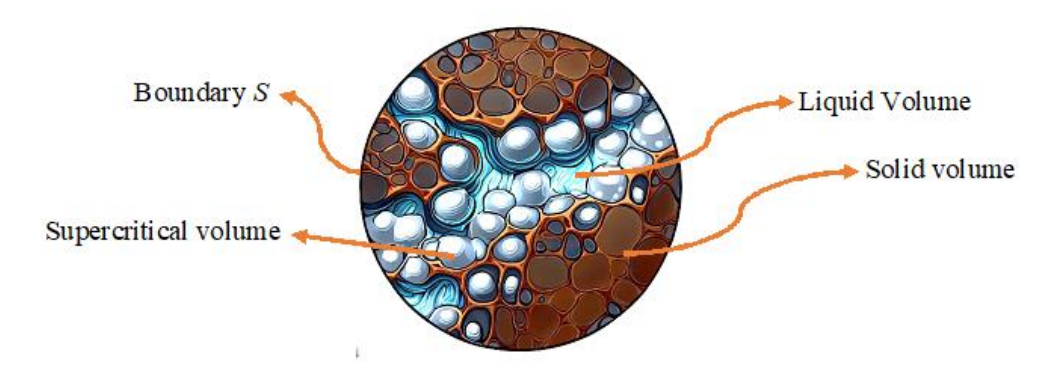


Figure 6.1: Representative Elementary Volume (REV)

6.2.2 Chemical reaction

If a chemical reaction take place between solid phase and aquatic solution, and the reaction result of dissolution of the solid as: $v_x X_{(s)} + v_y Y_{(aq)} \rightarrow v_z Z_{(aq)}$, then the change in extent of the reaction $d\xi$ is described as:

$$d\xi = \frac{dn_i}{V \, \mathcal{W}^i} \tag{6.7}$$

 ξ is extent of reaction, $X_{(s)}$, $Y_{(aq)}$, $Z_{(aq)}$ are the solid reactant, acoustic reactant, and the acoustic product respectively. v^x , v^y , and v^z are stoichiometric coefficient, dn_i is the change in number of moles, V is the volume of the pore and χ can be -1, 0, or 1 and is reflect the reaction state (dissolution, no reaction, precipitation).

The chemical affinity A' of the reaction can be defined as (Kondepudi and Prigogine, 2014):

$$A = -\sum_{i} \chi \chi^{i} M^{i} \mu^{i} = v^{x} M^{x} \mu^{x} + v^{y} M^{y} \mu^{y} - v^{z} M^{z} \mu^{z}$$
(6.8)

where μ is the chemical potential of the species and M^{i} is the molar mass.

6.2.3 Fluid mass balance equation

The mass balance equation for the REV is

$$\frac{D}{Dt} \left(\int_{V} \rho^{\beta} dV \right) = -\int_{S} \mathbf{I}^{\beta} \cdot \mathbf{n} dS + \int_{V} \chi v^{\beta} M^{\beta} \dot{\xi} dV \tag{6.9}$$

where \mathbf{n} is outward unit normal vector, the material time derivative can be introduced as

$$\frac{D}{Dt} = \partial t + \mathbf{v}^s \cdot \nabla \tag{6.10}$$

then, the differential form of equation (6.9) can be written as

$$\dot{\rho}^{\beta} + \rho^{\beta} \nabla \cdot \mathbf{v}^{s} + \nabla \cdot \mathbf{I}^{\beta} - \chi v^{\beta} M^{\beta} \dot{\xi} = 0$$
 (6.11)

6.2.4 Entropy balance equation

For an irreversible transport process, the alteration in entropy can be delineated in terms of entropy flux interchange with the surroundings \mathbf{I}_{η} and the entropy per unit volume γ generated in the porous media due to irreversible heat and mass transfer, and chemical reactions. As a result, the entropy balance equation can be expressed as follows:

$$\frac{D}{Dt} \int_{V} \eta^{m} dV = -\int_{S} \mathbf{I}_{\eta} \cdot \mathbf{n} dS + \int_{V} \gamma dV$$
 (6.12)

where η^m represents the mixture entropy density, encompassing both fluid and solid phases. By applying the material time derivative, the differential local form can be articulated as:

$$\dot{\boldsymbol{\eta}}^m + \boldsymbol{\eta}^m \nabla \cdot \mathbf{v}^s + \nabla \cdot \mathbf{I}_n - \gamma = 0 \tag{6.13}$$

The entropy flux I_n can be defined as (Katchalsky and Curran, 1965):

$$\mathbf{I}_{\eta} = \frac{\mathbf{q} - \sum \mu^{\beta} \mathbf{I}^{\beta}}{T} = \frac{\mathbf{q}'}{T} + \sum \eta^{\beta} \mathbf{I}^{\beta}$$
 (6.14)

 ${f q}$ is the total heat flow, ${f q}'$ is the reduced heat flow, T is the mixture temperature, μ^{β} is the chemical potential of fluid β . The chemical potential can be expressed in term of enthalpy h^{β} , temperature T and entropy density as

$$\mu^{\beta} = h^{\beta} - T \eta^{\beta} \tag{6.15}$$

the reduced heat flow which represents the heat exchange occurring via direct contact at the boundary with the surroundings (heat transfer by conduction) is expressed as

$$\mathbf{q}' = -\lambda \nabla T \tag{6.16}$$

where λ is thermal conductivity.

6.3 Helmholtz free energy

6.3.1 The balance of internal energy

Taking into account only the mechanical work and heat exchange, and by disregarding the heat change resulting from chemical reactions or any other point sources, the internal energy balance equation can be formulated as follows:

$$\dot{\varepsilon}^m + \varepsilon^m \nabla \cdot \mathbf{v}^s - \nabla \cdot \left(\mathbf{\sigma} \mathbf{v}^s \right) + \nabla \cdot \mathbf{q}' + \nabla \cdot \sum h^{\beta} \mathbf{I}^{\beta} = 0$$
 (6.17)

where σ is the Cauchy stress tensor.

6.3.2 Helmholtz free energy balance equation

Helmholtz free energy ψ of a mixture can be obtained by subtracting the contribution of entropy $T\eta^m$ from the internal energy ε^m , as $\psi = \varepsilon^m - T\eta^m$. using the material derivative equation (6.10), the local form equation can be then described as

$$\dot{\psi} + \psi \nabla \cdot \mathbf{v}^{s} = \dot{\varepsilon}^{m} + \varepsilon^{m} \nabla \cdot \mathbf{v}^{s} - \left(\dot{T} + T \nabla \cdot \mathbf{v}^{s}\right) \eta^{m} - T \left(\dot{\eta}^{m} + \eta^{m} \nabla \cdot \mathbf{v}^{s}\right)$$
(6.18)

by substituting equation (6.13) and (6.17) into equation (6.18), it leads to

$$-\dot{\psi} - \psi \nabla \cdot \mathbf{v}^{s} + \nabla \cdot (\sigma \mathbf{v}^{s}) - \nabla \cdot \mathbf{q}' - (\dot{T} + T \nabla \cdot \mathbf{v}^{s}) \eta^{m} - \nabla \cdot \sum h^{\beta} \mathbf{I}^{\beta} - T \nabla \cdot \mathbf{I}_{\eta} = T \gamma$$
(6.19)

6.4 Constitutive framework

6.4.1 Transport law, entropy production and phenomenological equations

In most literature, the transport of fluid β in porous media simplified to a simple Darcy velocity as

$$\mathbf{u}^{\beta} = S^{\beta} \phi \left(\mathbf{v}^{\beta} - \mathbf{v}^{s} \right) \tag{6.20}$$

The entropy production equation for the system can be written as:

$$0 \le T \ \gamma = -\mathbf{I}_{\eta} \cdot \nabla T - \sum \mathbf{I}^{\beta} \cdot \nabla \mu^{\beta} + A \dot{\xi}$$
 (6.21)

Using equation (6.4) into entropy production equation (6.21):

$$0 \le T \gamma = -\mathbf{I}_{\eta} \cdot \nabla T - \sum \rho^{\beta} \left(\mathbf{v}^{\beta} - \mathbf{v}^{s} \right) \cdot \nabla \mu^{\beta} + A \dot{\xi}$$
 (6.22)

by replacing β with the three species w, c, and Sc, the equation can be rearranged as

$$0 \le T \ \gamma = -\mathbf{I}_{\eta} \cdot \nabla T - \rho^{w} \left(\mathbf{v}^{w} - \mathbf{v}^{s} \right) \cdot \nabla \mu^{w}$$

$$-\rho^{Sc} \left(\mathbf{v}^{Sc} - \mathbf{v}^{s} \right) \cdot \nabla \mu^{Sc} - \rho^{c} \left(\mathbf{v}^{c} - \mathbf{v}^{s} \right) \cdot \nabla \mu^{w} + A \dot{\xi}$$

$$(6.23)$$

Using Gibbs-Duhem relation, the relation between phase pressure and chemical potential can be found as:

$$\nabla p^{l} = \rho_{l}^{w} \nabla \mu^{w} + \rho_{l}^{c} \nabla \mu^{c}$$

$$\nabla p^{Sc} = \rho_{Sc}^{Sc} \nabla \mu^{Sc}$$
(6.24)

by using equation (6.20), and substituting equation (6.24) into (6.23)

$$0 \le T \gamma = -\mathbf{I}_{\eta} \cdot \nabla T - \mathbf{u}^{l} \cdot \nabla p^{l} - \mathbf{J}^{c} \cdot \nabla \left(\mu^{c} - \mu^{w}\right) - \mathbf{u}^{Sc} \cdot \nabla p^{Sc} + A \dot{\xi}$$
 (6.25)

The above equation shows the entropy product due to five terms each containing flow and driving force. Term $-\mathbf{I}_{\eta} \cdot \nabla T$ is the entropy exchange driven by temperature gradient, $-\mathbf{u}^{sc} \cdot \nabla p^{sc}$ supercritical phase flow driven by supercritical pressure gradient, $-\mathbf{J}^c \cdot \nabla \left(\mu^c - \mu^w\right)$ is the chemical diffusion in the liquid driven by chemical potential gradient, and finally, $+A\dot{\xi}$ is the change in chemical extent driven by the affinity of the reaction. Since the last term driving force is scalar quantity and not a vector, and as per Curie-Prigogione principle, this term cannot be included in the phenomenological coupling relation (Katchalsky and Curran, 1965). To simplify the discussion, the convection heat transfer between the two fluids flow is neglected.

For isotropic medium, the phenomenological relation between four flows with three driving forces as:

$$\rho_{l}^{l}\mathbf{u}^{l} = -\frac{L_{11}}{\rho_{l}^{l}}\nabla p^{l} - \frac{L_{12}}{\rho_{Sc}^{Sc}}\nabla p^{Sc} - L_{13}\nabla(\mu^{c} - \mu^{w})$$

$$\rho_{Sc}^{Sc}\mathbf{u}^{Sc} = -\frac{L_{21}}{\rho_{l}^{l}}\nabla p^{l} - \frac{L_{22}}{\rho_{Sc}^{Sc}}\nabla p^{Sc} - L_{23}\nabla(\mu^{c} - \mu^{w})$$

$$\mathbf{J}^{c} = -\frac{L_{31}}{\rho_{l}^{l}}\nabla p^{l} - \frac{L_{32}}{\rho_{Sc}^{Sc}}\nabla p^{Sc} - L_{33}\nabla(\mu^{c} - \mu^{w})$$
(6.26)

The relation between chemical potential and the unitless mass fraction of chemical species c', c' can be describes as:

$$\frac{\partial \mu^c}{\partial c^c} = \frac{RT}{M^c c^c} \tag{6.27}$$

R is gas constant and M^{c} is the molar mass of the chemical specie 'c'.

If the following parameters defined as

$$k_{abs} \frac{k_{rl}}{v^{l}} = \frac{L_{11}}{\left(\rho_{l}^{l}\right)^{2}}, r_{1} = -\frac{L_{12}}{L_{11}}, r_{2} = -\frac{L_{13}}{L_{11}}, r_{3} = -\frac{L_{21}}{L_{22}}, r_{4} = -\frac{L_{23}}{L_{22}}$$

$$L^{l} = -\frac{L_{31}p^{l}}{\left(\rho_{l}^{l}\right)^{2}}, L^{g} = -\frac{L_{32}p^{Sc}}{\left(\rho_{Sc}^{Sc}\right)^{2}}, D = \frac{L_{33}}{c^{w}} \frac{\partial \mu^{c}}{\rho_{l}^{l}} \frac{\partial \mu^{c}}{\partial c^{c}}$$

$$(6.28)$$

Then the Darcy's flows and diffusion can be introduced as:

$$\mathbf{u}^{l} = -k_{abs} \frac{k_{rl}}{v^{l}} \left(\nabla p^{l} - r_{1} \frac{\rho_{l}^{l}}{\rho_{Sc}^{Sc}} \nabla p^{Sc} - r_{2} \rho_{l}^{l} \left(\frac{1}{c^{w}} \frac{\partial \mu^{c}}{\partial c^{c}} \nabla c^{c} \right) \right)$$

$$\mathbf{u}^{Sc} = -k_{abs} \frac{k_{rSc}}{v^{Sc}} \left(-r_{3} \frac{\rho_{Sc}^{Sc}}{\rho_{l}^{l}} \nabla p^{l} + \nabla p^{Sc} - \rho_{Sc}^{Sc} r_{4} \left(\frac{1}{c^{w}} \frac{\partial \mu^{c}}{\partial c^{c}} \nabla c^{c} \right) \right)$$

$$\mathbf{J}^{c} = -\left(\frac{L^{l} \rho_{l}^{l}}{p^{l}} \right) \nabla p^{l} - \left(\frac{L^{Sc} \rho_{Sc}^{Sc}}{p^{Sc}} \right) \nabla p^{Sc} - D \rho^{l} \nabla c^{c}$$

$$(6.29)$$

6.4.2 Mechanical deformation

Assuming mechanical equilibrium $(\nabla \cdot \mathbf{\sigma} = 0)$, using the entropy production equation (6.23) and Helmholtz free energy balance equation (6.19), the following equation is established:

$$\dot{\psi} + \psi \nabla \cdot \mathbf{v}^{s} = (\mathbf{\sigma} : \nabla \mathbf{v}^{s}) - (\dot{T} + T \nabla \cdot \mathbf{v}^{s}) \eta^{m} - \sum \mu^{\beta} \nabla \cdot \mathbf{I}^{\beta} - A \dot{\xi}$$
(6.30)

by substituting $\nabla \cdot \mathbf{I}^{\beta}$ from equation (6.11) in (6.30),

$$\dot{\psi} + \psi \nabla \cdot \mathbf{v}^{s} = (\mathbf{\sigma} : \nabla \mathbf{v}^{s}) - (\dot{T} + T \nabla \cdot \mathbf{v}^{s}) \eta^{m} +$$

$$\sum (\mu^{\beta} \dot{\rho}^{\beta} + \mu^{\beta} \rho^{\beta} \nabla \cdot \mathbf{v}^{s} - \mu^{\beta} \chi v^{\beta} M^{\beta} \dot{\xi}) - A \dot{\xi}$$
(6.31)

then by using equation (6.8), $\sum \left(\mu^{\beta} \chi v^{\beta} M^{\beta} \dot{\xi}\right) - A \xi = -\mu^{x} v^{x} M^{x} \dot{\xi} = -A_{s} \dot{\xi}$. The reactant x is the solid component that dissolve within the dissolution reaction, and thus A_{s} is the solid affinity.

Finally, the free Helmholtz free energy equation can be presented as

$$\dot{\psi} + \psi \nabla \cdot \mathbf{v}^{s} = (\mathbf{\sigma} : \nabla \mathbf{v}^{s}) - (\dot{T} + T \nabla \cdot \mathbf{v}^{s}) \eta^{m} + \sum_{s} (\mu^{\beta} \dot{\rho}^{\beta} + \mu^{\beta} \rho^{\beta} \nabla \cdot \mathbf{v}^{s}) - A_{s} \dot{\xi}$$

$$(6.32)$$

where $A_s \dot{\xi}$ signifies the alteration in the Helmholtz free energy of the solid stemming from reactive dissolution.

If **F,E**, and **T** are the solid deformation tensor, the Green strain tensor and the second Piola-Kirchhoff stress tensor respectively, the following equations can be presented as:

$$\mathbf{F} = \frac{\partial \mathbf{x}}{\partial \mathbf{X}} (\mathbf{X}, t), \mathbf{E} = \frac{1}{2} (\mathbf{F}^{\mathsf{T}} \mathbf{F} - \mathbf{I})$$
 (6.33)

$$\mathbf{T} = \mathbf{J}\mathbf{F}^{-1}\mathbf{\sigma}\mathbf{F}^{-T} \tag{6.34}$$

the Jacobian J is the determinant of the solid deformation tensor, and it is a measure the volume change which can be describes as

$$J = \frac{dV}{dV_o}, \dot{J} = J\nabla \cdot \mathbf{v}^s \tag{6.35}$$

where dV is the volume at current configuration, dV_0 is the volume at the reference configuration. Then, using equation (6.32), the free Helmholtz free energy equation in reference configuration is

$$\dot{\Psi} = \operatorname{tr}(\mathbf{T}\mathbf{E}) + \mu^{w} \dot{m}^{w} + \mu^{Sc} \dot{m}^{Sc} + \mu^{c} \dot{m}^{c} - J \eta^{m} \dot{T} - A_{s} \dot{\varsigma}$$
(6.36)

where $\Psi = J\psi$, $m^{\beta} = J\rho^{\beta} = JS^{\beta}\phi\rho^{\beta}_{\beta}$, $\zeta = J\xi$ and they represent the quantities in the reference configuration.

6.4.3 Helmholtz free energy of pore space

The expression for the Helmholtz free energy of the pore space can be formulated as

$$\psi^{pore} = -p^p + S^{\beta} \sum_{k \in \beta} \rho_{\beta}^k \mu^k \tag{6.37}$$

where the average pore pressure is defined as

$$p^{p} \approx S^{l} p^{l} + S^{sc} p^{sc} = S^{l} p^{l} + p^{sc} - S^{l} p^{sc}$$
(6.38)

replacing β with fluids species, equation (6.37) can be written as

$$\psi^{\text{pore}} = -p^{p} + S^{l} \left(\mu^{w} \rho_{l}^{w} + \mu^{c} \rho_{l}^{c} \right) + S^{Sc} \mu^{Sc} \rho_{Sc}^{Sc}$$
 (6.39)

and the differential form is

$$\dot{\psi}^{\text{pore}} = -\dot{p}^{p} + \dot{\mu}^{w} \left(S^{l} \rho_{l}^{w} \right) + \mu^{w} \left(S^{l} \rho_{l}^{w} \right) + \dot{\mu}^{c} \left(S^{l} \rho_{l}^{c} \right) + \mu^{c} \left(S^{l} \rho_{l}^{c} \right)$$

$$+ \dot{\mu}^{Sc} \left(S^{Sc} \rho_{Sc}^{Sc} \right) + \mu^{Sc} \left(S^{Sc} \rho_{Sc}^{Sc} \right)$$
(6.40)

the pore pressure derivative can be obtained from equation (6.38) as

$$\dot{p}^{p} = (S^{l} + C^{s} p^{c}) \dot{p}^{l} + (S^{Sc} - C^{s} p^{c}) \dot{p}^{Sc}$$
(6.41)

where the specific moisture capacity is defined as $C^s = \frac{\partial S^l}{\partial p^c}$, and the capillary pressure

is
$$p^c = p^{Sc} - p^l$$
.

6.4.4 Free energy density of the solid matrix and Maxwell relations

the free energy for the of the system is the combination of the free energy of the liquid phase, the free energy of the supercritical phase and the free energy of the solid

$$(\Psi - J\phi\psi^{pore}) = \dot{\Psi} - (J\phi\psi^{pore}) = \dot{\Psi} - (J\phi)\psi^{pore} - J\phi\dot{\psi}^{pore}$$
(6.42)

since $m^{\beta} = J \rho^{\beta} = J S^{\beta} \phi \rho_{\beta}^{\beta}$, then

$$\mu^{\beta}\dot{m}^{\beta} - \mu^{\beta} \left(\upsilon S^{\beta} \rho_{\beta}^{\beta} \right) = 0 \tag{6.43}$$

also, from Gibbs-Duhem equation, the fluid derivative pressure can be expressed as

$$\dot{p}^{\beta} = \sum_{k \in I} \rho_{\beta}^{k} \dot{\mu}^{k} + \eta_{\beta}^{\beta} \dot{T}$$
 (6.44)

Assuming the value of $C^s p^c$ is negligible, then, by using equation (6.36), (6.39), (6.40), (6.43), and Gibbs-Duhem equation (6.44) with (6.41) into equation (6.42), the following equation is obtained:

$$(\Psi - J\phi\psi^{pore}) = \dot{\Psi} - (\upsilon\psi^{pore}) = tr(\mathbf{T}\dot{\mathbf{E}}) + \dot{p}^{p}\dot{\upsilon} - H^{s}\dot{T} - A_{s}\dot{\varsigma}$$
(6.45)

where $H^s = J\eta^s = J\eta^m - \sum \eta^\beta$ is the entropy density of the solid matrix, $\upsilon = J\phi$

Let's define the dual potential W as

$$W = (\Psi - \nu \psi^{pore}) - p^p \nu \tag{6.46}$$

if \mathbf{E}, p^p, ζ , and T are the state variables, and therefore W can be expressed as

$$\dot{W}\left(\mathbf{E}, p^{p}, \varsigma, T\right) = tr\left(\mathbf{T}\dot{\mathbf{E}}\right) - \upsilon \dot{p}^{p} - A_{s}\dot{\varsigma} - H^{s}\dot{T} \tag{6.47}$$

since the dual potential is a function of $\mathbf{E}, p^p, \varsigma$, and T, the Maxwell relations can be used as

$$T_{ij} = \left(\frac{\partial W}{\partial E_{ij}}\right)_{p^{p},\varsigma,T}, \upsilon = -\left(\frac{\partial W}{\partial p^{p}}\right)_{E_{ij},\varsigma,T},$$

$$A_{s} = -\left(\frac{\partial W}{\partial \varsigma}\right)_{E_{ij},p^{p},T}, H^{s} = -\left(\frac{\partial W}{\partial T}\right)_{E_{ij},p^{p},\varsigma}$$

$$(6.48)$$

then, \dot{W} can be written as

$$\dot{W}\left(\mathbf{E}, p^{p}, \varsigma, T\right) = \left(\frac{\partial W}{\partial E_{ij}}\right)_{p^{p}, \varsigma, T} \dot{\mathbf{E}}_{ij} + \left(\frac{\partial W}{\partial p^{p}}\right)_{E_{ij}, \varsigma, T} \dot{p}^{p} + \left(\frac{\partial W}{\partial \varsigma}\right)_{E_{ij}, p^{p}, \varsigma} \dot{\varsigma} + \left(\frac{\partial W}{\partial T}\right)_{E_{ij}, p^{p}, \varsigma} \dot{T}$$
(6.49)

Then, the following stress \dot{T}_{ij} , porosity υ , solid affinity A_s , and entropy of the solid H_s are:

$$\dot{T}_{ii} = L_{iikl} \dot{E}_{kl} - M_{ii} \dot{p}^{l} - H_{ii} \dot{\zeta} - F_{ii} \dot{T}$$
 (6.50)

$$\dot{\upsilon} = M_{ij} \dot{E}_{ij} + Q \dot{p}^{l} + D \dot{\varsigma} + N \dot{T}$$
 (6.51)

$$\dot{A}_{s} = H_{ii} \dot{E}_{ii} + D\dot{p}^{l} + Y \dot{\varsigma} + V\dot{T}$$
 (6.52)

$$\dot{H}_{s} = F_{ij}\dot{E}_{ij} + N\dot{p}^{l} + V\dot{\varsigma} + U\dot{T}$$
 (6.53)

the above equations contain a set of 15 coefficients that need to be determined:

$$L_{ijkl}\,,M_{ij}\,,H_{ij}\,,F_{ij}\,,Q\,,D\,,N\,,Y\,,V\,,U$$

6.5 THMC governing equations

6.5.1 Solid phase behaviour

Equations listed in (6.50)-(6.53) illustrate the change in stress, porosity, solid affinity, and entropy concerning the Green Strain tensor, fluid pressure, reaction extent, and temperature. These equations are not limited to specific scenarios and have broad applicability. Nonetheless, the derivation of the governing equations calls for assumptions of small strain, isotropy, and symmetry. The small strain assumption allows for substitution of Green Strain tensor E_{ij} and Piola-Kirchhoff stress T_{ij} with strain tensor ε_{ij} and Cauchy stress σ_{ij} , respectively as:

$$E_{ij} \approx \varepsilon_{ij}, T_{ij} \approx \sigma_{ij}, \frac{\partial \sigma_{ij}}{\partial x_{i}} = 0$$
 (6.54)

If the material assumed to be a fully isotropic and symmetric, then the following tensors can be substituted with scalar coefficients utilizing Kronecker delta,

$$M_{ij} = \zeta \delta_{ij}, \qquad H_{ij} = \omega_R \delta_{ij}, \qquad F_{ij} = \omega_T \delta_{ij}$$
 (6.55)

where ω_{R} , ω_{r} , and ω_{T} can be expressed as (Tao et al., 2019; Yue et al., 2022),

$$\omega_{R} = \omega_{r} K$$

$$\omega_{r} = \frac{M^{x}}{\rho_{x}^{x} (1 - \phi)} = \frac{V^{x}}{(1 - \phi)}$$
(6.56)

$$\omega_T = K \alpha_s$$

 α_s is the thermal expansion coefficient of the solid. For coefficients Q and ζ , they are defined as (Heidug and Wong, 1996):

$$Q = \frac{\zeta - \phi}{K^s}, \qquad \zeta = 1 - \frac{K}{K^s} \tag{6.57}$$

 ζ is defined as biot's coefficient, K and K^s are the bulk modulus of the porous media and the solid grain respectively. Coefficients N and D are:

$$N = -(\zeta - \phi)\alpha_s, \qquad D = \frac{M^x}{\rho_s^x}$$
 (6.58)

where D is the molar volume. Finally, the last coefficient L_{ijkl} is the stiffness tensor and can be expressed as

$$L_{ijkl} = G\left(\delta_{ik}\delta_{jl} + \delta_{il}\delta_{jk}\right) + \left(K - \frac{2G}{3}\right)\delta_{ij}\delta_{kl}$$
(6.59)

G and K are the shear modulus and the bulk modulus respectively.

Using equation (6.54), (6.55), and (6.59) to rewrite the stress \vec{T} expression in equation (6.50), and assuming J = 1, the change in stress can be expressed as

$$\dot{\sigma}_{ij} = \left(K - \frac{2G}{3}\right)\dot{\varepsilon}_{kk}\,\delta_{ij} + 2G\,\dot{\varepsilon}_{ij} - \zeta\,\dot{p}^{\,p}\,\delta_{ij} - \frac{V^{\,x}K\,\dot{\xi}\delta_{ij}}{1-\phi} - \omega_{T}\dot{T}\,\delta_{ij}$$
(6.60)

where V^x is the molar volume of the solid reactant.

by substituting the above equation with the average pore pressure derivative \dot{p}^p in equation (6.41), and using the bulk modulus K and shear modulus G relationship as $G = 3K(1-2\theta)/2(1+\theta)$, where θ is the Poisson's ratio, the final governing equation for the solid phase can be presented as:

$$G\nabla^{2}\dot{\mathbf{d}} + \left(\frac{G}{1-2\theta}\right)\nabla\left(\nabla\cdot\dot{\mathbf{d}}\right) - \zeta\nabla\left[\left(S^{T} + C^{S}p^{c}\right)\dot{p}^{T}\right] - \zeta\nabla\left[\left(S^{Sc} - C^{S}p^{c}\right)\dot{p}^{Sc}\right] - \frac{V^{x}}{1-\phi}\nabla\dot{\xi} - \alpha_{s}\dot{T} = 0$$

$$(6.61)$$

where $\dot{\mathbf{d}}$ is the change in the solid deformation. Moreover, the porosity can be expressed as

$$\dot{\upsilon} = \zeta \dot{\varepsilon}_{ii} + Q \dot{p}^{p} + D \dot{\xi} + N \dot{T}$$
 (6.62)

6.5.2 Liquid phase behaviour

To describe the liquid motion, the density definition is substituted by $\rho^l = \phi S^l \rho_l^l$ and flux definition $\mathbf{I}^{\beta} = \rho_{\beta}^{\beta} \mathbf{u}^{\beta}$ in the mass balance equation (6.11) as:

$$(\phi S^{l} \rho_{l}^{l}) + \phi S^{l} \rho_{l}^{l} \nabla \cdot \mathbf{v}^{s} + \nabla \cdot (\rho_{l}^{l} \mathbf{u}^{l}) - \chi v^{\beta} M^{\beta} \dot{\xi} = 0$$

$$(6.63)$$

then multiply by Jacobian J and assuming uncompressible liquid, then,

$$\left(\upsilon S^{l} \rho_{l}^{l}\right) + J \nabla \cdot \left(\rho_{l}^{l} \mathbf{u}^{l}\right) - J \chi v^{\beta} M^{\beta} \dot{\xi} = 0$$

$$(6.64)$$

by expanding the derivative term $\left(\upsilon S^{\,l}\,\rho_l^{\,l}\right)^{\dot{}}$ and substituting with equation (6.62) for the dynamic porosity $\dot{\upsilon}$, then replacing the derivative of the average pore pressure $\dot{p}^{\,p}$ with equation (6.41) and the coefficients Q, D, and N with their values from equations (6.57) and (6.58), equation (6.64) becomes:

$$S^{l} \rho_{l}^{l} \zeta \dot{\varepsilon}_{ii} + S^{l} \rho_{l}^{l} Q \left(S^{l} + C^{s} p^{c} \right) \dot{p}^{l} + S^{l} \rho_{l}^{l} Q \left(S^{sc} - C^{s} p^{c} \right) \dot{p}^{sc} + D \dot{\xi} S^{l} \rho_{l}^{l} - \left(\zeta - \phi \right) \alpha_{s} \dot{T} S^{l} \rho_{l}^{l} + \upsilon \dot{S}^{l} \rho_{l}^{l} + \upsilon S^{l} \dot{\rho}_{l}^{l} + \nabla \cdot \left(\rho_{l}^{l} \mathbf{u}^{l} \right) - J \chi v^{\beta} M^{\beta} \dot{\xi} = 0$$

$$(6.65)$$

according to Hosking et al. (2020), the relation between change in fluid density, pressure and temperature can be described as:

$$\dot{\rho}_l^l = \rho_l^l \left(\frac{1}{K^l} \, \dot{p}^l - \alpha_l \dot{T} \right) \tag{6.66}$$

where K^l is the bulk modulus of the liquid and α_l is liquid thermal expansion coefficient. Additionally, the strain $\varepsilon_{ij} = \frac{1}{2} \left(d_{i,j} + d_{j,i} \right)$, where $d_i \left(i = 1, 2, 3 \right)$, then, the displacement change can be expressed as

$$\nabla \cdot \dot{\mathbf{d}} = \delta_{ii} \dot{\varepsilon}_{ii} \tag{6.67}$$

Finally, by assuming that the Jacobian J=1 (small deformation), and by using the definition of $C^s = \frac{\partial S^l}{\partial p^c}$ and the above definitions, equation (6.65) can be written to be the governing equation for the liquid-phase as:

$$\zeta S^{l} \nabla \cdot \dot{\mathbf{d}} + \left(\frac{\zeta - \phi}{K^{s}} S^{l} S^{l} + S^{l} \frac{\phi}{K^{l}}\right) \dot{p}^{l} + \frac{\zeta - \phi}{K^{s}} S^{l} S^{sc} \dot{p}^{Sc} c_{H}^{\beta}$$

$$+ \frac{M^{x}}{\rho_{x}^{x}} \dot{\xi} S^{l} - \left(\frac{\zeta - \phi}{K^{s}} S^{l} p^{c} - \phi\right) \dot{S}^{l} - (\zeta - \phi) \alpha_{s} \dot{T} S^{l} - \alpha_{l} \dot{T} S^{l} \phi + \frac{\left(v_{y} M^{Y} \mu^{Y} - v_{z} M^{Z} \mu^{Z}\right)}{\rho_{l}^{l}}$$

$$+ \left[-k_{abs} \frac{k_{rl}}{v^{l}} \left(\nabla^{2} p^{l} - r_{1} \frac{\rho_{l}^{l}}{\rho_{Sc}^{Sc}} \nabla^{2} p^{Sc} - r_{2} \rho_{l}^{l} \left(\frac{1}{c^{w} c^{c}} \frac{RT}{M^{c}} \nabla^{2} c^{c}\right)\right)\right] = 0$$

$$(6.68)$$

6.5.3 Supercritical phase behaviour

By following the same steps, the supercritical-phase governing equation can be described as:

$$\zeta S^{Sc} \nabla \dot{\mathbf{d}} + \left(\frac{\zeta - \phi}{K^s} S^{Sc} S^{Sc} + S^{Sc} \frac{\phi}{K^{Sc}} \right) \dot{p}^{Sc} + \frac{\zeta - \phi}{K^s} S^{Sc} S^l \dot{p}^l
+ \frac{M^x}{\rho_x^x} \dot{\xi} S^l + \left(\frac{\zeta - \phi}{K^s} S^{Sc} p^c + \phi \right) \dot{S}^{Sc} - (\zeta - \phi) \alpha_s \dot{T} S^{Sc} - \alpha_{Sc} \dot{T} S^{Sc} \phi$$

$$+ \left[-k_{abs} \frac{k_{rSc}}{v^{Sc}} \left(\nabla^2 p^{Sc} - r_3 \frac{\rho_{Sc}^{Sc}}{\rho_l^l} \nabla^2 p^l - r_4 \rho_{lSc}^{Sc} \left(\frac{1}{c^w c^c} \frac{RT}{M^c} \nabla^2 c^c \right) \right) \right] = 0$$
(6.69)

it is worth to highlight that because it has been assumed that there is no direct chemical reaction between the supercritical-phase and the solid-phase, one terms that appears in the liquid-phase governing equation (6.68) has disappeared in equation (6.69). That term $\frac{\left(v_y M^Y \mu^Y - v_z M^Z \mu^Z\right)}{\rho_l^I}$ and which has a physical meaning of converting the solid mass

to liquid as a result of the dissolution process.

6.5.4 Chemical transport

If the solute $k \in l$ exists only in the liquid phase, then by using mass balance equation of the chemical can be described by using equation (6.11), the definition of Darcy velocity \mathbf{u}^l , and flux \mathbf{I}^k and diffusion \mathbf{J}^k relationship in equation (6.6), the mass balance equation for the chemical solute can be re-written as:

$$\left(\phi S^{l} \rho_{l}^{k}\right) + \nabla \cdot \mathbf{J}^{k} + \nabla \cdot \left(\rho_{l}^{k} \mathbf{u}^{l}\right) - \chi v^{k} M^{k} \dot{\xi} = 0$$

$$(6.70)$$

the chemical fraction can be defined as $c^k = \frac{\rho_l^k}{\rho_l^l}$, then the final governing equation for the chemical phase transport is presented as:

$$\phi S^{l} \rho_{l}^{l} \dot{c}^{k} + \nabla \cdot \mathbf{J}^{k} + \rho_{l}^{l} \mathbf{u}^{l} \cdot \nabla c^{k} - \chi v^{k} M^{k} \dot{\xi} + c^{k} \sum_{k} \chi v^{k} M^{k} \dot{\xi} = 0$$
 (6.71)

6.5.5 Thermal transport

the thermal balance equation for the mixture can be written as

$$\dot{q}^{s} + \dot{q}^{l} + \dot{q}^{Sc} + \left(q^{s} + q^{l} + q^{Sc}\right) \nabla \cdot \mathbf{v}^{s} + \nabla \cdot \mathbf{q}' + \nabla \cdot \left(h^{l} \mathbf{I}^{l} + h^{sc} \mathbf{I}^{Sc}\right) = \dot{\Omega} \quad (6.72)$$

where the heat densities $q^s = \rho^s c_H^s T$, $q^l = \rho^l c_H^l T$, and $q^{Sc} = \rho^{Sc} c_H^{Sc} T$; is the heat capacity for β phase. $\dot{\Omega}$ is the heat change by the chemical reaction, to simplify the discussion, the heat that may generated or absorbed by the chemical reaction will be neglected in this model $(\dot{\Omega} = 0)$. h^l and h^{Sc} are the enthalpy for the liquid-phase and supercritical-phase respectively. The phase heat densities can be described as:

$$q^{s} = (1 - \phi)q_{s}^{s}, \ q^{l} = \phi^{l}q_{l}^{l}, \ q^{Sc} = \phi^{Sc}q_{Sc}^{Sc}$$
 (6.73)

using equation (6.73) and $\phi^{\beta} = S^{\beta} \phi$, equation (6.72) in reference configuration can be written as:

$$\left(\left(1-\upsilon\right)\rho_{s}^{s}c_{H}^{s}T\right)^{\cdot}+\left(\upsilon S^{l}\rho_{l}^{l}c_{H}^{l}T\right)^{\cdot}+\left(\upsilon S^{sc}\rho_{Sc}^{Sc}c_{H}^{Sc}T\right)^{\cdot}+J\nabla\cdot\mathbf{q}'+J\nabla\cdot\left(h^{l}\mathbf{I}^{l}+h^{sc}\mathbf{I}^{Sc}\right)=0$$

for small deformation where J=1, if the reduced heat flux ${\bf q}'=-\lambda\nabla T$,, and $h^{Sc}{\bf I}^{Sc}=\rho^{Sc}_{Sc}c^{Sc}_HT{\bf u}^{Sc}$, then equation (6.74) becomes:

$$((1-\upsilon)\rho_{s}^{s}c_{H}^{s}T)^{\cdot} + (\upsilon S^{l}\rho_{l}^{l}c_{H}^{l}T)^{\cdot} + (\upsilon S^{sc}\rho_{sc}^{Sc}c_{H}^{Sc}T)^{\cdot} - \nabla \cdot (\lambda \nabla T) +$$

$$\rho_{l}^{l}c_{H}^{l}T\nabla \cdot \mathbf{u}^{l} + \rho_{sc}^{Sc}c_{H}^{Sc}T\nabla \cdot \mathbf{u}^{Sc} = 0$$

$$(6.75)$$

Equation (6.75) is the final governing equation for the thermal transport of the system, where $\lambda = (1-\phi)\lambda^s + \lambda^l S^l \phi + \lambda^{sc} S^{sc} \phi$; λ^s, λ^l , and λ^{sc} are the thermal conductivity coefficient for the solid, liquid and supercritical phase respectively. If the porosity assumed to be a constant, then ν can be approximated to ϕ .

in equation (6.75), the coupling between thermal transport and the solid deformation, pressure and chemical reaction is embedded in the derivative of the porosity term. As equation (6.62), all these variables are included in the porosity change and thus the coupling is implied.

6.6 Numerical solution:

The objective of this section is to underline the impact of thermal transport on the twophase THMC system for the CCS process. To do so, a comparison between a case under
isothermal conditions (HMC coupled model with no thermal transport) and a nonisothermal case (THMC coupled model with thermal transport) is conducted. The
investigation includes a comparison between fluid pressure, solid deformation, chemical
reaction (dissolution rate), porosity, and permeability change.

The simulation is performed using a Finite Element Method (FEM). COMSOL Multiphysics® software, a general FEM solver, is used to solve the governing equations. The software allows the built-in general equations to be modified to align with the equations introduced in this paper. However, it should be mentioned that the dynamic

viscosity of the fluids is assumed to be constant despite the change in pressure and temperature.

For the model itself, a conceptual 2D cylindrical model of limestone rock is considered. The cylindrical sample is assumed to be 20cm in diameter and 100cm in length. The sample is assumed to be rich in calcite minerals ($CaCO_3$) and has an injection port (hole) that is 50mm in diameter and 100mm in depth on one side (the left side) of the cylindrical sample. The sample is initially semi-saturated with carbonic acid H_2CO_3 . This assumption is made because the system is assumed to be immiscible and does not account for mass exchange between the injected $ScCO_2$ and the liquid ($ScCO_2$ dissolving process); however, the chemical reaction only occurs when the $ScCO_2$ is dissolved in the liquid (to create H_2CO_3). The supercritical carbon dioxide is then injected through the injection port. The supercritical fluid is allowed to enter the sample only from the bottom flat surface of the hole while the wall of the hole is considered isolated for both flow and thermal transport.

Given that the focus of this paper is on the impact of thermal transport in THMC modelling, two scenarios are compared. In the first scenario (HMC isothermal model), the $ScCO_2$ is injected with a temperature equal to the initial rock temperature $T_{in} = T_i = 303K$. In the second scenario (THMC non-isothermal model), the injected fluid has a temperature higher than the rock's initial temperature $T_{in} = 350K > T_i = 303K$, while the other side of the sample maintains a constant temperature of 303K. A horizontal cross line is chosen to measure and plot the pressure,

temperature, horizontal deformation, and dissolution rate. Also, a sample point in the middle (point 1) is selected to measure and plot the porosity and permeability at different times.

Figure 6.2 shows the initial and boundary conditions of the rock sample, as well as the horizontal section line and sample point 1.

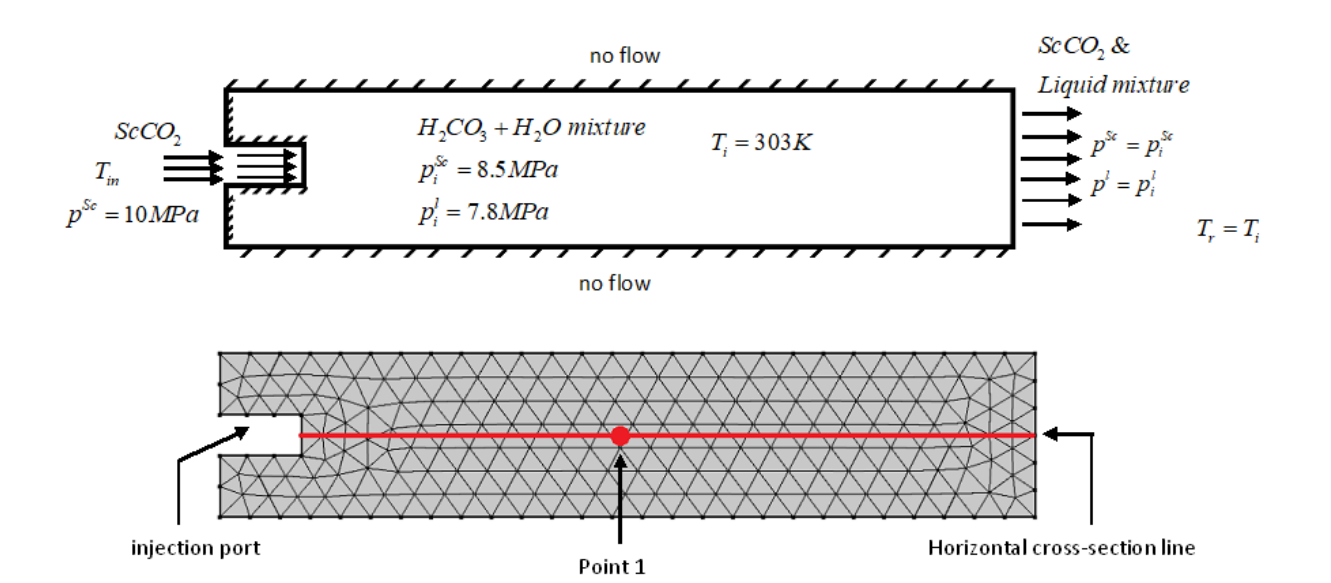


Figure 6.2: 2D model of cylindrical limestone rock sample with injection port in the centre left side.

6.6.1 Chemical reaction

The chemical reaction will take place between the carbonic acid and the calcite. In reality, the $ScCO_2$ dissolves in the saline water once the injection starts, which triggers the dissolution chemical reaction. However, as the system does not take into account the dissolving process (immiscible system), it is assumed that the CO_2 is already dissolved in the water, and the reaction will commence immediately after the $ScCO_2$ injection process begins. Furthermore, the dissolution reaction between carbonic acid H_2CO_3 and

calcite CaCO₃ is an exothermic reaction that generates heat. However, for the sake of simplification, the heat produced by the chemical reaction is ignored in the numerical simulation. The dissolution reaction can be expressed as follows (Zerai et al., 2006):

$$CaCO_3 + H_2CO_3 \Rightarrow Ca^{2+} + 2HCO_3$$
 (6.76)

while the kinetic dissolution rate for the above reaction can be expressed as (Steefel and Lasaga, 1994):

$$r = k_{rate} A rea \left(1 - \frac{Q}{K_{eq}} \right) \tag{6.77}$$

where r is the kinetic rate of the reaction (dissolution), k_{rate} is the rate of the reaction, Area is reactive surface area, K_{eq} is the equilibrium constant, and Q is the ions activity product. To calculate the dissolution rate constant, the following equation is used (Steefel and Lasaga, 1994):

$$k_{rate} = k_{r25} \exp \left[-\frac{E_a}{R} \left(\frac{1}{T} - \frac{1}{298.15} \right) \right]$$
 (6.78)

 k_{r25} is rate constant measured at $T=25C^{\circ}$, E_a is the activation energy, and R is the universal gas constant. Plummer and Busenberg (1982) presented a correlation as a function of temperature T to calculate the logarithm of K_{eq} for calcite in carbonic mixture:

$$\log(K_{eq}) = -1228.732 - 0.299444(T) + \frac{35512.75}{T} + 485.818 \times \log(T) \quad (6.79)$$

It should be noted that there is a difference between the rate of dissolution r in equation (6.77) and the solid affinity rate \dot{A}_s given by equation (6.52). While \dot{A}_s is concerned with how the thermodynamic favourability or "urge" for the reaction to occur is changing over time, the rate of dissolution r is concerned with how quickly the reaction is actually occurring. They are both important aspects of understanding a chemical reaction, but they provide information about different facets of the reaction dynamics, further details can be found in (Zhang and Zhong, 2017a; Zhang and Zhong, 2017b; Zhang and Zhong, 2018; Yue et al., 2022). Moreover, in this numerical simulation, the rate of extent of the reaction is assumed to be equal to dissolution rate.

6.6.1.1 Saturation and dynamic permeability

The equation introduced by Van Genuchten (1980a) can be utilised to calculate the saturation of both the liquid and supercritical phases. The liquid saturation is a function of the capillary pressure p^c , and two rock property-related constants: M and m. M characterises the distribution of pore sizes - the greater the value of M, the smaller the pores and the tighter the liquid is held within the solid matrix. Conversely, the parameter m indicates the uniformity of the pore size distribution (Vereecken et al., 1989; Carsel and Parrish, 1988; Ma et al., 2020b; Van Genuchten, 1980a):

$$S^{w} = \left[\left(\frac{\left| p^{c} \right|}{M} \right)^{\frac{1}{1-m}} + 1 \right]^{-m} \tag{6.80}$$

then, the relative permeability for the liquid and Sc phase can be described as:

$$k_{rl} = (S^{l})^{0.5} \times \left[1 - \left(1 - \left((S^{l})^{\frac{1}{m}}\right)\right)^{m}\right]^{2}$$
 (6.81)

$$k_{rSc} = (1 - S^{l})^{0.5} \times \left[1 - \left(1 - \left((1 - S^{l})^{\frac{1}{m}}\right)\right)^{m}\right]^{2}$$
 (6.82)

The Kozeny-Carman relation is employed to gauge the change in permeability, which is a function of the initial absolute permeability $(k_{abs})_i$, the initial porosity ϕ_i , and the current porosity value ϕ (Xu et al., 2003). It can be expressed as follows:

$$k_{abs} = \left(k_{abs}\right)_{i} \times \left(\frac{\phi}{\phi_{i}}\right)^{3} \left(\frac{1-\phi_{i}}{1-\phi}\right)^{2}$$
(6.83)

6.6.2 Properties and constants

The fluid and limestone properties and constants have been sourced from the literature. Table 6.1 displays the properties and constants used for the fluid and solid phases, along with their respective references.

Table 6.1: Properties/ parameters used in the simulation

| Physical meaning | Reference | Values and units |
|-------------------------------|-----------|--|
| | (Zhou and | _ |
| Young's modulus (Limestone) | Burbey, | $E = 33 \times 10^3 \mathrm{MPa}$ |
| | 2014b) | |
| | (Zhou and | |
| Liquid density | Burbey, | $\rho_l^l = 1000 \mathrm{kg/m^3}$ |
| | 2014b) | |
| | (Zhou and | |
| Carbon dioxide density (Sc) | Burbey, | $\rho_{Sc}^{Sc} = 660 \mathrm{kg/m^3}$ |
| | 2014b) | |
| | (Zhou and | |
| Solid density | Burbey, | $\rho^s = 2600 \mathrm{kg/m^3}$ |
| | 2014b) | , |
| | (Zhou and | |
| Poisson's ratio | Burbey, | θ = 0.26 |
| | 2014b) | |

| | (Li and | |
|--|----------------|--|
| Biot's coefficient | Laloui, | $\zeta = 1$ |
| | 2016a) | |
| | (Zhou and | |
| Porosity | Burbey, | $\phi = 0.123$ |
| - | 2014b) | |
| | (Zhou and | |
| Dynamic viscosity of liquid | Burbey, | $v^l = 1 \times 10^{-3} \mathrm{Pa} \cdot \mathrm{s}$ |
| y y 1 | 2014b) | , |
| Dynamic viscosity of carbon dioxide | (Zhou and | |
| | Burbey, | $v^{Sc} = 6 \times 10^{-5} \mathrm{Pa} \cdot \mathrm{s}$ |
| (Sc) | 2014b) | v = 0×10 Tu s |
| | (Zhou and | |
| Bulk modulus of liquid | Burbey, | $K_1 = 2.2 \times 10^3 \text{ MPa}$ |
| Bulk modulus of fiquid | • . | $K_l = 2.2 \times 10^{-1} M$ |
| | 2014b) | |
| Delle we delete of sed on \mathcal{C}_{α} | (Zhou and | $V = 50 \text{MD}_0$ |
| Bulk modulus of carbon dioxide (Sc) | Burbey, | $K_{Sc} = 58 \text{MPa}$ |
| | 2014b) | |
| | (Zhou and | V 74CD |
| Bulk modulus of solid | Burbey, | $K_s = 74 \mathrm{GPa}$ |
| | 2014b) | |
| chemical rate constant CaCO ₃ | (Xu et al., | $k_{mte} = 1.6 \times 10^{-9} \text{ mol} \cdot \text{m}^{-2} \cdot \text{s}^{-1}$ |
| chemical rate constant Suco3 | 2003) | rate = 1.0×10 mor m |
| | (Sokama- | |
| Specific heat capacity of ScCO ₂ | Neuyam et | $c_H^{Sc} = 0.895 \mathrm{kJ \cdot kg^{-1} \cdot K^{-1}}$ |
| | al., 2022) | |
| Charific heat come sites of sucton | (Wagner and | $c_H^W = 4.180 \mathrm{kJ \cdot kg^{-1} \cdot K^{-1}}$ |
| Specific heat capacity of water | Pruß, 2002) | $C_H = 4.160 \mathrm{KJ \cdot Kg} \cdot \mathrm{K}$ |
| | (Waples and | |
| | Waples, | s 0.7701 I 1 -1 IV-1 |
| Specific heat capacity of limestone | 2004; Xiong | $c_H^s = 0.770 \mathrm{kJ} \cdot \mathrm{kg}^{-1} \cdot \mathrm{K}^{-1}$ |
| | et al., 2020) | |
| Thermal expansion coefficient for | (Alungbe et | 6 1 |
| limestone | al., 1992) | $\alpha_s = 9.9 \times 10^{-6} \mathrm{K}^{-1}$ |
| innestone | (Irvine Jr and | |
| Thermal expansion coefficient for | , | $\alpha_{w} = 2.1 \times 10^{-4} \mathrm{K}^{-1}$ |
| water | Duignan, | $\alpha_w = 2.1 \times 10^{\circ} \text{ K}$ |
| Thermal expension coefficient for | 1985) | |
| Thermal expansion coefficient for | (Teymourtash | $\alpha_{sc} = 0.06 \mathrm{K}^{-1}$ |
| $ScCO_2$ | et al., 2013) | α_{Sc} 0.0011 |
| | (Rutqvist et | 14 5001 B |
| Van Genuchten parameters | al., 2002) | $M = 500 \mathrm{kPa}$ |
| | (Rutqvist et | |
| Van Genuchten parameters | al., 2002) | m = 0.43 |
| | (Gaus et al., | |
| | 2005; Lee | |
| Reactive surface area for calcite | | $A rea = 6.71 \times 10^{-2} \text{ m}^2/\text{g}$ |
| | and Morse, | Ç |
| | 1999) | |

| Calcite molar volume | (Gaus et al., 2005; Lee and Morse, 1999) | $V_m^s = 36.93 \times 10^{-6} \mathrm{m}^3/\mathrm{mol}$ |
|--|---|--|
| Rate constant @ $T = 25C^{\circ}$ | (Xu et al., 2003) | $k_{r25} = 1.6 \times 10^{-9} \text{ mol} \cdot \text{m}^2 \cdot \text{s}^1$ |
| Activation energy | (Xu et al., 2003) | 41.87 kJ/mol E_a = |
| Absolute permeability | Assumed | $k_{abs} = 1.4 \times 10^{-17} \text{ m}^2$ |
| Thermal conductivity for limestone | (Çanakci et al., 2007; Stylianou et al., 2016) | $\lambda_s = 2.4 \mathrm{W/m} \cdot \mathrm{K}$ |
| Thermal conductivity for water | (Ramires et al., 1995) | $\lambda_{w} = 0.6 \mathrm{W/m}\cdot\mathrm{K}$ |
| Thermal conductivity for ScCO ₂ | (Sokama- Neuyam et al., 2022) | $\lambda_{Sc} = 0.0339 \mathrm{W/m} \cdot \mathrm{K}$ |

6.7 Results and discussion

Although CO_2 injection often leads to a potential decrease in temperature, this is not always the case. A temperature decrease may occur in low-pressure formations; however, this cooling effect is not universal across all formations or scenarios. In formations with high geothermal gradients, for example, the injected CO_2 may maintain or even temporarily increase the local temperature due to compressive forces and heat exchange with the surrounding rock. Furthermore, the cooling effect may be less pronounced in high-pressure formations, where CO_2 remains in a supercritical phase without significant expansion, allowing for greater storage capacity due to its higher density. It is also

important to note that the presented framework is capable of simulating the opposite effect.

While the thermal energy related to chemical reactions has been ignored to simplify the discussion, it is worth noting that the dissolution process of calcite in carbonic acid is exothermic, with an enthalpy change (ΔH) of approximately -19.5 kJ/mol added to the system.

For this study, in the first scenario, the first scenario, a non-isothermal case, $ScCO_2$ is injected with a temperature $T_{in}=350K$, while the initial rock temperature is $T_i=303K$, and the right boundary condition of the rock sample is kept constant at $T_r=303K$. T_r remains constant to represent the far side of the rock formation in the CCS injection process, which, in reality, is too distant for the temperature to change significantly over time. Conversely, for the isothermal case, the injected temperature is assumed to remain constant at $T_{in}=T_i=T_r=303K$.

Figure 6.3 illustrates the change in temperature across the rock sample. Given the relatively small size of the sample and its high thermal conductivity, the temperature stabilises rapidly, within 200h. As anticipated, the temperature has a significant impact on the chemical reaction leading to dissolution. Figure 6.4 compares the reaction rate between the isothermal and non-isothermal scenarios. The heightened reaction rate resulting from the temperature increase leads to a quicker dissolution process, as shown by the concentration of the dissolved calcite in Figure 6.5 for both isothermal and non-isothermal conditions. Moreover, in Figure 6.4, the rate of dissolution for the non-

isothermal case follows the temperature distribution (Figure 6.3), stabilising at 200h. Conversely, for the isothermal case, the constant temperature leads to a reduction in the reaction rate over time as the reaction kinetics are approached.

The change in rock sample permeability is regarded as a critical factor in practical applications. In CCS, an increase in permeability means it is easier to inject more carbon without needing more advanced equipment to handle higher pressures. According to the Kozeny-Carman relation, described in Equation (6.83), permeability is directly related to dynamic porosity.

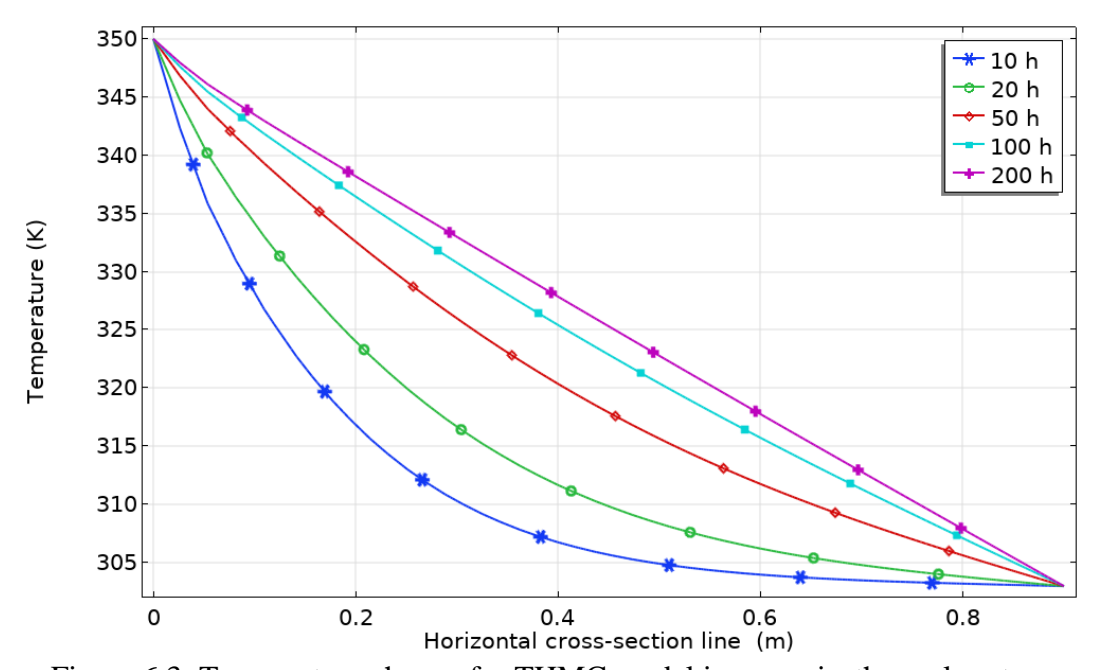


Figure 6.3: Temperature change for THMC model in a non-isothermal system.

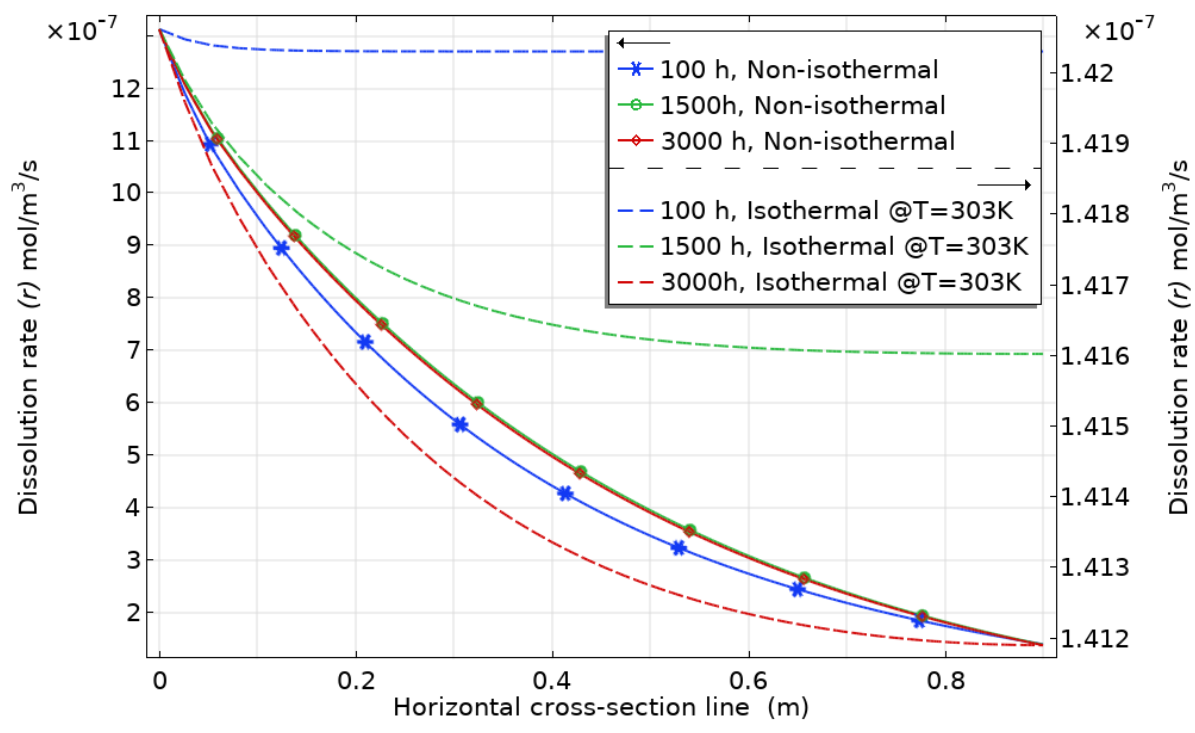


Figure 6.4: Dissolution rate *r* for THMC vs HMC model.

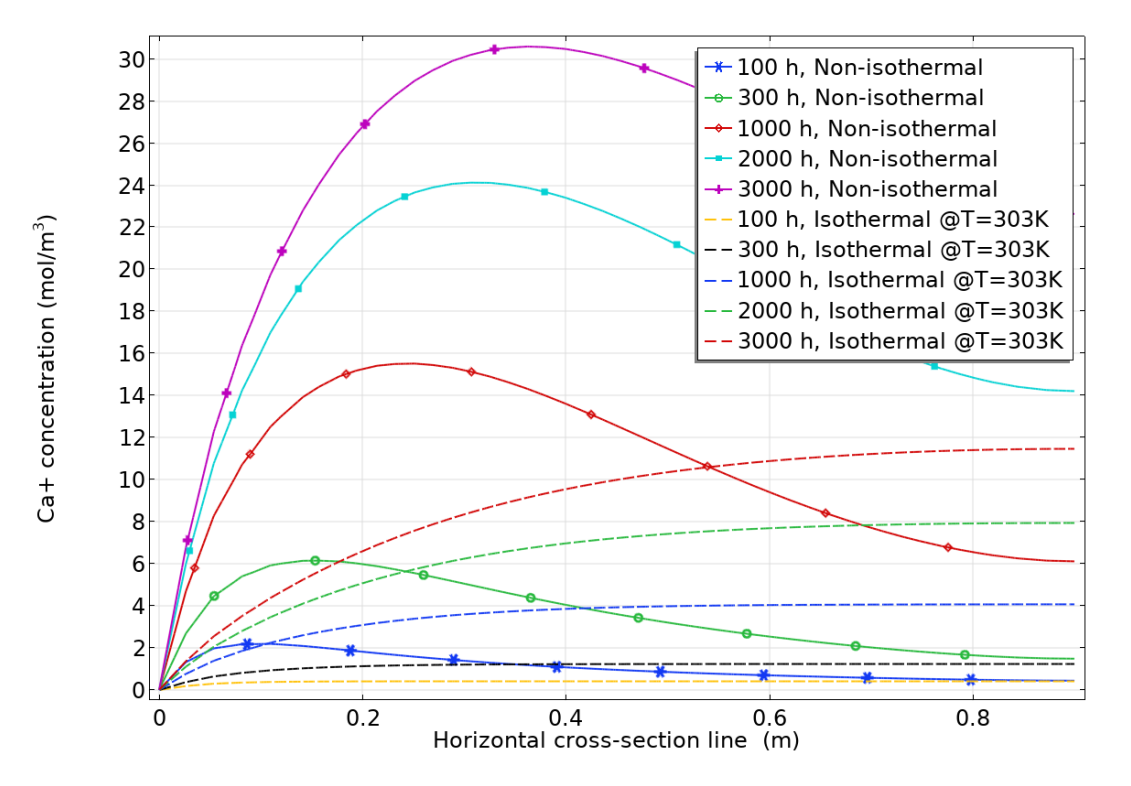


Figure 6.5: Calcium ions concentration in isothermal (HMC) vs non-isothermal (THMC) condition.

Equation (6.51) indicates that there are four coupling terms that affect dynamic porosity and thus, permeability. To investigate the effect of each term, the value of each component at Point 1 is plotted in Figure 6.6. The terms are: strain component $\zeta \varepsilon_{ii}$, pressure component Qp^p , thermal component NT, and chemical reaction component $D\xi$. The strain component $\zeta \varepsilon_{ii}$ has a negative value, indicating reduction effect on the porosity, but it has a relatively small effect compared to the thermal and chemical effect. The pressure term Qp^p maintains steady positive values, as expected, demonstrating an effect of pushing the pore from the inside out, and thus, increasing the porosity. Rock properties such as Young's modulus directly influence the pressure coupling term, since harder rock is more difficult to deform and thus, the effect of pressure on porosity is less pronounced.

The thermal term NT has the most reduction effect on the porosity. Because the thermal term is a function of the thermal expansion of the solid, as the solid heats up, it expands, compressing the pores and subsequently reducing their size, which is evidenced by the negative value on the graph. Furthermore, since thermal equilibrium reached quickly, around 200h, the primary decline in the porosity term occurs within this timeframe. After this point, the figure shows an almost steady flat line, indicating that the direct reduction effect of thermal expansion has ended. The chemical term $D\xi$ has also notable impact on porosity by dissolving the solid and creating additional voids or pores in the solid matrix. It is important to note that the chemical term is also coupled with the thermal part, in which the kinetic and rate constants are functions of the temperature. Therefore, the rate of the reaction will increase with the rise in temperature. While the rise in the

temperature of the solid matrix reduces porosity, the dissolution process will continue to happen beyond the 3000h as shown in Figure 6.7 and Figure 6.8.

Figure 6.7 illustrates the change in porosity and permeability for r both the HMC and THMC models over a period of 3000h. The porosity and permeability in the THMC have more reduction due to higher heat transfer. However, Figure 6.8 presents the evolution of porosity beyond the 3000h mark. A red circle and arrow highlight the area where the porosity first decreases and then rises again, and this zone is separately depicted in Figure 6.9. The chemical dissolution process leads to an increase in porosity, which subsequently returns to its initial value of 0.123 over a span of approximately 7.5 months, as demonstrated in Figure 6.9. Following this period, the porosity continues to ascend, reaching a value of 0.134 over 20 years, as depicted in Figure 6.8.

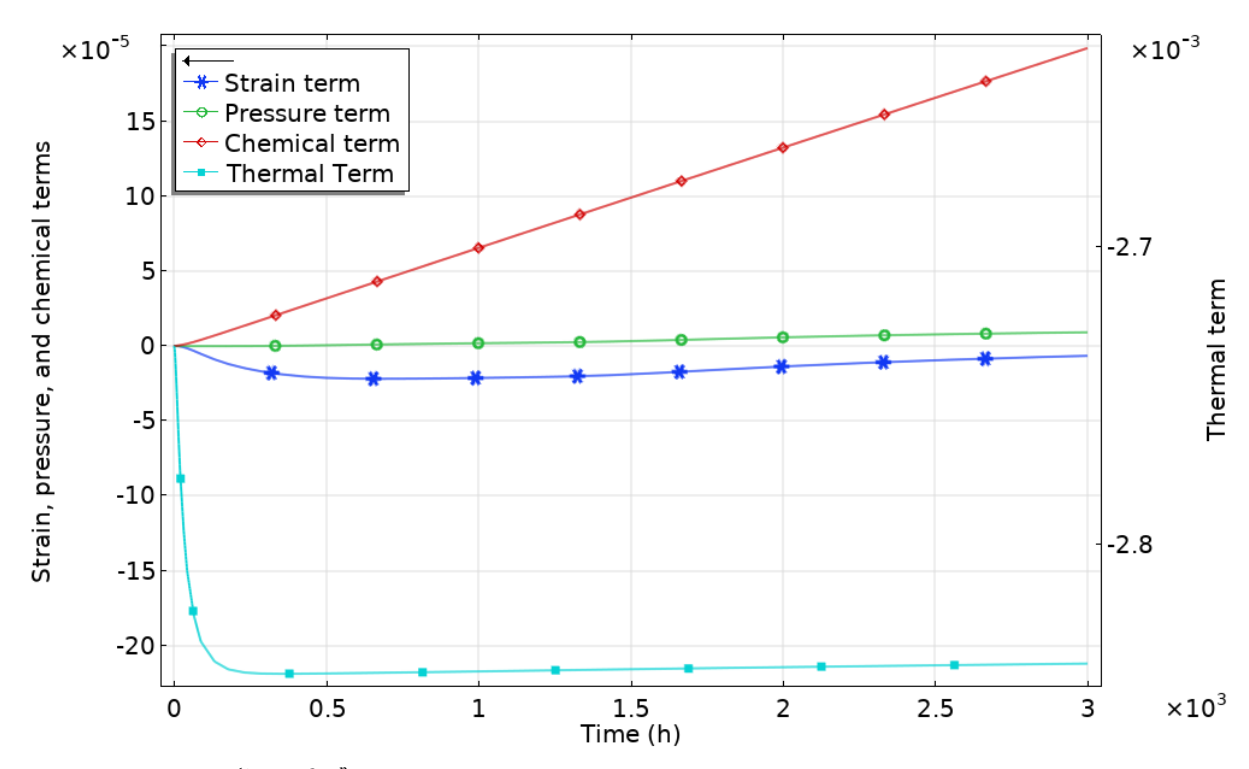


Figure 6.6: $\zeta \mathcal{E}_{ii}$, Qp^p , $D \xi$, and NT coupling terms of the dynamic porosity for THMC model.

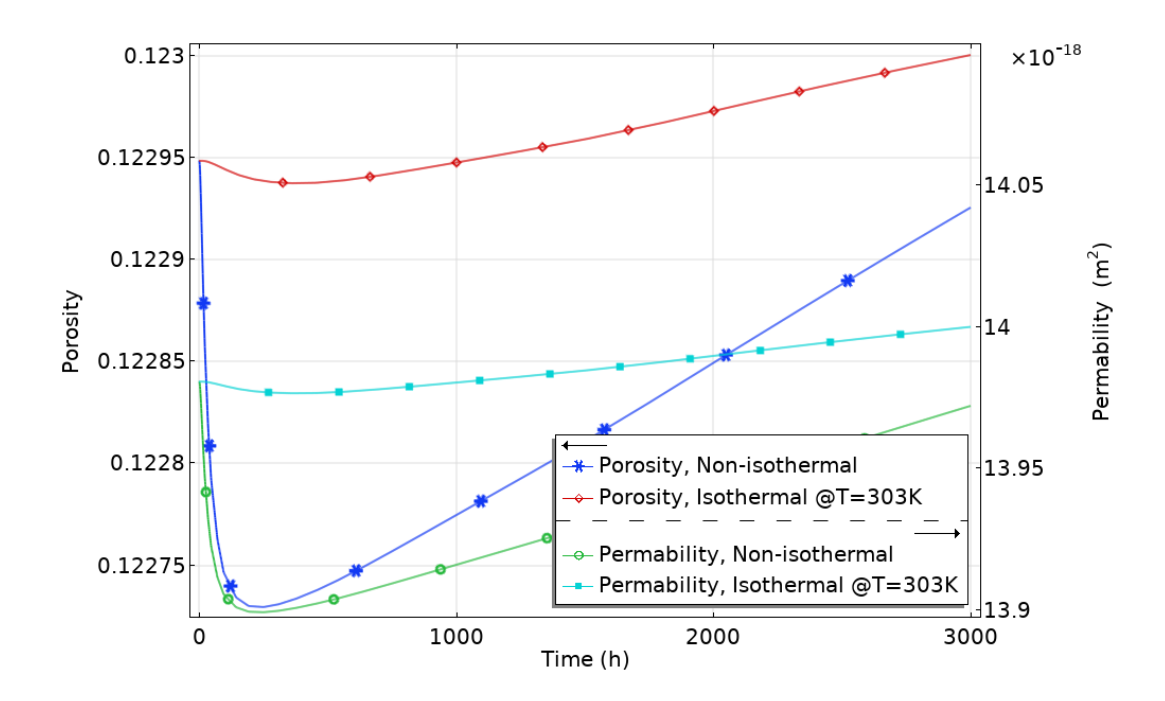


Figure 6.7: Change in porosity and permeability for HMC vs THMC model in 3000h.

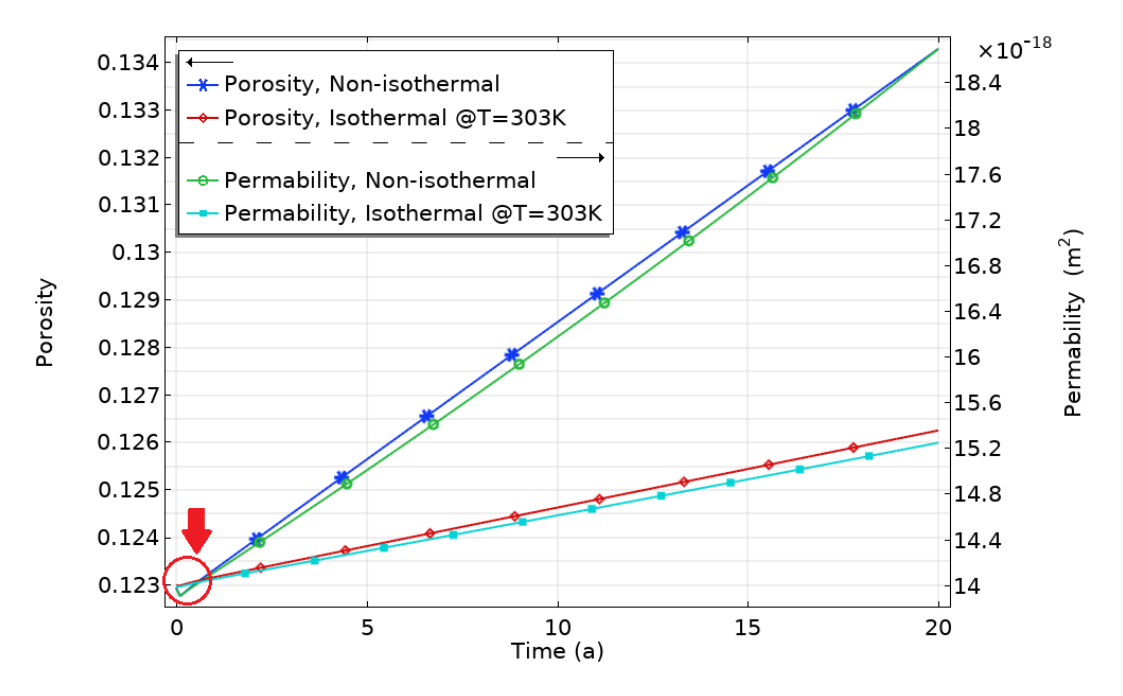


Figure 6.8: Change in porosity and permeability for HMC vs THMC model in 20 years.

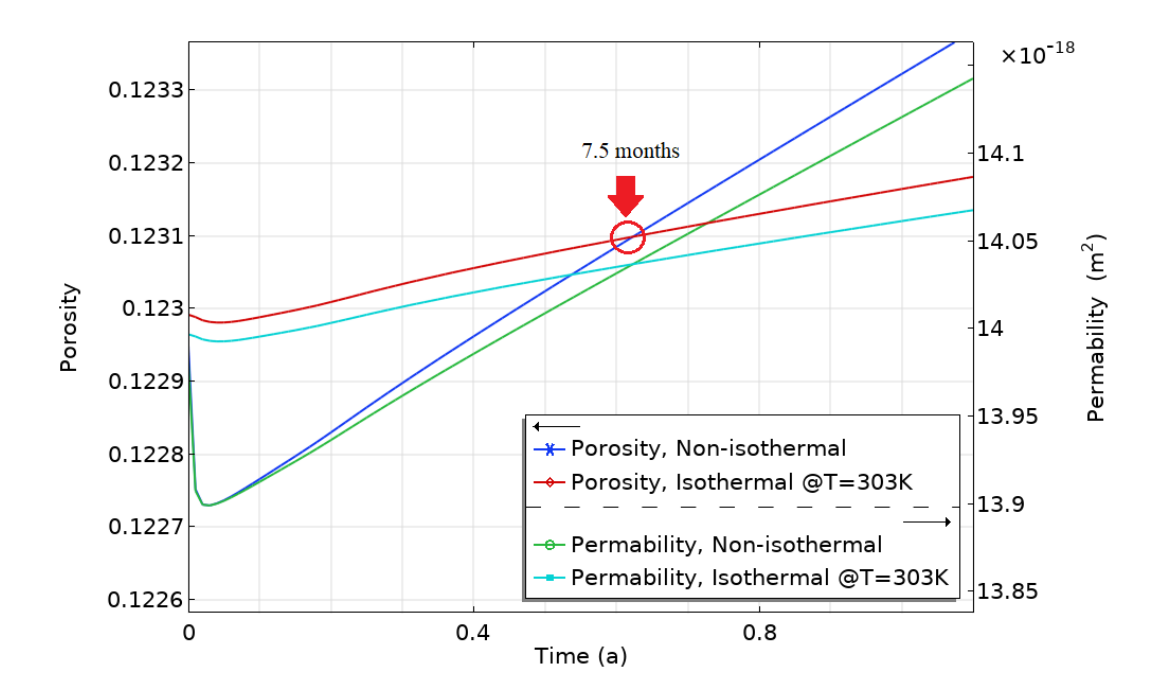


Figure 6.9: The porosity returns to its initial value in about 7.5 months.

Figure 6.10 illustrates the horizontal displacement (deformation) of the porous media across the sample for both isothermal and non-isothermal case scenarios. In the isothermal model, there is more deformation up to 1000h. However, upon reaching 2000h, the displacement reduces. This reduction is a result of the chemo-thermal coupling effect on the mechanical deformation term. As the temperature rises for the non-isothermal condition, the dissolution rate accelerates, leading to an increase in porosity and a lessening effect on the stress.

The deformation directly correlates with the capillary pressure p^c and the physical properties of the solid matrix. Figure 6.11 displays the inverse relationship between the capillary pressure and the deformation of the porous media.

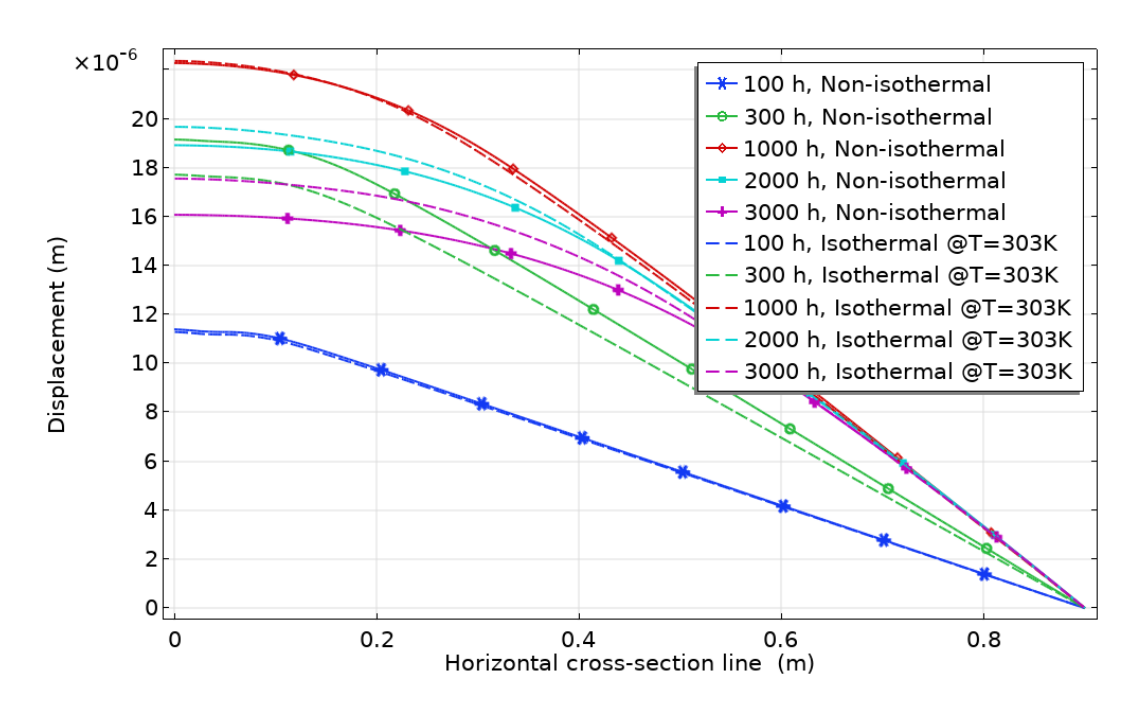


Figure 6.10: Horizontal displacement across the rock sample at different times for HMC vs THMC model.

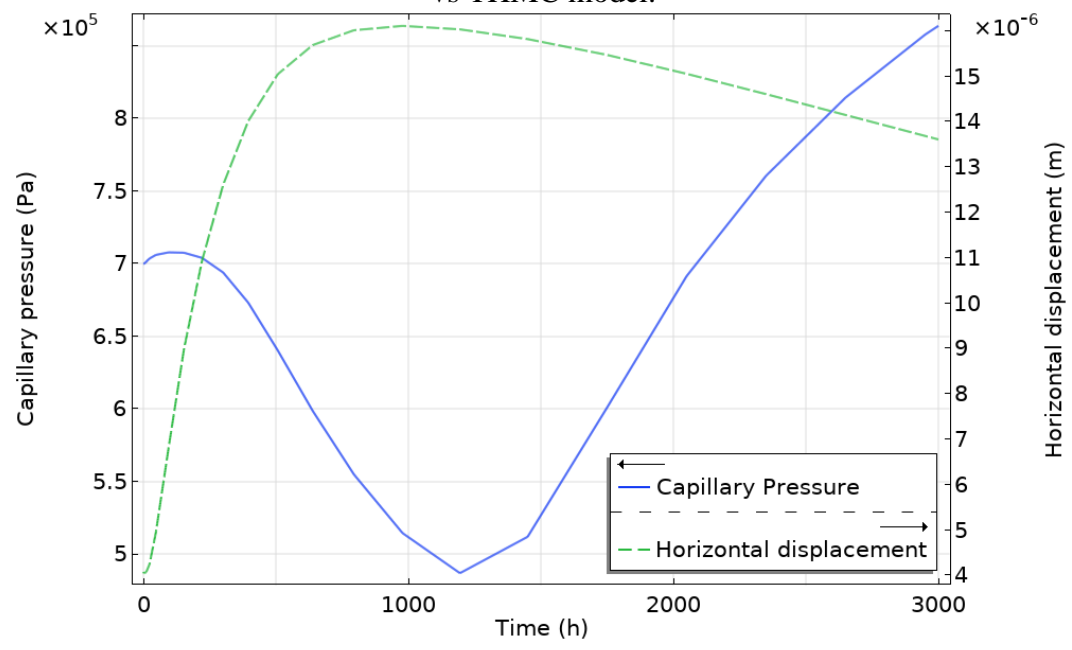


Figure 6.11: Horizontal displacement (deformation) and capillary pressure at Point 1 in the sample for HMC vs THMC model.

Figure 6.12 and Figure 6.13 present a comparison of the liquid and supercritical fluid pressure in both case scenarios (isothermal vs non-isothermal), demonstrating the impact of temperature on pressure. The shift in pressure is associated with various physical properties, but the dominant factor is the dynamic porosity (and subsequently, fluid

permeability), which is tightly coupled with temperature via dissolution. Both isothermal and non-isothermal cases start with nearly the same pressure, but as time progresses, the pressure difference between the two scenarios increases. This is because thermal transport accelerates the dissolution rate and enhances permeability over time. This also explains why the pressure in the non-isothermal case reaches equilibrium more quickly than in the isothermal scenario.

Figure 6.14 illustrates the permeability of the liquid $(k_1 = k_{sl} \cdot k_{abs})$, while Figure 6.15 presents the permeability for the supercritical phase. These plots reflect the Van Genuchten equations, with relative permeability being a function of saturation, and saturation in turn being a function of capillary pressure p^c . The correlation between the behaviour of liquid permeability and the liquid saturation (as seen in Figure 6.16) is noticeable, with a similar correlation observed between Figure 6.15 and Figure 6.17 for the supercritical phase. Furthermore, Figure 6.17 reveals that for the non-isothermal case scenario, the $ScCO_2$ saturation s^{sc} at the left boundary decreases, even as the $scco_2$ permeability k_{sc} increases (as shown in Figure 6.15). This is because the absolute permeability is increasing as the porosity enlarges, which heightens the $scco_2$ permeability $scco_2$ permeability $scco_3$ permeability $scco_4$ permeability $scco_5$ permeability $scco_6$ permeability $scco_6$ permeability $scco_6$ permeability $scco_6$ permeability $scco_6$ permeability $scco_6$ permeability permeability permeability $scco_6$ permeability permeability

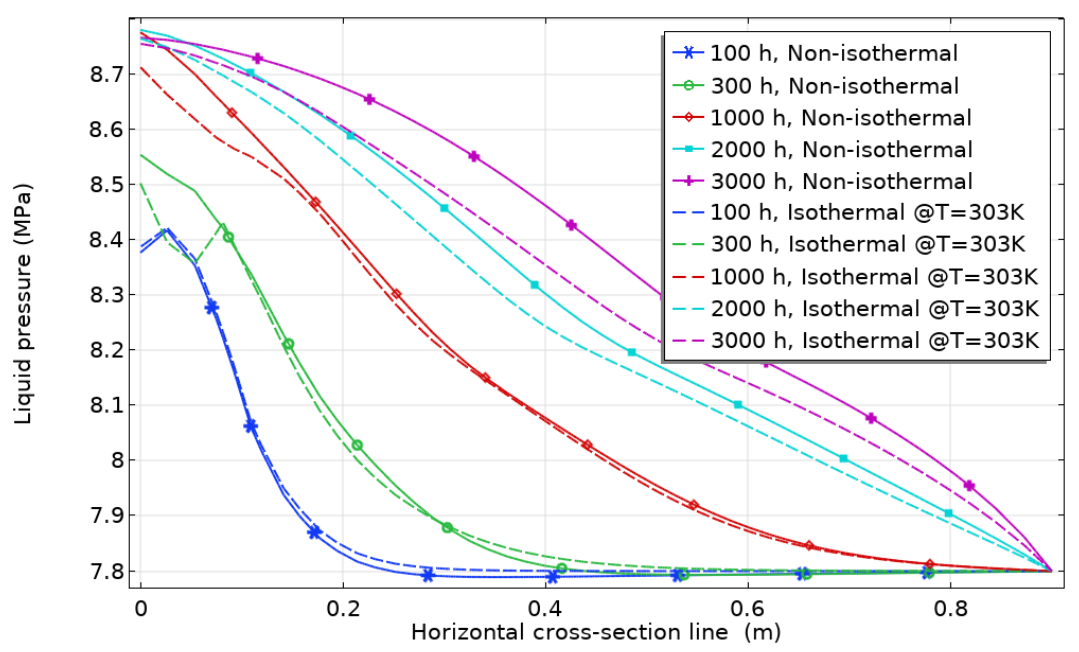


Figure 6.12: Liquid pressure for isothermal and non-isothermal conditions at various times across the horizontal section of the sample rock for HMC vs THMC model.

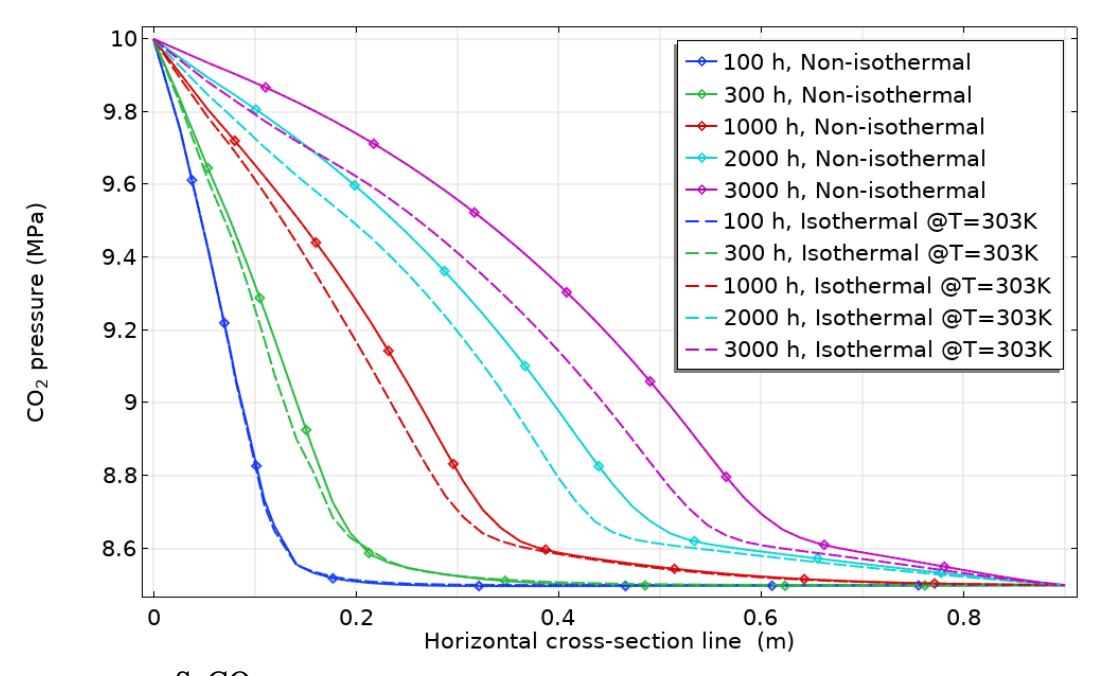


Figure 6.13: ScCO₂ pressure for isothermal and non-isothermal conditions at various times across the horizontal section of the sample rock for HMC vs THMC model.

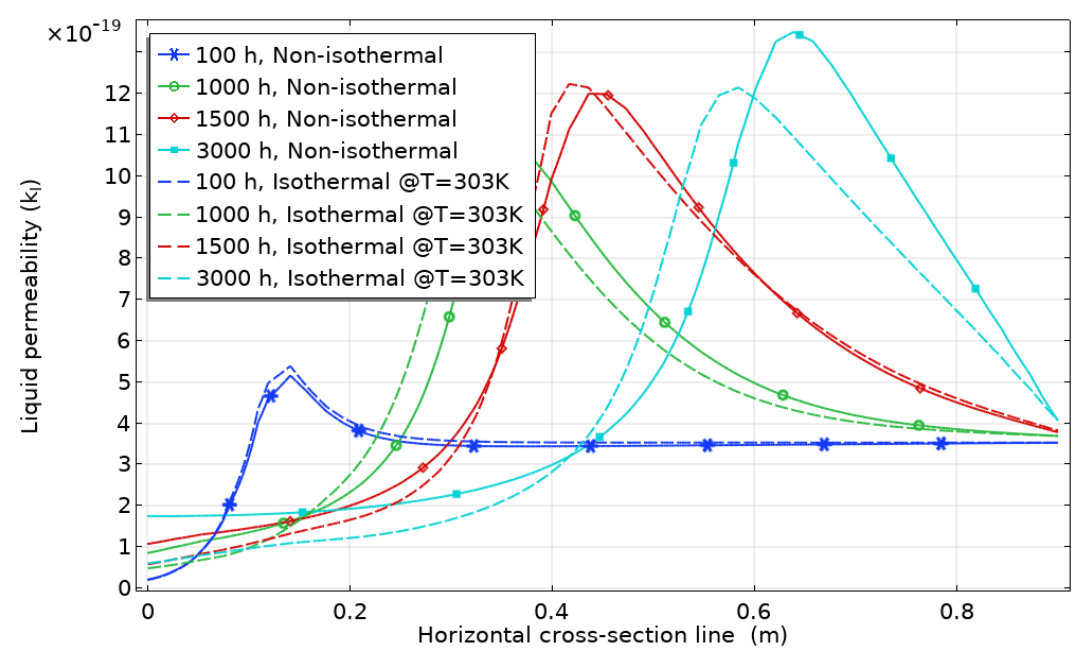


Figure 6.14: Permeability of the liquid for HMC vs THMC model.

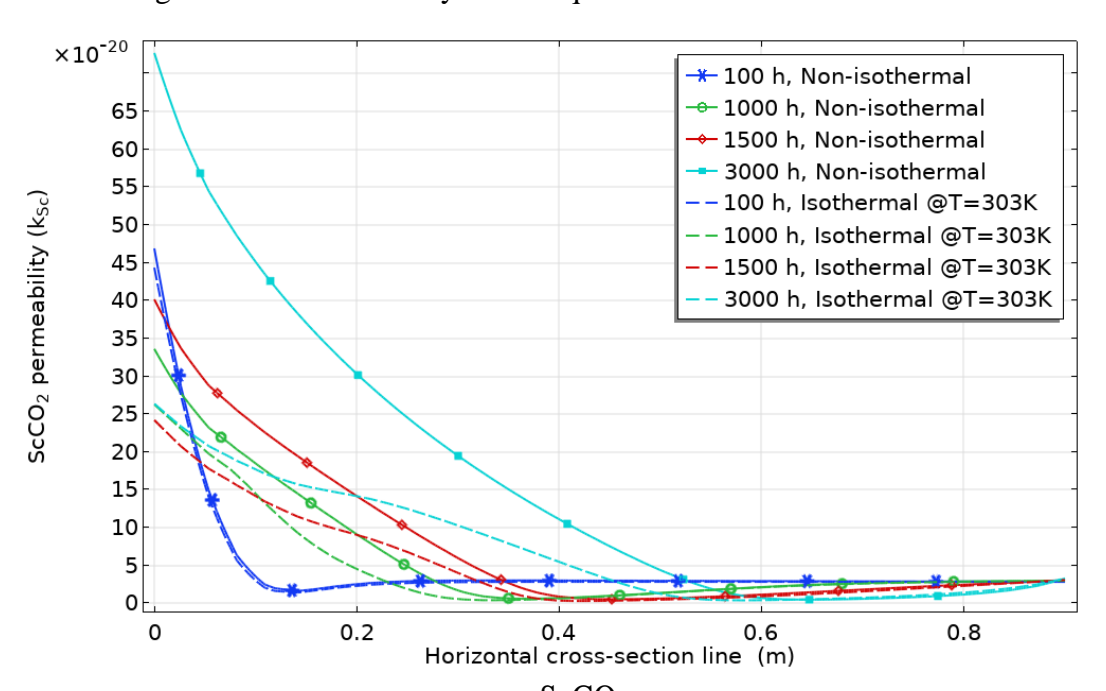


Figure 6.15: Permeability of the $ScCO_2$ for HMC vs THMC model.

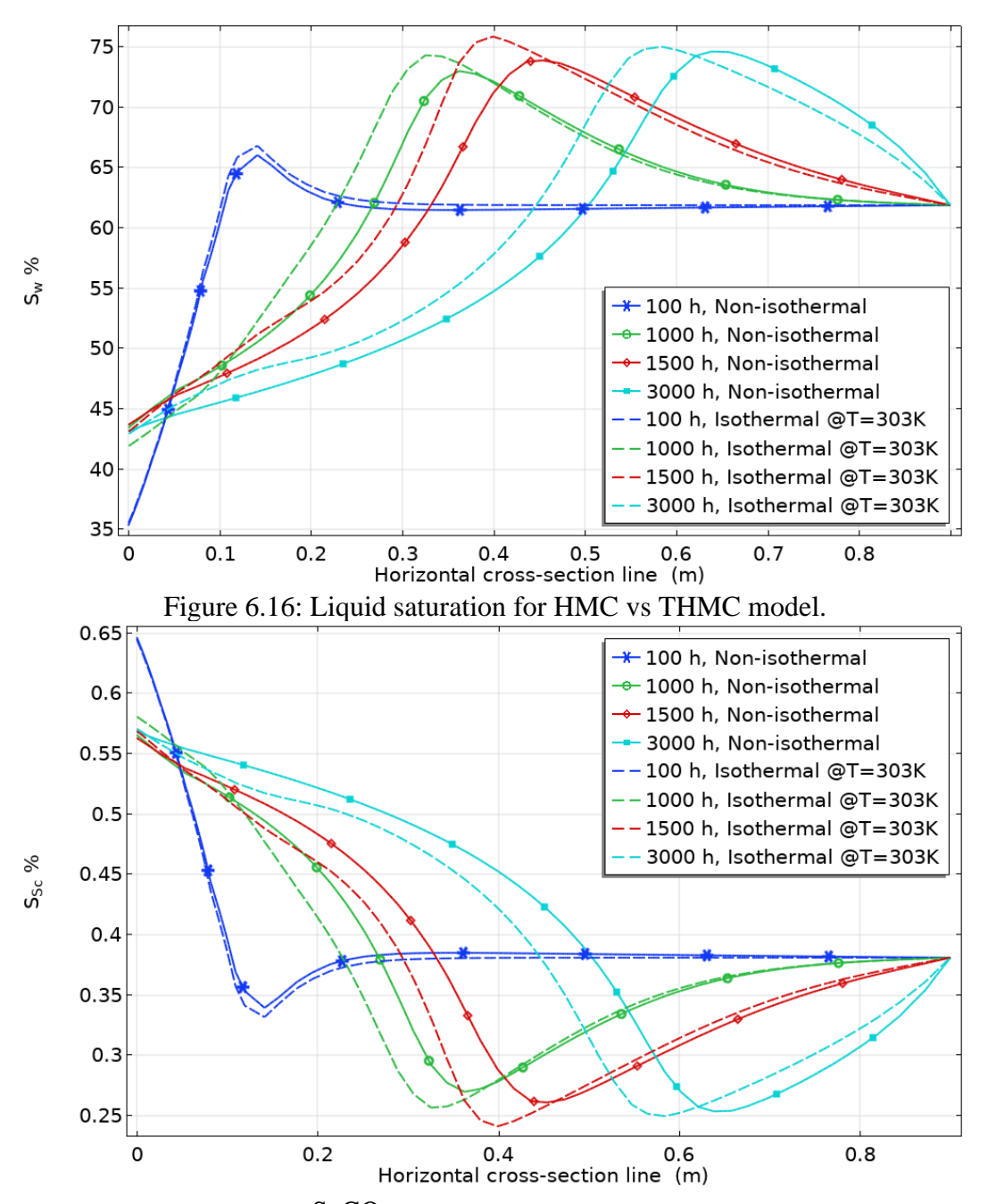


Figure 6.17: $ScCO_2$ saturation for HMC vs THMC model.

In conclusion, the coupling effects in THMC are complex, even when the focus is solely on the impact of temperature. There are both direct and indirect coupling mechanisms at play. Direct coupling refers to the inclusion of the temperature term directly in the governing equations of the solid, liquid, supercritical phase, and chemical reactions. Indirect coupling, however, occurs when temperature affects porosity through the thermal

expansion of the solid, which in turn impacts all other states. Additionally, temperature influences chemical reactions (like dissolution), which affect porosity by increasing void spaces (pores), once again affecting all states.

6.8 Conclusion

This research culminated in the development of a fully coupled Thermo-Hydro-Mechanical-Chemical (THMC) model. This was derived utilising an energy approach known as the mixture-coupling theory. This method employs the entropy balance equation alongside the mass balance equation. Additionally, phenomenological equations are utilised to determine the coupling effect between four flows and three driving forces. Notably, Maxwell's relations were pivotal in revealing the intricate coupling amongst mechanical properties (stress/porosity), hydraulic aspects (pressure), chemical reactions, and thermal elements (temperature).

Five governing equations have been established to effectively capture the behaviours of the solid, liquid, supercritical phase, chemical, and thermal constituents. The model takes into account a two-phase flow consisting of a liquid phase and a supercritical phase. Within the chemical reaction dimension, only the dissolution process has been incorporated. A conceptual model was then numerically solved utilising the finite element method via COMSOL Multiphysics® software.

The numerical model facilitated exploration of various aspects, including the impact of temperature coupling on calcite dissolution during the injection process, and its subsequent effects on pressure. The influence of temperature coupling was investigated by juxtaposing a non-thermal transport Hydro-Mechanical-Chemical (HMC) coupled

model under isothermal conditions with a THMC coupled model under non-isothermal condition cases.

The results reveal that non-isothermal conditions significantly influence the dissolution process, notably affecting porosity evolution, permeability, pressure, and strain. Porosity evolution is governed by four primary coupling terms that depend on strain, pressure, chemical reaction rate, and temperature. The numerical simulation shows that strain has the least reduction effect on porosity and permeability, while thermal transport has the most pronounced reduction impact until thermal equilibrium is reached. This leads to a decline in porosity and permeability in the initial months of the injection process. However, as thermal equilibrium is approached, chemical dissolution begins to increase porosity and permeability again. As the reaction rate increases with higher temperatures, both porosity and permeability increase, enhancing the injectivity of CO₂. Moreover, the influence of pore pressure on porosity is greater than that of strain, but less than chemical dissolution and thermal effects. In summary, if chemical reactions are overlooked, thermal transport decreases porosity, while pressure increases it. These effects are dependent on the thermal expansion and mechanical properties of the solid matrix. Additionally, a higher injection temperature leads to improved injectivity in the long run for calcite-rich formations.

For future research, several recommendations can be suggested. These include incorporating mass exchange between fluid phases, such as evaporation and solubility in liquid water, which can influence the pH of the liquid. The relationship between solubility in liquid water and temperature could improve the accuracy of the dissolution rate prediction. Including convective heat transfer between fluids, and taking into account the

precipitation process, which could have a significant impact on porosity, are also crucial for future investigations. Additionally, the heat energy generated (exothermic reactions) or absorbed (endothermic reactions) should be incorporated into the model for more accurate predictions, as these reactions can significantly affect temperature, fluid properties, and chemical reaction rates.

Chapter 7: Conclusion and future work recommendations

7.1 Conclusion

In the conclusion, this thesis walks through the process of creating a two-phase fully coupled THMC reactive transport model for fluids in deformable porous media that can be used in CCS application. The model is based on an energy approach that utilise equilibrium thermodynamics and continuum mechanics to derive the main equations (mixture-coupling theory). The aim of this research was to advance the existing model further and improve the coupling relations of the THMC framework specifically for the CCS injection process. This thesis employs a build-up method to develop complex governing equations, starting with a basic two-phase novel model and progressively building upon it in each chapter. Advanced finite element software has been used in each chapter to demonstrate the capability of the model compared to some other existing ones. The summary of the build-up progress can be layout as following:

Chapter 3: This chapter developed a hydro-mechanical-gas (HMG) model by extending the mixture-coupling theory to include water and gas flow. It integrates Helmholtz free energy equations and Biot's model to examine the interplay between solid deformation and pressure changes, including water saturation and gas flow effects. Validated against experimental data from Liakopoulos (1965a) and Popp et al. (2008), and compared with Schrefler and Scotta (2001) solutions, the model was numerically solved using COMSOL software. It showed good agreement with experimental findings, with minor deviations in air pressure results attributed to differences in governing equations and solution algorithms. The model's gas flowrate validation indicated strong concordance in the

elastic phase. Primarily beneficial for oil field studies, specifically in ${\rm CO_2}$ injection simulations, this study opens avenues for future research, suggesting the inclusion of variable boundary conditions and further experiments on two-phase fluid flow in deformable porous media.

Chapter 4: This chapter introduced a comprehensive multi-phase hydro-mechanical-supercritical-chemical (HMScC) model under isothermal conditions, formulated using mixture-coupling theory. It innovatively incorporates terms that describe the interactions between supercritical and liquid phases and their coupling with chemical solute transport, alongside considering the relationship between solid deformation and pressure changes. Grounded in Helmholtz's free energy equations and Biot's poroelasticity model, the model's validity was confirmed with experimental data and solved numerically via COMSOL Multiphysics® using the finite element method (FEM). The results closely matched experimental observations and the findings of Schrefler and Scotta (2001). While the introduced terms' influence appears minimal due to the slow flow nature of the experiments, it's anticipated that their impact would be more pronounced under conditions of faster fluid injection, suggesting a potentially aggressive two-phase interaction. The model currently simulates a single solute, but in larger applications like carbon sequestration, the presence of multiple solutes could significantly enhance the model's applicability and impact.

Chapter 5: This chapter introduced a cutting-edge methodology for modelling carbon dioxide sequestration through a reactive multi-phase hydro-mechanical chemical system, leveraging coupling mixture theory to bridge the existing knowledge gap between chemical and mechanical interactions, particularly their connection to stress and strain.

By incorporating reaction extent and solid affinity, the study illustrates the essential role of chemical reactions within the hydro-mechanical context. Using limestone samples, the simulations conducted under isothermal conditions underscored how chemical reactions critically influence porosity and mechanical strain in geological formations, demonstrating changes in liquid pressure, supercritical pressure, solid deformation, and porosity over time. This work establishes a fundamental framework for understanding the impact of chemical reactions on the hydro-mechanical properties of geological formations, essential for advancing carbon sequestration strategies. However, the model assumes negligible energy loss from solute transport and simplifies liquid properties, indicating areas for future enhancements, such as incorporating thermal dynamics, precipitation, and mass transfer processes to improve the model's accuracy and relevance.

Chapter 6: This chapter successfully developed a Thermo-Hydro-Mechanical-Chemical (THMC) model, leveraging mixture-coupling theory and an energy-based approach that integrates the entropy and mass balance equations, alongside phenomenological equations to explore the interactions among mechanical properties, hydraulic pressures, chemical reactions, and thermal elements. Key to this approach were Maxwell's relations, which elucidated the complex interdependencies within the model. The framework comprises five core equations addressing the behaviour of solid, liquid, supercritical, chemical, and thermal elements, focusing on a two-phase flow and specifically modelling the dissolution process in the chemical component. The model was executed through COMSOL Multiphysics® using the finite element method.

The study primarily investigated how temperature affects calcite dissolution during CO₂ injection and its subsequent influence on pressure, contrasting the findings with those from a non-thermal transport Hydro-Mechanical-Chemical model under isothermal conditions. Findings indicate that non-isothermal conditions significantly impact dissolution rates, affecting porosity evolution, permeability, pressure, and strain. Notably, thermal transport had the most substantial effect on reducing porosity and permeability until thermal equilibrium was achieved, after which chemical dissolution started to reverse this trend, increasing both porosity and permeability due to higher reaction rates at elevated temperatures. This enhancement in porosity and permeability boosts injectivity in calcite-rich formations.

The study underscores the critical role of thermal and chemical dynamics in the injection process, suggesting future research should address mass exchange between fluid phases, the impact of temperature on liquid water's solubility and pH, convective heat transfer, and the precipitation process to refine the model's accuracy and extend its applicability.

7.2 limitation, and future work recommendations

In this work, a fully coupled two-phase THMC has been established to simulate CCS transport process, however, there is more work need to be done to improve the model even further. Future research may investigate the following:

1. Miscible and Immiscible Systems: This research focused on immiscible systems and assumed that CO₂ remained in its supercritical phase throughout the simulations. However, at the reservoir scale, phase transitions between supercritical CO₂ (ScCO₂) and gaseous CO₂ can occur due to variations in

pressure and temperature. These transitions can significantly affect the behaviour of CO₂, including its solubility in water and its interactions within the porous media. Future research should explore the impact of these phase transitions, as well as the dynamic interaction between miscible and immiscible systems, to better capture the complexities of CO₂ transport and storage in real-world CCS scenarios.

- 2. Fractured Porous Media: This model did not explore fractured media; however, many CCS applications exist in fractured environments. Injecting CO₂ into fractured porous media might be more efficient due to increased permeability.
- 3. Heat Transfer Among Fluids: Besides heat transfer between the porous media (solid phase) and the mixture (fluid phase), heat transfer occurs among the fluids themselves (e.g., ScCO₂ and liquid water). This research assumed local equilibrium, simplifying complex phase interactions into manageable mathematical relationships. Future models could extend to non-local equilibrium transport, although this might not be critical for CCS transport due to the typically slow rates of transport where local equilibrium may closely approximate reality.
- 4. Energy from Chemical Reactions: This research did not include the heat energy generated by exothermic reactions or absorbed by endothermic reactions. Incorporating these energy changes in future models is crucial for more accurate predictions, as such reactions can significantly influence temperature, fluid properties, and chemical reaction rates.
- 5. Precipitation Processes: Although dissolution processes are included (as described in Chapter 6, precipitation was not addressed. Adding precipitation processes could be crucial for CCS, as various minerals might react, precipitate,

- and subsequently reduce both porosity and permeability, affecting injection rates. Further chemical reactions should also be considered to simulate more complex and realistic scenarios.
- 6. Isotropic vs. Anisotropic Porous Media: This research dealt only with isotropic porous media, suitable for homogeneous formation layers distant from reservoir boundaries. However, modelling transition zones between different formations might require addressing anisotropic media, which could be explored in future research.
- 7. Joule-Thomson Cooling: In scenarios where high-pressure CO₂ is injected into pressure-depleted formations, the sudden pressure drop may induce a temperature decrease, potentially freezing parts of the mixture near the injection bore and temporarily reducing permeability. This effect, known as Joule-Thomson cooling, was not included in this research but could be explored in future studies.
- 8. Field Data Comparison: While this research includes many simulation cases, some against experimental data, it lacks comparison with field data directly related to CCS processes. Future studies could employ 3D simulations or compare findings with actual field data to validate the model against real CCS scenarios.
- 9. Elasticity: This model assumes that the solid porous media are elastic; however, in reality, rocks can reach plastic deformation if the stress exceeds a certain value. Different formations, such as clay, sand, dolomite, and others, have distinct elastic/plastic properties. The impact of plasticity needs to be addressed in future research.

- 10. Swelling: The swelling effect that may occur when some fluids react with the solid matrix, such as water and clay, was not considered in this model. Future research could extend the model to include the swelling effect.
- 11. Challenges of Scaling to Larger Spatial Scales: The current model uses small spatial scales in the simulations, which are suitable for proving the concept and aid in computational efficiency and detail. However, scaling up to larger, real-world scales may present additional challenges. These include the increased computational cost of simulating larger domains, especially for 3D models. Larger scales can introduce new complexities, requiring more advanced numerical methods and higher computational power to maintain accuracy (such as solving a large number of fine mesh elements). Future research should address these challenges to better adapt the model for larger-scale applications, such as industrial-scale CCS operations.

These recommendations aim to address current model limitations and expand the applicability and accuracy of future simulations. By exploring and integrating these enhancements, the model can better adapt to reflect the complexities of real-world processes. This progression will not only improve predictive capabilities but also foster more robust and comprehensive tools for scientific and industrial applications.

References

- ABDULLAH, S., MA, Y., CHEN, X. & KHAN, A. 2022. A fully coupled hydro-mechanical-gas model based on mixture coupling theory. *Transport in Porous Media*, 1-22.
- ABIDOYE, L. K., KHUDAIDA, K. J. & DAS, D. B. 2015. Geological carbon sequestration in the context of two-phase flow in porous media: a review. *Critical Reviews in Environmental Science and Technology*, 45, 1105-1147.
- ADU, E., ZHANG, Y. & LIU, D. 2019. Current situation of carbon dioxide capture, storage, and enhanced oil recovery in the oil and gas industry. *The Canadian Journal of Chemical Engineering*, 97, 1048-1076.
- AHMADI GOLTAPEH, S., RAHMAN, M. J., MONDOL, N. H. & HELLEVANG, H. 2022. Artificial Neural Network-Based Caprock Structural Reliability Analysis for CO2 Injection Site—An Example from Northern North Sea. *Energies*, 15, 3365.
- AKONO, A. T., DRUHAN, J. L., DÁVILA, G., TSOTSIS, T., JESSEN, K., FUCHS, S., CRANDALL, D., SHI, Z., DALTON, L., TKACH, M. K., GOODMAN, A. L., FRAILEY, S. & WERTH, C. J. 2019. A review of geochemical–mechanical impacts in geological carbon storage reservoirs. *Greenhouse Gases: Science and Technology*, 9, 474-504.
- ALCALDE, J., HEINEMANN, N., JAMES, A., BOND, C. E., GHANBARI, S., MACKAY, E. J., HASZELDINE, R. S., FAULKNER, D. R., WORDEN, R. H. & ALLEN, M. J. 2021. A criteria-driven approach to the CO2 storage site selection of East Mey for the acorn project in the North Sea. *Marine and Petroleum Geology*, 133, 105309.
- ALONSO, J., NAVARRO, V., CALVO, B. & ASENSIO, L. 2012. Hydro-mechanical analysis of CO₂ storage in porous rocks using a critical state model. *International Journal of Rock Mechanics and Mining Sciences*, 54, 19-26.
- ALUNGBE, G. D., TIA, M. & BLOOMQUIST, D. G. 1992. Effect of aggregate, water-cement ratio, and curing on the coefficient of linear thermal expansion of concrete. *Journal of the Transportation Research Record*, 1335, 44-51.

- ANDRÉ, L., AUDIGANE, P., AZAROUAL, M. & MENJOZ, A. 2007a. Numerical modeling of fluid—rock chemical interactions at the supercritical CO2—liquid interface during CO2 injection into a carbonate reservoir, the Dogger aquifer (Paris Basin, France). *Energy conversion and management*, 48, 1782-1797.
- ANDRÉ, L., AUDIGANE, P., AZAROUAL, M. & MENJOZ, A. 2007b. Numerical modeling of fluid—rock chemical interactions at the supercritical CO₂—liquid interface during CO₂ injection into a carbonate reservoir, the Dogger aquifer (Paris Basin, France). *Energy Conversion and Management*, 48, 1782-1797.
- AUDIGANE, P., GAUS, I., CZERNICHOWSKI-LAURIOL, I., PRUESS, K. & XU, T. 2007. Two-dimensional reactive transport modeling of CO2 injection in a saline aquifer at the Sleipner site, North Sea. *American journal of science*, 307, 974-1008.
- BACHU, S., GUNTER, W. & PERKINS, E. 1994. Aquifer disposal of CO2: hydrodynamic and mineral trapping. *Energy Conversion and management*, 35, 269-279.
- BAI, T. & TAHMASEBI, P. 2022. Coupled hydro-mechanical analysis of seasonal underground hydrogen storage in a saline aquifer. *Journal of Energy Storage*, 50, 104308.
- BANDARA, S., FERRARI, A. & LALOUI, L. 2016. Modelling landslides in unsaturated slopes subjected to rainfall infiltration using material point method. *International Journal for Numerical and Analytical Methods in Geomechanics*, 40, 1358-1380.
- BAO, J., XU, Z. & FANG, Y. 2014. A coupled thermal-hydro-mechanical simulation for carbon dioxide sequestration. *Environmental Geotechnics*, 3, 312-324.
- BAQER, Y. & CHEN, X. 2022. A review on reactive transport model and porosity evolution in the porous media. *Environmental Science and Pollution Research*, 29, 47873-47901.
- BEA, S. A., MAYER, U. & MACQUARRIE, K. 2016. Reactive transport and thermo hydro mechanical coupling in deep sedimentary basins affected by glaciation cycles: model development, verification, and illustrative example. *Geofluids*, 16, 279-300.
- BEA, S. A., WILSON, S. A., MAYER, K. U., DIPPLE, G. M., POWER, I. M. & GAMAZO, P. 2012. Reactive transport modeling of natural carbon sequestration inultramafic mine tailings. *Vadose Zone Journal*. 11.
- BEAR, J. 2013. Dynamics of fluids in porous media, Courier Corporation.

- BEMER, E. & LOMBARD, J. 2010. From injectivity to integrity studies of CO2 geological storage-chemical alteration effects on carbonates petrophysical and geomechanical properties. *Oil & Gas Science and Technology–Revue de l'Institut Français du Pétrole*, 65, 445-459.
- BIOT, M. A. 1941. General Theory of Three Dimensional Consolidation. *Journal of Applied Physics*, 12, 155-164.
- BIOT, M. A. 1955. Theory of Elasticity and Consolidation for a Porous Anisotropic Solid. *Journal of Applied Physics*, 26, 182-185.
- BIOT, M. A. 1962. Mechanics of Deformation and Acoustic Propagation in Porous Media. *Journal of Applied Physics*, 33, 1482-1498.
- BIOT, M. A. & TEMPLE, G. 1972. Theory of finite deformations of porous solids. *Indiana University Mathematics Journal*, 21, 597-620.
- BIRD, R. B., STEWART, W. & LIGHTFOOT, E. 2006. Transport Phenomena.(4thedn). Wiley and Sons: New York.
- BIRKHOLZER, J. T., ZHOU, Q. & TSANG, C.-F. 2009. Large-scale impact of CO2 storage in deep saline aquifers: A sensitivity study on pressure response in stratified systems. *international journal of greenhouse gas control*, 3, 181-194.
- BISSELL, R., VASCO, D., ATBI, M., HAMDANI, M., OKWELEGBE, M. & GOLDWATER, M. 2011. A full field simulation of the In Salah gas production and CO2 storage project using a coupled geomechanical and thermal fluid flow simulator. *Energy Procedia*, 4, 3290-3297.
- BITZER, K. 1996. Modeling consolidation and fluid flow in sedimentary basins. *Computers & Geosciences*, 22, 467-478.
- BJØRNARÅ, T. I., MATHIAS, S. A., NORDBOTTEN, J. M., PARK, J. & BOHLOLI, B. 2014. Capturing the coupled hydro-mechanical processes occurring during CO2 injection example from In Salah. *Energy Procedia*, 63, 3416-3424.
- BOWEN, R. M. 1980. Incompressible porous media models by use of the theory of mixtures. *International Journal of Engineering Science*, 18, 1129-1148.
- BOWEN, R. M. 1982. Compressible porous media models by use of the theory of mixtures. *International Journal of Engineering Science*, 20, 697-735.
- BOWKER, K. A. & SHULER, P. 1991. Carbon dioxide injection and resultant alteration of the Weber Sandstone, Rangely Field, Colorado. *AAPG bulletin*, 75, 1489-1499.

- BROOKS, R. H. & COREY, A. T. 1966. Properties of porous media affecting fluid flow. *Journal of the irrigation and drainage division*, 92, 61-88.
- BROWN, K., WHITTAKER, S., WILSON, M., SRISANG, W., SMITHSON, H. & TONTIWACHWUTHIKUL, P. 2017. The history and development of the IEA GHG Weyburn-Midale CO2 Monitoring and Storage Project in Saskatchewan, Canada (the world largest CO2 for EOR and CCS program). *Petroleum*, 3, 3-9.
- BUCHWALD, J., KAISER, S., KOLDITZ, O. & NAGEL, T. 2021. Improved predictions of thermal fluid pressurization in hydrothermal models based on consistent incorporation of thermomechanical effects in anisotropic porous media. *International Journal of Heat and Mass Transfer*, 172, 121127.
- BUI, M., ADJIMAN, C. S., BARDOW, A., ANTHONY, E. J., BOSTON, A., BROWN, S., FENNELL, P. S., FUSS, S., GALINDO, A. & HACKETT, L. A. 2018. Carbon capture and storage (CCS): the way forward. *Energy & Environmental Science*, 11, 1062-1176.
- CAILLY, B., LE THIEZ, P., EGERMANN, P., AUDIBERT, A., VIDAL-GILBERT, S. & LONGAYGUE, X. 2005. Geological storage of CO2: A state-of-the-art of injection processes and technologies. *Oil & gas science and technology*, 60, 517-525.
- CALVIN, M. 1976. PHOTOSYNTHESIS AS A RESOURCE FOR ENERGY AND MATERIALS*. *Photochemistry and Photobiology*, 23, 425-444.
- ÇANAKCI, H., DEMIRBOĞA, R., KARAKOÇ, M. B. & ŞIRIN, O. 2007. Thermal conductivity of limestone from Gaziantep (Turkey). *Building and environment*, 42, 1777-1782.
- CARDOSO, L., FRITTON, S. P., GAILANI, G., BENALLA, M. & COWIN, S. C. 2013. Advances in assessment of bone porosity, permeability and interstitial fluid flow. *Journal of biomechanics*, 46, 253-265.
- CARRILLO, F. J. & BOURG, I. C. 2021. Modeling Multiphase Flow Within and Around Deformable Porous Materials: A Darcy-Brinkman-Biot Approach. *Water Resources Research*, 57, e2020WR028734.
- CARROLL, S., CAREY, J. W., DZOMBAK, D., HUERTA, N. J., LI, L., RICHARD, T., UM, W., WALSH, S. D. & ZHANG, L. 2016. Role of chemistry, mechanics, and transport on well integrity in CO2 storage environments. *International Journal of Greenhouse Gas Control*, 49, 149-160.

- CARSEL, R. F. & PARRISH, R. S. 1988. Developing joint probability distributions of soil water retention characteristics. *Water resources research*, 24, 755-769.
- CASERINI, S., STORNI, N. & GROSSO, M. 2022. The availability of limestone and other raw materials for ocean alkalinity enhancement. *Global Biogeochemical Cycles*, 36, e2021GB007246.
- CAVANAGH, A. & RINGROSE, P. 2014. Improving oil recovery and enabling CCS: a comparison of offshore gas-recycling in Europe to CCUS in North America. *Energy Procedia*, 63, 7677-7684.
- CHADWICK, A., WILLIAMS, G., DELEPINE, N., CLOCHARD, V., LABAT, K., STURTON, S., BUDDENSIEK, M. L., DILLEN, M., NICKEL, M., LIMA, A. L., ARTS, R., NEELE, F. & ROSSI, G. 2010. Quantitative analysis of time-lapse seismic monitoring data at the Sleipner CO2 storage operation. *Leading Edge (Tulsa, OK)*, 29, 170-177.
- CHATURVEDI, K. R. & SHARMA, T. 2023. Comparative analysis of carbon footprint of various CO2-enhanced oil recovery methods: A short experimental study. *Chemical Engineering Communications*, 1-8.
- CHEN, L., LIU, Y. M., WANG, J., CAO, S. F., XIE, J. L., MA, L. K., ZHAO, X. G., LI, Y. W. & LIU, J. 2014. Investigation of the thermal-hydro-mechanical (THM) behavior of GMZ bentonite in the China-Mock-up test. *Engineering Geology*, 172, 57-68.
- CHEN, M., HOSKING, L. J., SANDFORD, R. J. & THOMAS, H. R. 2019. Dual porosity modelling of the coupled mechanical response of coal to gas flow and adsorption. *International Journal of Coal Geology*, 205, 115-125.
- CHEN, W., TAN, X., YU, H., WU, G. & JIA, S. 2009a. A fully coupled thermo-hydro-mechanical model for unsaturated porous media. *Journal of Rock Mechanics and Geotechnical Engineering*, 1, 31-40.
- CHEN, X. 2010. Unsaturated hydro-chemo-mechanical modelling based on modified mixture theory, The University of Manchester (United Kingdom).
- CHEN, X. 2013. Constitutive unsaturated hydro-mechanical model based on modified mixture theory with consideration of hydration swelling. *International Journal of Solids and Structures*, 50, 3266-3273.
- CHEN, X. & HICKS, M. A. 2010. Influence of water chemical potential on the swelling of water sensitive materials. *Computers & structures*, 88, 1498-1505.

- CHEN, X. & HICKS, M. A. 2011. A constitutive model based on modified mixture theory for unsaturated rocks. *Computers and Geotechnics*, 38, 925-933.
- CHEN, X., PAO, W., THORNTON, S. & SMALL, J. 2016. Unsaturated hydro-mechanical—chemical constitutive coupled model based on mixture coupling theory: Hydration swelling and chemical osmosis. *International Journal of Engineering Science*, 104, 97-109.
- CHEN, X., THORNTON, S. F. & PAO, W. 2018a. Mathematical model of coupled dual chemical osmosis based on mixture-coupling theory. *International Journal of Engineering Science*, 129, 145-155.
- CHEN, X., WANG, M., HICKS, M. A. & THOMAS, H. R. 2018b. A new matrix for multiphase couplings in a membrane porous medium. *International Journal for Numerical and Analytical Methods in Geomechanics*, 42, 1144-1153.
- CHEN, Y., ZHOU, C. & JING, L. 2009b. Modeling coupled THM processes of geological porous media with multiphase flow: Theory and validation against laboratory and field scale experiments. *Computers and Geotechnics*, 36, 1308-1329.
- COUSSY, O., DORMIEUX, L. & DETOURNAY, E. 1998. From mixture theory to Biot's approach for porous media. *International Journal of Solids and Structures*, 35, 4619-4635.
- CRIPPA, M., GUIZZARDI, D., BANJA, M., SOLAZZO, E., MUNTEAN, M., SCHAAF, E., PAGANI, F., MONFORTI-FERRARIO, F., OLIVIER, J. & QUADRELLI, R. 2022. CO2 emissions of all world countries. *JRC Science for Policy Report, European Commission, EUR*, 31182.
- DAI, Z., XU, L., XIAO, T., MCPHERSON, B., ZHANG, X., ZHENG, L., DONG, S., YANG, Z., SOLTANIAN, M. R. & YANG, C. 2020. Reactive chemical transport simulations of geologic carbon sequestration: Methods and applications. *Earth-Science Reviews*, 208, 103265.
- DARMON, A., BENZAQUEN, M., SALEZ, T. & DAUCHOT, O. 2014. Two-phase flow in a chemically active porous medium. *The Journal of Chemical Physics*, 141, 244704.
- DETOURNAY, E. & CHENG, A. H.-D. 1993. Fundamentals of poroelasticity. *Analysis and design methods*. Elsevier.
- DODS, M. N., KIM, E. J., LONG, J. R. & WESTON, S. C. 2021. Deep CCS: moving beyond 90% carbon dioxide capture. *Environmental Science & Technology*, 55, 8524-8534.

- ELLIS, B. R., FITTS, J. P., BROMHAL, G. S., MCINTYRE, D. L., TAPPERO, R. & PETERS, C. A. 2013. Dissolution-driven permeability reduction of a fractured carbonate caprock. *Environmental engineering science*, 30, 187-193.
- ENNIS-KING, J. & PATERSON, L. 2005. Role of convective mixing in the long-term storage of carbon dioxide in deep saline formations. *Spe Journal*, 10, 349-356.
- ERSHADNIA, R., HAJIREZAIE, S., AMOOIE, A., WALLACE, C. D., GERSHENZON, N. I., HOSSEINI, S. A., STURMER, D. M., RITZI, R. W. & SOLTANIAN, M. R. 2021. CO2 geological sequestration in multiscale heterogeneous aquifers: Effects of heterogeneity, connectivity, impurity, and hysteresis. *Advances in Water Resources*, 151, 103895.
- FALL, M., NASIR, O. & NGUYEN, T. 2014a. A coupled hydromechanical model for simulation of gas migration in host sedimentary rocks for nuclear waste repositories. *Engineering Geology*, 176, 24-44.
- FALL, M., NASIR, O. & NGUYEN, T. S. 2014b. A coupled hydromechanical model for simulation of gas migration in host sedimentary rocks for nuclear waste repositories. *Engineering Geology*, 176, 24-44.
- FAN, C., ELSWORTH, D., LI, S., CHEN, Z., LUO, M., SONG, Y. & ZHANG, H. 2019a. Modelling and optimization of enhanced coalbed methane recovery using CO2/N2 mixtures. *Fuel*, 253, 1114-1129.
- FAN, C., ELSWORTH, D., LI, S., ZHOU, L., YANG, Z. & SONG, Y. 2019b. Thermo-hydro-mechanical-chemical couplings controlling CH4 production and CO2 sequestration in enhanced coalbed methane recovery. *Energy*, 173, 1054-1077.
- FAN, C., YANG, L., SUN, H., LUO, M., ZHOU, L., YANG, Z. & LI, S. 2023. Recent Advances and Perspectives of CO2-Enhanced Coalbed Methane: Experimental, Modeling, and Technological Development. *Energy & Fuels*, 37, 3371-3412.
- FAVIER, S., TEITLER, Y., GOLFIER, F. & CATHELINEAU, M. 2024. Reactive transport modeling in porous fractured media: Application to weathering processes. *Water Resources Research*, 60, e2023WR035283.
- FIGUEIREDO, B., TSANG, C.-F., RUTQVIST, J., BENSABAT, J. & NIEMI, A. 2015. Coupled hydro-mechanical processes and fault reactivation induced by Co2 Injection in a three-layer storage

- formation. *International Journal of Greenhouse Gas Control*, 39, 432-448.
- FISCHER, S., LIEBSCHER, A., ZEMKE, K., DE LUCIA, M. & TEAM, K. 2013. Does injected CO2 affect (chemical) reservoir system integrity?-A comprehensive experimental approach. *Energy Procedia*, 37, 4473-4482.
- FORSTER, P., STORELVMO, T., ARMOUR, K., COLLINS, W., DUFRESNE, J.-L., FRAME, D., LUNT, D., MAURITSEN, T., PALMER, M. & WATANABE, M. 2021. The Earth's energy budget, climate feedbacks, and climate sensitivity.
- GAN, Q., CANDELA, T., WASSING, B., WASCH, L., LIU, J. & ELSWORTH, D. 2021. The use of supercritical CO2 in deep geothermal reservoirs as a working fluid: Insights from coupled THMC modeling. *International Journal of Rock Mechanics and Mining Sciences*, 147, 104872.
- GAUS, I., AUDIGANE, P., ANDRÉ, L., LIONS, J., JACQUEMET, N., DURST, P., CZERNICHOWSKI-LAURIOL, I. & AZAROUAL, M. 2008a. Geochemical and solute transport modelling for CO2 storage, what to expect from it? *International Journal of Greenhouse Gas Control*, 2, 605-625.
- GAUS, I., AUDIGANE, P., ANDRÉ, L., LIONS, J., JACQUEMET, N., DURST, P., CZERNICHOWSKI-LAURIOL, I. & AZAROUAL, M. 2008b. Geochemical and solute transport modelling for CO₂ storage, what to expect from it? *International Journal of Greenhouse Gas Control*, 2, 605-625.
- GAUS, I., AZAROUAL, M. & CZERNICHOWSKI-LAURIOL, I. 2005. Reactive transport modelling of the impact of CO2 injection on the clayey cap rock at Sleipner (North Sea). *Chemical Geology*, 217, 319-337.
- GAWIN, D., PESAVENTO, F. & SCHREFLER, B. 2003. Modelling of hygro-thermal behaviour of concrete at high temperature with thermo-chemical and mechanical material degradation. *Computer methods in applied mechanics and engineering*, 192, 1731-1771.
- GAWIN, D., PESAVENTO, F. & SCHREFLER, B. A. 2008. Modeling of cementitious materials exposed to isothermal calcium leaching, considering process kinetics and advective water flow. Part 1: Theoretical model. *International journal of solids and structures*, 45, 6221-6240.
- GAWIN, D. & SANAVIA, L. 2009. A unified approach to numerical modeling of fully and partially saturated porous materials by

- considering air dissolved in water. Computer Modeling in Engineering and Sciences (CMES), 53, 255.
- GAWIN, D., SIMONI, L. & SCHREFLER, B. Numerical model for hydromechanical behaviour in deformable porous media: a benchmark problem. Proceedings of the 9th International Conference on Computer Methods and Advances in Geomechanics, 1997. 1143-8.
- GE, S., MA, Y., WANG, K., ZHENG, L., XIE, X., CHEN, X. & YU, H.-S. 2023. Unsaturated hydro-mechanical-electro-chemical coupling based on mixture-coupling theory: a unified model. *International Journal of Engineering Science*, 191, 103914.
- GENS, A., GUIMARAES, L. D. N., GARCIA-MOLINA, A. & ALONSO, E. 2002. Factors controlling rock—clay buffer interaction in a radioactive waste repository. *Engineering geology*, 64, 297-308.
- GHOLAMI, R., RAZA, A. & IGLAUER, S. 2021. Leakage risk assessment of a CO2 storage site: A review. *Earth-Science Reviews*, 223, 103849.
- GRAY, F., CEN, J. & BOEK, E. 2016. Simulation of dissolution in porous media in three dimensions with lattice Boltzmann, finite-volume, and surface-rescaling methods. *Physical Review E*, 94, 043320.
- GRAZIANI, A. & BOLDINI, D. 2012. Influence of Hydro-Mechanical Coupling on Tunnel Response in Clays. *Journal of Geotechnical and Geoenvironmental Engineering*, 138, 415-418.
- GRISAK, G. E. & PICKENS, J.-F. 1980. Solute transport through fractured media: 1. The effect of matrix diffusion. *Water resources research*, 16, 719-730.
- GUIMARÃES, L. D. N., GENS, A. & OLIVELLA, S. 2007. Coupled thermo-hydro-mechanical and chemical analysis of expansive clay subjected to heating and hydration. *Transport in porous media*, 66, 341-372.
- GUNTER, W., WIWEHAR, B. & PERKINS, E. 1997a. Aquifer disposal of CO2-rich greenhouse gases: extension of the time scale of experiment for CO2-sequestering reactions by geochemical modelling. *Mineralogy and petrology*, 59, 121.
- GUNTER, W., WIWEHAR, B. & PERKINS, E. 1997b. Aquifer disposal of CO 2-rich greenhouse gases: extension of the time scale of experiment for CO 2-sequestering reactions by geochemical modelling. *Mineralogy and petrology*, 59, 121-140.
- GUNTER, W. D., PERKINS, E. H. & MCCANN, T. J. 1993. Aquifer disposal of CO2-rich gases: reaction design for added capacity. *Energy Conversion and management*, 34, 941-948.

- HAN, D.-R., NAMKUNG, H., LEE, H.-M., HUH, D.-G. & KIM, H.-T. 2015. CO2 sequestration by aqueous mineral carbonation of limestone in a supercritical reactor. *Journal of Industrial and Engineering Chemistry*, 21, 792-796.
- HART, D. J. & WANG, H. F. 1995. Laboratory measurements of a complete set of poroelastic moduli for Berea sandstone and Indiana limestone. *Journal of Geophysical Research: Solid Earth*, 100, 17741-17751.
- HAXAIRE, A. & DJERAN-MAIGRE, I. 2009. Influence of dissolution on the mechanical behaviour of saturated deep argillaceous rocks. *Engineering Geology*, 109, 255-261.
- HEIDUG, W. & WONG, S. W. 1996. Hydration swelling of water absorbing rocks: a constitutive model. *International journal for numerical and analytical methods in geomechanics*, 20, 403-430.
- HILL, L. B., LI, X. & WEI, N. 2020. CO2-EOR in China: A comparative review. *International Journal of Greenhouse Gas Control*, 103, 103173.
- HITCHON, B. 1996. Aquifer disposal of carbon dioxide: hydrodynamic and mineral trapping-proof of concept.
- HOSKING, L. J., CHEN, M. & THOMAS, H. R. 2020. Numerical analysis of dual porosity coupled thermo-hydro-mechanical behaviour during CO2 sequestration in coal. *International Journal of Rock Mechanics and Mining Sciences*, 135, 104473.
- HOUSE, K. Z., BACLIG, A. C., RANJAN, M., VAN NIEROP, E. A., WILCOX, J. & HERZOG, H. J. 2011. Economic and energetic analysis of capturing CO2 from ambient air. *Proceedings of the National Academy of Sciences*, 108, 20428-20433.
- HU, M., STEEFEL, C. I., RUTQVIST, J. & GILBERT, B. 2022.

 Microscale THMC Modeling of Pressure Solution in Salt Rock:

 Impacts of Geometry and Temperature. *Rock Mechanics and Rock Engineering*.
- HU, R., CHEN, Y. & ZHOU, C. 2011. Modeling of coupled deformation, water flow and gas transport in soil slopes subjected to rain infiltration. *Science China Technological Sciences*, 54, 2561-2575.
- HURTER, S., BERGE, J. G. & LABREGERE, D. Simulations for CO2 injection projects with compositional simulator. Offshore Europe, 2007. Society of Petroleum Engineers.
- ILGEN, A. G. & CYGAN, R. T. 2016. Mineral dissolution and precipitation during CO2 injection at the Frio-I Brine Pilot:

- Geochemical modeling and uncertainty analysis. *International Journal of Greenhouse Gas Control*, 44, 166-174.
- IRVINE JR, T. F. & DUIGNAN, M. R. 1985. Isobaric thermal expansion coefficients for water over large temperature and pressure ranges. *International communications in heat and mass transfer*, 12, 465-478.
- ISLAM, M., HUERTA, N. & DILMORE, R. 2020. Effect of computational schemes on coupled flow and geo-mechanical modeling of CO₂ leakage through a compromised well. *Computation*, 8, 98.
- IYER, J., LACKEY, G., EDVARDSEN, L., BEAN, A., CARROLL, S. A., HUERTA, N., SMITH, M. M., TORSÆTER, M., DILMORE, R. M. & CERASI, P. 2022. A review of well integrity based on field experience at carbon utilization and storage sites. *International Journal of Greenhouse Gas Control*, 113, 103533.
- IZGEC, O., DEMIRAL, B., BERTIN, H. & AKIN, S. 2008. CO2 injection into saline carbonate aquifer formations I. *Transport in porous media*, 72, 1-24.
- JAYASEKARA, D. W. & RANJITH, P. G. 2021. Effect of Geochemical Characteristics on Caprock Performance in Deep Saline Aquifers. *Energy & Fuels*, 35, 2443-2455.
- JIA, B., TSAU, J.-S. & BARATI, R. 2019. A review of the current progress of CO2 injection EOR and carbon storage in shale oil reservoirs. *Fuel*, 236, 404-427.
- JOHNSON, J. W., NITAO, J. J. & KNAUSS, K. G. 2004. Reactive transport modelling of CO2 storage in saline aquifers to elucidate fundamental processes, trapping mechanisms and sequestration partitioning. *Geological Society, London, Special Publications*, 233, 107-128.
- JOHNSON, J. W., NITAO, J. J., STEEFEL, C. I. & KNAUSS, K. G. Reactive transport modeling of geologic CO2 sequestration in saline aquifers: the influence of intra-aquifer shales and the relative effectiveness of structural, solubility, and mineral trapping during prograde and retrograde sequestration. First national conference on carbon sequestration, 2001. National Energy and Technology Laboratory USA, 14-17.
- KALDI, J., DANIEL, R., TENTHOREY, E., MICHAEL, K., SCHACHT, U., NICOL, A., UNDERSCHULTZ, J. & BACKE, G. 2013. Containment of CO2 in CCS: Role of Caprocks and Faults. *Energy Procedia*, 37, 5403-5410.

- KARRECH, A. 2013. Non-equilibrium thermodynamics for fully coupled thermal hydraulic mechanical chemical processes. *Journal of the Mechanics and Physics of Solids*, 61, 819-837.
- KATACHALSKY, A. & CURRAN, P. F. 1965. *Nonequilibrium thermodynamics in biophysics*, Cambridge, MA, Harvard University Press.
- KATCHALSKY, A. & CURRAN, P. 1965. Frontmatter. Cambridge (MA): Harvard University Press.
- KAUFMANN, G. & DREYBRODT, W. 2007. Calcite dissolution kinetics in the system CaCO3–H2O–CO2 at high undersaturation. *Geochimica et Cosmochimica Acta*, 71, 1398-1410.
- KEDEM, O. & KATCHALSKY, A. 1961. A physical interpretation of the phenomenological coefficients of membrane permeability. *The Journal of general physiology*, 45, 143-179.
- KELEMEN, P., BENSON, S. M., PILORGÉ, H., PSARRAS, P. & WILCOX, J. 2019. An overview of the status and challenges of CO2 storage in minerals and geological formations. *Frontiers in Climate*, 1, 9.
- KHAN, M. N., SIDDIQUI, S. & THAKUR, G. C. 2024. Recent Advances in Geochemical and Mineralogical Studies on CO2–Brine–Rock Interaction for CO2 Sequestration: Laboratory and Simulation Studies. *Energies*, 17, 3346.
- KHAZAEI, C. & CHALATURNYK, R. 2017. A Reservoir— Geomechanical Model to Study the Likelihood of Tensile and Shear Failure in the Caprock of Weyburn CCS Project with Regard to Interpretation of Microseismic Data. *Geotechnical and Geological Engineering*, 35, 2571-2595.
- KHURSHID, I. & FUJII, Y. 2021. Geomechanical analysis of formation deformation and permeability enhancement due to low-temperature CO 2 injection in subsurface oil reservoirs. *Journal of Petroleum Exploration and Production*, 11, 1915-1923.
- KIM, Y.-S. & KIM, J. 2013. Coupled hydromechanical model of twophase fluid flow in deformable porous media. *Mathematical Problems in Engineering*, 2013.
- KLEIN, E., DE LUCIA, M., KEMPKA, T. & KÜHN, M. 2013. Evaluation of long-term mineral trapping at the Ketzin pilot site for CO2 storage: An integrative approach using geochemical modelling and reservoir simulation. *International Journal of Greenhouse Gas Control*, 19, 720-730.

- KLIKA, V. 2014. A guide through available mixture theories for applications. *Critical reviews in solid state and materials sciences*, 39, 154-174.
- KOLDITZ, O., BAUER, S., BÖTTCHER, N., ELSWORTH, D., GÖRKE, U. J., MCDERMOTT, C. I., PARK, C. H., SINGH, A. K., TARON, J. & WANG, W. 2012. Numerical simulation of two-phase flow in deformable porous media: Application to carbon dioxide storage in the subsurface. *Mathematics and Computers in Simulation*, 82, 1919-1935.
- KONDEPUDI, D. & PRIGOGINE, I. 2014. *Modern thermodynamics: from heat engines to dissipative structures*, John Wiley & Sons.
- KRISHNAN, J. M. & RAO, C. L. 2000. Mechanics of air voids reduction of asphalt concrete using mixture theory. *International Journal of Engineering Science*, 38, 1331-1354.
- KUEPER, B. H. & FRIND, E. O. 1991. Two phase flow in heterogeneous porous media: 1. Model development. *Water resources research*, 27, 1049-1057.
- KUHL, D., BANGERT, F. & MESCHKE, G. 2004. Coupled chemomechanical deterioration of cementitious materials. Part I: Modeling. *International Journal of Solids and Structures*, 41, 15-40.
- KUMAR, P., ERTURK, V. S., BANERJEE, R., YAVUZ, M. & GOVINDARAJ, V. 2021. Fractional modeling of plankton-oxygen dynamics under climate change by the application of a recent numerical algorithm. *Physica Scripta*, 96, 124044.
- KUMAR, Y. & SANGWAI, J. S. 2023. Environmentally Sustainable Large-Scale CO2 Sequestration through Hydrates in Offshore Basins: Ab Initio Comprehensive Analysis of Subsea Parameters and Economic Perspective. *Energy & Fuels*.
- LACKNER, K. S., WENDT, C. H., BUTT, D. P., JOYCE JR, E. L. & SHARP, D. H. 1995. Carbon dioxide disposal in carbonate minerals. *Energy*, 20, 1153-1170.
- LADD, A. J. & SZYMCZAK, P. 2021. Reactive flows in porous media: challenges in theoretical and numerical methods. *Annual review of chemical and biomolecular engineering*, 12, 543-571.
- LALOUI, L., KLUBERTANZ, G. & VULLIET, L. 2003. Solid—liquid—air coupling in multiphase porous media. *International Journal for Numerical and Analytical Methods in Geomechanics*, 27, 183-206.
- LEE, Y.-J. & MORSE, J. W. 1999. Calcite precipitation in synthetic veins: implications for the time and fluid volume necessary for vein filling. *Chemical Geology*, 156, 151-170.

- LEI, H., CAI, Y., LU, M., LI, X. & CONNELL, L. D. 2020. A study on the thermal-hydrodynamical-coupled CO2 flow process in the Ordos CCS-geological-formation. *International Journal of Greenhouse Gas Control*, 95.
- LEWIS, R. W. & SCHREFLER, B. A. 1987. The finite element method in the deformation and consolidation of porous media.
- LEWIS, R. W. & SCHREFLER, B. A. 1998a. The finite element method in the static and dynamic deformation and consolidation of porous media, John Wiley.
- LEWIS, R. W. & SCHREFLER, B. A. 1998b. The Finite Element Method in the Static and Dynamic Deformation and Consolidation of Porous Media, Wiley.
- LI, C. & LALOUI, L. 2016a. Coupled multiphase thermo-hydro-mechanical analysis of supercritical CO2 injection: Benchmark for the In Salah surface uplift problem. *International Journal of Greenhouse Gas Control*, 51, 394-408.
- LI, C. & LALOUI, L. 2016b. Coupled multiphase thermo-hydro-mechanical analysis of supercritical CO 2 injection: Benchmark for the In Salah surface uplift problem. *International Journal of Greenhouse Gas Control*, 51, 394-408.
- LI, C. & LALOUI, L. 2017. Coupled Thermo-hydro-Mechanical Effects on Caprock Stability During Carbon Dioxide Injection. *Energy Procedia*, 114, 3202-3209.
- LI, H., WANG, F., PAN, H., WU, M., WANG, Y., TIAN, H., YUAN, Y. & YANG, Z. 2022. Effects of different mineral reaction kinetics equations on predicting long term CO2 mineral sequestration.

 International Journal of Energy Research, 46, 14505-14516.
- LI, X., LI, Q., BAI, B., WEI, N. & YUAN, W. 2016. The geomechanics of Shenhua carbon dioxide capture and storage (CCS) demonstration project in Ordos Basin, China. *Journal of Rock Mechanics and Geotechnical Engineering*, 8, 948-966.
- LIAKOPOULOS, A. 1965a. Transient flow through unsaturated porous media [Ph. D. thesis]. *University of California, Berkeley, Calif, USA*.
- LIAKOPOULOS, A. 1965b. *Transient flow through unsaturated porous media*, D. Eng. dissertation, Univ. of Calif., Berkeley.
- LICHTSCHLAG, A., HAECKEL, M., OLIEROOK, D., PEEL, K., FLOHR, A., PEARCE, C. R., MARIENI, C., JAMES, R. H. & CONNELLY, D. P. 2021. Impact of CO2 leakage from sub-seabed carbon dioxide storage on sediment and porewater geochemistry. *International Journal of Greenhouse Gas Control*, 109, 103352.

- LIU, A., LIU, S., LIU, P. & WANG, K. 2021a. Water sorption on coal: effects of oxygen-containing function groups and pore structure. *International Journal of Coal Science & Technology*, 8, 983-1002.
- LIU, F., LU, P., ZHU, C. & XIAO, Y. 2011. Coupled reactive flow and transport modeling of CO₂ sequestration in the Mt. Simon sandstone formation, Midwest USA. *International Journal of Greenhouse Gas Control*, 5, 294-307.
- LIU, T., LIN, B., FU, X. & LIU, A. 2021b. Mechanical criterion for coal and gas outburst: a perspective from multiphysics coupling. *International Journal of Coal Science & Technology*, 8, 1423-1435.
- LU, P., APPS, J., ZHANG, G., GYSI, A. & ZHU, C. 2024. Knowledge gaps and research needs for modeling CO2 mineralization in the basalt-CO2-water system: A review of laboratory experiments. *Earth-Science Reviews*, 104813.
- LU, W. & ZHANG, X. 2020. Coupled thermo-hydro-mechanical modelling of carbon dioxide sequestration in saline aquifers considering phase change. *CURRENT SCIENCE*, 119, 973.
- LUO, A., LI, Y., CHEN, X., ZHU, Z. & PENG, Y. 2022. Review of CO2 sequestration mechanism in saline aquifers. *Natural Gas Industry B*, 9, 383-393.
- LUO, S., XU, R. & JIANG, P. 2012. Effect of reactive surface area of minerals on mineralization trapping of CO 2 in saline aquifers. *Petroleum Science*, 9, 400-407.
- MA, J., LI, L., WANG, H., DU, Y., MA, J., ZHANG, X. & WANG, Z. 2022a. Carbon capture and storage: history and the road ahead. *Engineering*, 14, 33-43.
- MA, T., RUTQVIST, J., OLDENBURG, C. M. & LIU, W. 2017. Coupled thermal—hydrological—mechanical modeling of CO2-enhanced coalbed methane recovery. *International Journal of Coal Geology*, 179, 81-91.
- MA, Y., CHEN, X.-H. & YU, H.-S. 2020a. An extension of Biot's theory with molecular influence based on mixture coupling theory:

 Mathematical model. *International Journal of Solids and Structures*, 191, 76-86.
- MA, Y., CHEN, X.-H. & YU, H.-S. 2020b. An extension of Biot's theory with molecular influence based on mixture coupling theory:

 Mathematical model. *International Journal of Solids and Structures*, 191-192, 76-86.
- MA, Y., CHEN, X. H., HOSKING, L. J., YU, H. S., THOMAS, H. R. & NORRIS, S. 2021. The influence of coupled physical swelling and

- chemical reactions on deformable geomaterials. *International Journal for Numerical and Analytical Methods in Geomechanics*, 45, 64-82.
- MA, Y., FENG, J., GE, S., WANG, K., CHEN, X. & DING, A. 2023. Constitutive Modeling of Hydromechanical Coupling in Double Porosity Media Based on Mixture Coupling Theory. *International Journal of Geomechanics*, 23, 04023056.
- MA, Y., GE, S., YANG, H. & CHEN, X. 2022b. Coupled thermo-hydro-mechanical-chemical processes with reactive dissolution by non-equilibrium thermodynamics. *Journal of the Mechanics and Physics of Solids*, 169.
- MAINA, F. Z. & ACKERER, P. 2017. Ross scheme, Newton–Raphson iterative methods and time-stepping strategies for solving the mixed form of Richards' equation. *Hydrology and Earth System Sciences*, 21, 2667-2683.
- MANNINEN, M., TAIVASSALO, V. & KALLIO, S. 1996. On the mixture model for multiphase flow. Technical Research Centre of Finland Finland.
- MASSON-DELMOTTE, V., ZHAI, P., PÖRTNER, H.-O., ROBERTS, D., SKEA, J. & SHUKLA, P. R. 2022. Global Warming of 1.5° C: IPCC Special Report on Impacts of Global Warming of 1.5° C above Preindustrial Levels in Context of Strengthening Response to Climate Change, Sustainable Development, and Efforts to Eradicate Poverty, Cambridge University Press.
- MATTER, J. M., BROECKER, W., STUTE, M., GISLASON, S., OELKERS, E., STEFÁNSSON, A., WOLFF-BOENISCH, D., GUNNLAUGSSON, E., AXELSSON, G. & BJÖRNSSON, G. 2009. Permanent carbon dioxide storage into basalt: the CarbFix pilot project, Iceland. *Energy Procedia*, 1, 3641-3646.
- MATTHEWS, H. D. & WYNES, S. 2022. Current global efforts are insufficient to limit warming to 1.5 C. *Science*, 376, 1404-1409.
- MAZZOTTI, M., PINI, R. & STORTI, G. 2009. Enhanced coalbed methane recovery. *The Journal of Supercritical Fluids*, 47, 619-627.
- MEHRABI, R. & ATEFI-MONFARED, K. 2022. A coupled bio-chemo-hydro-mechanical model for bio-cementation in porous media. *Canadian Geotechnical Journal*, 59, 1266-1280.
- MEIRI, D. 1981. Two phase flow simulation of air storage in an aquifer. *Water Resources Research*, 17, 1360-1366.

- MENG, J., LIAO, W. & ZHANG, G. 2021. Emerging CO2-mineralization technologies for co-utilization of industrial solid waste and carbon resources in China. *Minerals*, 11, 274.
- MILLY, P. C. D. 1982. Moisture and heat transport in hysteretic, inhomogeneous porous media: A matric head based formulation and a numerical model. *Water Resources Research*, 18, 489-498.
- NARASIMHAN, T. 1979. The significance of the storage parameter in saturated unsaturated groundwater flow. *Water Resources Research*, 15, 569-576.
- NARASIMHAN, T. N. & WITHERSPOON, P. 1978. Numerical model for saturated unsaturated flow in deformable porous media: 3. Applications. *Water Resources Research*, 14, 1017-1034.
- NARDI, A., IDIART, A., TRINCHERO, P., DE VRIES, L. M. & MOLINERO, J. 2014. Interface COMSOL-PHREEQC (iCP), an efficient numerical framework for the solution of coupled multiphysics and geochemistry. *Computers & Geosciences*, 69, 10-21.
- NASVI, M., RANJITH, P., SANJAYAN, J. & HAQUE, A. 2013. Sub-and super-critical carbon dioxide permeability of wellbore materials under geological sequestration conditions: An experimental study. *Energy*, 54, 231-239.
- NASVI, M. C. M., RANJITH, P. G. & SANJAYAN, J. 2014. A numerical study of CO2 flow through geopolymer under down-hole stress conditions: Application for CO2 sequestration wells. *Journal of Unconventional Oil and Gas Resources*, 7, 62-70.
- NATH, S. 2024. Thermodynamic analysis of energy coupling by determination of the Onsager phenomenological coefficients for a 3×3 system of coupled chemical reactions and transport in ATP synthesis and its mechanistic implications. *BioSystems*, 240, 105228.
- OLIVELLA, S., CARRERA, J., GENS, A. & ALONSO, E. 1994. Nonisothermal multiphase flow of brine and gas through saline media. *Transport in porous media*, 15, 271-293.
- PANELLI, R. & AMBROZIO FILHO, F. 2001. A study of a new phenomenological compacting equation. *Powder Technology*, 114, 255-261.
- PARK, C.-H., TARON, J., GÖRKE, U.-J., SINGH, A. K. & KOLDITZ, O. 2011. The fluidal interface is where the action is in CO2 sequestration and storage: Hydromechanical analysis of mechanical failure. *Energy Procedia*, 4, 3691-3698.

- PARKHURST, D. L. & APPELO, C. 2013. Description of input and examples for PHREEQC version 3—a computer program for speciation, batch-reaction, one-dimensional transport, and inverse geochemical calculations. *US geological survey techniques and methods*, 6, 497.
- PENG, C., CRAWSHAW, J. P., MAITLAND, G. C. & TRUSLER, J. M. 2015. Kinetics of calcite dissolution in CO2-saturated water at temperatures between (323 and 373) K and pressures up to 13.8 MPa. *Chemical Geology*, 403, 74-85.
- PESAVENTO, F., GAWIN, D., SCHREFLER, B. A. & KONIORCZYK, M. Modelling chemical processes in cement based materials by means of multiphase porous media mechanics. Engineering Systems Design and Analysis, 2012. American Society of Mechanical Engineers, 81-88.
- PESAVENTO, F., SCHREFLER, B. A. & SCIUMÈ, G. 2017. Multiphase flow in deforming porous media: a review. *Archives of Computational Methods in Engineering*, 24, 423-448.
- PETIT, A., CEREPI, A., LOISY, C., LE ROUX, O., ROSSI, L., ESTUBLIER, A., GANCE, J., GARCIA, B., HAUTEFEUILLE, B., LAVIELLE, B., BRICHART, T., NOIREZ, S., MARTIN, F., TEXIER, B., KENNEDY, S. & EL KHAMLICHI, A. 2021. Aquifer-CO2 leak project: Physicochemical characterization of the CO2 leakage impact on a carbonate shallow freshwater aquifer. *International Journal of Greenhouse Gas Control*, 106, 103231.
- PLEASE, C., PETTET, G. & MCELWAIN, D. 1998. A new approach to modelling the formation of necrotic regions in tumours. *Applied mathematics letters*, 11, 89-94.
- PLUMMER, L. N. & BUSENBERG, E. 1982. The solubilities of calcite, aragonite and vaterite in CO2-H2O solutions between 0 and 90 C, and an evaluation of the aqueous model for the system CaCO3-CO2-H2O. *Geochimica et cosmochimica acta*, 46, 1011-1040.
- PLUMMER, L. N. & WIGLEY, T. 1976. The dissolution of calcite in CO2-saturated solutions at 25 C and 1 atmosphere total pressure. *Geochimica et Cosmochimica Acta*, 40, 191-202.
- POPP, T. & SALZER, K. 2007. Anisotropy of seismic and mechanical properties of Opalinus clay during triaxial deformation in a multi-anvil apparatus. *Physics and Chemistry of the Earth, Parts A/B/C*, 32, 879-888.
- POPP, T., SALZER, K. & MINKLEY, W. 2008. Influence of bedding planes to EDZ-evolution and the coupled HM properties of Opalinus

- Clay. Physics and Chemistry of the Earth, Parts A/B/C, 33, S374-S387.
- PÖRTNER, H.-O., ROBERTS, D., TIGNOR, M., POLOCZANSKA, E., MINTENBECK, K., ALEGRÍA, A., CRAIG, M., LANGSDORF, S., LÖSCHKE, S., MÖLLER, V., OKEM, A., RAMA, B., BELLING, D., DIECK, W., GÖTZE, S., KERSHER, T., MANGELE, P., MAUS, B., MÜHLE, A. & WEYER, N. 2022. Climate Change 2022: Impacts, Adaptation and Vulnerability Working Group II Contribution to the Sixth Assessment Report of the Intergovernmental Panel on Climate Change.
- PRUESS, K. 2005. Numerical studies of fluid leakage from a geologic disposal reservoir for CO2 show self limiting feedback between fluid flow and heat transfer. *Geophysical research letters*, 32.
- PRUESS, K., GARCÍA, J., KOVSCEK, T., OLDENBURG, C., RUTQVIST, J., STEEFEL, C. & XU, T. 2004. Code intercomparison builds confidence in numerical simulation models for geologic disposal of CO2. *Energy*, 29, 1431-1444.
- PUNNAM, P. R., DUTTA, A., KRISHNAMURTHY, B. & SURASANI, V. K. 2022. Study on utilization of machine learning techniques for geological CO2 sequestration simulations. *Materials Today: Proceedings*.
- QIAO, Y., ANDERSEN, P. Ø., EVJE, S. & STANDNES, D. C. 2018. A mixture theory approach to model co- and counter-current two-phase flow in porous media accounting for viscous coupling. *Advances in Water Resources*, 112, 170-188.
- QUIBÉN, J. M. & THOME, J. R. 2007. Flow pattern based two-phase frictional pressure drop model for horizontal tubes, Part II: New phenomenological model. *International Journal of Heat and Fluid Flow*, 28, 1060-1072.
- RAHMAN, M. J., FAWAD, M., JAHREN, J. & MONDOL, N. H. 2022. Influence of depositional and diagenetic processes on Caprock properties of CO2 storage sites in the Northern North Sea, offshore Norway. *Geosciences*, 12, 181.
- RAMADHAN, R., MON, M. T., TANGPARITKUL, S., TANSUCHAT, R. & AGUSTIN, D. A. 2024. Carbon capture, utilization, and storage in Indonesia: an update on storage capacity, current status, economic viability, and policy. *Energy Geoscience*, 100335.
- RAMIRES, M. L., NIETO DE CASTRO, C. A., NAGASAKA, Y., NAGASHIMA, A., ASSAEL, M. J. & WAKEHAM, W. A. 1995.

- Standard reference data for the thermal conductivity of water. Journal of Physical and Chemical Reference Data, 24, 1377-1381.
- RANGRIZ SHOKRI, A., TALMAN, S., CHALATURNYK, R. J. & NICKEL, E. On the Temporal Evolution of Non-Isothermal Injectivity Behaviour at an Active CO2 Injection Site. 55th US Rock Mechanics/Geomechanics Symposium, 2021. OnePetro.
- RASTOGI, R. P., SINGH, K. & SRIVASTAVA, M. 1969. Cross-phenomenological coefficients. XI. Nonlinear transport equations. *The Journal of Physical Chemistry*, 73, 46-51.
- RATHNAWEERA, T., RANJITH, P., PERERA, M., RANATHUNGA, A., WANNIARACHCHI, W., YANG, S., LASHIN, A. & AL ARIFI, N. 2017. An experimental investigation of coupled chemicomineralogical and mechanical changes in varyingly-cemented sandstones upon CO2 injection in deep saline aquifer environments. *Energy*, 133, 404-414.
- RIAZ, A. & CINAR, Y. 2014. Carbon dioxide sequestration in saline formations: Part I—Review of the modeling of solubility trapping. *Journal of Petroleum Science and Engineering*, 124, 367-380.
- RICHARDS, L. A. 1931. Capillary conduction of liquids through porous mediums. *Physics*, 1, 318-333.
- ROCHELLE, C. A., CZERNICHOWSKI-LAURIOL, I. & MILODOWSKI, A. 2004. The impact of chemical reactions on CO2 storage in geological formations: a brief review. *Geological Society, London, Special Publications*, 233, 87-106.
- RUTQVIST, J. 2017. An overview of TOUGH-based geomechanics models. *Computers & Geosciences*, 108, 56-63.
- RUTQVIST, J., LIU, H.-H., VASCO, D. W., PAN, L., KAPPLER, K. & MAJER, E. 2011. Coupled non-isothermal, multiphase fluid flow, and geomechanical modeling of ground surface deformations and potential for induced micro-seismicity at the In Salah CO2 storage operation. *Energy Procedia*, 4, 3542-3549.
- RUTQVIST, J. & TSANG, C.-F. 2002. A study of caprock hydromechanical changes associated with CO2-injection into a brine formation. *Environmental Geology*, 42, 296-305.
- RUTQVIST, J., WU, Y.-S., TSANG, C.-F. & BODVARSSON, G. 2002. A modeling approach for analysis of coupled multiphase fluid flow, heat transfer, and deformation in fractured porous rock. *International Journal of Rock Mechanics and Mining Sciences*, 39, 429-442.
- SAINZ-GARCIA, A., ABARCA, E., NARDI, A., GRANDIA, F. & OELKERS, E. H. 2017. Convective mixing fingers and chemistry

- interaction in carbon storage. *International Journal of Greenhouse Gas Control*, 58, 52-61.
- SAMPATH, K. H. S. M., PERERA, M. S. A., MATTHAI, S. K., RANJITH, P. G. & DONG-YIN, L. 2020. Modelling of fully-coupled CO2 diffusion and adsorption-induced coal matrix swelling. *Fuel*, 262, 116486.
- SANAVIA, L., SCHREFLER, B. & STEINMANN, P. 2002. A formulation for an unsaturated porous medium undergoing large inelastic strains. *Computational Mechanics*, 28, 137-151.
- SASAKI, K., FUJII, T., NIIBORI, Y., ITO, T. & HASHIDA, T. 2008. Numerical simulation of supercritical CO₂ injection into subsurface rock masses. *Energy Conversion and Management*, 49, 54-61.
- SCHREFLER, B. A. & SCOTTA, R. 2001. A fully coupled dynamic model for two-phase fluid flow in deformable porous media. *Computer methods in applied mechanics and engineering*, 190, 3223-3246.
- SCHREFLER, B. A. & XIAOYONG, Z. 1993. A fully coupled model for water flow and airflow in deformable porous media. *Water Resources Research*, 29, 155-167.
- SEETHARAM, S. C., THOMAS, H. R. & CLEALL, P. J. 2007. Coupled thermo/hydro/chemical/mechanical model for unsaturated soils—Numerical algorithm. *International Journal for Numerical Methods in Engineering*, 70, 1480-1511.
- SHEVALIER, M., DALKHAA, C., HUMEZ, P., MAYER, B., BECKER, V., NIGHTINGALE, M., ROCK, L. & ZHANG, G. 2014. Coupling of TOUGHREACT-Geochemist Workbench (GWB) for Modeling Changes in the Isotopic Composition of CO2 Leaking from a CCS Storage Reservoir. *Energy Procedia*, 63, 3751-3760.
- SHUKLA POTDAR, R. & VISHAL, V. 2016. Trapping mechanism of CO 2 storage in deep saline aquifers: Brief review. *Geologic Carbon Sequestration: Understanding Reservoir Behavior*, 47-58.
- SIDDIQUE, J., AHMED, A., AZIZ, A. & KHALIQUE, C. 2017. A Review of Mixture Theory for Deformable Porous Media and Applications. *Applied Sciences*, 7.
- SIDDIQUI, M. A., REGENAUER-LIEB, K. & ROSHAN, H. 2023. Thermo-Hydro-Chemo-Mechanical (THCM) Continuum Modelling of Subsurface Rocks: A Focus On Thermodynamics-based Constitutive Models. *Applied Mechanics Reviews*, 1-62.

- SIDDIQUI, M. A. Q., REGENAUER-LIEB, K. & ROSHAN, H. 2024. Thermo-Hydro-Chemo-Mechanical (THCM) Continuum Modeling of Subsurface Rocks: A Focus on Thermodynamics-Based Constitutive Models. *Applied Mechanics Reviews*, 76.
- ŠIMŮNEK, J. & SUAREZ, D. L. 1993. Modeling of carbon dioxide transport and production in soil: 1. Model development. *Water Resources Research*, 29, 487-497.
- SIQUEIRA, T. A., IGLESIAS, R. S. & KETZER, J. M. 2017. Carbon dioxide injection in carbonate reservoirs a review of CO₂ water rock interaction studies. *Greenhouse Gases: Science and Technology*, 7, 802-816.
- SOKAMA-NEUYAM, Y. A., AGGREY, W. N., BOAKYE, P., SARKODIE, K., ODURO-KWARTENG, S. & URSIN, J. R. 2022. The effect of temperature on CO2 injectivity in sandstone reservoirs. *Scientific African*, 15, e01066.
- SONG, Y., JUN, S., NA, Y., KIM, K., JANG, Y. & WANG, J. 2023. Geomechanical challenges during geological CO2 storage: A review. *Chemical Engineering Journal*, 456, 140968.
- STEEFEL, C. I. & LASAGA, A. C. 1994. A coupled model for transport of multiple chemical species and kinetic precipitation/dissolution reactions with application to reactive flow in single phase hydrothermal systems. *American Journal of science*, 294, 529-592.
- STEVENS, S. H., KUUSKRAA, V. A., GALE, J. & BEECY, D. 2001. CO2 injection and sequestration in depleted oil and gas fields and deep coal seams: worldwide potential and costs. *Environmental Geosciences*, 8, 200-209.
- STEWART, S. A. & RIDDELL, L. A. 2022. Hydrodynamic invalidation of synformal traps for dissolved CO2. *Geology*, 50, 1121-1124.
- STYLIANOU, I. I., TASSOU, S., CHRISTODOULIDES, P., PANAYIDES, I. & FLORIDES, G. 2016. Measurement and analysis of thermal properties of rocks for the compilation of geothermal maps of Cyprus. *Renewable Energy*, 88, 418-429.
- TAO, J., WU, Y., ELSWORTH, D., LI, P. & HAO, Y. 2019. Coupled thermo-hydro-mechanical-chemical modeling of permeability evolution in a CO₂-circulated geothermal reservoir. *Geofluids*, 2019, 5210730.
- TARON, J. & ELSWORTH, D. 2009. Thermal—hydrologic—mechanical—chemical processes in the evolution of engineered geothermal reservoirs. *International Journal of Rock Mechanics and Mining Sciences*, 46, 855-864.

- TARON, J., ELSWORTH, D. & MIN, K.-B. 2009. Numerical simulation of thermal-hydrologic-mechanical-chemical processes in deformable, fractured porous media. *International Journal of Rock Mechanics and Mining Sciences*, 46, 842-854.
- TERZAGHI, K. 1925. Erdbaumechanik auf bodenphysikalischer Grundlage.
- TEYMOURTASH, A. R., KHONAKDAR, D. R. & RAVESHI, M. R. 2013. Natural convection on a vertical plate with variable heat flux in supercritical fluids. *The Journal of Supercritical Fluids*, 74, 115-127.
- THOMAS, H., REES, S. & SLOPER, N. 1998. Three dimensional heat, moisture and air transfer in unsaturated soils. *International journal for numerical and analytical methods in geomechanics*, 22, 75-95.
- THOMAS, H. R. & SANSOM, M. R. 1995. Fully coupled analysis of heat, moisture, and air transfer in unsaturated soil. *Journal of Engineering Mechanics*, 121, 392-405.
- TONG, F., JING, L. & ZIMMERMAN, R. W. 2010. A fully coupled thermo-hydro-mechanical model for simulating multiphase flow, deformation and heat transfer in buffer material and rock masses. *International Journal of Rock Mechanics and Mining Sciences*, 47, 205-217.
- TRUESDELL, C. 1957. Sulle basi della termomeccanica. *Rend. Lincei*, 22, 33-38.
- TRUESDELL, C. & TOUPIN, R. 1960. The classical field theories. Principles of classical mechanics and field theory/Prinzipien der Klassischen Mechanik und Feldtheorie. Springer.
- UNGER, V. & KEMPKA, T. 2015. Hydro-mechanical Simulations of Well Abandonment at the Ketzin Pilot Site for CO2 Storage Verify Wellbore System Integrity. *Energy Procedia*, 76, 592-599.
- VAN DER MEER, L. 1992. Investigations regarding the storage of carbon dioxide in aquifers in the Netherlands. *Energy Conversion and management*, 33, 611-618.
- VAN GENUCHTEN, M. T. 1980a. A Closed-form Equation for Predicting the Hydraulic Conductivity of Unsaturated Soils. *Soil Science Society of America Journal*, 44, 892-898.
- VAN GENUCHTEN, M. T. 1980b. A closed form equation for predicting the hydraulic conductivity of unsaturated soils. *Soil science society of America journal*, 44, 892-898.
- VAN PHAM, T. H., AAGAARD, P. & HELLEVANG, H. 2012. On the potential for CO2mineral storage in continental flood basalts—

- PHREEQC batch-and 1D diffusion—reaction simulations. *Geochemical transactions*, 13, 1-12.
- VEREECKEN, H., MAES, J., FEYEN, J. & DARIUS, P. 1989. Estimating the soil moisture retention characteristic from texture, bulk density, and carbon content. *Soil science*, 148, 389-403.
- VEVEAKIS, E., ALEVIZOS, S. & POULET, T. 2017. Episodic Tremor and Slip (ETS) as a chaotic multiphysics spring. *Physics of the Earth and Planetary Interiors*, 264, 20-34.
- VICENTE-SERRANO, S. M., QUIRING, S. M., PEÑA-GALLARDO, M., YUAN, S. & DOMÍNGUEZ-CASTRO, F. 2020. A review of environmental droughts: Increased risk under global warming? *Earth-Science Reviews*, 201, 102953.
- VILARRASA, V., BOLSTER, D., OLIVELLA, S. & CARRERA, J. 2010. Coupled hydromechanical modeling of CO2 sequestration in deep saline aquifers. *International Journal of Greenhouse Gas Control*, 4, 910-919.
- VILARRASA, V., RINALDI, A. P. & RUTQVIST, J. 2017. Long-term thermal effects on injectivity evolution during CO2 storage. *International Journal of Greenhouse Gas Control*, 64, 314-322.
- VILARRASA, V. & RUTQVIST, J. 2017. Thermal effects on geologic carbon storage. *Earth-Science Reviews*, 165, 245-256.
- VOSKOV, D. V., HENLEY, H. & LUCIA, A. 2017. Fully compositional multi-scale reservoir simulation of various CO₂ sequestration mechanisms. *Computers & Chemical Engineering*, 96, 183-195.
- WAGNER, W. & PRUß, A. 2002. The IAPWS formulation 1995 for the thermodynamic properties of ordinary water substance for general and scientific use. *Journal of physical and chemical reference data*, 31, 387-535.
- WANG, B. & BAUER, S. 2019. Induced geochemical reactions by compressed air energy storage in a porous formation in the North German Basin. *Applied Geochemistry*, 102, 171-185.
- WANG, H., KOU, Z., JI, Z., WANG, S., LI, Y., JIAO, Z., JOHNSON, M. & MCLAUGHLIN, J. F. 2023a. Investigation of enhanced CO2 storage in deep saline aquifers by WAG and brine extraction in the Minnelusa sandstone, Wyoming. *Energy*, 265, 126379.
- WANG, H., PILCHER, D. J., KEARNEY, K. A., CROSS, J. N., SHUGART, O. M., EISAMAN, M. D. & CARTER, B. R. 2023b. Simulated Impact of Ocean Alkalinity Enhancement on Atmospheric CO2 Removal in the Bering Sea. *Earth's Future*, 11, e2022EF002816.

- WANG, K., ZHOU, J., MA, Y., DING, A. & CHEN, X. 2023c. Constitutive and numerical modeling for the coupled thermal-hydromechanical processes in dual-porosity geothermal reservoir. *Applied Thermal Engineering*, 223, 120027.
- WANG, L., WANG, S., ZHANG, R., WANG, C., XIONG, Y., ZHENG, X., LI, S., JIN, K. & RUI, Z. 2017. Review of multi-scale and multi-physical simulation technologies for shale and tight gas reservoirs. *Journal of Natural Gas Science and Engineering*, 37, 560-578.
- WANG, X., SHAO, H., HESSER, J., ZHANG, C., WANG, W. & KOLDITZ, O. 2014. Numerical analysis of thermal impact on hydromechanical properties of clay. *Journal of Rock Mechanics and Geotechnical Engineering*, 6, 405-416.
- WANG, Y., VUIK, C. & HAJIBEYGI, H. 2022. CO2 Storage in deep saline aquifers: impacts of fractures on hydrodynamic trapping. *International Journal of Greenhouse Gas Control*, 113, 103552.
- WAPLES, D. W. & WAPLES, J. S. 2004. A review and evaluation of specific heat capacities of rocks, minerals, and subsurface fluids. Part 1: Minerals and nonporous rocks. *Natural resources research*, 13, 97-122.
- WEI, B., ZHONG, M., GAO, K., LI, X., ZHANG, X., CAO, J. & LU, J. 2020a. Oil recovery and compositional change of CO2 huff-n-puff and continuous injection modes in a variety of dual-permeability tight matrix-fracture models. *Fuel*, 276, 117939.
- WEI, H., CHEN, J.-S., BECKWITH, F. & BAEK, J. 2020b. A naturally stabilized semi-Lagrangian meshfree formulation for multiphase porous media with application to landslide modeling. *Journal of Engineering Mechanics*, 146, 04020012.
- WERTZ, F., GHERARDI, F., BLANC, P., BADER, A.-G. & FABBRI, A. 2013. Cement CO2-alteration propagation at the well–caprock–reservoir interface and influence of diffusion. *International Journal of Greenhouse Gas Control*, 12, 9-17.
- WHITAKER, S. 1986. Flow in porous media I: A theoretical derivation of Darcy's law. *Transport in porous media*, 1, 3-25.
- WHITE, S. K., SPANE, F. A., SCHAEF, H. T., MILLER, Q. R., WHITE, M. D., HORNER, J. A. & MCGRAIL, B. P. 2020. Quantification of CO2 mineralization at the Wallula Basalt Pilot project. *Environmental Science & Technology*, 54, 14609-14616.
- WOLF, J. L., NIEMI, A., BENSABAT, J. & REBSCHER, D. 2016. Benefits and restrictions of 2D reactive transport simulations of CO₂ and SO₂ co-injection into a saline aquifer using TOUGHREACT V3.

- 0-OMP. International Journal of Greenhouse Gas Control, 54, 610-626.
- WRIGGERS, P. 2008. *Nonlinear finite element methods*, Springer Science & Business Media.
- WU, S., LI, Z., WANG, Z., SARMA, H. K., ZHANG, C. & WU, M. 2020. Investigation of CO2/N2 injection in tight oil reservoirs with confinement effect. *Energy Science & Engineering*, 8, 1194-1208.
- XIAO, Y., XU, T. & PRUESS, K. 2009. The effects of gas-fluid-rock interactions on CO₂ injection and storage: insights from reactive transport modeling. *Energy Procedia*, 1, 1783-1790.
- XIONG, J., LIN, H., DING, H., PEI, H., RONG, C. & LIAO, W. 2020. Investigation on thermal property parameters characteristics of rocks and its influence factors. *Natural Gas Industry B*, 7, 298-308.
- XU, C., YANG, J., HE, L., WEI, W., YANG, Y., YIN, X., YANG, W. & LIN, A. 2021. Carbon capture and storage as a strategic reserve against China's CO2 emissions. *Environmental Development*, 37, 100608.
- XU, R., LI, R., MA, J., HE, D. & JIANG, P. 2017. Effect of mineral dissolution/precipitation and CO2 exsolution on CO2 transport in geological carbon storage. *Accounts of chemical research*, 50, 2056-2066.
- XU, T., APPS, J. A. & PRUESS, K. 2003. Reactive geochemical transport simulation to study mineral trapping for CO₂ disposal in deep arenaceous formations. *Journal of Geophysical Research: Solid Earth*, 108.
- XU, T., APPS, J. A. & PRUESS, K. 2004a. Numerical simulation of CO2 disposal by mineral trapping in deep aquifers. *Applied geochemistry*, 19, 917-936.
- XU, T., APPS, J. A. & PRUESS, K. 2005. Mineral sequestration of carbon dioxide in a sandstone–shale system. *Chemical geology*, 217, 295-318.
- XU, T., KHARAKA, Y. K., DOUGHTY, C., FREIFELD, B. M. & DALEY, T. M. 2010. Reactive transport modeling to study changes in water chemistry induced by CO2 injection at the Frio-I Brine Pilot. *Chemical Geology*, 271, 153-164.
- XU, T. & PRUESS, K. 2001. Modeling multiphase non-isothermal fluid flow and reactive geochemical transport in variably saturated fractured rocks: 1. Methodology. *American Journal of Science*, 301, 16-33.

- XU, T., SONNENTHAL, E., SPYCHER, N. & PRUESS, K. 2004b. TOUGHREACT user's guide: A simulation program for non-isothermal multiphase reactive geochemical transport in variable saturated geologic media. Lawrence Berkeley National Lab.(LBNL), Berkeley, CA (United States).
- XU, T., SONNENTHAL, E., SPYCHER, N. & PRUESS, K. 2006. TOUGHREACT—A simulation program for non-isothermal multiphase reactive geochemical transport in variably saturated geologic media: Applications to geothermal injectivity and CO2 geological sequestration. *Computers & Geosciences*, 32, 145-165.
- YAMAMOTO, S., MIYOSHI, S., SATO, S. & SUZUKI, K. 2013. Study on geomechanical stability of the aquifer -caprock system during CO₂ sequestration by coupled hydromechanical modelling. *Energy Procedia*, 37, 3989-3996.
- YIN, S., DUSSEAULT, M. B. & ROTHENBURG, L. 2011. Coupled THMC modeling of CO2 injection by finite element methods. *Journal of Petroleum Science and Engineering*, 80, 53-60.
- YUE, M., SHANGQI, G., HE, Y. & XIAOHUI, C. 2022. Coupled Thermo-Hydro-Mechanical-Chemical processes with reactive dissolution by non-equilibrium thermodynamics. *Journal of the Mechanics and Physics of Solids*, 105065.
- ZERAI, B., SAYLOR, B. Z. & MATISOFF, G. 2006. Computer simulation of CO2 trapped through mineral precipitation in the Rose Run Sandstone, Ohio. *Applied Geochemistry*, 21, 223-240.
- ZHANG, R., WINTERFELD, P. H., YIN, X., XIONG, Y. & WU, Y.-S. 2015. Sequentially coupled THMC model for CO2 geological sequestration into a 2D heterogeneous saline aquifer. *Journal of Natural Gas Science and Engineering*, 27, 579-615.
- ZHANG, R., YIN, X., WINTERFELD, P. H. & WU, Y.-S. A fully coupled model of nonisothermal multiphase flow, geomechanics, and chemistry during CO2 sequestration in brine aquifers. Proceedings of the TOUGH Symposium, 2012. 838-848.
- ZHANG, R., YIN, X., WINTERFELD, P. H. & WU, Y.-S. 2016. A fully coupled thermal-hydrological-mechanical-chemical model for CO₂ geological sequestration. *Journal of Natural Gas Science and Engineering*, 28, 280-304.
- ZHANG, S. & LIU, H.-H. 2016. Porosity—permeability relationships in modeling salt precipitation during CO2 sequestration: Review of conceptual models and implementation in numerical simulations. *International Journal of Greenhouse Gas Control*, 52, 24-31.

- ZHANG, X. & ZHONG, Z. 2017a. A coupled theory for chemically active and deformable solids with mass diffusion and heat conduction. *Journal of the Mechanics and Physics of Solids*, 107, 49-75.
- ZHANG, X. & ZHONG, Z. 2017b. A thermodynamic framework for thermo-chemo-elastic interactions in chemically active materials. *SCIENCE CHINA Physics, Mechanics & Astronomy*, 60, 084611.
- ZHANG, X. & ZHONG, Z. 2018. Thermo-chemo-elasticity considering solid state reaction and the displacement potential approach to quasi-static chemo-mechanical problems. *International Journal of Applied Mechanics*, 10, 1850112.
- ZHENG, L. & SAMPER, J. 2008. A coupled THMC model of FEBEX mock-up test. *Physics and Chemistry of the Earth, Parts A/B/C*, 33, S486-S498.
- ZHOU, H., HU, D., ZHANG, F., SHAO, J. & FENG, X. 2016. Laboratory investigations of the hydro-mechanical—chemical coupling behaviour of sandstone in CO2 storage in aquifers. *Rock Mechanics and Rock Engineering*, 49, 417-426.
- ZHOU, X., AL-OTAIBI, F. & KOKAL, S. 2017. Investigation of Relative Permeability Characteristics for Supercritical CO2 Displacing Water and Remaining Oil after Seawater Flooding in Carbonate Rocks at Reservoir Conditions. *SPE Middle East Oil & Gas Show and Conference*. Manama, Kingdom of Bahrain: Society of Petroleum Engineers.
- ZHOU, X. & BURBEY, T. J. 2014a. Fluid effect on hydraulic fracture propagation behavior: a comparison between water and supercritical CO₂ like fluid. *Geofluids*, 14, 174-188.
- ZHOU, X. & BURBEY, T. J. 2014b. Fluid effect on hydraulic fracture propagation behavior: a comparison between water and supercritical CO 2 like fluid. *Geofluids*, 14, 174-188.
- ZHOU, X., LIANG, D., LIANG, S., YI, L. & LIN, F. 2015. Recovering CH4 from natural gas hydrates with the injection of CO2–N2 gas mixtures. *Energy & fuels*, 29, 1099-1106.
- ZHU, C., LI, Y., ZHAO, Q., GONG, H., SANG, Q., ZOU, H. & DONG, M. 2018a. Experimental study and simulation of CO2 transfer processes in shale oil reservoir. *International Journal of Coal Geology*, 191, 24-36.
- ZHU, H., TANG, X., LIU, Q., LI, K., XIAO, J., JIANG, S. & MCLENNAN, J. D. 2018b. 4D multi-physical stress modelling during shale gas production: A case study of Sichuan Basin shale gas

reservoir, China. *Journal of Petroleum Science and Engineering*, 167, 929-943.